Author:
Wilkinson, Harry J A

Title:
Exploring iron speciation in cross-coupling chemistry

Exploring Iron Speciation in Cross-Coupling Chemistry

Harry J. Wilkinson

A thesis submitted to the University of Bristol in accordance with the requirements of the degree of Doctor of Philosophy in the School of Chemistry, Faculty of Science

March 2022

Abstract

The replacement of palladium in cross-coupling chemistry with iron has been a long-term goal in the realm of sustainable chemistry, with new methodologies opening the way for new mechanistic investigations which in turn inform the development of new, more effective, methodologies. These investigations have shown a wide range in accessible iron species, oxidation states, and ligand roles in this chemistry dependent on a wide variety of factors in the reaction.

Chapter 2 reports a study of the reactivity of the homoleptic organoiron complexes Fe_2Mes_4 and $[FeMes_3]^-$ with the main group salts $ZnBr_2$ and $MgBr_2$ as well as the reactivity with the boronic esters ^nBuBPin and ^tBuBPin, species all formed as side products in different cross-coupling reactions. The use of ^1H NMR spectroscopy enabled the identification of a heteroleptic organoiron-bromide species $[FeBrMes_2]^-$ as being formed upon reaction of these complexes with the Mg, Zn or Fe bromide salts. This was then isolated and characterised by X-ray diffraction. The capacity of iron-mesityl complexes to transmetallate reversibly to these main group salts was also uncovered.

Chapter 3 details a mechanistic investigation of an iron-catalysed Kumada cross-coupling between an aryl Grignard reagent and an alkyl halide. Through the profiling of stoichiometric reactions of a series of iron-mesityl complexes with OctBr, their respective rates of reaction were determined, and a radical, $Fe^{II}/Fe^{III}/Fe^{IV}$-based catalytic cycle has been proposed.

In Chapter 4, another aspect of iron catalysis is explored, namely the iron-catalysed reduction of N_2 to NH_3. Taking inspiration from previously reported synthetic iron-based N_2 reduction catalysts, a series of iron complexes bearing ferrocenyl-diphosphine ligands were synthesised as potential pre-catalysts for N_2 reduction. However, this reactivity was prevented by the reduction of the ferrocenyl ligand occurring before N_2 binding occurs. As an alternative, a series of octanuclear, $[Fe_8S_4]$ clusters supported by pyrazolate ligands were synthesised, taking a cue from the use of nitrogenase enzymes which bear a carbide core embedded in an iron-sulphur cluster. These clusters were characterised by ^1H NMR, before being reacted with aryl and acetylyl organolithium reagents, to give organometallic products.

Acknowledgments

My first thanks must go to Robin, without whom none of this work would have been possible. His ideas, enthusiasm, and passion for the subject have been a constant boon to my work and made me a better chemist.

I've had the privilege and joy to work with many wonderful people during my time at Bristol. Thanks to Stephen and Harry for showing me the ropes in the lab and seeing me off on the journey which is now coming to end, Sanita for lending an ear and pretending to laugh whenever I tried to be funny, and Mattia for his genuine interest in my work and constantly helpful advice.

Thanks also to Ben for DJing a significant portion of my time in the lab, even for the times it was J Cole; to Rob for always being ready to help me work through a problem and offering the best solution, especially when it wasn't the one I wanted to hear. I only wish I could have had more time working with Joe and Michael, who were a pleasure to get to know in the final stages of my time in the lab and who I'm sure both will go on to do great things.

I also can't forget to mention our lab neighbours in the Pringle and Bower groups for making me feel a part of the bigger community on the fifth floor.

Finally, I have to thank Amy for always being by my side, and for pushing me to be the person that I am today.

Declaration

I declare that the work in this thesis was carried out in accordance with the regulations of the University of Bristol and no part of this thesis has been submitted for any other academic award. The work is original, except where indicated by reference in the text and any work done in collaboration with, or with the assistance of others, is indicated as such. Any views expressed are those of the author.

Harry JA Wilkinson

University of Bristol

March 2021

Abbreviations

12c4	12-crown-4	dippf	1,1'-bis (diisopropylphosphino) ferrocene
acac	acetylacetonate		
Ar	aryl	dpbz	1,2-bis (diphenylphosphino) benzene
ATP	Adenosine triphosphate		
ATRP	Atom Transfer Radical Polymerisation	dppf	1,1'-bis (diisophenylphosphino) ferrocene
BAr^F	Tetrakis(3,5-bis(trifluorophenyl)phenyl) borate		
		EAM	Earth Abundant Metal
Bn	Benzyl	EPR	Electron Paramagnetic Resonance
CAAC	Cyclic(alkyl)(amino)carbene		
Cp	Cyclopentadienyl	Et	Ethyl
Cp*	Pentamethyl-cyclopentadienyl	EXAFS	Extended X-ray Absorption Fine Structure
Cy	Cyclohexyl	FeMoco	Iron-Molybdenum Cofactor
DBE	1,2-dibromoethane	GC-FID	Gas-Chromatography-Flame Ionisation Detection
depe	1,2-bis (diethylphosphino)ethane		
depf	1,1'-bis(diethylphosphino) ferrocene	HMTA	hexamethylenetetraamine
		IMes	1,3-bis-(2,4,6-trimethylphenyl)imidazol-2-ylidene
DFT	Density Functional Theory		
Dipp	Diisopropylphenyl	IPr =	1,3-bis-(2,6-diisopropylphenyl)imidazol-2-ylidene

iPr	Isopropyl	SciOPP	1,2-bis[bis{3,5-di(tert-butyl)phenyl}phosphino]benzene
k	reaction rate		
Lut	2,6-Lutidine	SIPr	1,3-Bis(2,6-diisopropylphenyl)imidaolidin2-ylidene
MCD	Molecular Circular Dichroism		
Me	Methyl	tBu	tert-butyl
Mes	2,4,6-trimethylphenyl	THF	Tetrahydrofuran
Min	minutes	TM	Transition Metal
Naph	Naphthyl	TMEDA	Tetramethyl-ethylenediamine
nBu	n-butyl		
NHC	N-Heterocyclic Carbene	TOF	Turnover Frequency
NMP	N-Methylpyrrolidine	TON	Turnover Number
NMR	Nuclear Magnetic Resonance	XAS	X-ray Absorption Spectroscopy
OAc	Acetate	XRD	X-Ray Diffraction
Oct	Octyl	Xyl	2,6-dimethylphenyl
OTf	trifluoromethanesulfonyl		
OTs	toluenesulfonyl		
PCET	Proton-Coupled Electron Transfer		
Ph	Phenyl		
Pin	Pinacol		
p-Tol	4-methylphenyl		
pz	pyrazolate		

Table of Contents

1. Chapter 1 – Introduction

1.1 – Palladium-Catalysed Cross-Coupling Chemistry

In the realm of synthetic chemistry, few advancements could be considered to have been as revolutionary as the development of cross-coupling reactions to form C-C bonds. This impact was recognised in the award of the 2010 Nobel Prize in Chemistry to Richard Heck, Ei-ichi Negishi, and Akira Suzuki '*for palladium-catalysed cross couplings in organic synthesis*'.[1]

Cross-coupling refers to a reaction type in which an organic halide or pseudo-halide (triflate, tosylate, etc) is coupled with an organometallic nucleophile through the use of a transition metal catalyst. (Scheme 1.1)

$$R - X + R' - M \xrightarrow{[TM]} R - R' + M - X$$

R, R' = alkyl, aryl, alkenyl...
X = Cl, Br, I, OTf, OTs...
[TM] = Pd, Ni, Fe...
M = MgX (Kumada-Corriu), BY$_2$ (Suzuki-Miyaura), ZnX (Negishi)...
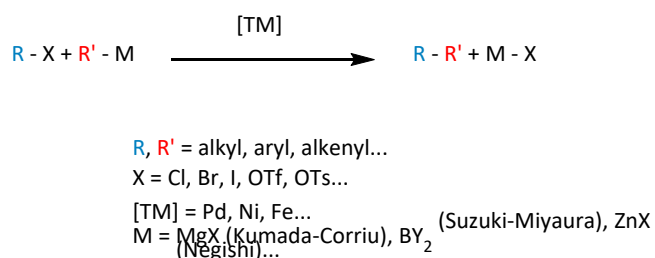
Scheme 1.1: The general form of a cross-coupling reaction.

Such chemistry is predominant across the whole field of organic synthesis, including in academia and industry. It has been used in the syntheses of many large-scale pharmaceutical products, including Naproxen, a popular over-the-counter painkiller (Scheme 1.2).[2]
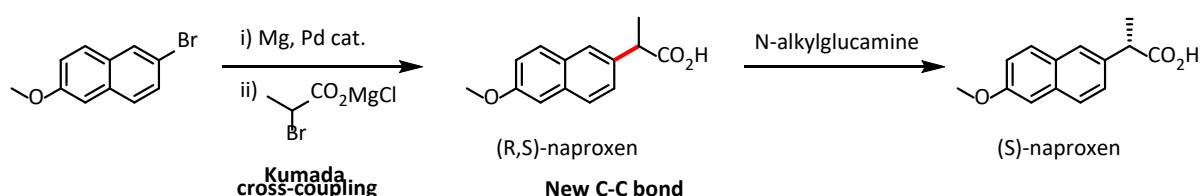
Scheme 1.2: The final stages of the synthesis of (S)-naproxen, including a Kumada cross-coupling reaction.

As suggested by the title of the 2010 Nobel Prize, the current transition metal of choice for these reactions is palladium, having been the basis for the myriad breakthroughs in the field through the 1970's with the initial reports of the Suzuki[3], Kumada[4], and Negishi[5] cross-coupling reactions, amongst many others.

With the wealth of mechanistic investigation that has accompanied the dominance of palladium in this area, a firm picture of the typical mechanistic pathway has formed.[6] (Scheme 1.3)
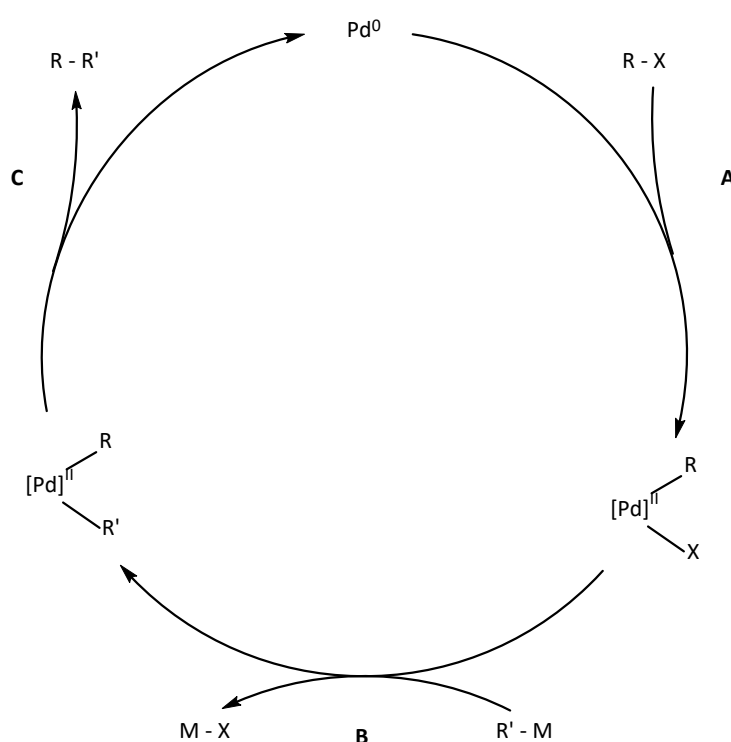
Scheme 1.3: The generic catalytic cycle for a palladium-catalysed cross-coupling reaction.

While Pd^{II} salts are often used as pre-catalysts due to their stability under aerobic conditions, and despite some mechanistic investigations initially invoking a Pd^{II}/Pd^{IV} cycle[7,8] common wisdom now accepts that these Pd^{II} species are reduced *in situ* by the nucleophile to form the Pd^0 active species.

From a Pd^0 pre-catalyst, the first step (**A**) is oxidative addition of the electrophile to the palladium centre, followed by transmetallation with the organic nucleophile (**B**), before final reductive elimination of the cross-coupled product (**C**).

The oxidative addition step has been determined to occur through 2-electron pathways, as opposed to radical pathways for both sp^3 and sp^2 electrophiles.[9–11]

In most cases, the facility of the oxidative addition step follows the trend I > Br > Cl, with palladium catalysts particularly struggling with the activation of C-Cl bonds. This lower reactivity with organochlorides can be mitigated to some extent by the use of bulky monophosphine or phosphite ligands which promote the oxidative addition step.[12–14]

The use of palladium has been favoured so heavily due to its incredibly high reactivity and selectivity for this chemistry, and in certain examples can be used in loadings as low as 0.0005 mol%.[12,15] Its high activity is such that there have been multiple occasions in which protocols reported as 'transition metal-free' were later found to be caused by ultra-low loadings of palladium impurities in other components of the reaction.[16–19] This potential for low loading mitigates some issues commonly associated with the use of palladium such as the high cost and environmental impact.[20]

Aside from the need to compensate for generally poorer ability to activate C-Cl bonds, one major drawback to the use of palladium catalysts for industrial applications, particularly pharmaceuticals, is the issue of toxicity, which necessitates stringent regulation over the allowable palladium content in pharmaceutical products, with an upper concentration limit of 10 ppm permitted.[21] This regulation has implications for their potential roles in industry; often steps involving the use of palladium are pushed earlier in the synthesis of such chemicals to increase the number of purification steps occurring between the use of metal and the final product. Otherwise, extra purification methods are required, such as repeated recrystallisation of the product, or the use of palladium scavengers, both of which lower yield and drive up cost.[22]

These concerns, along with a wider drive to more sustainable methods in industry,[23] has led research efforts to explore alternative metals for cross-coupling chemistry.

1.2 – Iron-Catalysed Cross-Coupling Reactions

Aside from nickel, iron has been the most well studied of the first-row transition metals for cross-coupling chemistry, with early work mostly focussing on Kumada-Corriu cross-coupling, although several examples of both Negishi and Suzuki couplings have been reported as well.[24–27]

Iron holds some advantages for use as a catalyst over palladium, most obvious is its high abundance and low cost, with a monetary value that is orders of magnitude below palladium.[20] It also generally has a much lower toxicity than palladium, being a significant micronutrient present in human diets on the scale of several mg a day.[28] This translates to a higher allowable limit in pharmaceutical products. If palladium-catalysed steps may be replaced with those catalysed by iron in industrial processes, this has the potential to drastically lower the monetary cost and carbon footprint associated with the final product.

Many of the early examples of iron-catalysed cross-coupling reactions were Kumada cross-couplings, beginning with Kharasch's early report of various metal halides catalysing the homo-coupling of aryl Grignard reagents, or cross-coupling with organic halides.[29] After this discovery, the field lay dormant for many decades before Kochi's report of what is now called a Kumada-Corriu cross-coupling in 1971.[30] Through the use of low loadings of $FeCl_3$ as a catalyst, the coupling of simple alkyl Grignard reagents with vinyl bromides was achieved with moderate yields. (Scheme 1.4)
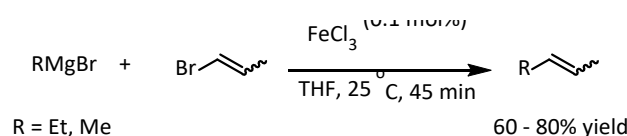
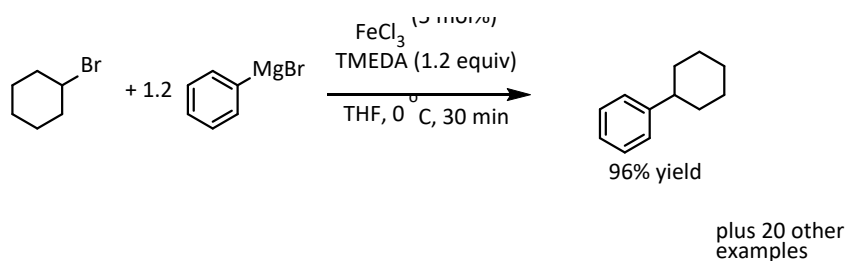
Scheme 1.4: The Kumada cross-coupling of alkyl Grignard reagents with vinyl bromides as reported by Kochi.

Later work by Cahiez and co-workers showed a drastic improvement in the yields possible with this reaction through addition of NMP (N-Methylpyrrolidone), amongst other polar co-solvents,[31] though they were unable to assign the role of NMP beyond acting as a co-solvent. (Scheme 1.5)

THF: 5%

THF/NMP: 85%
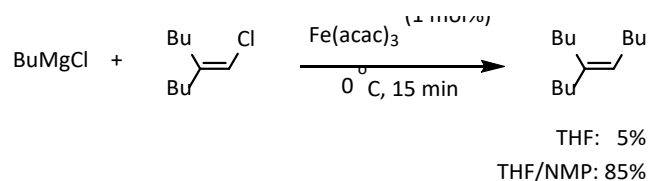
Scheme 1.5: Cahiez's report of iron-catalysed Kumada cross-coupling.

Improvement of this protocol came with the report by Nakamura and co-workers, reporting near-quantitative yields in the coupling of alkyl halides with aryl Grignard reagents through the addition of TMEDA (Tetramethylethylenediamine) at a molar loading comparable with that of the coupling partners.[32] (Scheme 1.6)

96% yield

plus 20 other examples

Scheme 1.6: Nakamura's protocol for the FeCl$_3$-catalysed cross-coupling of alkyl halides with aryl Grignard reagents.

Also vital for maintaining such high yields was slow addition of a pre-stirred mixture of TMEDA and the Grignard reagent.

Turning to Negishi cross-coupling, in 2009 Bedford reported high yields in the coupling of benzyl halides with arylzinc reagents through the use of a pre-formed iron-diphosphine catalyst, FeCl$_2$(dpbz)$_2$.[33] (Scheme 1.7)
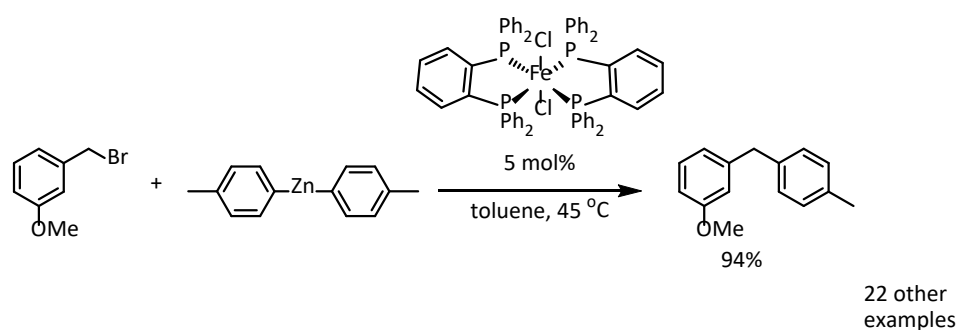
Scheme 1.7: Bedford's report of an iron-phosphine catalysed Negishi cross-coupling.[33]

Finally, an iron-catalysed Suzuki reaction was first achieved by Nakamura in 2010, in which the coupling of alkyllithium-activated boronate esters with alkyl halides was achieved.[34] (Scheme 1.8)

Scheme 1.8: Nakamura's protocol for a Suzuki cross-coupling with alkyl halides.[34]

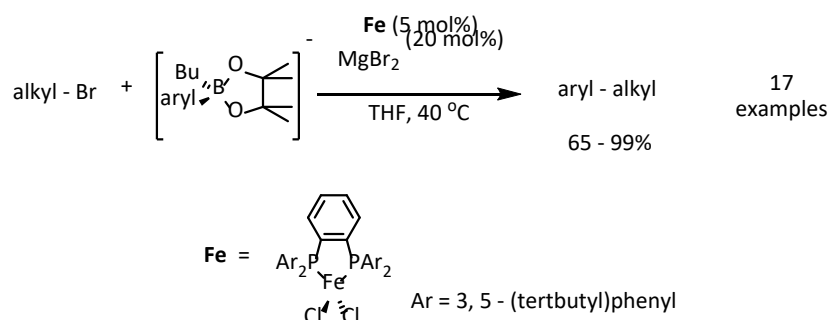Interestingly, it was reported that the addition of $MgBr_2$ was vital for reactivity to occur, with 0% yield observed in its absence. The precise role of $MgBr_2$ was undetermined but was assigned as an aid to transmetallation.

Later work reported by Bedford reported the first examples of the synthesis of biaryls through iron-catalysed Suzuki coupling. This was achieved through the use of a N-pyrrole amide directing group, as well as repeating the use of $MgBr_2$ as an additive. Through an extensive mechanistic investigation they were able to assign its role not as an aid to transmetallation, but a bromide source.[24] (Scheme 1.9)
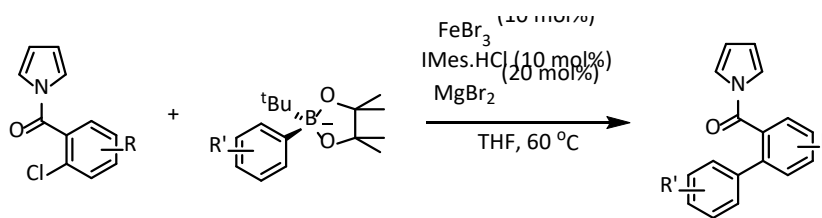
Scheme 1.9: Bedford's report of an iron-catalysed Suzuki biaryl cross-coupling.[24]

The need for activated boronate esters was addressed by Byers in 2018 in his report on Suzuki coupling with unactivated boronic esters, in which the use of an amide ligand in conjunction with the addition of a lithium amide base allowed coupling with a simple boronic ester.[26] (Scheme 1.10)
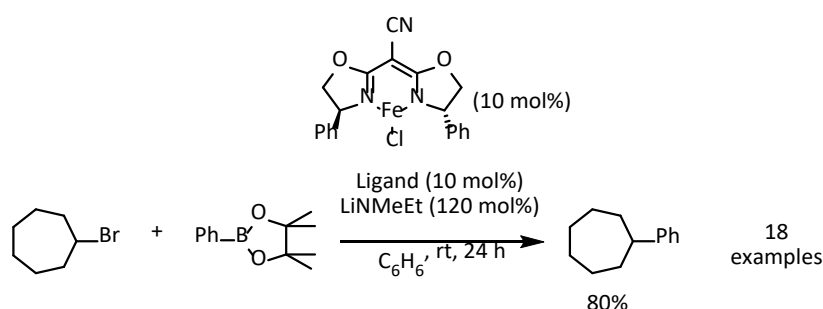
Scheme 1.10: Byers' protocol for an iron-catalysed Suzuki coupling with unactivated boronic esters.[26]

Despite these multiple successes, some issues arise with the use of iron from the specifics of its chemistry. Iron-containing catalytic intermediates are often extremely air- and moisture-sensitive, rendering their isolation difficult and complicating characterisation by X-ray diffraction or mass spectrometry. Alongside this, many of these intermediates are paramagnetic rendering more standard characterisation by standard ^{1}H NMR impossible. Instead, researchers must rely on paramagnetic NMR spectroscopy, or more niche techniques such as Electron Paramagnetic Resonance (EPR), or Mossbauer spectroscopies to gain structural insights.

These factors have all contributed to a great difficulty in determining the mechanistic pathways through which iron-catalysed reactions occur. The ambiguity is such that active

oxidation states in iron-catalysed cross-couplings have been proposed between Fe^{-II} [35] and Fe^{IV},[36] both through 1-electron[37] and 2-electron pathways[38], and with neutral, anionic, or cationic iron complexes. This is the case even discounting examples in which a ligand is added to improve reactivity.

1.1.1 – Mechanisms of Ligand-Free Iron-catalysed Cross-coupling Reactions
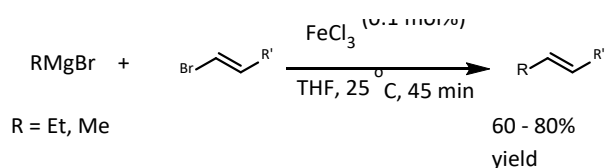
Scheme 1.11: The Kumada cross-coupling of alkyl Grignard reagents with vinyl bromides as reported by Kochi.

In the case of Kochi's 1971 report of a Kumada cross-coupling, EPR analysis of the reaction mixtures identified an S = ½ intermediate[39] which was initially assigned as an Fe^{I} species, later deemed the 'Kochi complex'. It was, however, not isolated at the time, nor was its structure determined.[38] From this data, Kochi assigned an Fe^{I}/Fe^{III} mechanism essentially identical to the Pd^{0}/Pd^{II} cycle proposed for palladium-catalysed cross-couplings; with oxidative addition to this Fe^{I} intermediate, followed by transmetallation with the Grignard reagent and reductive elimination of the cross-coupled product. (Scheme 1.12)
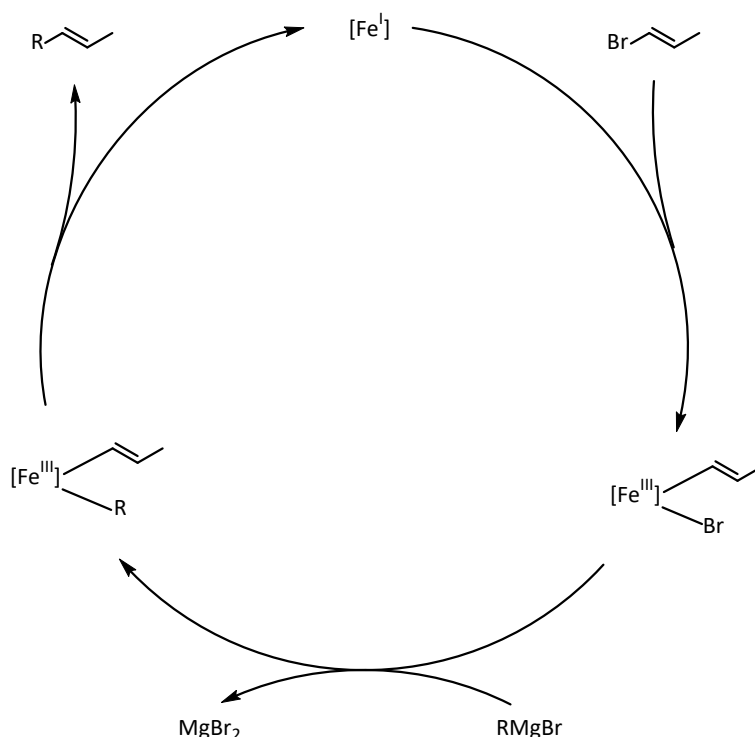
Scheme 1.12: The catalytic cycle proposed by Kochi for an iron-catalysed cross-coupling.

Such a mechanism was later supported by a combined experimental and computational work published by Norrby[40], which demonstrated the feasibility of oxidative addition to an Fe^I complex, and reductive elimination from an Fe^{III}. It was also noted that there was little energetically separating oxidative addition or transmetallation from occurring as the first step in the cycle, leading to more in-depth mechanistic investigations later.

Further insight into this came when Neidig and co-workers reported their isolation and characterisation of the 'Kochi complex', assigning it as a $[Fe_8Me_{12}]^-$ cluster of a mixed Fe^I/Fe^{II} oxidation state (**1**).[41] Interestingly, the complex was not found to be reactive directly with an electrophile, but rather a resting state from which catalysis can be 'switched on' by addition of further Grignard reagent. Subsequent to this, reaction with electrophile gives quantitative conversion to the cross-coupled product. (Scheme 1.13)
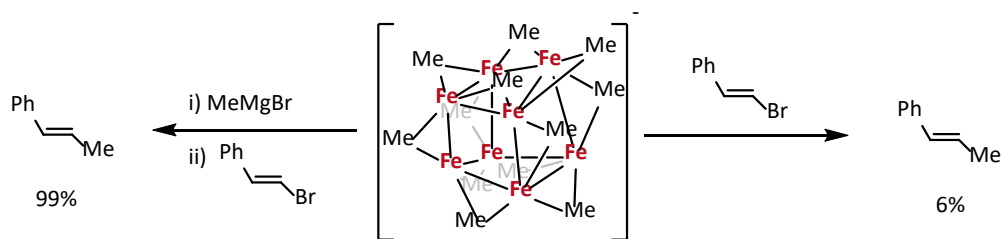
Scheme 1.13: The reactivity of the 'Kochi complex' $[Fe_8Me_{12}]^-$ (**1**) with electrophile.

Neidig and co-workers were later also able to discern the mechanistic role of NMP in these reactions, in which Cahiez observed a drastic increase in yield upon its addition as co-solvent with THF.[31] Neidig discovered that in the presence of NMP, **1** does not form.[42] Instead a trimethyl ferrate species $[FeMe_3][Mg(NMP)_6]$ forms, which is able to react quantitatively with electrophile to produce the cross-coupled product (Scheme 1.14). The role of NMP, and presumably other polar co-solvents, is therefore to ligate the magnesium counterion, furnishing the more reactive ferrate species to perform the reaction.
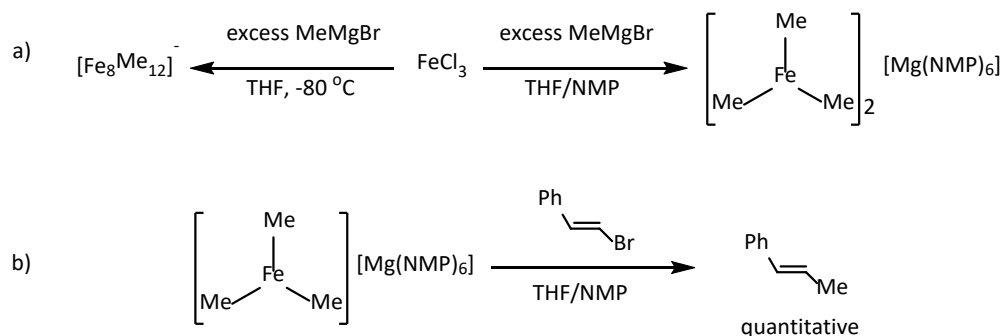
Scheme 1.14: a) The reactivity of $FeCl_3$ with MeMgBr in the presence of NMP giving $[FeMe_3]^-$, and in its absence (b), forming **1**.

In 2002, Fürstner reported the first iron-catalysed coupling of aryl halides, notably reporting a system which showed improved reactivity with aryl chlorides in direct comparison with the corresponding bromides and iodides.[35] They also achieved yields >95% with aryl tosylates and triflates. (Scheme 1.15) This provided a good showcase of the differing capability of iron catalysts versus the palladium standard, for which reaction with chloro-electrophiles presents issues.
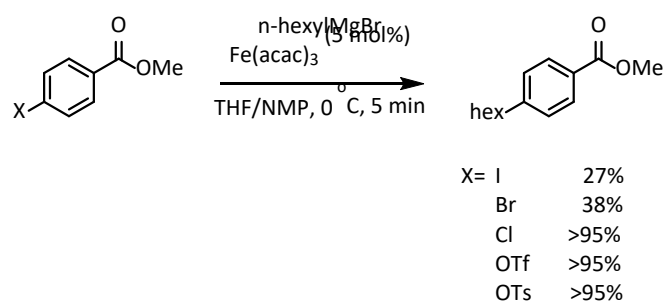
Scheme 1.15: Fürstner's iron-catalysed Kumada cross-coupling with aryl (pseudo)halides, showing the variance in yield with the identity of the (pseudo)halide.

An alternative mechanism to the Fe^{I}/Fe^{III} pathway was proposed by Fürstner for this transformation, assigning the lowest oxidation state of iron as Fe^{-II}, proposed to be accessed through formation of an 'inorganic Grignard reagent' $Fe^{-II}(MgBr)_2$ as proposed by Bogdanovic.[43] (Scheme 1.16)

Fürstner supported this assignment with later results that purported to find that such Fe^{-II} complexes were competent pre-catalysts for cross-coupling, outperforming comparable species in higher oxidation states.[44]
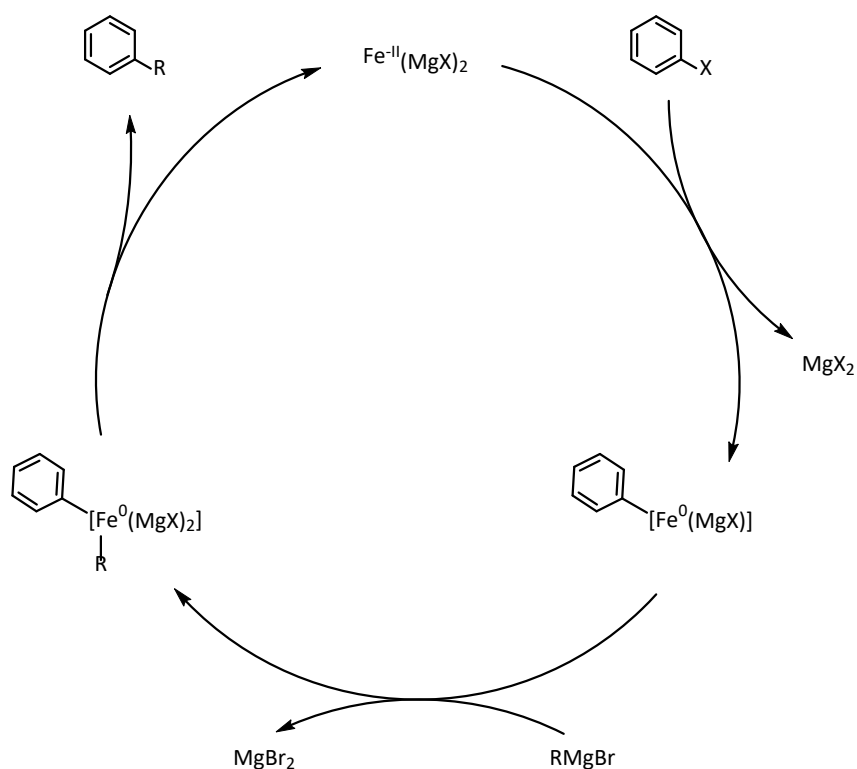
Scheme 1.16: The Fe^{-II}/Fe^0 catalytic cycle as proposed by Furstner.

Computational work by Norrby examined the facility of this Fe^{-II}/Fe^0 cycle, along with Fe^0/Fe^{II} and Fe^I/Fe^{III} and found that the reductive elimination step from an Fe^0 centre to form Fe^{-II} was thermodynamically inaccessible; therefore, this cycle is incredibly unlikely to be operative in catalysis. Fürstner's observation of Fe^{-II} species being competent as pre-catalysts was reasoned to be due to the oxidative addition and transmetallation steps being more favourable at such an oxidation state. This allows two oxidative addition steps to occur consecutively, forming an Fe^{II} species which may then go on to perform catalysis.[40] The same study assigned Fe^I/Fe^{III} as the most plausible of the examined redox couples to be active, with Fe^{II}/Fe^0 being described as "thermodynamically feasible but kinetically implausible".[45]

These findings were later supported by an EXAFS study reported by Bauer and co-workers, in which they found no evidence of Fe-Mg pairs during turnover.[46] Furthermore, they also assigned an Fe^I oxidation state as operative, specifically ruling out Fe^{II} and Fe^{-II} states that had been proposed previously.[47,48]

Such a cycle does, however, depend on Fe^I being an accessible oxidation state in the first place. The most common iron pre-catalysts used are Fe^{II} or Fe^{III} salts, therefore accessing Fe^I requires a reductive process to occur before turnover may commence. Commonly, the route through which this occurs is by reaction with the nucleophile, reductively eliminating the homo-coupled product. (Scheme 1.17)
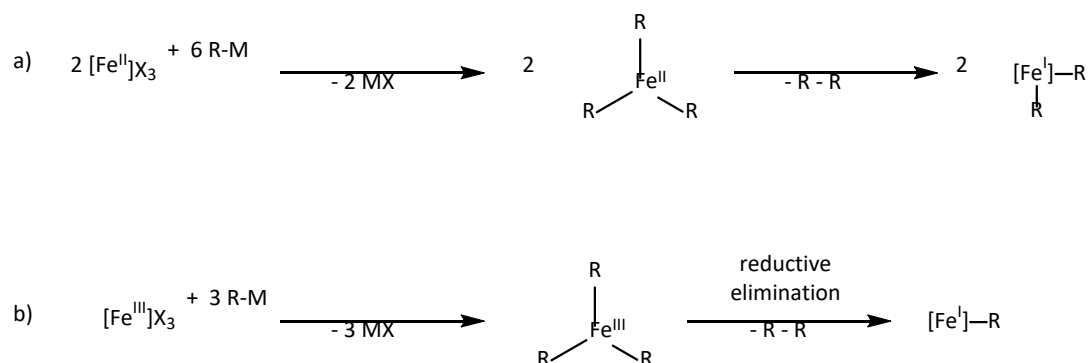
Scheme 1.17: The production of an Fe^i active species from a) Fe^{II} and b) Fe^{III} pre-catalysts.

In the case of Fe^{II} pre-catalysts, this is a bimetallic process. The occurrence of such processes has been supported by the isolation of Fe^I species from catalytically representative solutions with phenyl or tolyl substrates as the nucleophilic partner.[27,49]

The radical nature of iron-catalysed cross-couplings has been proposed for many systems. A report by Norrby and co-workers comprised a DFT investigation and a competitive Hammett study, investigating the activation of aryl and alkyl halides in a ligand-free reaction using $FeBr_3$ as pre-catalyst.[50] Their findings supported the assignment of a 2-electron Fe^I-Fe^{III} redox couple for aryl or alkenyl substrates, but a radical ATRP (Atom Transfer Radical Polymerisation) mechanism for alkyl halides.

However, such a process is not necessarily accessible for all substrates. In particular, more sterically bulky substrates disfavour elimination steps, being kinetically stabilised in the Fe^{II} oxidation state. This has been shown for benzyl,[51] mesityl,[52] and (trimethylsilyl)methyl[53] substituents. While reactions with these substituents may not access Fe^I, they do show catalytic activity. It appears then, that the identity of the nucleophile in reaction has an acute effect on the mechanisms accessed in cross-coupling reactions.

Furthermore, a recent report by Lefevre showed that from Fe^{II} intermediates, the identity of the electrophile can also change the mechanistic pathway that is followed. Two separate pathways were proposed, with the facility of each determined by the oxidation potential of the electrophile used.[54] For substrates that are easily reduced, a single-electron process between Fe^{II} and Fe^{III} was proposed as seen in (Scheme 1.18). In the case of electrophiles that are not so easily reduced, a Fe^{0}/Fe^{II} cycle may dominate instead; setting off from transient Fe^{0} species generated by the slow reduction elimination step, see (Scheme 1.18). Both cycles may also occur concurrently in the case of moderately oxidising substrates.
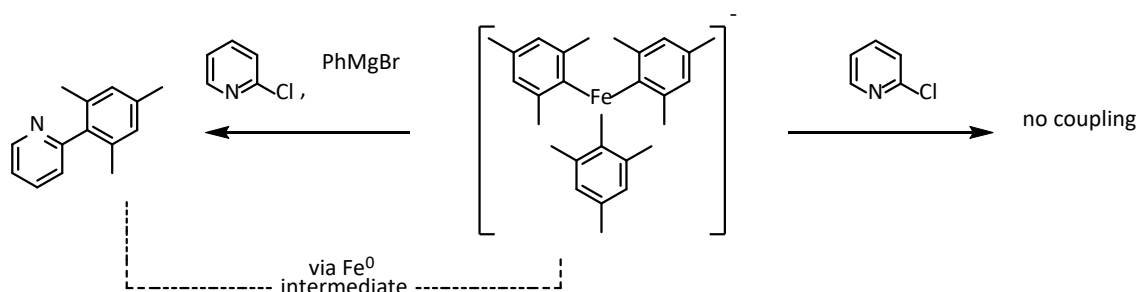
Scheme 1.18: Experiments performed by Lefevre and co-workers showing the capability of Fe^{0} intermediates to couple with less oxidising substrates.

1.1.2 – Mechanisms of Ligand-Added Iron-Catalysed Cross-Coupling Reactions

Alongside the ligand-free examples discussed up to this point, there have also been many reports of iron-catalysed cross-coupling reactions in which an added ligand is used to enable higher turnover. Mechanistic investigations of these protocols have revealed a common theme of stabilising higher oxidation states.

Neidig and co-workers performed a mechanistic investigation of Nakamura's alkyl-aryl Suzuki cross-coupling reaction (Scheme 1.19)[34] in which addition of the diphosphine ligand SciOPP (1,2-bis[bis{3,5-di(tert-butyl)phenyl}phosphino]benzene) enabled turnover.[55]
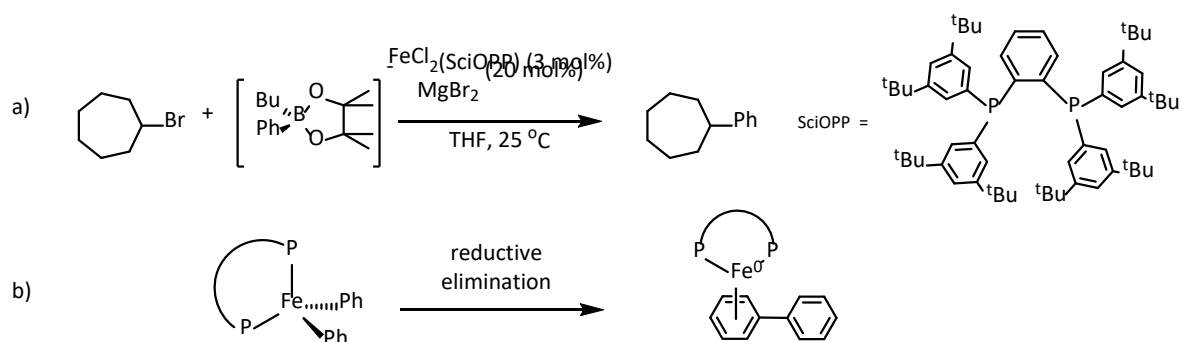
Scheme 1.19: a) The iron-catalysed Suzuki cross-coupling reaction reported by Nakamura. b) The formation of Fe^{0}SciOPP(biphenyl) by reductive elimination.

They found that while Fe^0 species were accessible through reductive processes (Scheme 14b), comparative head-to-head reactions of Fe^0 and Fe^{II} complexes showed that Fe^{II} acted as a more effective pre-catalyst, they therefore assigned Fe^0 species as off-cycle to a productive Fe^{II}/Fe^{III} catalytic cycle. A similar mechanism was proposed to be operative in Nakamura's TMEDA-ligated Kumada cross-coupling.[56]
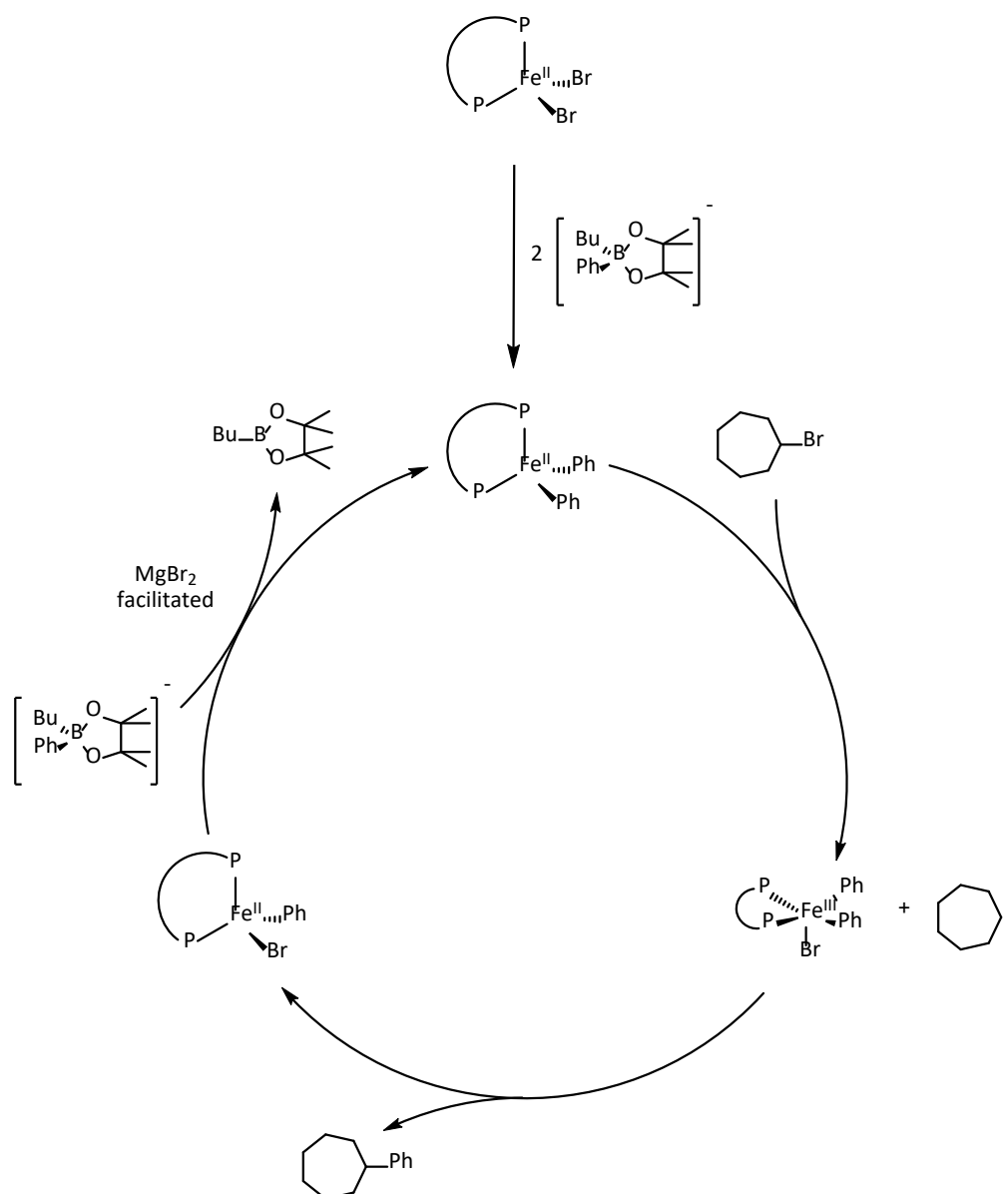
Scheme 1.20: The Fe^{II}/Fe^{III} catalytic cycle proposed by Neidig for a Suzuki cross-coupling.[55]

In contrast, analysis of Bedford's Negishi cross-coupling system assigned Fe^{I} species as the lowest catalytically relevant oxidation state.[27] By quantification of the produced quantity of the homo-coupled nucleophile, 4,4'-bitolyl, from the Fe^{II} pre-catalyst, $FeCl_2(dpbz)_2$, the bulk oxidation state in reaction was determined to be Fe^{I}. Potential candidates for the *in situ* generated Fe^{I} species, $FeCl(dpbz)_2$ (**2**) and $Fe(p\text{-}tol)(dpbz)_2$ (**3**) were then synthesised.

3 was produced by reaction of the FeCl$_2$(dpbz)$_2$ with (4-tol)$_2$Zn, with concomitant formation of 0.5 molar equivalents of the homo-coupled nucleophile observed. **2** was synthesised by reaction with BnMgCl. (Scheme 1.21)
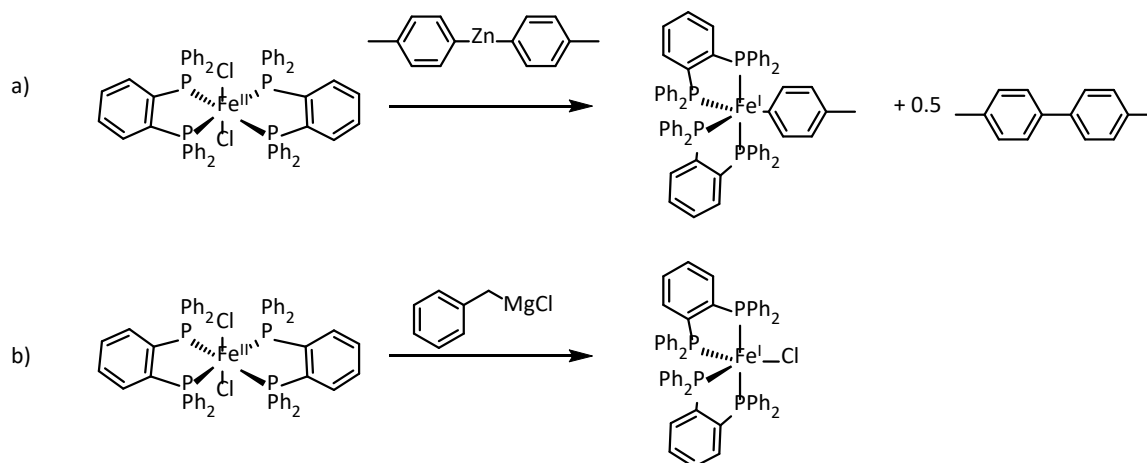
Scheme 1.21: The syntheses of Fe^I complexes as intermediates in Negishi cross-coupling.

In reactivity studies, both Fe^I species showed competence in catalysis, with **2** in particular performing similarly as the Fe^{II} pre-catalyst. From this result, it was assigned as being on the catalytic cycle. **3**, on the other hand, coupled at a rate 5 times slower than the others and was therefore assigned as an off-cycle species.

Interestingly, a brief kinetic study showed a second-order dependence of the Fe^{II} pre-catalyst on reaction rate, suggesting a bi-molecular reduction process occurring, once again supporting the assignment of an Fe^I active catalyst.

A computational study by Nakamura and co-workers also supported the assignment of a Fe^I active oxidation state for reactions incorporating phosphine ligands. They assigned a Fe^I/Fe^{II}/Fe^{III} cycle as operative in the coupling of aryl Grignard reagents with alkyl halides with a SciOPP ligand added.[57] (Scheme 1.22) Notably, these results agreed with their mechanistic investigation[58] of their report of the first enantioselective iron-catalysed cross-coupling reaction, in which a chiral phosphine ligand is used.[59]

a)

R

$Cl \overset{R}{\underset{}{\wedge}} CO_2R'$ + ArMgBr

tBu, P P, Me
Me tBu (6 mol%)
(3 mol%)
Fe(acac)$_3$
THF, 0 °C

$Ar \overset{R}{\underset{}{\wedge}} CO_2R'$

b)

P Fe^{II} Cl
P Cl

ArMgBr

MgBrCl

Cl
$\wedge CO_2R$

$\cdot \wedge CO_2R$

P Fe^{I} —Cl
P

P Fe^{II} Cl
P Ar

Ar
$\wedge CO_2R$

P CO$_2$
P Fe^{III}
Cl Ar
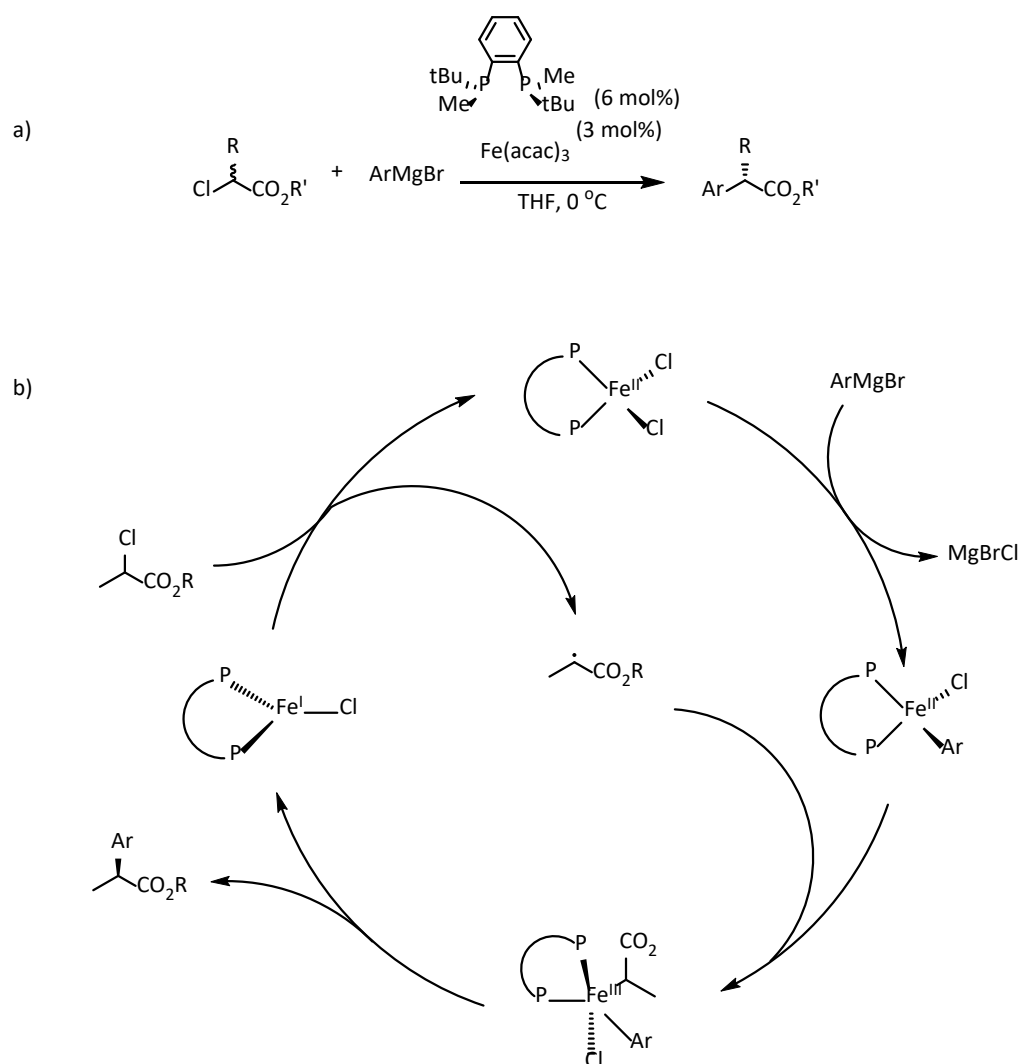
Scheme 1.22: a) Nakamura's protocol for the first enantioselective iron-catalysed cross-coupling reaction.[60] b) The Fe^{I}/Fe^{II}/Fe^{III} mechanism proposed by the Nakamura group for this reaction.[61]

Bedford later returned to the Negishi cross-coupling reaction with another mechanistic study on an iron-phosphine-catalysed aryl-alkyl coupling. (Scheme 1.23)

Br + Zn (⬡)$_2$ 2 MgBr$_2$

FeBr$_2$ (1 mol%)
dpbz (2 mol%)
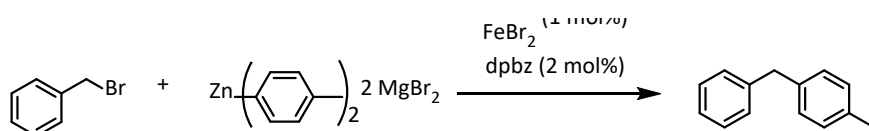
Scheme 1.23: The Iron-catalysed Negishi cross-coupling reaction studied by Bedford and co-workers.

Stoichiometric reactions showed the necessity of the presence of $MgBr_2$ to enable turnover; in the absence of $MgBr_2$, reaction of the $FeBr_2$ pre-catalyst with $Zn(p\text{-}tol)_2$ gave Fe^0 nanoparticles and homocoupled nucleophile, indicative of reductive elimination occurring. In the presence of $MgBr_2$, the formation of a salt pair $[FeBr_3][MgBr]$ is observed instead, but with the zinc nucleophile remaining unconsumed. (Scheme 1.24)
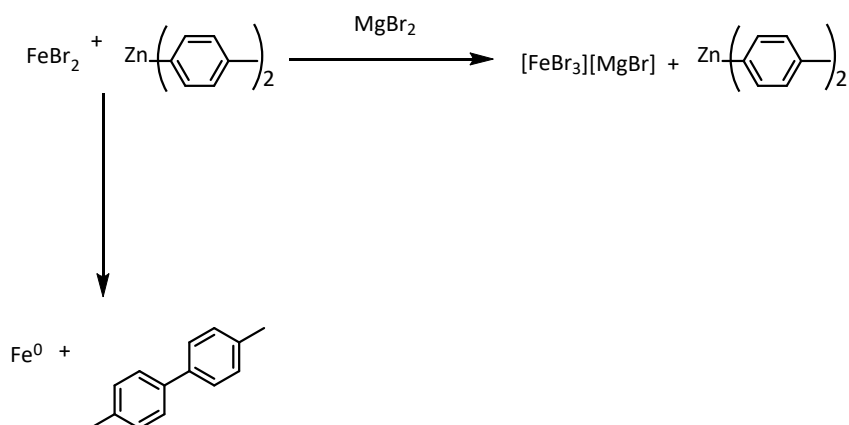
Scheme 1.24: Stoichiometric reactions of $FeBr_2$ with $Zn(p\text{-}tol)_2$ in the presence and absence of $MgBr_2$.

Only upon addition of large excesses of organozinc nucleophile is transmetallation to iron observed. This was observed with the mesityl substituent on the zinc nucleophile giving stability to the heteroleptic organoiron complexes that are proposed to be formed in reaction. (Scheme 1.25)
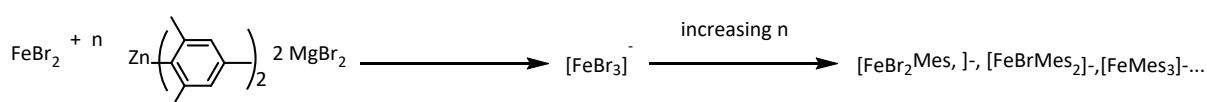
Scheme 1.25: The reaction of $FeBr_2$ with increasing quantities of $Zn(Mes)_2$.

Addition of the phosphine ligand dpbz to a solution of $[FeBr_3][MgBr]$ and $Zn(p\text{-}tol)_2$ gave the Fe^I species $FeBr(dpbz)_2$, analogous to that observed in Bedford's previous study (see Scheme 1.21a). This would appear to suggest that transmetallation to iron is predominately

facilitated by the chelation of phosphine to the iron centre. However, in the presence of an excess of organozinc nucleophile, as would be present in catalysis, no iron-phosphine species is observed. Instead, homo- and hetero-leptic iron species are observed. This observation, combined with XAFS (X-ray absorption fine structure) analysis of the reaction mixture during catalysis showing no Fe-P interactions led to the conclusion that the phosphine ligand is not bound to iron during turnover, but instead to the zinc nucleophile.

To summarise, while several proposals have been made for mechanistic pathways in iron-catalysed cross-coupling reactions, the high degree of complexity in such systems, along with the practical difficulties in their study, have prevented many concrete answers from being reached. This is the case even in systems without external ligands being added. What is clear is that a simple catalytic cycle covering all such reactions is unlikely to be operative. Instead, several, potentially overlapping, mechanisms may be at play depending on myriad factors including the identities of the electrophile and nucleophile, presence of ligands, and the loading of each component.

1.3 – Iron-catalysed N_2 Reduction

While in the realm of cross-coupling, iron catalysts are less well developed in comparison to metals like palladium and nickel, one area in which they are relatively dominant is in the reduction of N_2 to ammonia, so-called 'nitrogen fixation'.

The reduction of N_2 to more reactive products is one of the most important chemical transformations for both industry and biology, being the primary path through which nitrogen is made bioavailable. This makes it indispensable for the production of fertiliser at large scales and vital for combatting food insecurity the world over.

Industrially, the fixation of N_2 is performed in the Haber-Bosch process, in which NH_3 is produced directly from its constituent elements N_2 and H_2. (Scheme 1.26)

$$N_2 + 3 H_2 \xrightarrow[\text{Fe catalyst}]{450\ ^\circ C,\ 200\ atm} 2 NH_3$$
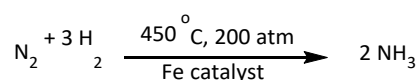
Scheme 1.26: The production of NH_3 from the Haber-Bosch process.

The catalyst used is predominately composed of Fe powder dispersed on an FeO carrier, with other additives including aluminium, calcium, and potassium.[62]

The impact of the development of this process was such that it was the subject of the 1918 Nobel Prize in chemistry, awarded to Fritz Haber.[63] Currently, the process provides the NH_3 responsible for around 450 million tonnes of fertiliser per year, and it is estimated that 80% of the nitrogen in the average human being was fixed through the Haber-Bosch process.[64] The scale of this reaction is such that 1-2% of the world's annual energy supply goes towards it, mainly in the production of H_2, along with 5% of the world's natural gas production.[65]

The high temperature and pressure requirements of this process have directed research efforts to more efficient methods to fix nitrogen, with many researchers looking to nature for inspiration.

In nature, the fixation of N_2 is accomplished by nitrogenase enzymes, in which N_2 is reduced under ambient conditions using biological sources of protons and electrons (Scheme 1.27), requiring a significant energy input of 16 molecules of ATP.[66]

$$N_2 + 8H_+ + 8e^- \xrightarrow{\text{Nitrogenase}} 2NH_3 + H_2$$
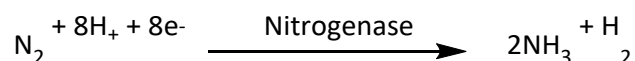
Scheme 1.27: The reduction of N_2 as performed by nitrogenase enzymes.

Nitrogenase enzymes come in a few distinct forms, either containing Fe/Mo, Fe/Fe, or Fe/V co-factors in their active sites, with a particular Fe/Mo co-factor (FeMoco) being the most well-studied (Figure 1.1).[67]
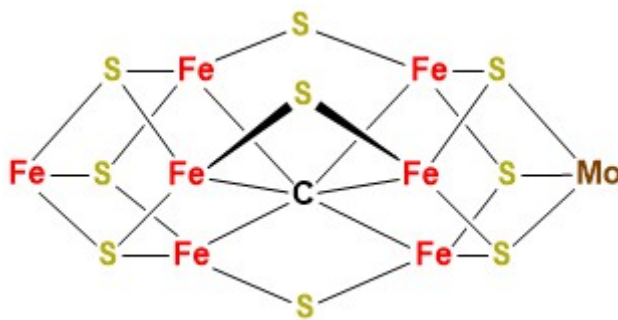
Figure 1.1: The Iron-molybdenum cofactor of Fe/Mo nitrogenase.

The general form of FeMoco was determined through X-ray diffraction in 2002 to a resolution of 1.16 Å[68]. While this was sufficient to understand the broad structure of the cofactor, it was not enough to determine the identity of the central atom. This assignment was accomplished later through a combination of high-resolution X-ray diffraction, X-ray emission spectroscopy, and NMR labelling experiments, finally assigning this central atom as carbon, in the carbide oxidation state (C^{4-}).[69,70]

The mechanism through which nitrogenase enzymes bind and reduce N_2 has been the subject of much disagreement and debate. Initial investigation of FeMoco, prior to the identification of Fe/Fe and Fe/V nitrogenases, assigned Mo as the site of N_2 binding,[67] but more recent works have assigned the binding site as the C-bound Fe atom.[71]

There remains debate as to what form this binding takes, with competing proposals each supported by reactivity studies with model iron complexes.[72,73]

The first proposal is that an iron-sulphur bond is cleaved concomitantly with N_2 binding to iron, giving a tetrahedral centre that retains an Fe-C bond to the carbide core. The alternative proposal is that the Fe-C bond is hemi-labile, and its lengthening and weakening facilitates the binding of N_2. (Scheme 1.28)
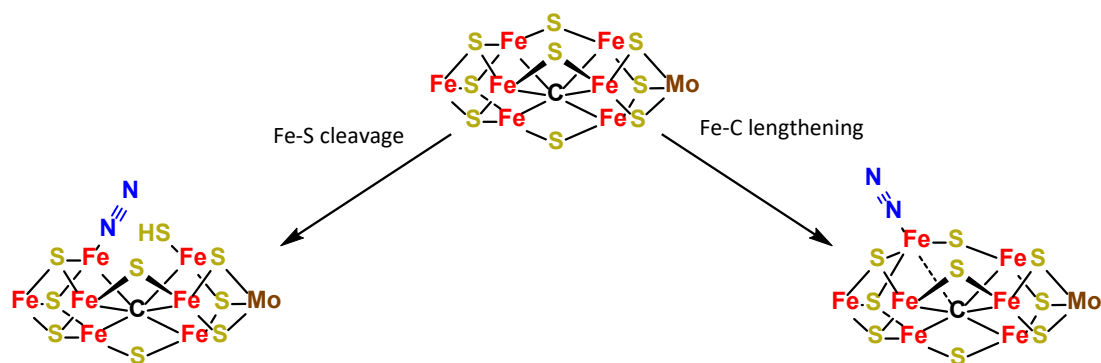
Scheme 1.28: Two potential first steps in N_2 binding to molybdenum nitrogenase.

More recent studies have pointed to a Fe-S cleavage step as operative in N_2 binding; however, the reduction mechanisms following on from this step remain undetermined.[74,75]

Driven by these observation, much work has been directed at attempting to use synthetic iron-sulphur complexes as molecular catalysts for the reduction of N_2 although no reports have been made of catalytic turnover being achieved on such complexes. Qu and co-workers reported the production of ammonia from a $[Fe_2S_2]$ nitrido complex upon reaction with H_2 or with H_2O and a reductant. It is worth noting, however, that the nitride moiety in this complex is not derived from N_2.[76] (Scheme 1.29)
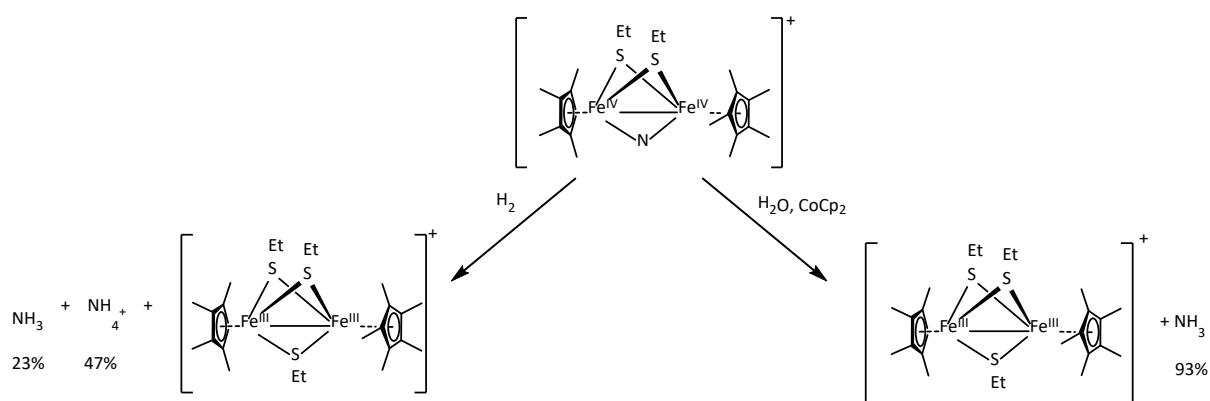
Scheme 1.29: The reactivity of a thiolate bridged Fe^{IV}-Fe^{IV} complex with H_2 or H_2O as reported by Qu and co-workers.[76]

Suess and co-workers reported the binding of N_2 to a molybdenum-iron-sulphur cluster supported by Cp and NHC ligands, the first example of N_2 binding to a synthetic iron-sulphur cluster.[77]
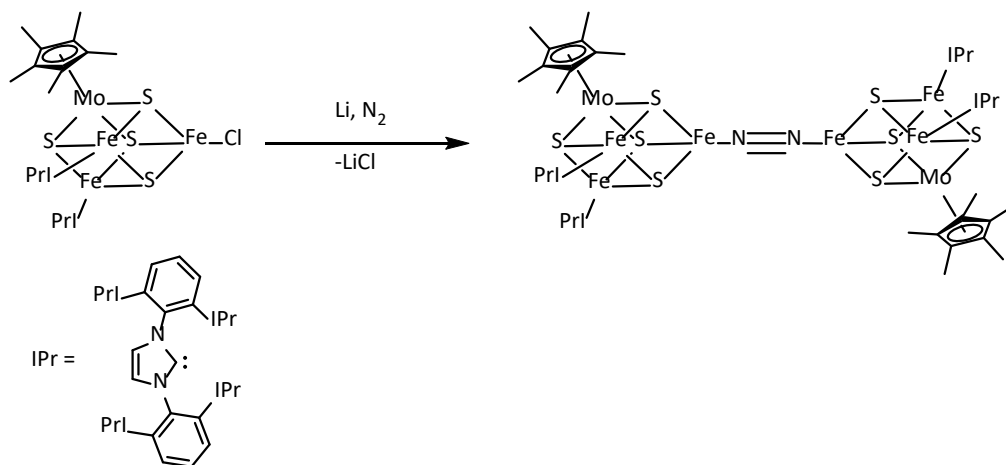
Scheme 1.30: Suess' system for N_2 binding at a molybdenum-iron-sulphur cluster.[77]

As for systems which achieve the catalytic reduction of N_2, research efforts have primarily focussed on Mo- and Fe-based molecular catalysts, although several other metals have been reported to be active for this transformation in stoichiometric reactions including cobalt,[78] vanadium,[79] osmium, and ruthenium.[80]

The first synthetic homogenous catalyst for N$_2$ reduction was reported by Schrock in 2003 when it was found that a tripodal molybdenum complex could readily bind N$_2$.[81] (Figure 1.2)
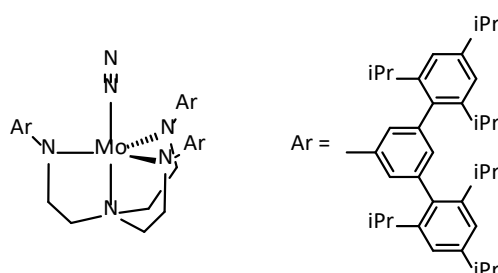
Figure 1.2: Schrock's Mo catalyst for nitrogen acidification.

The reaction of this complex with 1 molar equivalent of the acid [LutH][BArF] and 2 molar equivalents of the reductant Cp$_2$Co gave near-quantitative conversion to the diazo (NNH) analogue. See Scheme 1.31. Notably, the complex did not react with either of these reagents independently, but only with their combination.[82] This suggested a Proton Coupled Electron Transfer (PCET)-type process was occurring, meaning that the proton and electron are both transferred in a concerted fashion, rather than a more simple sequential protonation, then reduction.
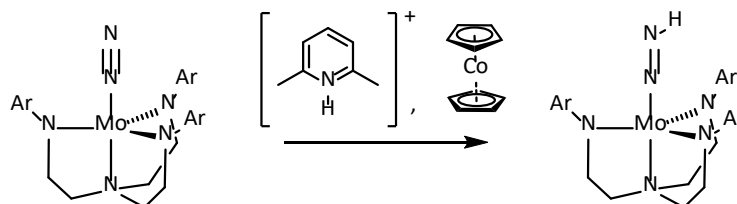
Scheme 1.31: Schrock's protocol for N$_2$ reduction with a molybdenum complex.

2 potential pathways of the PCET mechanism have been proposed. Chirik proposed that the reduction of the acid by the Cp$_2$Co occurs first, and that this reduced species has a weaker

N-H bond, facilitating the conversion to the diazo species.[83] Peters instead proposed that the Cp$_2$Co reductant may be protonated, weakening the C-H bonds that mediate this conversion.[84]

The catalytic formation of NH$_3$ from N$_2$ was accomplished by reaction of the Mo complex under N$_2$ atmosphere with 48 equivalents of [LutH]$^+$ and 36 equivalents of Cp*$_2$Cr, giving 8 equivalents of NH$_3$ product.[85] (Scheme 1.32)

$$N_2 \text{ (1 atm)} + 48 \text{ [LutH][BArF]} + 36 \text{ Cp*}_2\text{Cr} \xrightarrow[\text{heptane, 6 h}]{\text{[Mo]}} NH_3$$
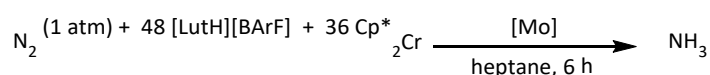
Scheme 1.32: The protocol for catalytic N$_2$ reduction by a molybdenum complex reported by Schrock.[85]

By isolation of intermediates and confirming their utility as pre-catalysts for the transformation, a mechanism was proposed in which PCET occurred first to the N atom distal to the Mo, releasing one molecule of NH$_3$, before beginning to react with the proximal nitrogen atom.[86] (Scheme 1.33)
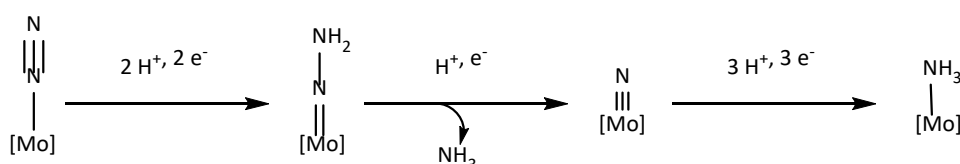
Scheme 1.33: The distal pathway of N$_2$ reduction as proposed by Schrock.

After this breakthrough result, molybdenum became the most well studied metal for nitrogen activation, with many molecular Mo catalysts reported, improving on Schrock's initial report (Figure 1.4).
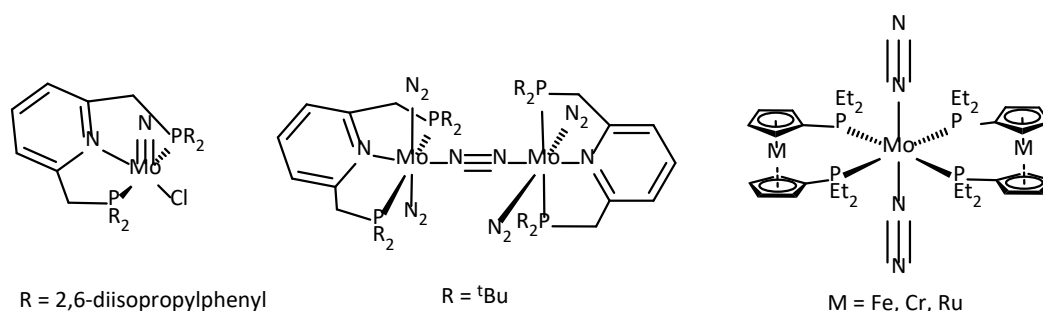
Figure 1.3: Examples of Mo-based catalysts for nitrogen fixation.[87–91]

Nishibayashi and co-workers noted an interesting feature of their Mo complexes bearing metallocenyldiphosphine ligands. Treatment of these complexes with acid (H_2SO_4, TfOH) gave high yields of ammonium, whereas the corresponding complexes bearing non redox-active diphosphine ligands such as 1,2-bis(diphenylphosphino)ethane (dppe) did not. This indicates that the metallocene ligands have some kind of redox interaction with the Mo centre that enables reduction of the Mo-bound N_2.[92]
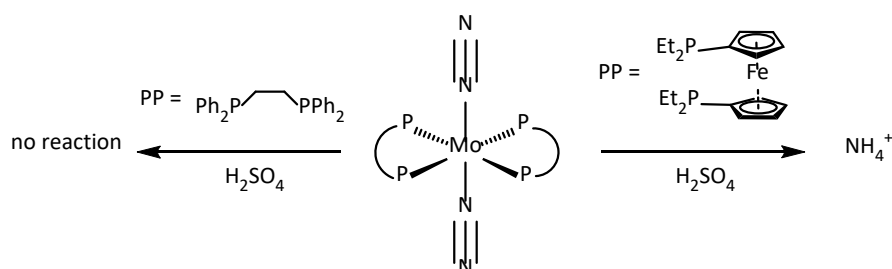
Scheme 1.34: The reactions of $Mo(PP)_2(N_2)_2$ complexes with H_2SO_4 as reported by Nishibayashi.

1.3.1 – Iron Catalysts for Nitrogen Fixation

Almost on a par with molybdenum, iron is perhaps the second most well-studied metal for N_2 reduction catalysts.

The first example of a homogenous catalytic system with iron was reported by Peters in 2013 with a tris(phosphine)borane-supported complex.[93]
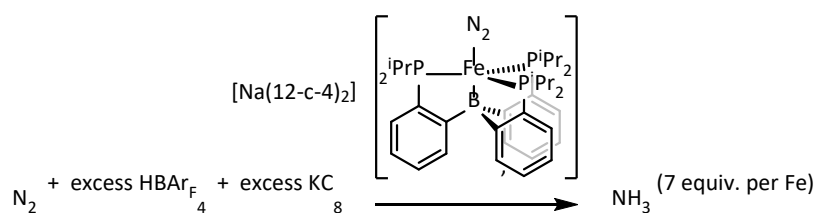
Scheme 1.35: Peters' first reported protocol for N_2 reduction.[93]

Once again, the successful reduction of N_2 with this metal inspired the development of a wealth of iron-based N_2 reduction catalysts.
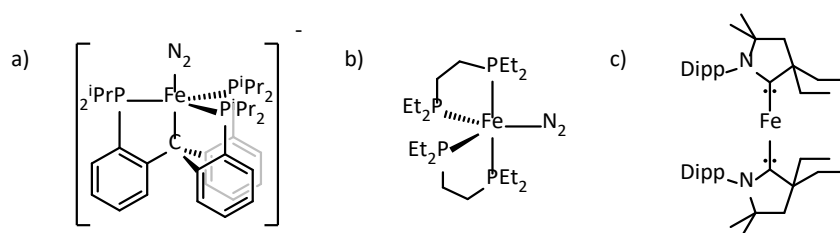
Figure 1.4: A selection of Fe catalysts reported to catalyse reduction of N_2. Dipp = 2,6-diisopropylphenyl.[94–96]

The Peters group iterated upon their tripodal system by substituting the boron with a carbon (Figure 1.5a). This created a model system to the Fe-N_2 binding site in FeMoco, in which the binding of N_2 lengthens the Fe-C bond.[94]
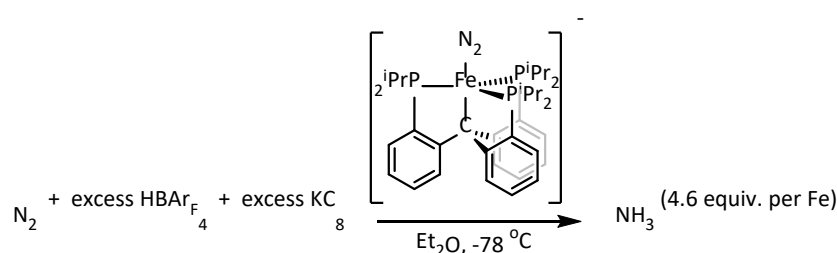
Scheme 1.36: Peters' protocol for N_2 reduction at an Fe-C site.

The Ashley group used a simple iron-phosphine complex, $FeN_2(depe)_2$ (Figure 1.5b) for N_2 reduction, finding that it selected not for NH_3 as other reported systems had, but for N_2H_4; meaning incomplete reduction was occurring. The system also produced a single equivalent

of NH_3 with respect to catalyst, implying its formation in a pre-activation state.[95] The same complex could also be applied to the silylation of N_2 to form $N(SiMe_3)_3$.[97]
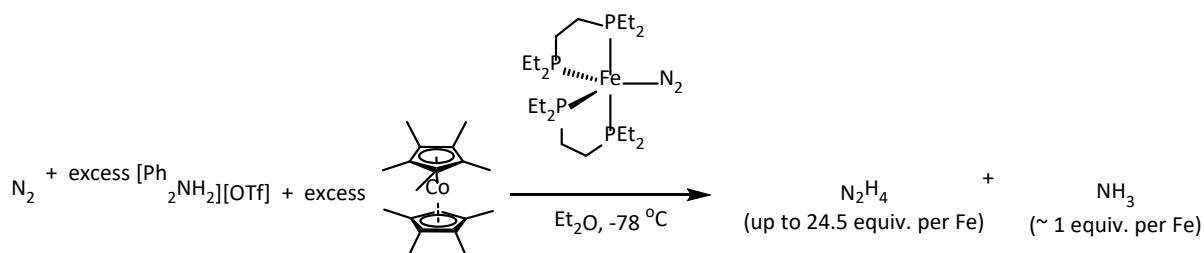
Scheme 1.37: Ashley's system for the production of N_2H_4 from N_2.

The first example of an iron-based N_2 reduction system not employing phosphine ligands came from Peters, who reported the use of a low-coordinate $(CAAC)_2Fe$ complex to bind and reduce N_2 (CAAC = Cyclic(alkyl)(amino)carbene) (Figure 1.5c).[96] Interestingly, N_2 binding and NH_3 generation was only observed to occur below temperatures of -80 °C. (Scheme 1.38)
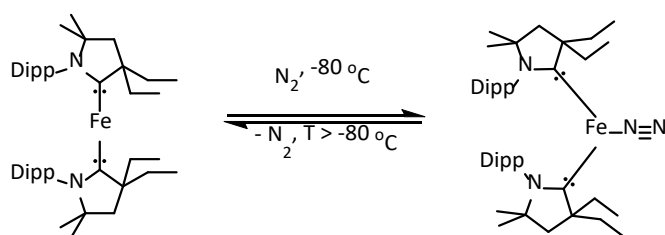
Scheme 1.38: The temperature dependence of N_2 binding on a $Fe(CAAC)_2$ complex reported by Peters.[96]

Common features of all reported systems for N_2 reduction include the need for incredibly strong reductants. Until relatively recently, the most commonly used reductants were alkali metal reductants such as Na/Hg or KC_8, which are now commonly omitted in favour of $CoCp*_2$. The use of these reductants has in turn necessitated another common reaction feature; namely, the use of low temperatures, most commonly -78 °C, to increase production of the reduced N product. This has dual benefits for catalysis. Firstly by increasing the solubility of N_2 in the reaction solvent, secondly by suppressing an undesirable side reaction enabled by the use of strong reductants; the direct reduction of

the acid to produce H_2. This side reaction may also be suppressed by choice of solvent; in Ashley's system, the $[Ph_2NH_2]^+$ acid was selected due to its low solubility in the Et_2O solvent.[95] This leads to a lower concentration of H^+ in solution, suppressing H_2 production. This hypothesis was supported by observation of a large increase in H_2 production when the reaction was performed in THF.

Overall, proper selection of ligand seems to be a key determining factor for the homogenous reduction of N_2, with species that enable transfer of electron density from the metal centre being particularly effective for this chemistry. Taking inspiration from nature also has borne fruit repeatedly in this area, using complexes that mimic the structure of FeMoco to achieve high levels of turnover of this exceeding difficult reaction.

1.4 – Project Aims

Despite the breadth of mechanistic investigations into iron-catalysed cross-coupling reactions, new reports often bring up more questions than answers. From Kochi's misassignment of an Fe^{I} active species in his seminal report, to more recent disagreements over whether ligands are coordinated during catalytic turnover, the properties of iron that make its study chemically interesting also often render such study difficult. Intermediate complexes in these reactions are commonly extremely reactive with multiple different components of reactions, potentially accessing an even wider range of species to be studied.

In Chapter 2, the reactivity of organoiron complexes of the type that are often intermediate in cross-coupling reactions are synthesised, and their reactivity to the side products of cross-coupling reactions investigated. This gave a greater insight into how the speciation of iron in these reactions may change throughout turnover in a catalytic reaction.

Chapter 3 details a mechanistic investigation of iron-catalysed Kumada cross-coupling in which these insights are applied. The range of potentially accessible oxidation states is probed, and the reactivity of multiple mesityl-iron species with electrophile analysed by GC-FID. From these data, a plausible catalytic cycle has been proposed.

In Chapter 4, attention is turned to iron-catalysed N_2 reduction. Inspiration was taken from both natural N_2-reduction systems and previously reported synthetic homogenous catalysts to synthesise a range of iron complexes relevant to N_2 reduction catalysis.

2. Chapter 2 – Reactivity Study of Organoiron Complexes with Byproducts of Cross-Coupling Chemistry

2.1 – Introduction

The relevance of homoleptic iron species in iron-catalysed cross-coupling reactions is becoming more and more clear as further studies are reported.[98] Even Kochi's initial work on FeCl$_3$-catalysed cross-coupling of alkyl halides with vinyl bromides was found to occur through an S = ½ species that was later assigned as a homoleptic [Fe$_8$Me$_{12}$]$^-$ cluster.[30,41]
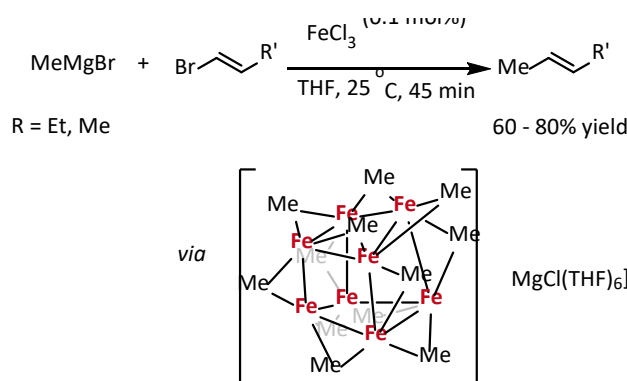
Scheme 2.1: Kochi's protocol for cross-coupling of alkyl Grignard reagents with vinyl bromides *via* a [Fe$_8$Me$_{12}$]$^-$ intermediate (**1**) as isolated by Neidig.[30,41]

Cahiez then reported the improvement of this system by addition of NMP, assigning its role as a 'co-solvent'.[31] Later work determined that NMP promoted the formation of the active species, a homoleptic [FeMe$_3$]$^-$ ferrate species over **1**, a resting state.[42]

Later works aimed to improve the selectivity and activity of iron catalysis for cross-coupling by addition of additional species as ligands; including amines,[32] phosphines,[99] and NHCs.[100–102] However, in many cases, further investigations into their mechanisms revealed homoleptic complexes as operative in catalysis, with the added ligands not being bound to iron during turnover, and instead performing different roles.

2.1.1 – Homoleptic Species in Cross-coupling

The procedure for an Fe-TMEDA-catalysed cross-coupling of alkyl halides with aryl Grignard reagents reported by Nakamura and co-workers,[32] is one such system in which a mechanistic investigation showed that despite the presence of species that ordinarily may chelate to iron, the reaction mechanism functioned in a 'ligand-free' manifold.

This reported protocol used a TMEDA (tetramethylethylenediamine) ligand at a loading of comparable stoichiometry to the substrates, this was later optimised in separate reports by Bedford[103] and Cahiez[104] who were able to drastically lower the loading of TMEDA, or use HMTA (hexamethylenetetraamine) in loadings as low as 5 mol%. (Scheme 2.2)
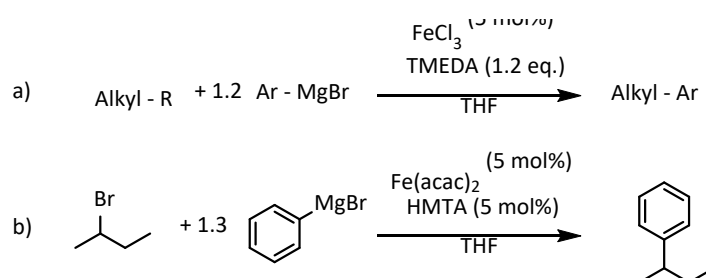
Scheme 2.2: The iron-catalysed Kumada coupling of alkyl halides with aryl Grignard reagents as reported by Nakamura (a)[32], and Cahiez (b)[104].

Later work by Nagashima and co-workers[56] proposed a mechanism in which a $FeR_2(TMEDA)$ complex is produced by reaction of the corresponding chloride species with the Grignard reagent. This then reacts with the electrophile, giving the cross-coupled product and $FeRBr(TMEDA)$ (**4**), which then reacts with a further equivalent of the Grignard to reform $FeR_2(TMEDA)$ (**5**). (Scheme 2.3)
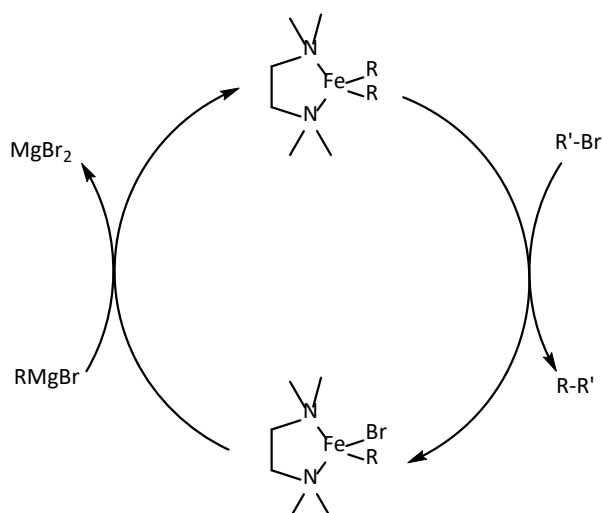
Scheme 2.3: The catalytic cycle proposed by Nagashima and co-workers for iron-catalysed cross-coupling with the amine ligand TMEDA.

Bedford and co-workers later investigated this system and showed that the proposed FeCl$_2$(TMEDA) intermediate is not accessible under catalytic conditions.[105] In fact, upon the reaction of **4** or **5** with even a slight excess of the Grignard reagent (as would be present in catalysis) all iron-bound amine ligand is displaced, instead exclusive formation of a homoleptic ferrate species of the form FeR$_3^-$ is observed, as displayed by paramagnetic ^{1}H NMR spectroscopy.
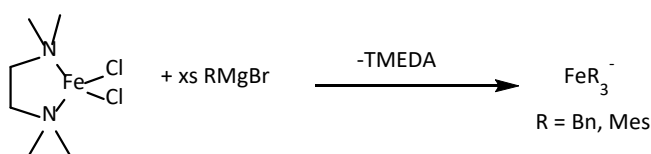
Scheme 2.4: The reaction of FeCl$_2$(TMEDA) with excess Grignard reagent to give the homoleptic ferrate complex.

Additionally, under equivalent conditions, the FeR$_3^-$ complexes were shown to react faster with electrophile than the corresponding FeR$_2$(TMEDA) complexes that had been proposed as active species in catalysis. Later work showed that amine ligands that bind more strongly to iron, so far as they are not displaced by the Grignard reagent under these conditions, show poorer catalytic activity compared to those which are more easily substituted, and

those that may be displaced showed decreasing activity with increased chelate effect.[106] Bedford therefore proposed that the amine ligand is not bound to the iron centre during turnover, but instead that its presence minimises the population of species that give way to alternative pathways that give poorer selectivity for cross-coupled product.

The propensity of ligand dissociation to occur in iron-catalysed cross-coupling reactions is not limited to Kumada cross-couplings, nor to those involving amine ligands. Bedford and co-workers investigated the mechanism of an iron-catalysed Negishi cross-coupling reaction with added diphosphine ligands and showed that at no point during turnover is the diphosphine ligand bound to iron. Instead, the phosphine binds to the zinc nucleophile, facilitating transmetallation to the iron centre and enabling formation of ferrate species.[107]
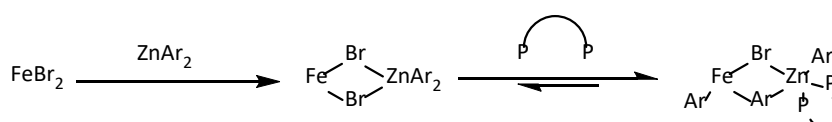
Scheme 2.5: The role of diphosphine ligand in iron-catalysed Negishi cross-coupling proposed by Bedford.[107]

2.1.2 – Iron-Mesityl Complexes as Model Systems

Homoleptic iron species are vitally important to a wide array of cross-coupling reactions. In order to enable study of such complexes, species bearing mesityl (2,4,6-trimethylphenyl) substituents are often used as models as the mesityl group has properties that confer stability to metal complexes that bear it. The foremost such effect is the resistance to reductive elimination promoted by the steric bulk of ortho-methyl groups on the phenyl ring. This has a kinetically stabilising effect on the iron complexes Fe_2Mes_4 (**6**) and $[FeMes_3]^-$ (**7**) (Figure 2.1) to such an extent that they are appreciably stable at room temperature, whereas the phenyl analogues decompose essentially immediately after their formation.
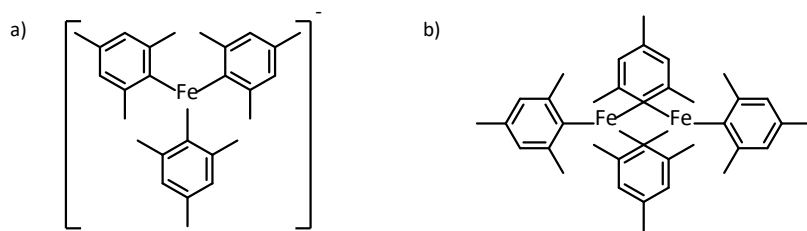
Figure 2.1: The iron-mesityl complexes [FeMes$_3$]$^-$ (**7**) (a) and Fe$_2$Mes$_4$ (**6**) (b).

A previous member of the Bedford group found that **7** could be reacted with XylMgBr to form the mixed species [FeMes$_2$Xyl]$^-$.
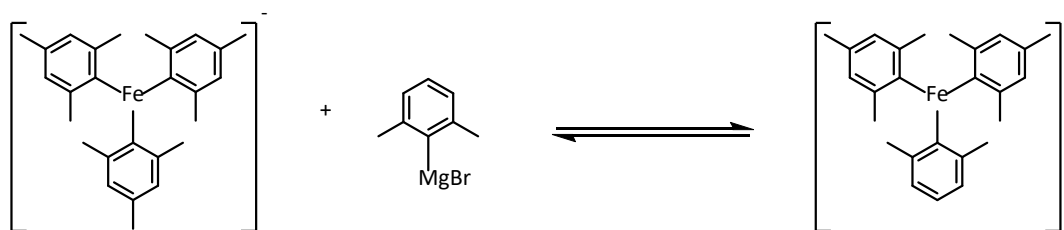
Scheme 2.6: The equilibrium of [FeMes$_3$]$^-$ reacting with XylMgBr to give the mixed species [FeMes$_2$Xyl]$^-$.

This shows a reversibility in the reaction of the organoferrate complex with the Grignard reagent, a reactivity that had not previously been identified. The reverse reaction likely involves transfer of a mesityl group from the iron centre to MgBr$_2$, a species that, aside from inherently being a product of Kumada cross-coupling, is also used as an additive in other examples of iron-catalysed cross-coupling reactions including Negishi[33] and Suzuki.[24]

Such reversibility may have implications for the roles of ferrates in catalysis, implying that rather than just reacting with the organic electrophile as previous studies have proposed, there are further interactions with other species present in solution. Any intermediate species in this equilibrium may also display such activity.

The Curtin-Hammett principle states that the observed ratio of species in an equilibrium mixture is not necessarily dictated solely by the equilibrium constant between the two, but by the difference in energy between the two rate-limiting transition states. Therefore, even

if intermediate species on the equilibrium between **7** and MgBr$_2$ exist only in low concentration, they may still be responsible for a large proportion of catalytic turnover provided their rate of reaction with electrophiles significantly outpaces **7**.[108]

The position of this equilibrium may therefore be a determining factor in the rate of catalytic turnover for reactions in which homoleptic iron complexes are identified as active catalysts. Additionally, identification and characterisation of intermediate species on this equilibrium is vital in order to fully determine the makeup of catalytic solution.

In this interest, the following chapter details an investigation into the reactivity of homoleptic iron-mesityl complexes with species relevant to iron-catalysed cross-coupling reactions, namely the bromide salts MgBr$_2$ and ZnBr$_2$ which are produced in Kumada and Negishi cross-coupling reactions respectively. In the interest of simplicity, all reactions were carried out in THF as solvent, and all halide species examined are bromides, although chlorides and iodides are also capable at cross-coupling chemistry.

2.2 – Reactions of Fe$_2$Mes$_4$ with Bromide Salts

As a model complex to study the equilibria between organoiron complexes and bromide salts, Fe$_2$Mes$_4$ (**6**) was used. This species was chosen due to its comparative stability as compared to other organoiron species, even **7** displays gradual decomposition at room temperature under inert atmosphere. This stabilising effect also prevents accessing lower oxidation states than Fe^{II}, which have been proposed as operative in several examples iron-catalysed cross-coupling reactions.[40,102]

Additionally, the ability to isolate **6** without any counterion is useful to ensure that consistent stoichiometries are used. **7**, on the other hand, is usually isolated as either the [MgBr]$^+$ or Mg^{2+} salt.[98,105] Therefore, testing its reactivity with MgBr$_2$ will have an inherent bottom limit of Mg loading that is not present in the reaction with **6**.

2.2.1 – Reaction of Fe$_2$Mes$_4$ with MgBr$_2$

6 was reacted with increasing loadings of MgBr$_2$, the inorganic side-product of the Kumada cross-coupling reaction, and the reaction solutions analysed by ^{1}H NMR and ^{13}C NMR

spectroscopies. Sweep widths for ^1H NMR spectroscopy were set wider than the standard in order to detect paramagnetic species, facilitating detection of organoiron products. ^{13}C NMR spectroscopy was used for determining the presence of any of the Grignard reagent, MesMgBr. From these experiments, it should be possible to determine the position of the equilibrium between each of the organometallic species.
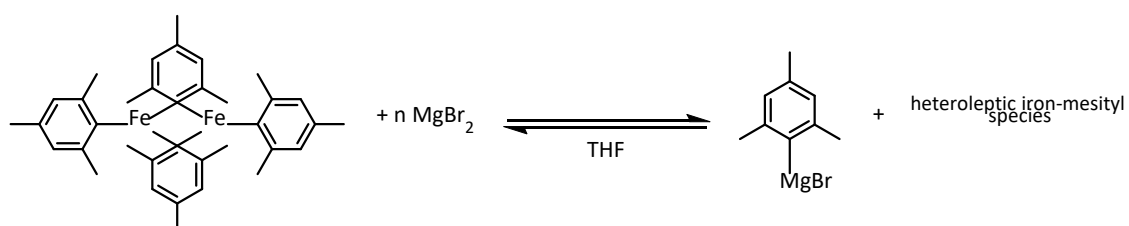
Scheme 2.7: The equilibrium resulting from the reaction of Fe_2Mes_4 and $MgBr_2$.

Table 2.1: Molar loadings of $MgBr_2$ with organoiron product observed by ^1H NMR spectroscopy.

Spectrum	Mg:Fe	Signal in ^{1}H
a	0.125	Fe_2Mes_4
b	0.250	Fe_2Mes_4, $[FeMes_3]^-$
c	0.375	Fe_2Mes_4, $[FeMes_3]^-$
d	0.500	Fe_2Mes_4, $[FeMes_3]^-$
e	0.625	Fe_2Mes_4, $[FeMes_3]^-$
f	1.25	Fe_2Mes_4, $[FeMes_3]^-$
g	2.50	Fe_2Mes_4, $[FeMes_3]^-$
h	5.00	New Iron Species
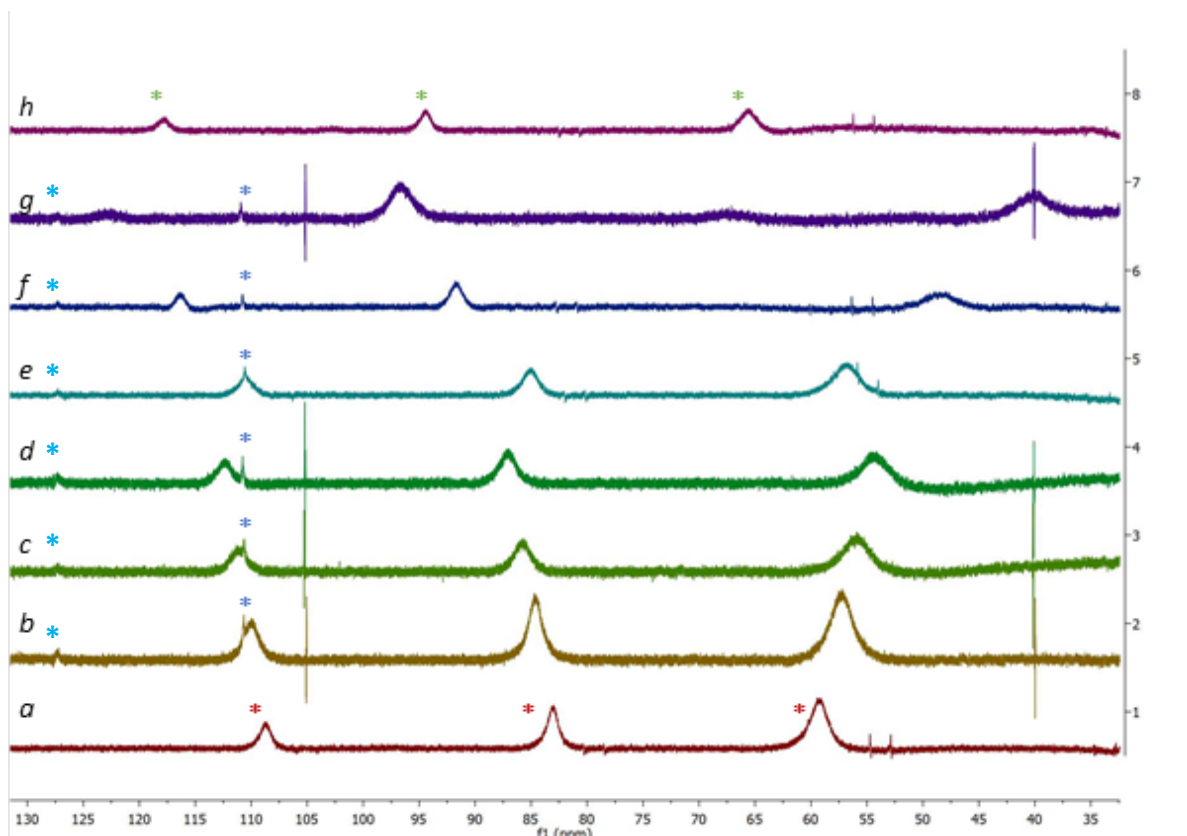
Figure 2.2: Stacked paramagnetic ^{1}H NMR spectra of Fe$_2$Mes$_4$ reacting with increasing molar equivalents of MgBr$_2$. (a = 0.125 equivalents, b = 0.25, c = 0.375, d = 0.5, e = 0.625, f = 1.25, g = 2.5, h = 5.0).

Analysis of the ^{1}H NMR data indicates that the speciation of iron is altered by increasing loading of MgBr$_2$. Spectrum *a* (corresponding to 0.125 molar equivalents of MgBr$_2$ with respect to Fe) shows **6** (109, 83, 60 ppm, indicated by '*') as the sole observable paramagnetic species. As the relative loading of MgBr$_2$ is increased, the signals are observed to 'drift' from these chemical shifts, while also broadening slightly; this likely indicates interaction of Fe$_2$Mes$_4$ with the dissolved MgBr$_2$. Beginning from spectrum *b*, (0.25 equivalents of MgBr$_2$) signals are also observed with chemical shifts indicating the presence of small amounts of **7** (111, 127 ppm indicated by '*'); these signals are observable up to spectrum *g*, (2.5 equivalents of MgBr$_2$).

The presence of **7** can be taken as indirect evidence of the formation of MesMgBr in solution by transmetallation to the MgBr$_2$ salt. Any formed MesMgBr will react with **6** to give the observed **7**.

Scheme 2.8: The reaction of Fe$_2$Mes$_4$ with MesMgBr to produce [FeMes$_3$]$^-$.

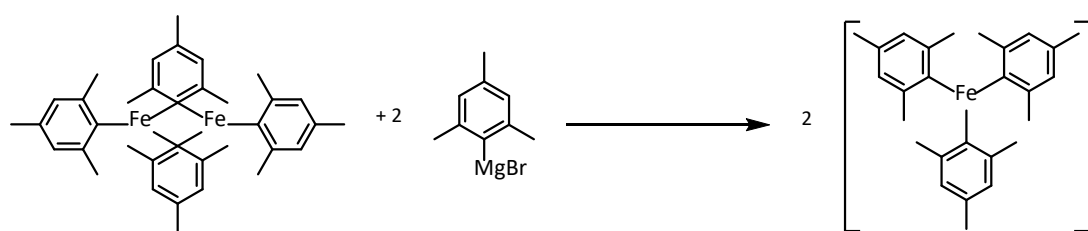The presence of low loadings of MesMgBr in solution was then confirmed by ^{13}C NMR.

Figure 2.3: Stacked ^{13}C NMR spectra of Fe$_2$Mes$_4$ reacting with increasing molar equivalents of MgBr$_2$. (a = 0.125 equivalents, b = 0.25, c = 0.375, d = 0.5, e = 0.625, f = 1.25, g = 2.5, h = 5.0). Spectrum of MesMgBr shown for comparison.

The observed production of MesMgBr from the reaction of MgBr$_2$ with **6** is direct evidence for transmetallation from Fe to Mg, and the reversibility of the formation of organoiron species from aryl Grignard reagents.

Interestingly, at the highest loading of MgBr$_2$ (Figure 2.2, spectrum *h*, 5.00 equivalents) signals can be observed for a new iron species. Integration of peak areas supports its assignment as an iron-mesityl species not corresponding to NMR data for any that has been previously reported.

It was hypothesised that this complex is the product of transmetallation of one of the mesityl groups to the MgBr$_2$, a heteroleptic iron-mesityl-bromide complex, therefore an investigation into its structure was performed.

2.2.2 – Reactions of Fe$_2$Mes$_4$ with FeBr$_2$

In order to begin to determine the identity of the new iron-mesityl species, the first question to be answered is whether the same species forms regardless of which metal salt is reacted with **6**, or if only MgBr$_2$ gives this product. To this end, an analogous set of reactions were performed with FeBr$_2$ in place of MgBr$_2$.
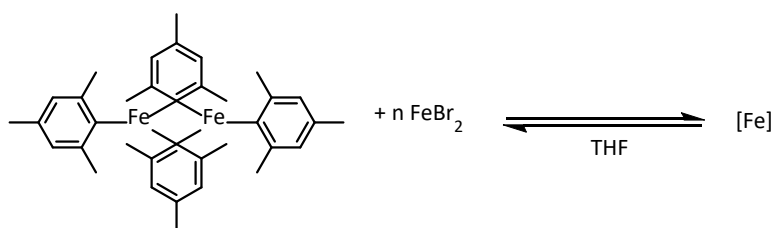
Scheme 2.9: The reaction of Fe$_2$Mes$_4$ with FeBr$_2$ to give an unknown iron-mesityl species.

Table 2.2: Loadings of $FeBr_2$ with respect to Fe_2Mes_4 with the observed product by ^1H NMR.

Spectrum	Br:Mes	Signal in ^1H
a	0.125	Fe_2Mes_4
b	0.250	Fe_2Mes_4
c	0.375	Fe_2Mes_4
d	0.500	Fe_2Mes_4
e	0.625	None
f	0.750	New Iron Species (trace)
g	0.875	New Iron Species
h	1.000	New Iron Species
i	1.125	New Iron Species
j	1.250	New Iron Species

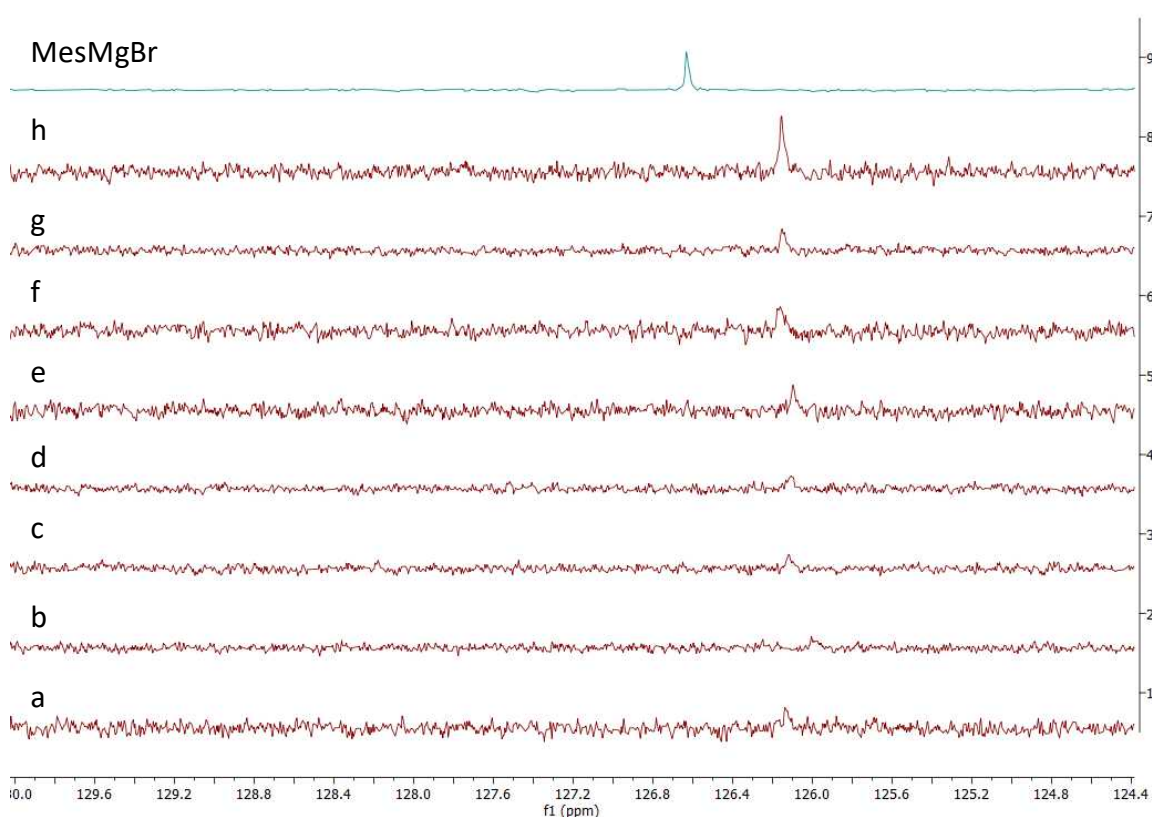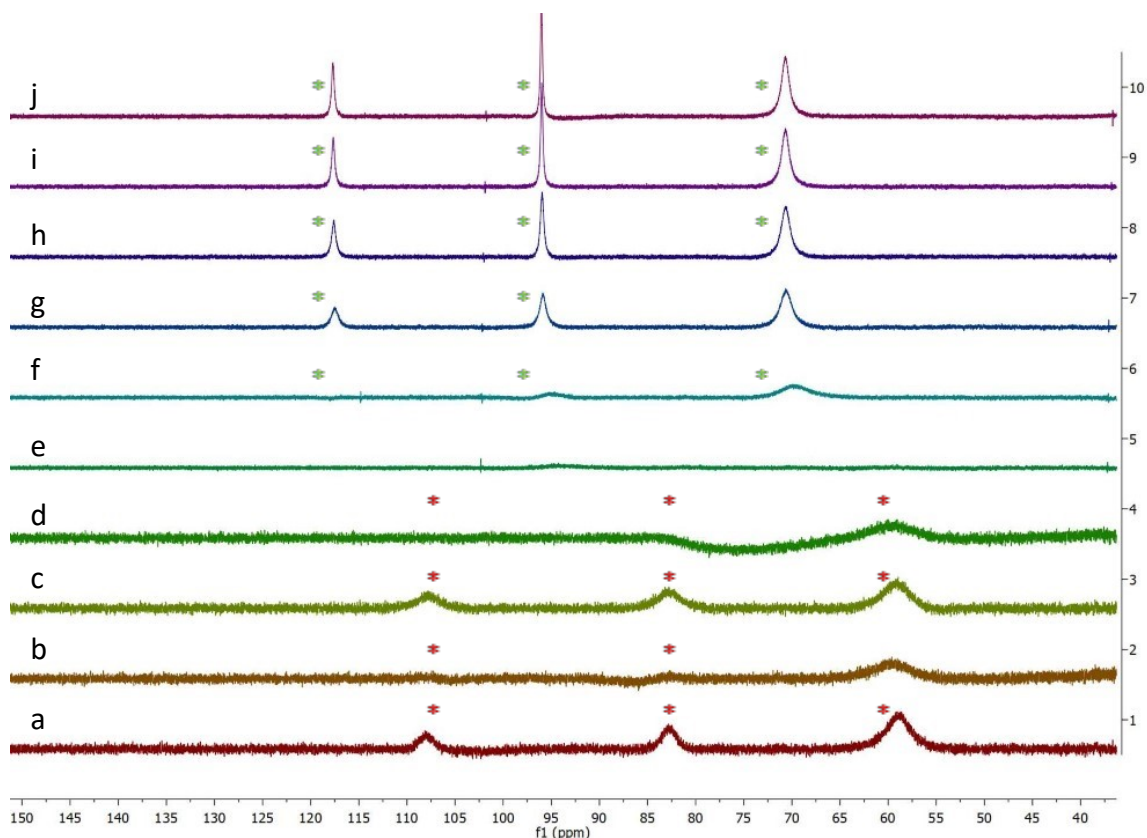**Figure 2.4:** Stacked paramagnetic ^1H NMR spectra of Fe_2Mes_4 reacting with increasing molar equivalents of $FeBr_2$. (a = 0.125 equivalents, b = 0.25, c = 0.375, d = 0.5, e = 0.625, f = 0.75, g = 0.875, h = 1.0, i = 1.125, j = 1.25).

At lower loadings of $FeBr_2$ (Figure 2.4, spectra a-*d*) **6** remains the sole observable paramagnetic species in solution. However, as $FeBr_2$ loading is increased beyond 0.625 molar equivalents (spectra *f-j*), the previously observed signals for the new iron species are observed. At intermediate loadings (spectra *d-f*), all signals are broadened out, which likely is indicating that the species are rapidly interconverting. From these data it can be inferred that the new species is likely a heteroleptic iron-mesityl-bromide complex.

By reaction of **6** with $MgBr_2$, the complex was isolated, crystals grown of it, and characterised by XRD, confirming the structure as an $[FeBrMes_2]^-$ anion (**8**), which was crystallised as $[FeBrMes_2]_2[Mg(THF)_6]$.
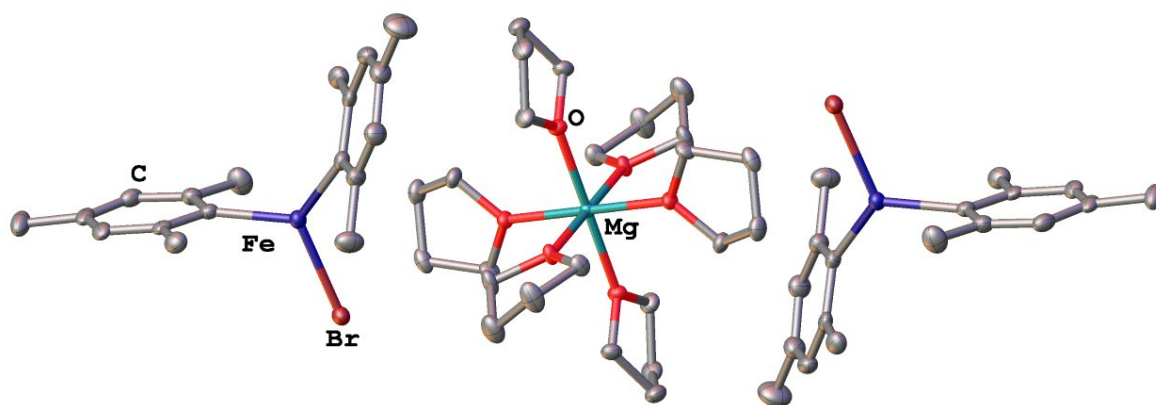
Figure 2.5: The crystal structure of [FeBrMes$_2$]$_2$[Mg(THF)$_6$] (**8**[Mg(THF)$_6$]). H atoms omitted for clarity.

The presence of 2 mesityl groups per iron in (**8**) means that its production from Fe$_2$Mes$_4$ with either MgBr$_2$ or FeBr$_2$ does not require transmetallation to the opposing metal centre, but rather the salts are simply acting as sources of bromide to split the dimer. The observation of MesMgBr in the reaction with MgBr$_2$ does, however, indicate that this transmetallation is occurring, but it is unclear whether this occurs from **6** or the brominated product **8**. The disappearance of signals corresponding to **7** at the highest loadings does, however, indicate that transmetallation is likely occurring from **7**.
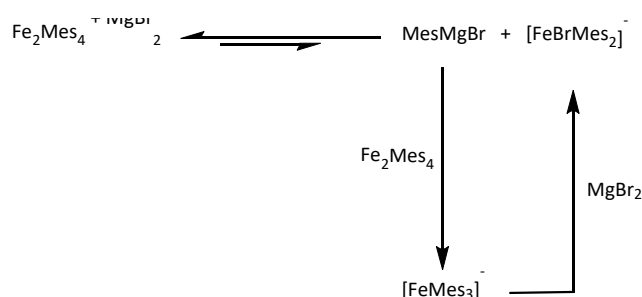
Scheme 2.10: The observed reactivity of Fe$_2$Mes$_4$ with MgBr$_2$.

2.2.3 – The reaction of Fe$_2$Mes$_4$ with ZnBr$_2$

While the equilibria between Mg salts and organoiron species relevant to Kumada cross-coupling had not previously been investigated, the interactions of such species with Zn salts

relevant to Negishi coupling has been extensively investigated and discussed by Bedford and co-workers.[107] Even so, the precise position of the Fe/Zn equilibrium is of interest.
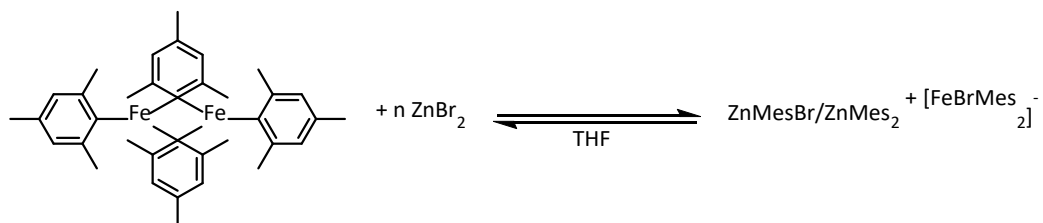
Scheme 2.11: The reaction of Fe_2Mes_4 with $ZnBr_2$.

Table 2.3: Loadings of $ZnBr_2$ with respect to Fe_2Mes_4.

Spectrum	Zn:Fe	Species Observed
a	0.125	$[FeBrMes_2]^-$
b	0.250	$[FeBrMes_2]^-$
c	0.375	$[FeBrMes_2]^-$
d	0.500	$[FeBrMes_2]^-$
e	0.625	None
f	1.25	None
g	2.50	None
h	5.00	None
i	10.0	None
j	25.0	None
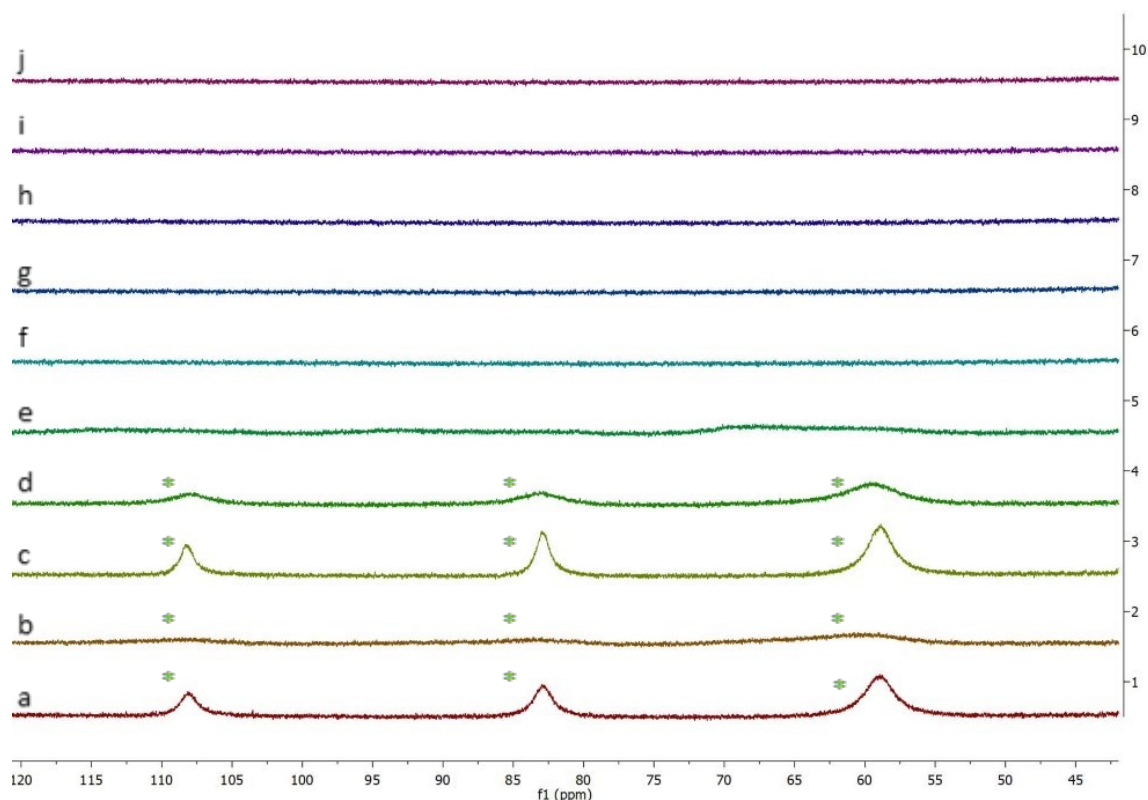
Figure 2.6: Stacked ^1H NMR spectra showing the reaction of Fe_2Mes_4 with increasing quantities of $ZnBr_2$.

Upon ^1H NMR analysis of the reaction of **6** with even a small quantity of $ZnBr_2$ (0.125 equivalents, Figure 2.6, spectrum *a*), no **6** is observed, instead the only observable paramagnetic species is **8** . Interestingly, at relative loadings above 0.625 equivalents, no paramagnetic species can be observed. This result, in concert with ^{13}C NMR data showing the presence of the organozinc products ZnBrMes and $ZnMes_2$ clearly displays the capacity of transmetallation to occur from **8** to $ZnBr_2$. Such a reaction may produce a neutral FeBrMes species, in the case of 1 mesityl group being transferred per iron, although it is likely that in this case such a species would also accept a bromide, as **6** does, to form a ferrate complex of the form $[FeBr_2Mes]^-$. If, however, both mesityl groups are transferred, then formation of $FeBr_2$, ultimately giving $[FeBr_3]^-$ would be occur concomitantly. The absence of a new species appearing in the paramagnetic ^1H NMR would seem to indicate the latter is taking place.

2.3 – Reactions of Fe$_2$Mes$_4$ with Boronic Esters

From the results gained thus far of the reactions of **6** with FeBr$_2$, MgBr$_2$, and ZnBr$_2$, it was observed that the organoiron species reacted initially as a bromide acceptor, and only upon forming the heteroleptic ferrate species [FeBrMes$_2$]$^-$ as transmetallation observed to occur to the metal bromide.

This has clear implications for their roles in Kumada, in the case of MgBr$_2$, and Negishi, in the case of ZnBr$_2$, cross-coupling reactions; however we cannot use this to make any predictions for the Suzuki reaction due to the lack of halides on the boronic species used.

Suzuki cross-coupling involves the use of organoboron species as nucleophiles, in place of the Grignard or organozinc reagents for Kumada and Negishi couplings. In the case of palladium, boronic esters are often used to the nucleophile, albeit usually activated *in situ* by the addition of base, which is vital for reaction to occur.

Examples of Suzuki cross-coupling *via* iron catalysis are relatively few, with the first examples reported by Guo and co-workers in a high-pressure system,[109] before Nakamura and co-workers reported their protocol for the coupling of lithium arylboronates with alkyl halides.[34]
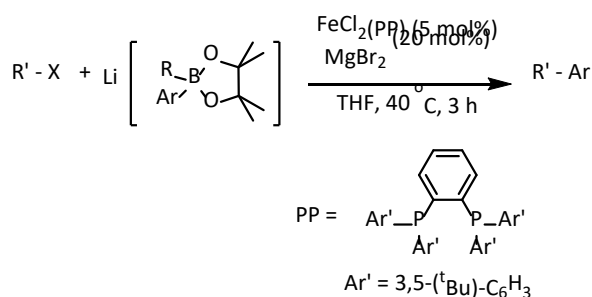
Scheme 2.12: Nakamura's protocol for the Suzuki cross-coupling of arylboronates with alkyl halides.[34]

Following on from this, Bedford and co-workers reported the use of cheap, simple phosphines for similar reactivity,[110,111] Nakamura and co-workers published a separate protocol to give alkyl-alkyl coupled products,[112] and, more recently, the Bedford group has reported the use of directing groups to enable the synthesis of biaryls.[24,25]

Common to these systems is the requirement to activate the boronic ester coupling partner to form a boronate ester, although work by Byers has recently skirted this requirement by use of a specialised ligand.[26] These boronate esters are formed from boronic esters that have been activated by reaction with a strong base, most commonly alkyllthiums, although alkoxide bases have shown utility as well in some cases.[113] This activation increases the nucleophilicity of the organic substituent.
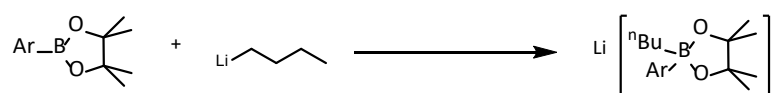
Scheme 2.13: The activation of an aryl boronic pinacol ester with ^{n}BuLi to form the more nucleophilic boronate ester.

When using these boronate esters as coupling partners, transfer of the organic substituent to the catalyst generates a boronic ester with the remaining organic residue being derived from the base used to activate. The production of this boronic ester in Suzuki coupling is analogous to the production of $MgBr_2$ in Kumada cross-coupling, or $ZnBr_2$ in Negishi cross-coupling. It therefore bears consideration how these esters may react with organoiron species in solution, and whether the transmetallation step with the boronate esters also shows a degree of reversibility as it does with $MgBr_2$ and $ZnBr_2$.

2.3.1 – The reaction of Fe_2Mes_4 with ^{n}BuBPin

^{n}BuLi is a common activating base used for EAM-catalysed Suzuki cross-coupling.[114] Therefore the first boronic ester trialled for reactivity with Fe_2Mes_4 was ^{n}BuBPin (**9**)**,** the product of transmetallation of an aryl group from an ^{n}BuLi-activated boronate ester.

Assuming transmetallation may occur to **9** from **6**, the expected product would be the boronate ester [Mes(^{n}Bu)BPin]$^-$ (**10**). To confirm the ^{11}B NMR signals for this product, it was independently synthesised by reaction of ^{n}BuBPin with MesLi. (Scheme 2.14)
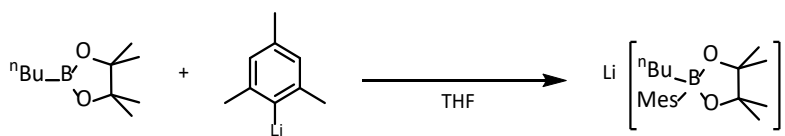
Scheme 2.14: The synthesis of Li[Mes^nBuBPin] ([Li]**10**).

^{11}B NMR analysis of this reaction showed a signal at 10.5 ppm, with a signal for the **10** starting material at a chemical shift of 34.9 ppm. This species was then isolated and its reactivity with iron tested by reaction with $FeCl_2$. This reaction reformed the ^{n}BuBPin starting material and produced **7**, indicating the facility of transmetallation to iron from these species. (Schem 2.15)
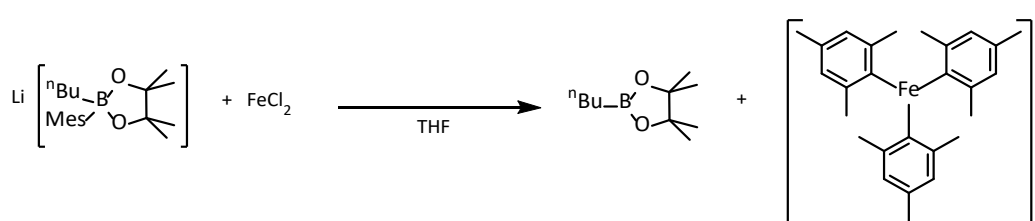
Scheme 2.15: The reaction of the boronate Li[Mes^nBuBPin] with $FeCl_2$.
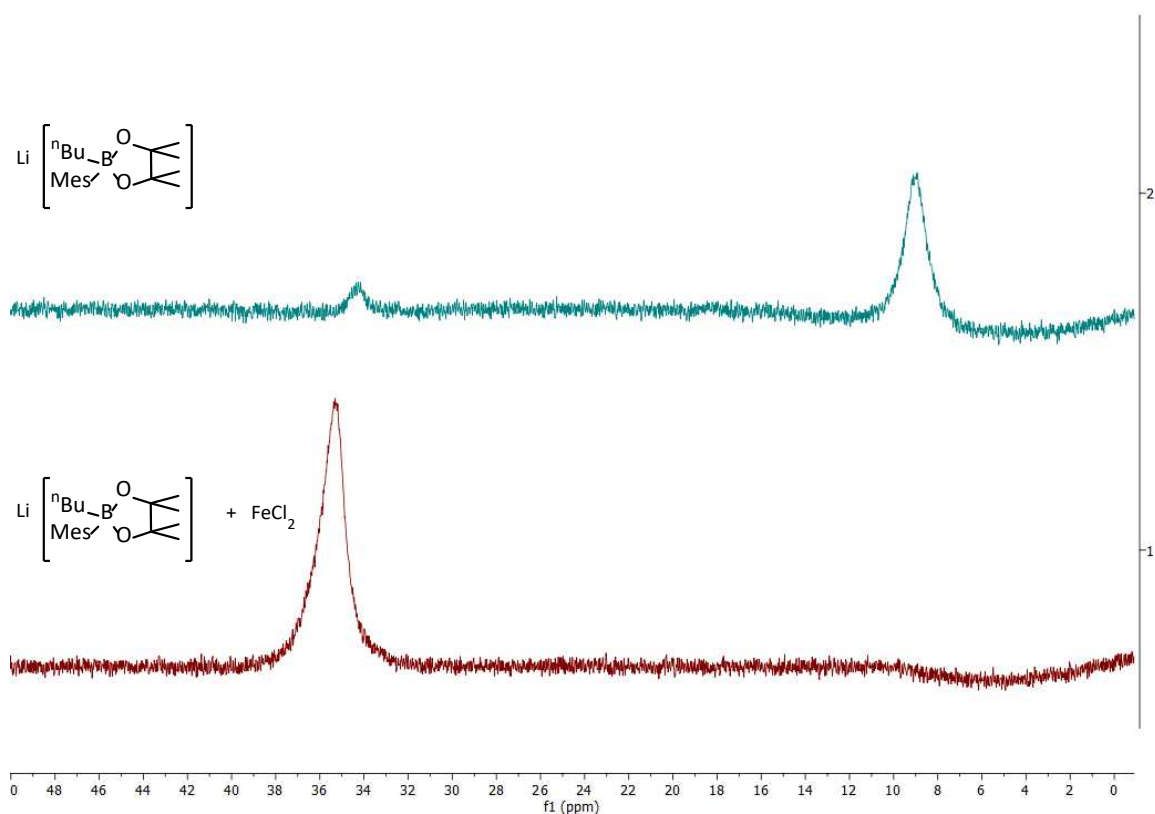
Figure 2.7: The ^{11}B NMR spectra of Li[Mes^{n}BuBPin] before and after reaction with FeCl$_2$.

Having established the ^{11}B NMR shifts of both expected boron species, the reactivity of ^{n}BuBPin with Fe$_2$Mes$_4$ was investigated by both ^{11}B and ^{1}H NMR.
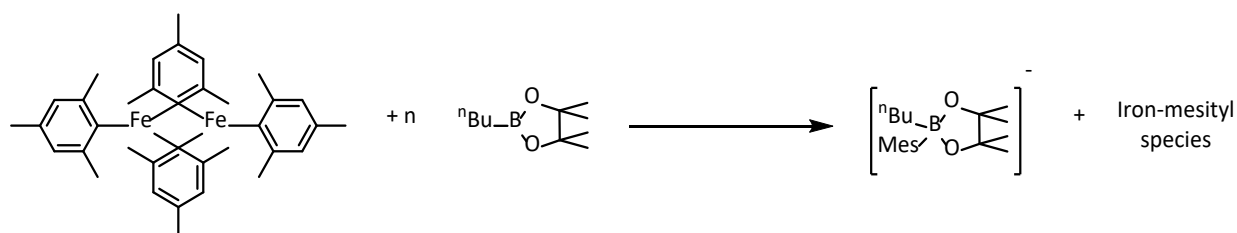
Scheme 2.16: The reaction of Fe$_2$Mes$_4$ with ^{n}BuBPin to form the boronate ester [Mes^{n}BuBPin]$^-$.

Table 2.4: Relative loadings of ^nBuBPin reacted with Fe_2Mes_4.

Entry	B:Fe	Signal in ^1H	Signal in ^{11}B
a	0.125	Fe_2Mes_4	^nBuBPin
b	0.250	Fe_2Mes_4	^nBuBPin
c	0.375	Fe_2Mes_4	^nBuBPin
d	0.500	Fe_2Mes_4	^nBuBPin
e	0.625	Fe_2Mes_4	^nBuBPin
f	1.25	Fe_2Mes_4, New Iron species	^nBuBPin
g	2.50	Fe_2Mes_4, New Iron species	^nBuBPin
h	5.00	Fe_2Mes_4, New Iron species	^nBuBPin
i	10.0	Fe_2Mes_4, New Iron species	^nBuBPin, New Boron Species
j	25.0	-	^nBuBPin, New Boron Species
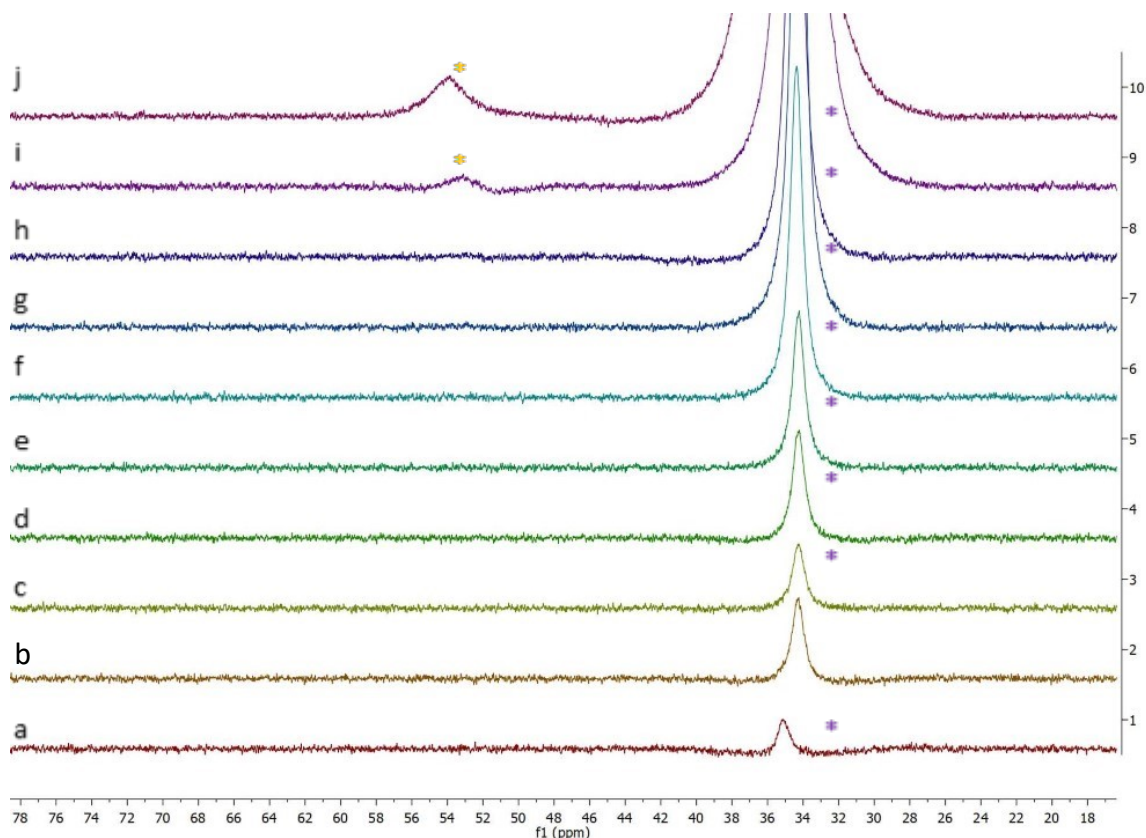
Figure 2.8: Stacked ^{11}B NMR spectra showing the reaction of Fe$_2$Mes$_4$ with increasing quantities of ^{n}BuBPin.

Looking first at the ^{11}B NMR data (Figure 2.8), the signal corresponding to the **9** (35 ppm, indicated by '*') starting material is the only one present until high loadings of 10 molar equivalents of boron with respect to iron are reached. At this point a new signal emerges at 53 ppm (*). Interestingly, this does not correspond to the boronate species **10** which would be expected at 10 ppm, where there is no signal observed. Such a chemical shift places this unknown species (**11**) in the range of expected chemical shift for a diaryl borinic ester of the form R$_2$B(OR').[115]

This suggests a two-fold reactivity with **6**, in which not only are mesityl substituents transferred to the boron centre, but the pinacol ester backbone is ring opened, potentially with one of the oxygen atoms binding to the iron, forming a new iron species. (Scheme 2.17)
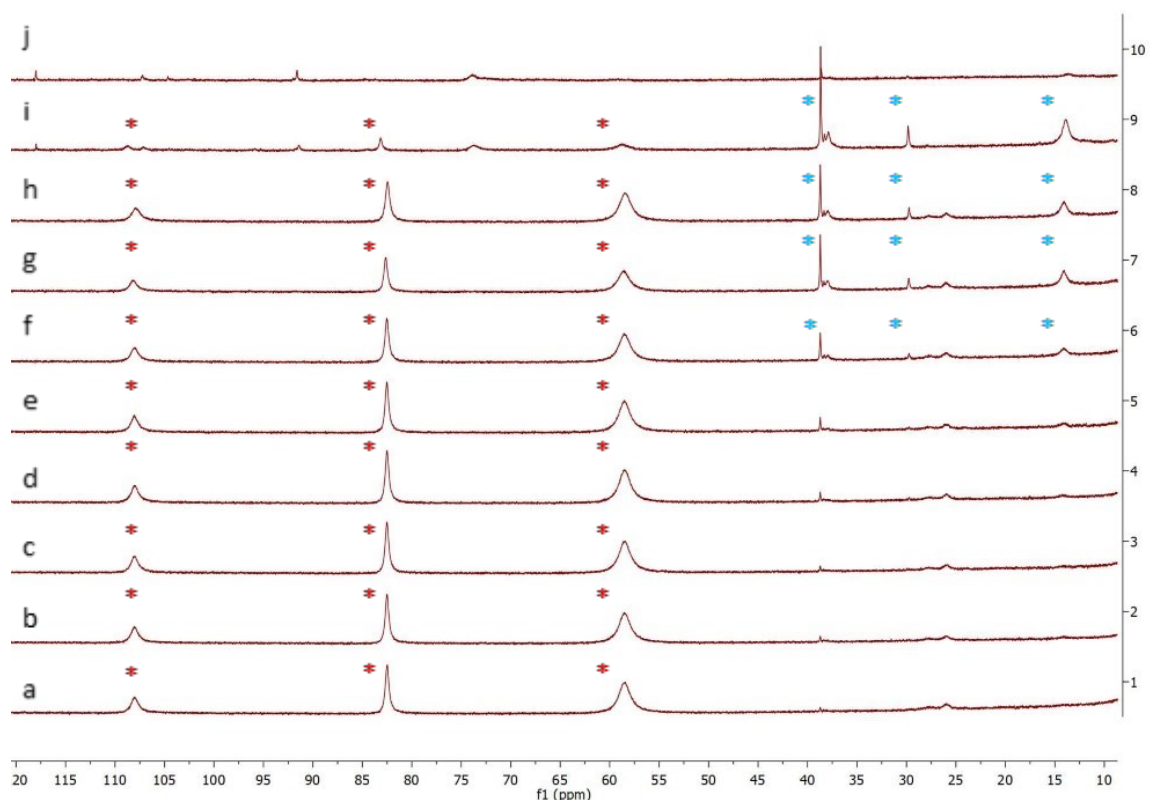
Figure 2.9: Stacked ^{1}H NMR spectra showing the paramagnetic products of the reaction of Fe$_2$Mes$_4$ with increasing loadings of ^{n}BuBPin. (a = 0.125 molar equivalents, b = 0.25, c = -.375, d = 0.5, e = 0.625, f = 1.25, g = 2.5, h = 5.0, i = 10.0, j = 25.0).
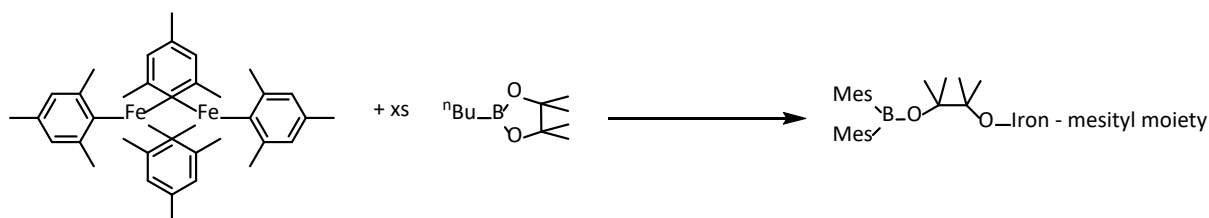
Scheme 2.17: The proposed product of the reaction of Fe$_2$Mes$_4$ with ^{n}BuBPin, forming a ring opened borinic ester.

Turning our attention then to the ^{1}H NMR speciation to gain insight into the structure of the iron product, **6** remains the most prominent species at lower loadings of ^{n}BuBPin. However, alongside these signals, a new set of signals ranging from approximately 15 to 40 ppm with three prominent peaks (38.7, 29.8, 13.9 ppm, indicated by $*$) are observed increasing in intensity with higher boron loading, before disappearing entirely at the highest examined loading of 25 equivalents (Figure 2.9 2.9, spectrum j). Unfortunately, the newly observed species could not be isolated. However, from its disappearance at the highest boron

loading, its unlikely to be the proposed iron-pinacol species, as such a species should be clearly visible at the higher boron loading. The species visible in the NMR spectra is then more likely to be an intermediate species between **6** and **11**, potentially a product of transmetallation of only 1 mesityl group from the Fe_2Mes_4 dimer.

Such a reaction would produce a new species with a mesityl : iron ratio of less than 2. In this case, a multinuclear cluster is a possibility. An iron-phenyl cluster $[Fe_4Ph_6]$ (i.e. an aryl:iron ratio of 1.5) was reported by Neidig and co-workers.[49] In this species, the iron has an average oxidation state of $Fe^{1.5}$, a mixture of Fe^I and Fe^{II}. To form an analogous mesityl species from the all-Fe^{II} Fe_2Mes_4 would therefore require a reductant. Given the absence of strongly reducing species in the reaction solution, this is perhaps not then accessible.

Discounting a multinuclear species, an alternative potential product of transmetallation may be a cationic $[Fe_2Mes_3]^+$ species, assuming a simple loss of a "Mes⁻" moiety from **6** with no further transformation occurring. (Scheme 2.18)
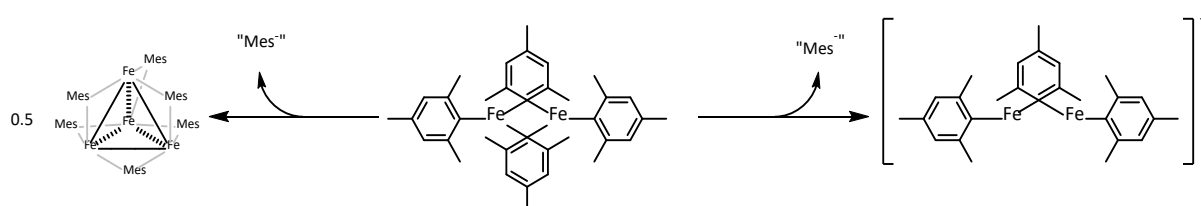
Scheme 2.18: Two potential structures of the product of transmetallation from Fe_2Mes_4 in the absence of halide.

As this product was not isolated, its structure could not be determined.

2.3.1 – The reaction of Fe_2Mes_4 with ^tBuBPin

As well as ^nBuLi, the more reactive ^tBuLi is often used as an activating base for EAM-catalysed Suzuki cross-coupling, in which the ^tBuLi-activated boronate esters are more nucleophilic than the ^nBuLi-activated analogues.[24] The reactivity of Fe_2Mes_4 with ^tBuBPin (**12**) was therefore investigated under similar conditions as with **9**. (Scheme 2.19)
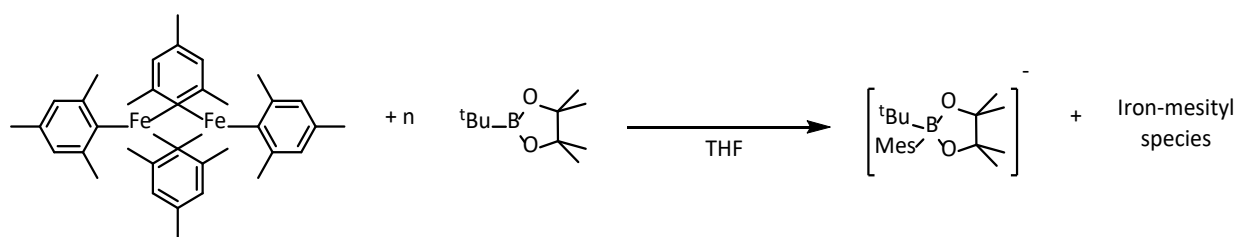
Scheme 2.19: The reaction of Fe_2Mes_4 with ^tBuBPin.

Table 2.5: Loadings of ^tBuBPin reacted with Fe_2Mes_4.

Entry	B:Fe	Signal in ^1H	Signal in ^{11}B
a	0.125	Fe_2Mes_4	^tBuBPin
b	0.250	Fe_2Mes_4	^tBuBPin
c	0.375	Fe_2Mes_4	^tBuBPin
d	0.500	Fe_2Mes_4	^tBuBPin
e	0.625	Fe_2Mes_4	^tBuBPin
f	1.25	Fe_2Mes_4	^tBuBPin
g	2.50	Fe_2Mes_4	^tBuBPin
h	5.00	Fe_2Mes_4	^tBuBPin
i	10.0	Fe_2Mes_4, New Iron Species	^tBuBPin, New Boron Species
j	25.0	New Iron Species	^tBuBPin, New Boron Species
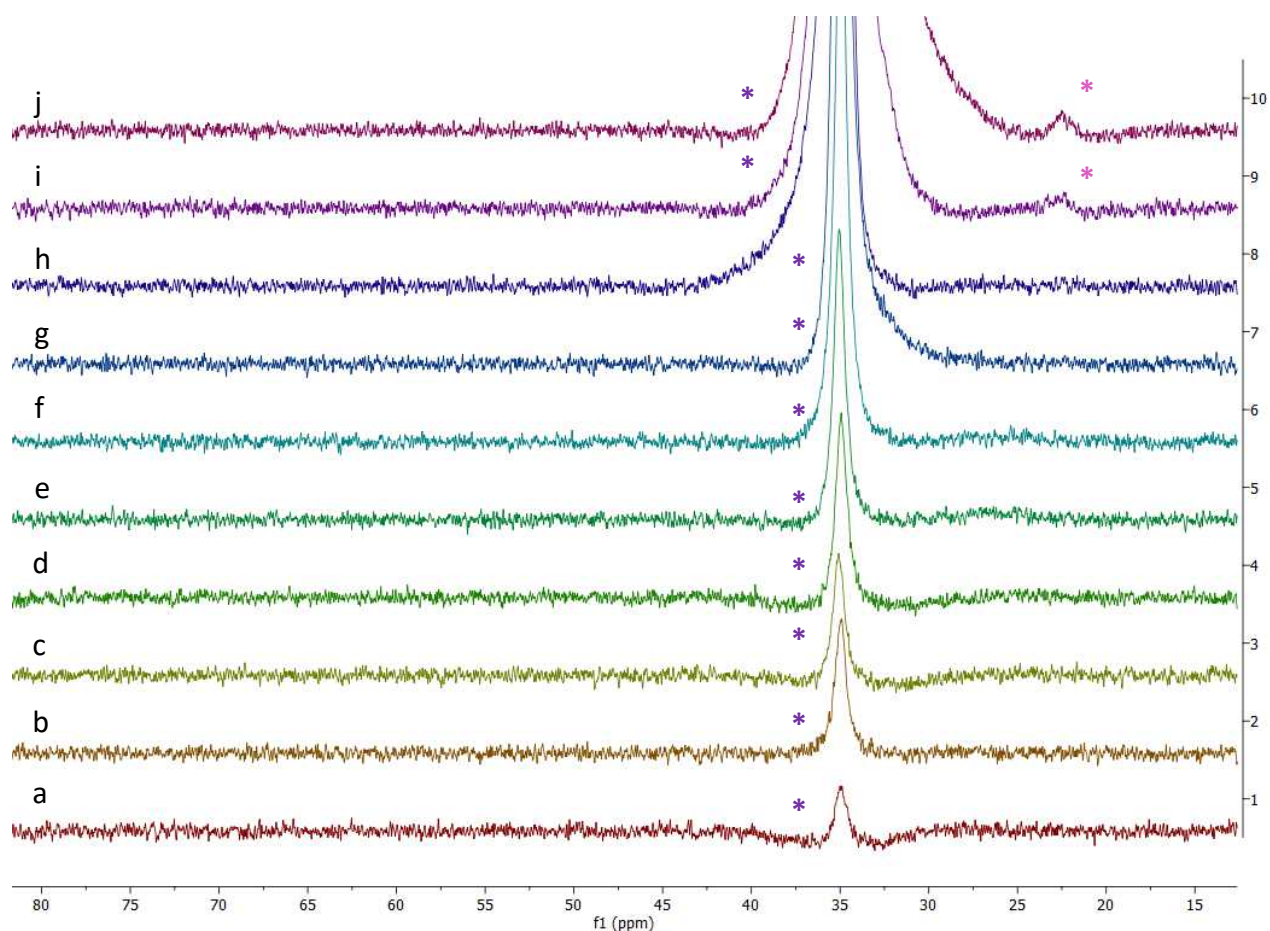
Figure 2.10: Stacked ^{11}B spectra showing the reaction of Fe_2Mes_4 with increasing loadings of ^tBuBpin. (a = 0.125 molar equivalents, b = 0.25, c = -.375, d = 0.5, e = 0.625, f = 1.25, g = 2.5, h = 5.0, i = 10.0, j = 25.0).

Once again in this case, the ^{11}B NMR shows no evidence of formation of the expected boronate ester, which would have an expected chemical shift in the range of 5-10 ppm.[116] However, alongside the signal corresponding to starting material, at the higher loadings (spectra *i*, *j*) a new signal appears at 24 ppm (*), far from the species observed in the ^nBuBPin reactions. This chemical shift matches closely with the reported ^{11}B chemical shift for MesBPin.[117] Curiously, this indicates that the ^tBu group has been substituted with Mes, rather than the formation of the boronate occurring. This raises the question of the fate of the ^tBu group. To answer this, we must look at the paramagnetic ^1H NMR data.
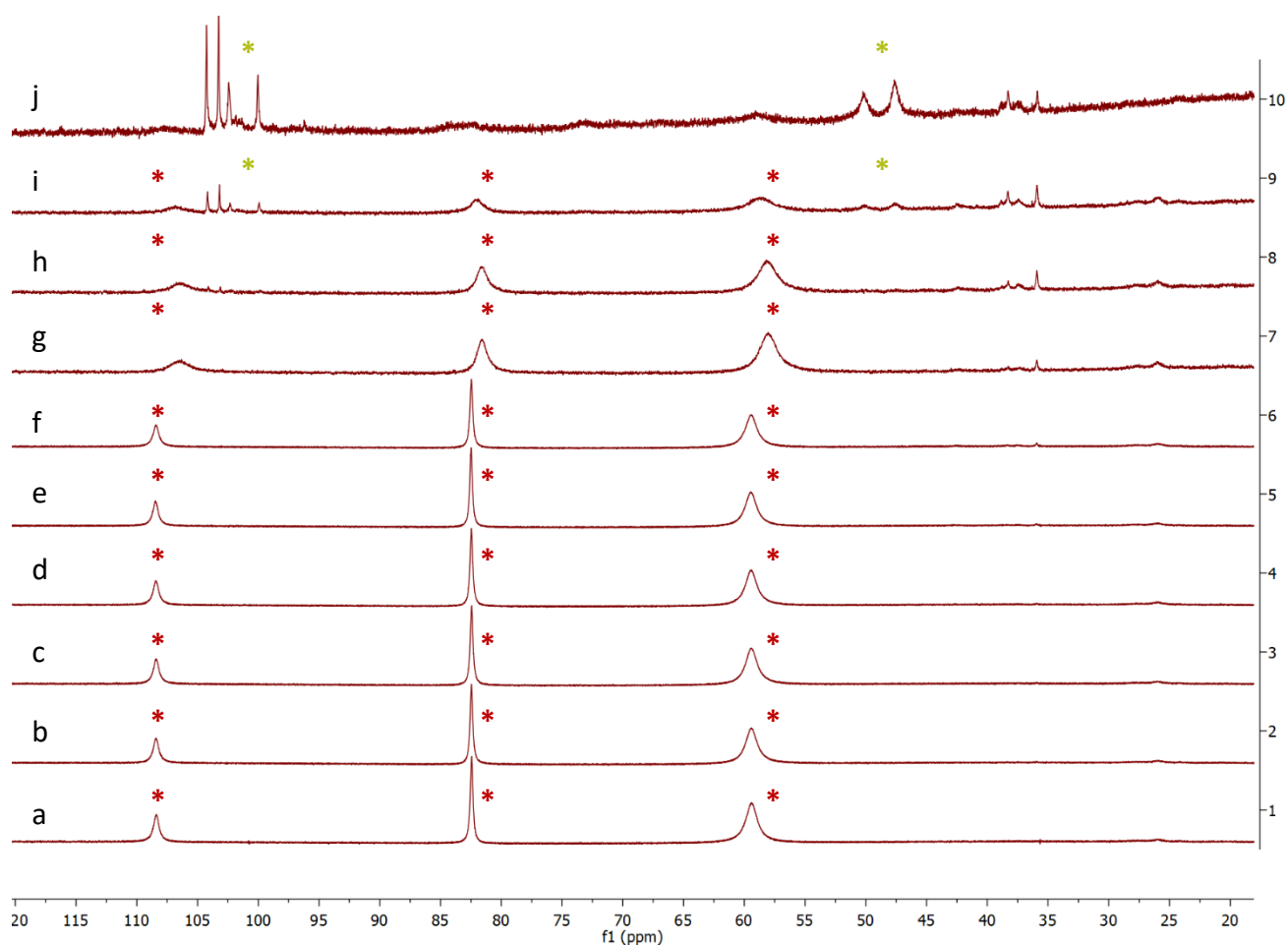
Figure 2.11: Stacked ^{1}H spectra showing the reaction of Fe$_2$Mes$_4$ with increasing loadings of ^{t}BuBpin. (a = 0.125 molar equivalents, b = 0.250, c = 0.375, d = 0.500, e = 0.625, f = 1.25, g = 2.50, h = 5.00, i = 10.0, j = 25.0).

At the higher B loadings, a new, unassigned species appears in the ^{1}H NMR spectra with several signals visible. As the ^{11}B NMR data seems to indicate the loss of ^{t}Bu from the boronic ester, it is possible that this new species incorporates this residue, although its precise structure has not been determined.
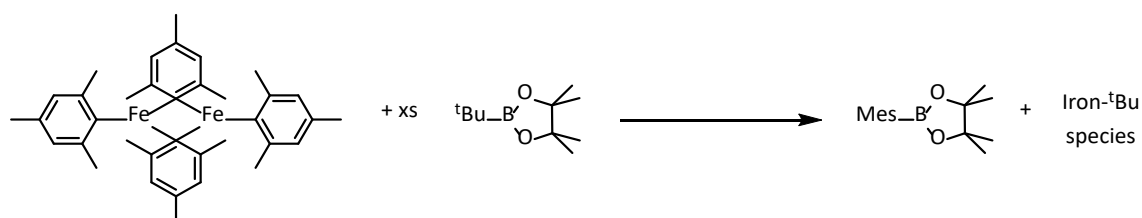
Scheme 2.20: The observed reactivity of Fe$_2$Mes$_4$ with ^{t}BuBPin.

2.4 – Transmetallation from [FeMes$_3$]$^-$

The work reported in Section 2.2 shows that in the reaction of **6** with MgBr$_2$ or ZnBr$_2$, **6** reacts first as a bromide acceptor to form **8**, which then undergoes transmetallation to the opposing metal. From the disappearance of its ^{1}H NMR signals upon reaction with excess MgBr$_2$, it appears that **7** may exhibit similar reactivity to **8**, i.e. enabling transmetallation of mesityl groups to MgBr$_2$. To probe this phenomenon further, the reactivity of **7** with MgBr$_2$, ZnBr$_2$ and FeBr$_2$ was then tested.

7 has several properties that are likely to prevent its acting as a bromide acceptor, namely, the steric shielding of the iron centre offered by the ortho-methyl groups of the mesityl moiety, and its anionic nature. Therefore, any conversion to heteroleptic species upon reaction with bromide salts is highly likely to be resultant from transmetallation.

2.4.1 – Transmetallation from [FeMes$_3$]$^-$ to FeBr$_2$

For the sake of simplicity, the first salt trialled for reaction with **7** was FeBr$_2$. Assuming transmetallation to FeBr$_2$ occurs, the products from FeBr$_2$ and **7** are likely to be the same; the heteroleptic **8** species identified previously.
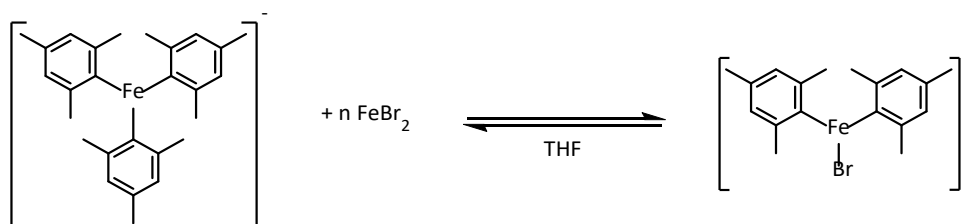
Scheme 2.21: The reaction of [FeMes$_3$]$^-$ with FeBr$_2$ to give [FeBrMes$_2$]$^-$.

Table 2.6: Loadings of FeBr$_2$ reacted with [FeMes$_3$]$^-$, with the product observed by ^{1}H NMR.

Entry	FeBr$_2$:[FeMes$_3$]$^-$	Signal in ^{1}H
a	0.125	[FeBrMes$_2$]$^-$
b	0.250	[FeBrMes$_2$]$^-$
c	0.375	[FeBrMes$_2$]$^-$
d	0.500	[FeBrMes$_2$]$^-$
e	0.625	[FeBrMes$_2$]$^-$
f	0.75	[FeBrMes$_2$]$^-$ (trace)
g	1.00	[FeBrMes$_2$]$^-$ (trace)
h	1.125	[FeBrMes$_2$]$^-$ (trace)
i	1.250	-
j	1.500	-
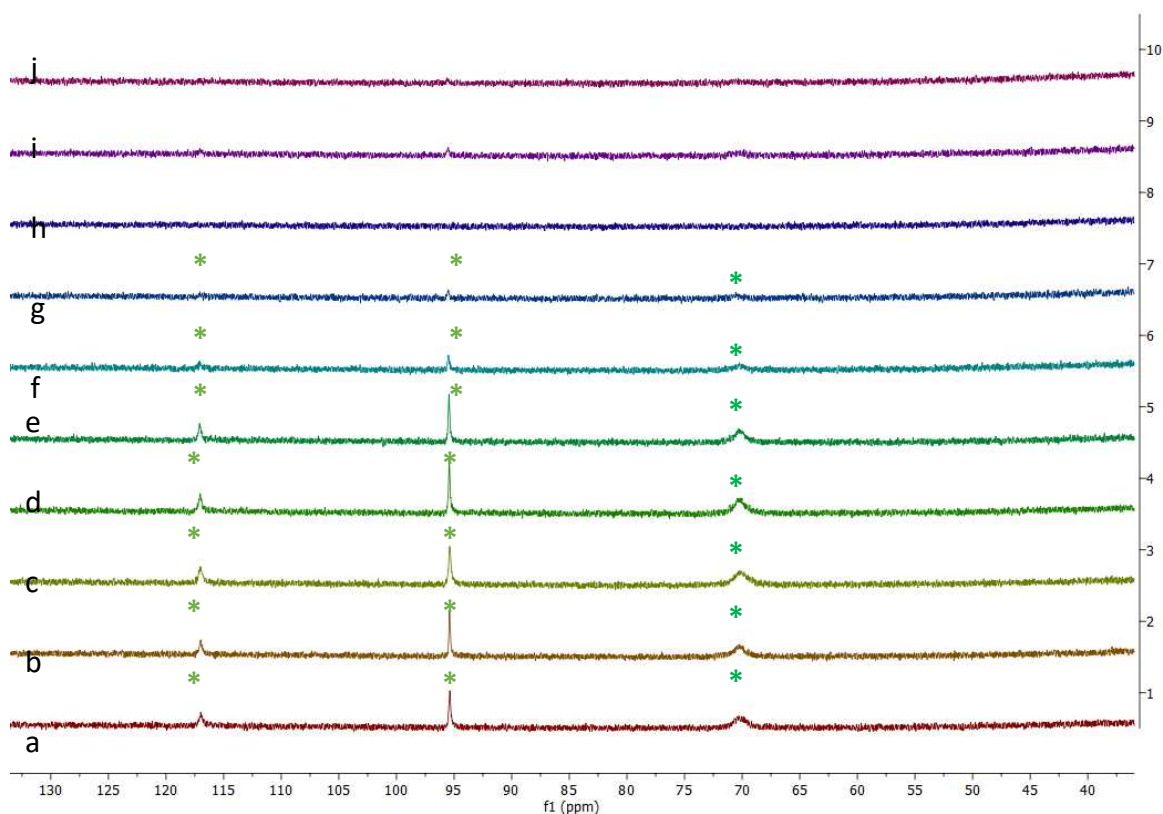
Figure 2.12: Stacked ^{1}H NMR spectra showing the product of [FeMes$_3$]$^-$ reacting with increasing loadings of FeBr$_2$. (a = 0.125 molar equivalents, b = 0.25, c = 0.375, d = 0.500, e = 0.625, f = 0.750, g = 1.000, h = 1.125, I = 1.250, j = 1.500)

Analysis by ^1H NMR shows that a low loading of $FeBr_2$ immediately gives formation of **8**, which indicates that **7** is readily able to transmetallate to $FeBr_2$. Furthermore, the disappearance of any ^1H NMR signals within the examined region at loadings above a 1:1 ratio of $FeBr_2$: **7** (Figure 2.12, spectra *g-j*) indicates that other species with lower Mes loading on iron are accessible by equilibria between **8** and $FeBr_2$.

2.4.2 – Transmetallation from [FeMes₃]⁻ to MgBr₂

Having established the capability of transmetallation to occur from **7** to $FeBr_2$, interest turned to its reactivity with $MgBr_2$. This has perhaps the most direct relevance to catalysis of the examined reactions thus far; with the presence of both species unambiguously determined in reported iron-catalysed Kumada cross-coupling reactions with MesMgBr.[51,105,118]
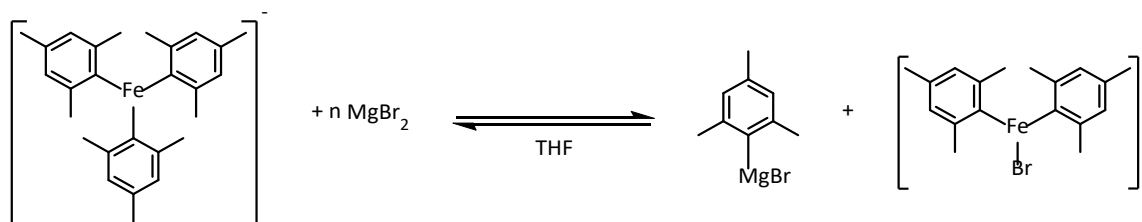
Scheme 2.22: The reaction of [FeMes₃]⁻ with MgBr₂, to form MesMgBr and [FeBrMes₂]⁻.

Table 2.7: Loadings of MgBr₂ being reacted with [FeMes₃]⁻, with the species observed by ^1H and ^{13}C NMR.

Entry	Mg:Fe	Signal in ^1H	Signal in ^{13}C
a	0.125	[FeMes₃]⁻, [FeBrMes₂]⁻	-
b	0.250	[FeMes₃]⁻, [FeBrMes₂]⁻	-
c	0.500	[FeMes₃]⁻, [FeBrMes₂]⁻	-
d	0.750	[FeMes₃]⁻, [FeBrMes₂]⁻	-
e	1.00	[FeMes₃]⁻, [FeBrMes₂]⁻	-
f	1.25	[FeMes₃]⁻, [FeBrMes₂]⁻	-
g	2.50	[FeBrMes₂]⁻	-

h	5.00	[FeBrMes$_2$]$^-$	MesMgBr

Figure 2.13: Stacked ^{1}H NMR spectra showing the reaction of [FeMes$_3$]$^-$ with increasing MgBr$_2$ loadings. (a = 0.125 molar equivalents, b = 0.250, c = 0.500, d = 0.750, e = 1.00, f = 1.25, g = 2.50, h = 5.00)

The ^{1}H NMR data unambiguously shows the formation of **8** occurring at a wide range of MgBr$_2$ loadings. In an interesting contrast to previous examples, these experiments show **7** and **8** being coincident in solution at loadings up to 1.25 equivalents of MgBr$_2$ (Figure 2.13, spectra a-f), whereas in all previous examples, the presence of one seemed to preclude the presence of the other. At loadings of 2.50 equivalents of MgBr$_2$ and up, only [FeBrMes$_2$]$^-$ is observed.

Analysis of ^{13}C NMR (Figure 14) once again showed evidence of formation of the Grignard reagent MesMgBr, albeit only at the highest MgBr$_2$ loading of 5 molar equivalents. However,

the lower concentration of the solution in this set of reactions as compared to those with **6** (necessitated by the low solubility of **7** in THF) may be responsible for this, along with the low sensitivity of ^{13}C NMR.
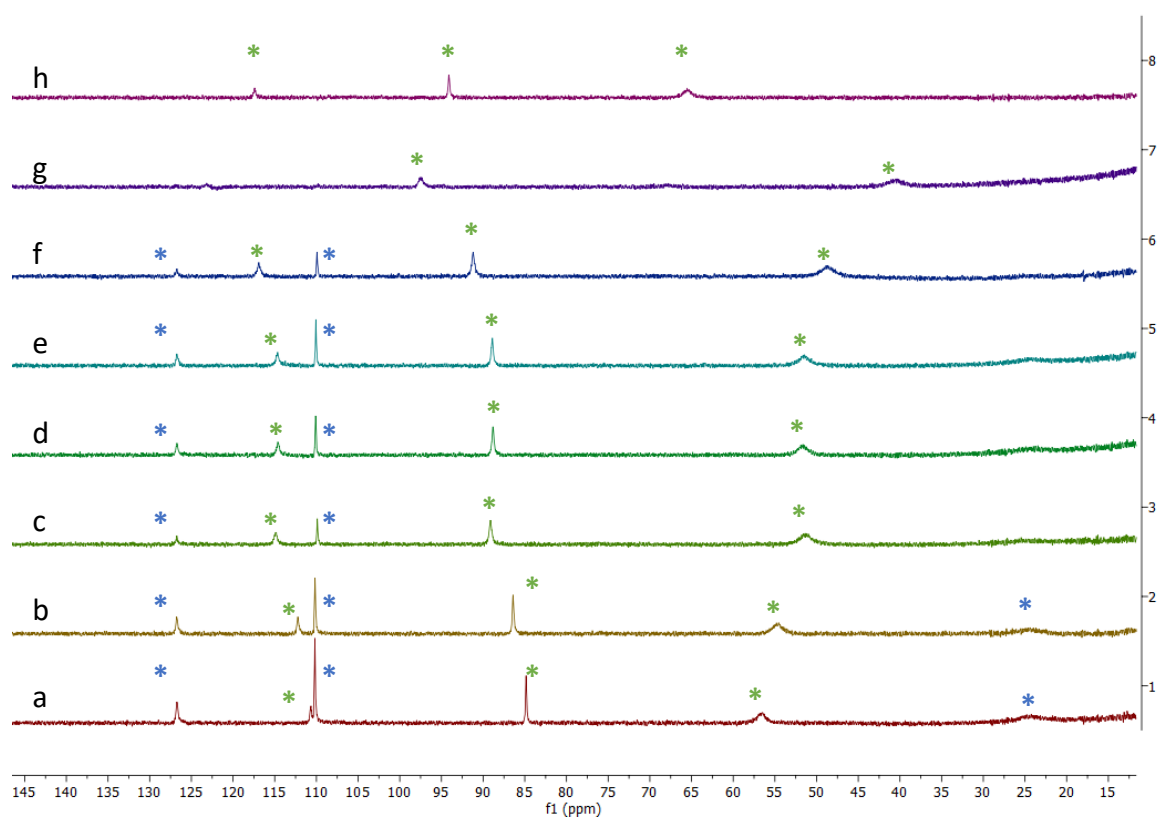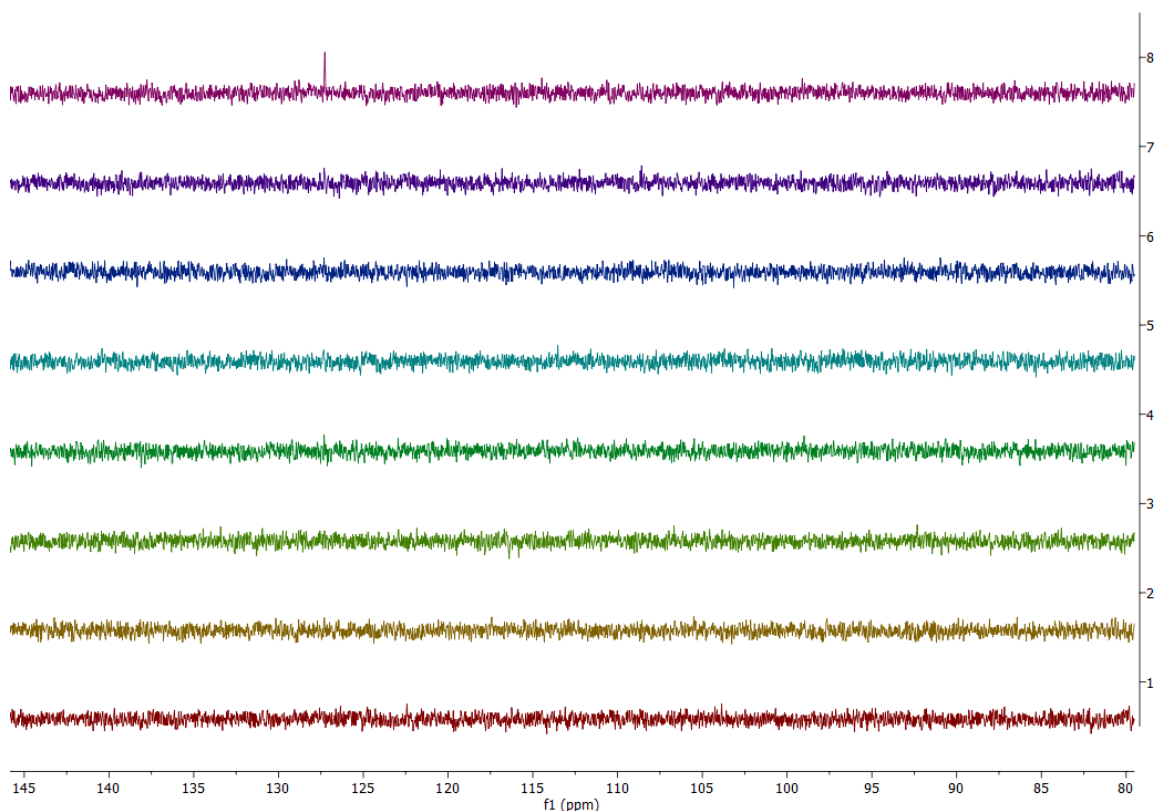

Figure 2.14: Stacked ^{13}C NMR spectra showing the reaction of [FeMes$_3$]$^-$ with increasing MgBr$_2$ loadings. (a = 0.125 molar equivalents, b = 0.250, c = 0.500, d = 0.750, e = 1.00, f = 1.25, g = 2.50, h = 5.00)

These results have striking implications for catalysis. **7** has been assigned as the sole iron species observable by ^1H NMR in Kumada cross-coupling reactions involving MesMgBr.[105] In these reactions, the concentration of MgBr$_2$ increases as the Grignard reagent is depleted. From these results, it can be inferred, at least in the absence of remaining Grignard, i.e. in the latter stages of turnover, that **7** may in fact not be present, and that instead, **8** is the most thermodynamically favoured species with even a small excess of MgBr$_2$ being present.

In the absence of a solid mechanistic understanding of iron-catalysed, ligand-free Kumada cross-coupling, it cannot be presumed how this may affect reaction rate, but confirming the

presence of heteroleptic species in reaction solution, likely increasing in concentration at later stages of catalysis, is a striking result regardless.

2.5 - Conclusions

An investigation into the reactivity of homoleptic iron-mesityl complexes with the inorganic products of cross-coupling reactions has been performed.

The homoleptic organoiron species Fe_2Mes_4 (**6**) readily reacts with inorganic bromide sources to form the novel heteroleptic ferrate $[FeBrMes_2]^-$ (**8**) which was isolated and characterised by ^1H NMR and single crystal X-ray diffraction as the Mg^{2+} salt. **8** was also observed upon the reaction of the homoleptic ferrate $[FeMes_3]^-$ with $MgBr_2$ and $FeBr_2$, demonstrating transmetallation is able to occur reversibly between organoiron and organomagnesium or organozinc species.

In solution with the bromide sources $MgBr_2$ and $ZnBr_2$, the capacity for **8** to perform transmetallation was also observed, forming the corresponding Grignard or organozinc reagent.
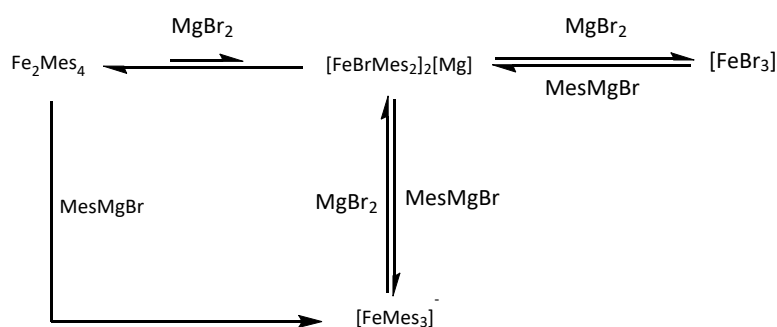
Scheme 2.23: The relationships between mesityliron species and mesitylmagnesium species uncovered in this study.

The scheme shows:

Fe$_2$Mes$_4$ $\xrightarrow{\text{ZnBr}_2}$ [FeBrMes$_2$]$_2$[Zn] $\xrightleftharpoons{\text{ZnBr}_2}$ [FeBr$_3$]$^-$ + MesZnBr/Mes$_2$Zn

with [FeMes$_3$]$^-$ at the bottom, connected upward via ZnBr$_2$ to [FeBrMes$_2$]$_2$[Zn].
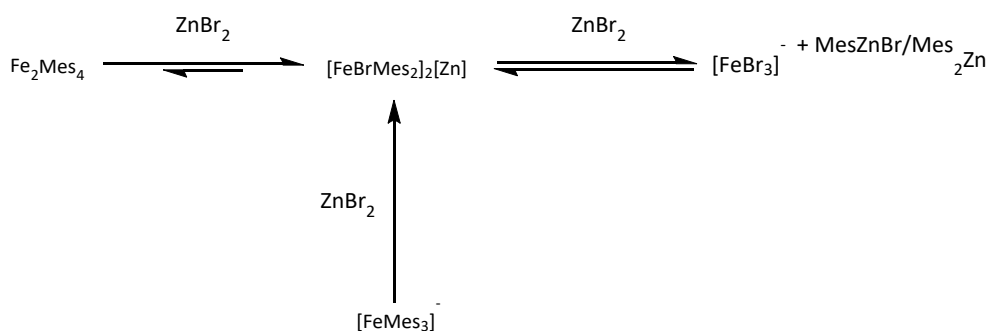
Scheme 2.24: The relationships between mesityliron and mesitylzinc species uncovered in this study.

Reactions of **6** with boronic esters do not appear to stop at the simple transmetallation of a mesityl group to the boron centre; instead, 2 different boron-based products are observed depending on whether the ^{t}Bu or ^{n}Bu substituents are present. Reaction with ^{n}BuBPin appears to generate a diaryl borinic ester, **11**, in which the pinacol ester backbone is opened by reaction with iron. Concomitantly, an unknown Fe-Mes complex is formed, tentatively assigned as either a [Fe$_2$Mes$_3$]$^+$ cation or a multinuclear cluster of some sort. Reaction with ^{t}BuBPin on the other hand produces Mes$_2$BPin, indicating a substitution of the organic substituent with the Fe$_2$Mes$_4$.

These results, in totality, show that organoiron species exist in equilibria with the organometallic nucleophiles used to produce them. This has significant implications for their intermediary roles in cross-coupling catalysis, not least showing that heteroleptic ferrate complexes are readily accessible under such conditions, given the contents of catalytic solutions.

This lends further complications to the already complex picture of the mechanisms at play in iron-catalysed cross-coupling reactions. The proceeding chapter aims to use these revelations to gain a greater understanding of iron-catalysed Kumada-Corriu cross-coupling.

3. Chapter 3 - A Mechanistic Investigation of Iron-Catalysed Ligand-Free Kumada-Corriu Cross-Coupling

3.1 - Introduction

In Chapter 2, the reactivity of homoleptic iron-mesityl species Fe_2Mes_4 (**6**) and $[FeMes_3]^-$ (**7**) with bromide salts and boronic esters was described, showing the production of the heteroleptic complex $[FeBrMes_2]^-$ (**8**) upon reaction with $MgBr_2$ or $ZnBr_2$, the side products in Kumada and Negishi cross-coupling reactions respectively. The presence of such heteroleptic species necessitates investigation of their reactivity under catalytic conditions, and their consideration as active species on the catalytic cycle for each of these reactions.

With the observations garnered from this study in hand, attention was turned towards applying them to a full mechanistic investigation of the Kumada cross-coupling reactions in which these homoleptic species are intermediates.

3.1.1 – Kinetic Studies of Iron-Catalysed Kumada Reactions

Mechanistic studies of the iron-catalysed Kumada cross-coupling reactions have tended to focus on the use of pre-formed iron-ligand complexes, such as the reports by Neidig[118] and Nagashima[56] which each assigned Fe^{II}/Fe^{III} cycles from the stoichiometric reactions of pre-formed $FeMes_2(SciOPP)$ and $FeMes_2(TMEDA)$ complexes with primary alkyl halides. (Scheme 3.1)
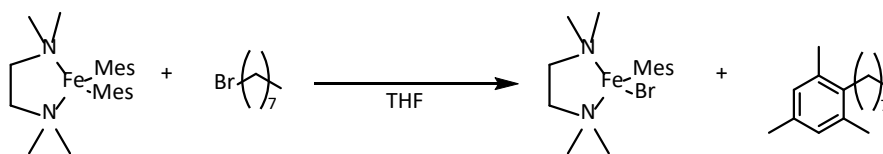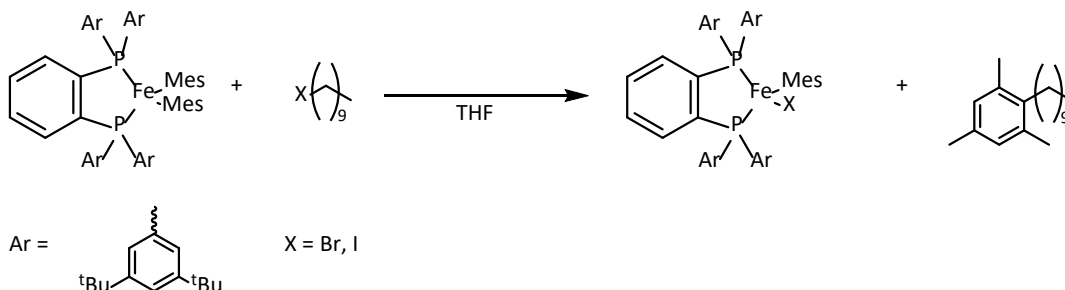
Scheme 3.1: The reactivity of pre-formed iron-ligand complexes with alkyl electrophiles as reported by (a) Nakamura and (b) Neidig.[56,118]

Nagashima's investigation of Nakamura's reported Fe-TMEDA catalysed reaction[37] consisted of stoichiometric reactions of the pre-formed complex $FeCl_2TMEDA$ (**13**)with OctBr, finding that a 1 : 1 reaction produced Fe(Mes)Cl(TMEDA) (**14**). Later work by Bedford found that not only did the presence of a slight excess MesMgBr lead to exclusive formation of $[FeMes_3]^-$ (**7**), but that **7** reacts faster with the OctBr electrophile to give the cross-coupled product than either of the TMEDA complexes.[105] (Scheme 3.2)
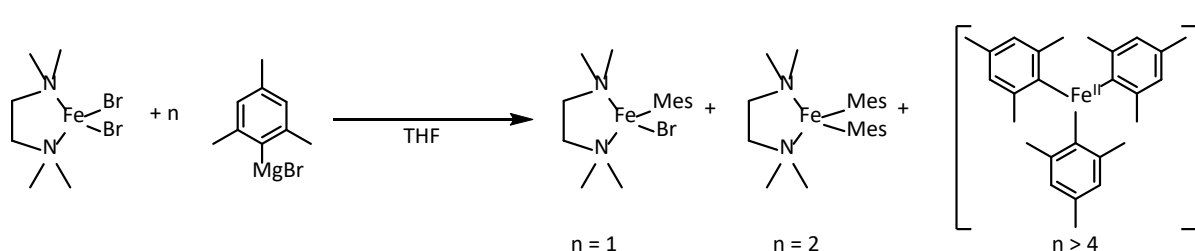
Scheme 3.2: The progressive reaction of $FeCl_2$(TMEDA) with MesMgBr.

Neidig's report showed differing results with the diphosphine ligand SciOPP. Through the use of a variety of techniques including Mössbauer spectroscopy, Magnetic Circular Dichroism (MCD) and DFT, they were able to determine a cycle shifting between a bis-

mesitylated iron-phosphine complex FeMes$_2$SciOPP (**15)** and the mesityl-bromide analogue **16**. Notably, in contrast to that found for **13** and **14**, they also found that under loadings of MesMgBr consistent with catalytic solution, particularly under the slow addition conditions of the protocol under investigation,[37] **15** remains the dominant species, and that only with loadings in excess of 20 equivalents with respect to iron is formation of **7** preferred.
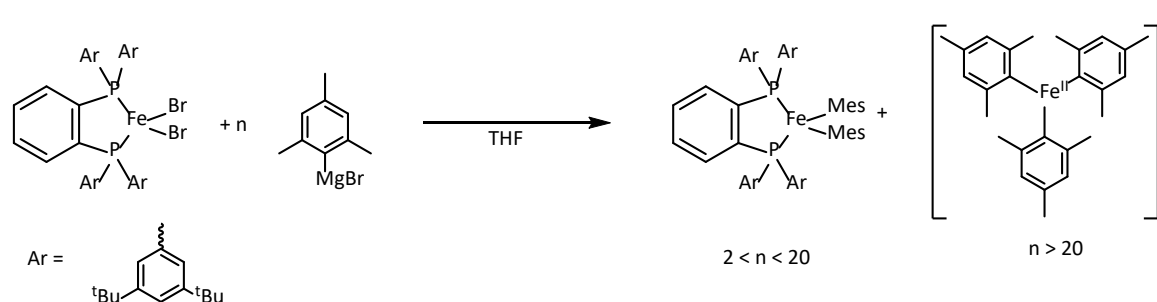
Scheme 3.3: The speciation of FeBr$_2$(SciOPP) with different loadings of MesMgBr.[118]

A comparative kinetic study also determined that **15** reacts more quickly with electrophile than **7,** as well as being more selective for the cross-coupled product.

Lefevre recently published work investigating homoleptic iron complexes for Kumada coupling with (hetero)aryl halides, showing a Fe^0/Fe^{II} cycle is operative, owing to the lower oxidation potential such electrophiles display when compared to alkyl counterparts.[54]

This chapter therefore applies the knowledge of iron speciation under catalytically representative conditions garnered in the previous chapter to a kinetic study of the mechanism of the iron-catalysed coupling of alkyl halides with aryl Grignard reagents under 'ligand-free' conditions.

3.2 – Determination of bulk oxidation state in catalysis

As a model reaction, the coupling of NaphMgBr with CyBr was chosen. Under conditions reported by Nakamura, the reaction proceeds with a yield of 97%,[32] within 30 minutes at room temperature, showing the capability of each substrate to undergo coupling (Scheme 3.4).
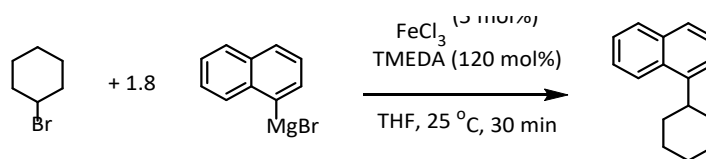
Scheme 3.4: Nakamura's protocol for the Kumada coupling of CyBr with NaphMgBr.[32]

To make the reaction suitable for profiling, some alterations were made to this protocol. First of all, the addition of TMEDA was omitted to maintain 'ligand-free' conditions. FeCl$_3$ was substituted with FeBr$_2$, keeping all the halides in reaction the same to ensure no halide effect is observed due to switching between chloride and bromide. To enable profiling, particularly of the early stages of the reaction, the rate of coupling must also be slowed down. This was accomplished through dilution and by running the reaction at -20 °C (Scheme 3.5).
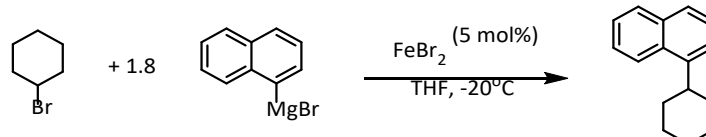
Scheme 3.5: The FeBr$_2$-catalysed cross-coupling of NaphMgBr and CyBr.

The first subject of study of this reaction was to investigate the bulk oxidation state of iron in the catalytic solution. While Bedford reported that only the Fe^{II} homoleptic complex **7** was observed in a comparable reaction with MesMgBr by ^{1}H NMR,[105] this does not negate the possibility of other species being present in forms that do not show signals in paramagnetic ^{1}H NMR.

The NaphMgBr reaction will also be compared with the coupling of MesMgBr. The Mes substituent has been shown to denote a strong stability to the Fe^{II} oxidation state in complexes bearing it, whereas this is not the case for comparable naphthyl complexes, in which reductive elimination (whether mono- or bi-molecular) is a more accessible pathway.

Reactions with the Naph substituent, or other aryl complexes which allow for reductive elimination, may therefore access lower oxidation steps.

Determination of bulk oxidation state was accomplished by profiling of similar reactions catalysed by $FeBr_3$ and $FeBr_2$. Assuming an oxidation state of Fe^{II} or lower is being reached a reductive process must occur from an Fe^{III} pre-catalyst in order to reach the active species. Such a process would occur concomitantly with the homo-coupling of the nucleophile, producing $Naph_2$. The quantity of $Naph_2$, as determined by GC-FID, observed can therefore be used to calculate the bulk oxidation state of iron in the reaction solution. (Scheme 3.6)
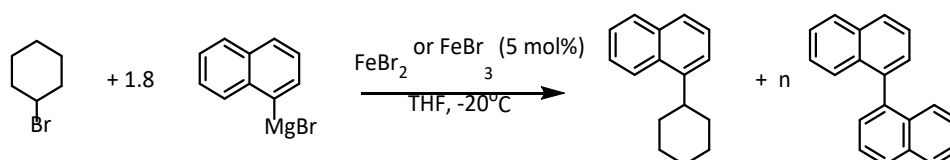
Scheme 3.6: The coupling of NaphMgBr and CyBr catalysed by $FeBr_2$ or $FeBr_3$.

Firstly, the formation of cross-coupled product was profiled in order to confirm the reaction is giving product. (Figure 3.1)
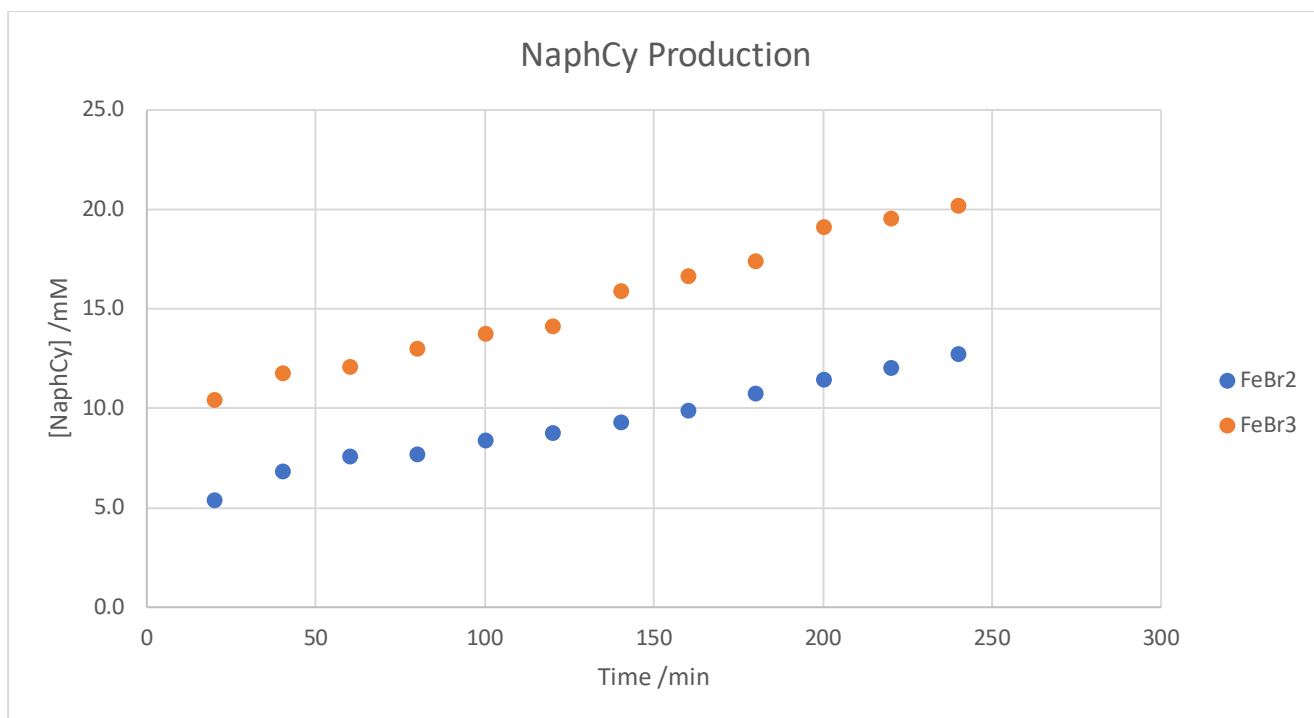
Figure 3.1: The production of NaphCy in the reaction of NaphMgBr with CyBr catalysed by FeBr$_2$ or FeBr$_3$. Initial [CyBr] = 83 mM.

Over the first 4 hours of reaction, conversion to NaphCy reached 17% and 21% for the FeBr$_2$- and FeBr$_3$-catalysed reactions respectively. Both follow a linear production of the NaphCy product at an approximately identical rate, with the sole difference being that the FeBr$_3$-catalysed reaction appears 'shifted' upwards in terms of yield. It seems then that any activation step also outputs cross-coupled product alongside the homo-coupled nucleophile. Fitting with this observation, neither line appears to regress back to the origin, suggesting that a significant amount of product formation occurs prior to the first data point in a 'burst phase'. This is an early indication that an activation process is occurring in both cases.

Turning to Naph$_2$ production; regardless of whether the bulk oxidation state in Fe^{II}, Fe^{I}, or Fe^0, a separation between the Naph$_2$ production of 2.5% should be expected, half of the mol% loading of pre-catalyst. (Scheme 3.2)
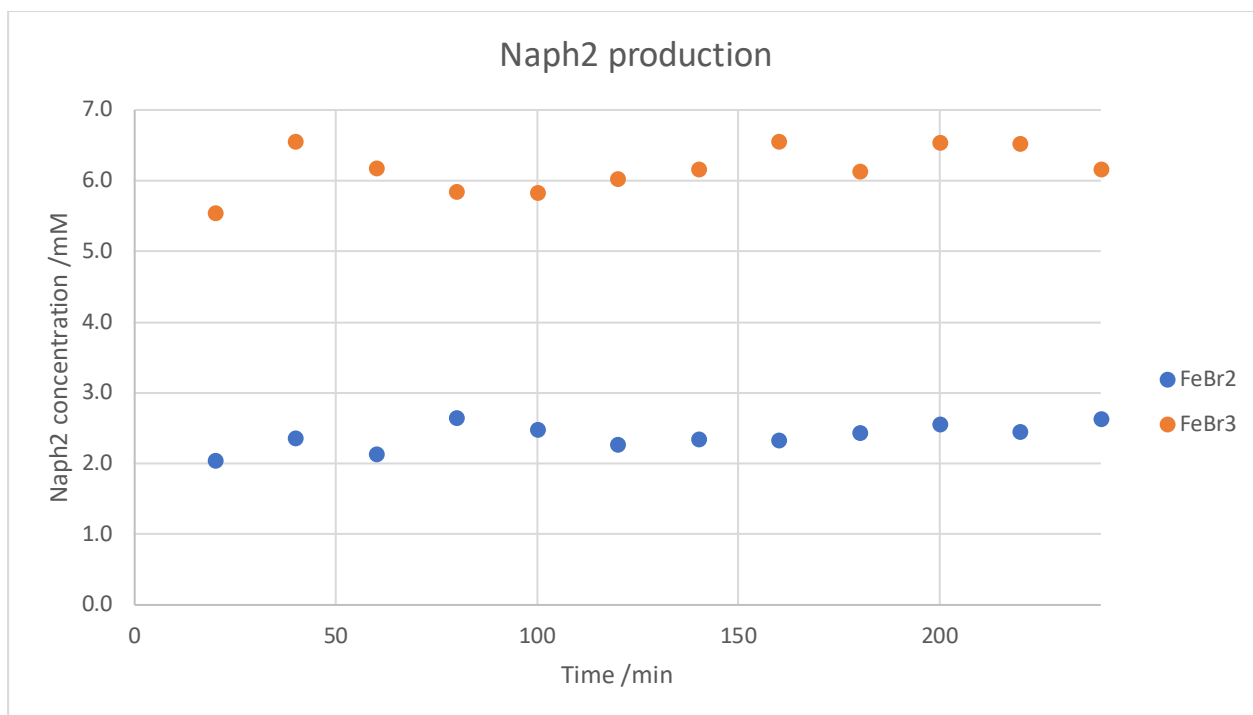
Figure 3.2: The production of Naph$_2$ in Kumada cross-coupled catalysed by FeBr$_2$ and FeBr$_3$. Initial [CyBr] = 83 mM.

In both reactions, Naph$_2$ formation occurred predominately before the first point was taken, consistent with its formation in an early activation process, although it is worth considering that significant amounts of homo-coupling may occur in the quench itself.[55] In any case, the Naph$_2$ quantity reaches approximately 3% for the FeBr$_2$-catalysed reaction and 6.5% for the FeBr$_3$-catalysed reaction. Such a separation is approximately consistent with the prediction of a 2.5% difference between the two. As for assignment of oxidation state, the FeBr$_2$ value being at an average of 3% is, assuming a quench-induced formation of Naph$_2$ of 0.5%, consistent with an Fe^I bulk oxidation state.

To compare, the coupling of CyBr with MesMgBr was also performed, with FeBr$_2$ catalyst and production of Mes$_2$ profiled. (Figure 3.3)
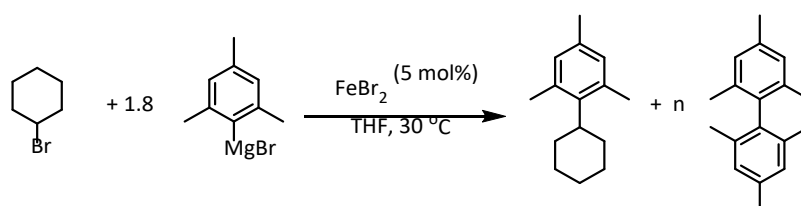
Scheme 3.7: The FeBr$_2$-catalysed Kumada coupling of CyBr with MesMgBr.
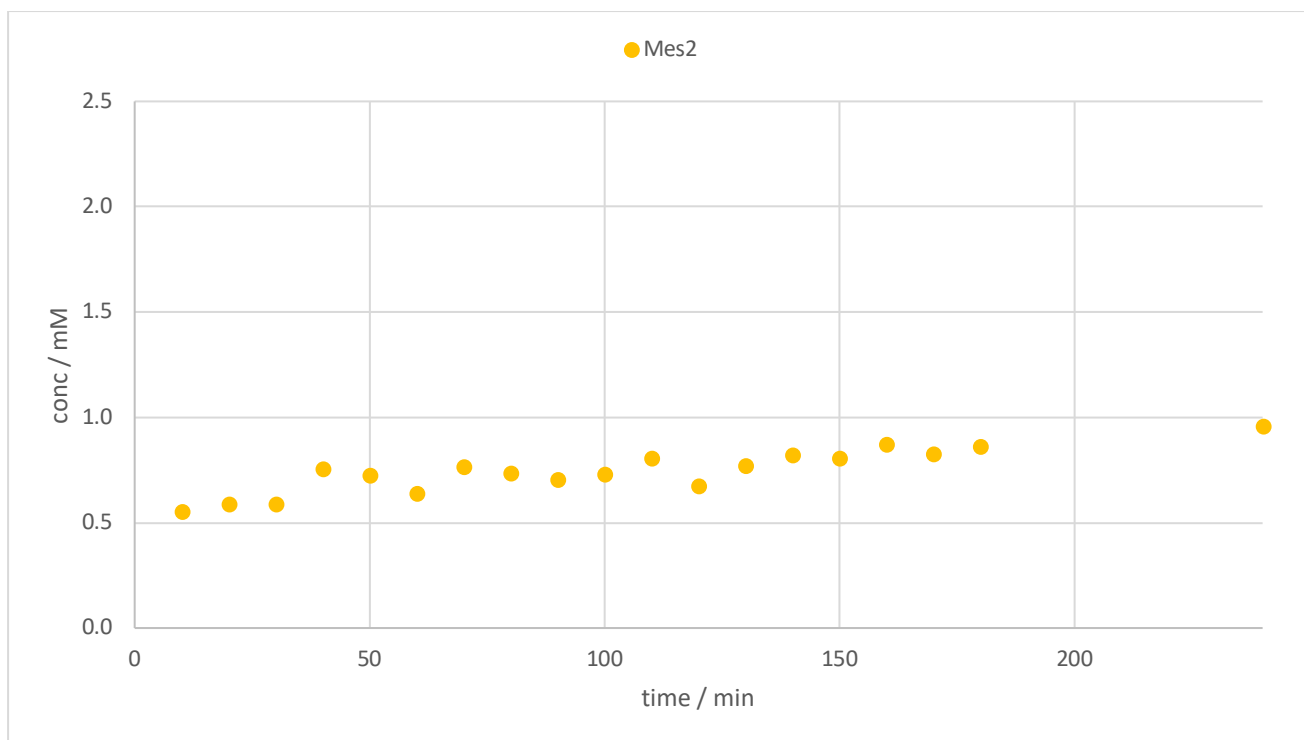
Figure 3.3: The production of Mes$_2$ in the FeBr$_2$-catalysed coupling of CyBr and MesMgBr.

In this case, production of Mes$_2$ seemed to occur gradually through reaction, and therefore the Mes$_2$ concentration at the first point is taken as an indication of bulk oxidation state after activation processes. This value corresponds to 0.6%, too low to assume any reduction process is occurring during activation, and therefore consistent with an Fe^{II} bulk, consistent with Bedford's assignment of the Fe^{II} species **7** being the main iron species in solution.[52]

The difference of bulk oxidation indicates that a change in mechanism of ligand-free iron-catalysed Kumada cross-coupling occurs depending on the properties of the nucleophile being used. It seems likely that a more efficient catalytic cycle is active when an Fe^{I} active species is accessible, potentially of the type proposed by Norrby.[40] The bulky Mes substituent likely disables an Fe^{I} pathway by resisting the reductive process that forms the active catalyst and undergoes a separate pathway instead.

The rest of this chapter will therefore examine the mechanism of coupling with the mesityl substituent, for which the homoleptic organoiron complexes have been well characterised and studied, as well as the heteroleptic complex [FeBrMes$_2$]$^-$ (**9**) being isolated earlier in this work and displaying relative stability in solution compared to the naphthyl analogues. The

disadvantage of using the mesityl substituent is that while Kumada coupling with NaphMgBr reaches yields over 90%,[32] the equivalent Mes reactions go at a much slower rate, and reach far lower yields even upon reaching completion.

By pre-forming the previously characterised iron-mesityl species Fe_2Mes_4 (**6**), $[FeMes_3]^-$ (**7**), and $[FeBrMes_2]^-$ (**9**) and testing the rates of formation of cross-coupled product upon their reactions with an electrophile, it is possible to identify which species are likely to be on the main catalytic cycle, and which are either off-cycle or not present in catalysis.

3.3 – Stoichiometric Reactions of Organoiron Species with OctBr

Initially, the reaction of MesMgBr with CyBr catalysed by $FeBr_2$ was investigated, but it was found that under the conditions used for profiling, the reaction was prohibitively slow, with cross-coupling not reaching a TON of 1 over 24 hours. Instead, the CyBr electrophile was entirely depleted by a competitive homocoupling reaction to form Cy_2. As many iron-catalysed reactions have been found to go by radical pathways,[118,119] it was reasoned that the secondary nature of the radical that would be formed from CyBr has sufficient stability that its concentration may reach levels high enough that the radical recombination reaction outpaces any cross-coupling. Therefore, further studies were performed with the primary halide OctBr in place of CyBr.
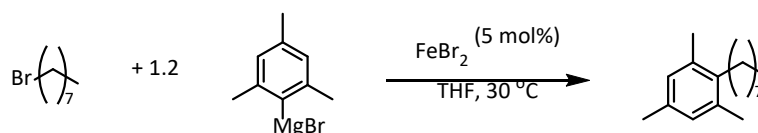
Scheme 3.8: The $FeBr_2$-catalysed cross-coupling of MesMgBr with OctBr.

The catalytic reaction under these conditions gave a cross-coupling yield of 9.5% after 24 h of reaction, and 21% after 72 h. From the 5 mol% loading of $FeBr_2$; this gives an approximate TOF of 2 turnovers every 24 hours.

Profiling this reaction revealed a linear rate of cross-coupling, with no evidence of any induction period or burst phases within the sampled portion (Figure 3.4).
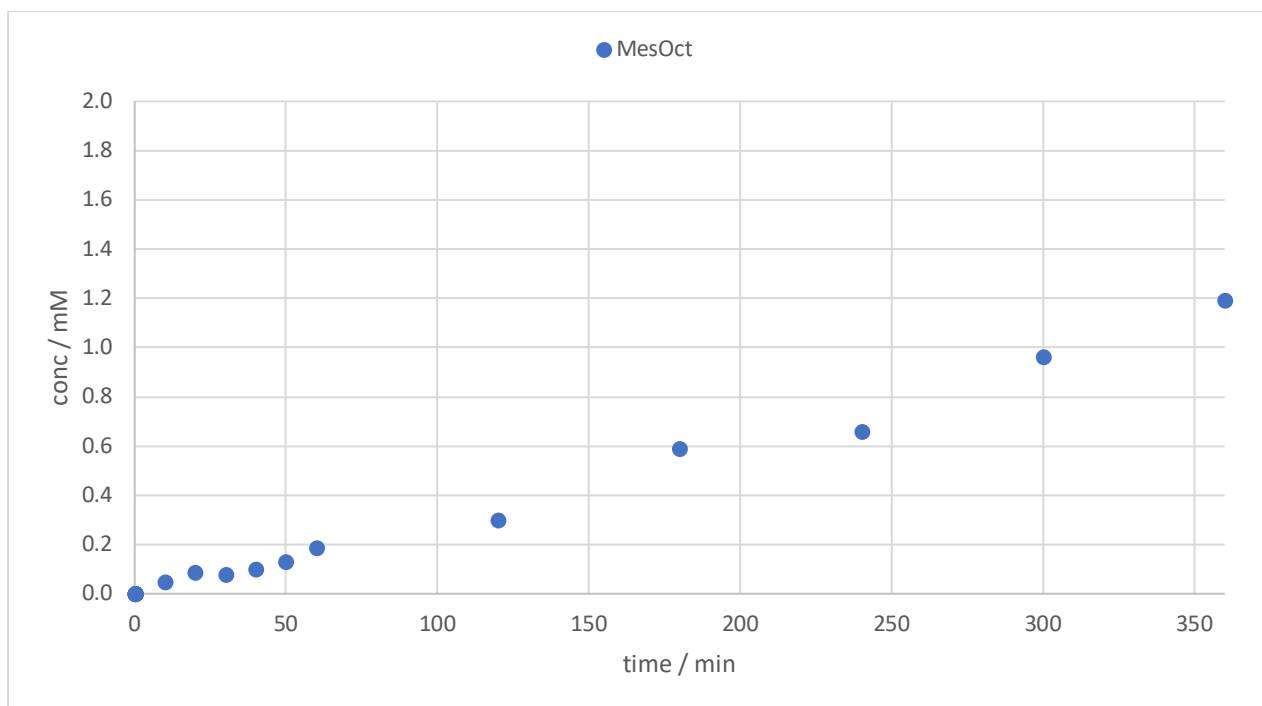
Figure 3.4: Profile of the production of MesOct from FeBr$_2$-catalysed cross-coupling of MesMgBr with OctBr.

^{1}H NMR analysis of the reaction solution during turnover revealed **7** as the only observable paramagnetic species, fitting with previous reports by the Bedford group.[51] For this reason, the stoichiometric reaction of **7** with electrophile was profiled to determine its role in catalysis.

7 was synthesised by the reaction of FeBr$_2$ with 3 equivalents of MesMgBr, with its formation confirmed by ^{1}H NMR, and was used upon its *in situ* formation without further purification performed.
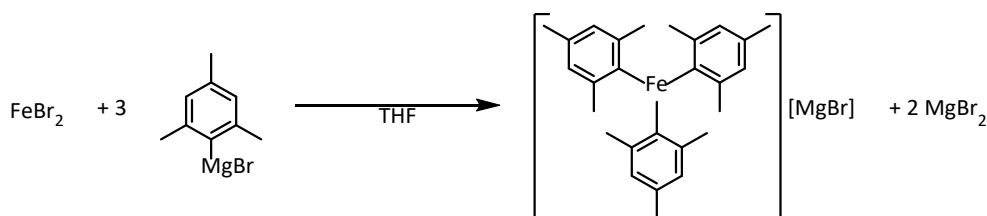
Scheme 3.9: The reaction of FeBr$_2$ with MesMgBr to form [FeMes$_3$]$^-$.

Its reaction with one equivalent of OctBr with respect to iron was then profiled over 6 hours, with aliquots being taken every 10 minutes for the first hour of reaction then every hour subsequently.

While this appears to be a simple stoichiometric reaction, it bears consideration, given the results discussed in the previous chapter, that formation of the Grignard reagent from the reversible transmetallation to $MgBr_2$ is very much accessible under these conditions, concomitantly with formation of **9.** (Scheme 3.11)
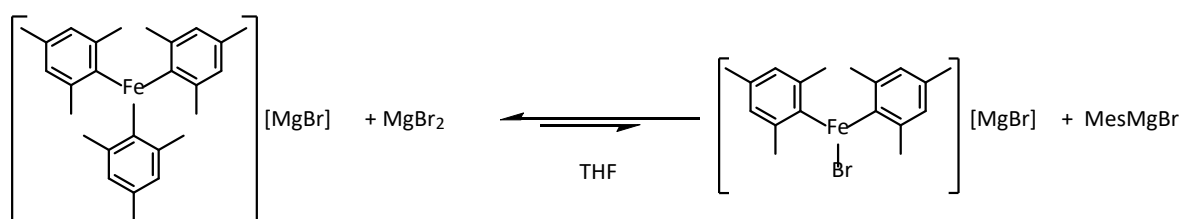
Scheme 3.10: The reversible formation of MesMgBr from the reaction of $[FeMes_3]^-$ with $MgBr_2$.
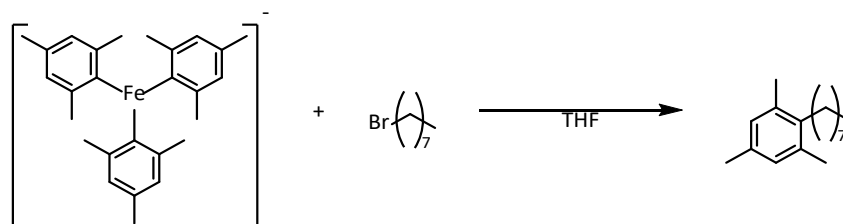
Scheme 3.11: The stoichiometric reaction of $[FeMes_3]^-$ with OctBr to give MesOct.
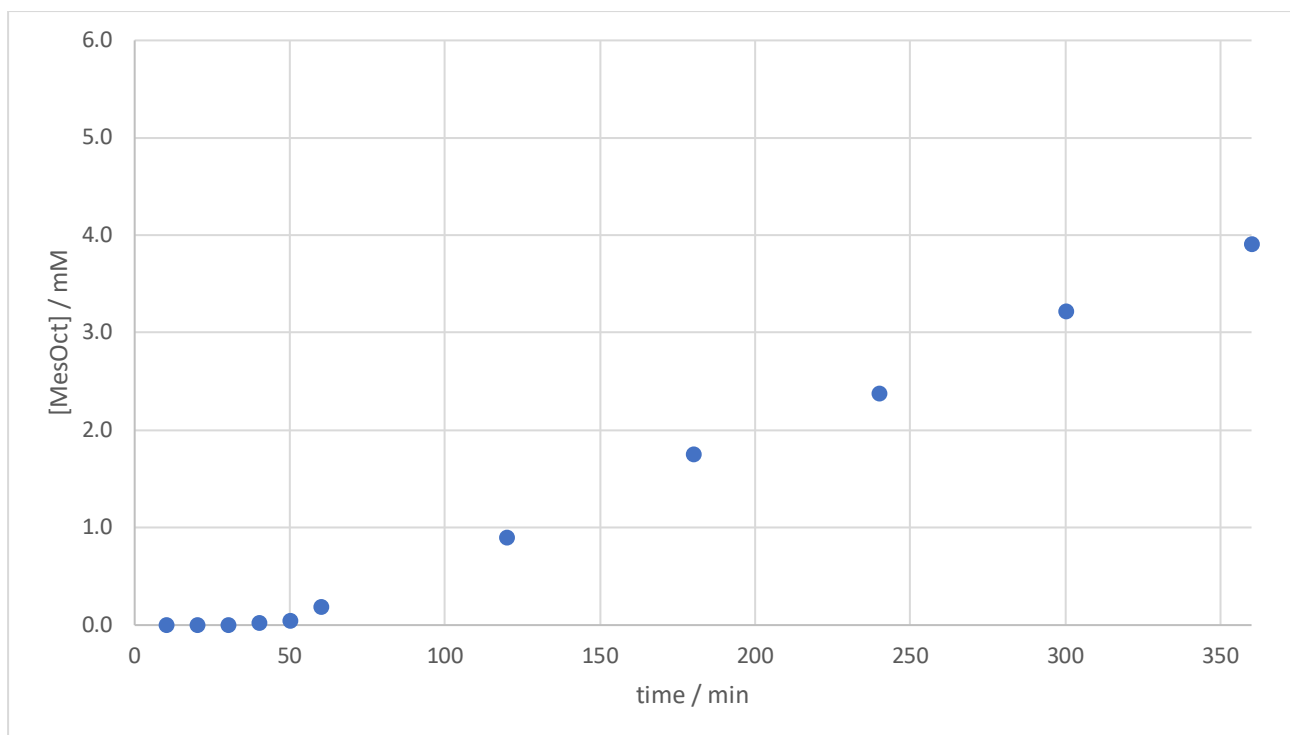
Figure 3.5: Reaction profile showing the formation of MesOct from the reaction of [FeMes$_3$]$^-$ with OctBr. Initial concentration of [FeMes$_3$]$^-$ = 33 mM in THF.

The most striking feature of this profile is the induction period observed for the first 50 minutes following addition of the electrophile. This induction period remains at the same length regardless of how long FeBr$_2$ was pre-stirred with MesMgBr prior to addition of OctBr, therefore it cannot correspond to the initial formation of **7**. Instead, it must be due to a process either directly induced or otherwise affected by addition of the electrophile. Whether this is a direct reaction of the two species, or a reaction of electrophile with a species in equilibrium with **7** remains unclear from this data. To determine this, the concentration of OctBr through this reaction must be examined, with the caveat that the quantification of organic bromides with GC-FID is limited by high uncertainty due to the flame retardant properties of such chemicals.[120]
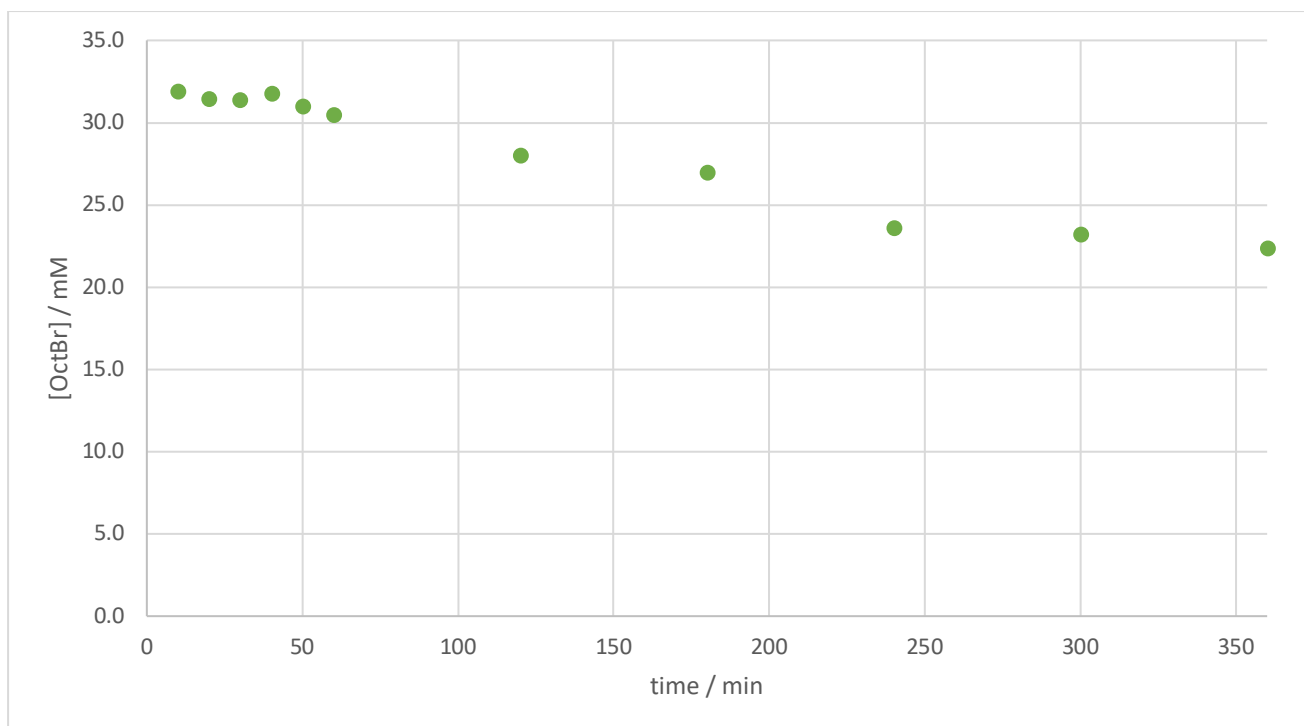
Figure 3.6: The concentration of OctBr throughout the reaction between $[FeMes_3]^-$ and OctBr. Initial [OctBr] = 33 mM.

The consumption of OctBr seems to match the shape of MesOct production, in that little change in concentration is observed during the first 50 minutes of reaction. This may indicate that the induction period process does not itself consume OctBr.

Interestingly, the formation of the homocoupling product Mes_2 in this reaction, while starting from a higher baseline due to its production during the quench, appears to follow the same shape as that for the cross-coupled product, in that no production is observed for the first 50 minutes and only subsequent to it, a linear production of Mes_2 is observed.
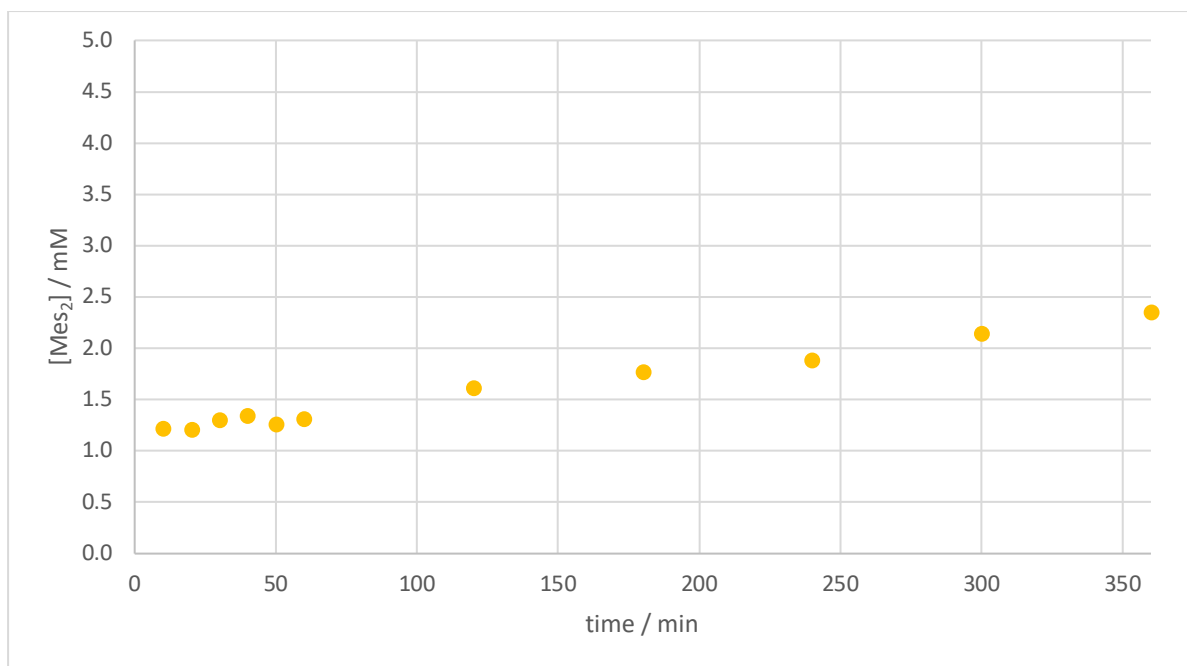
Figure 3.7: The production of Mes_2 from the reaction of $[FeMes_3]^-$ with OctBr. Initial concentration of $[FeMes_3]^- = 33$ mM in THF.

This implies that both products are formed from the same intermediate, with the ratio determined by the propensity of each product to be formed by a reductive elimination. In this case, the resistance to reductive elimination afforded by the ortho-methyl moieties on the mesityl groups should favour formation of the cross-coupled product. This also shows that the final intermediate preceding an elimination step is likely to bear at least 2 mesityl groups and 1 octyl group.
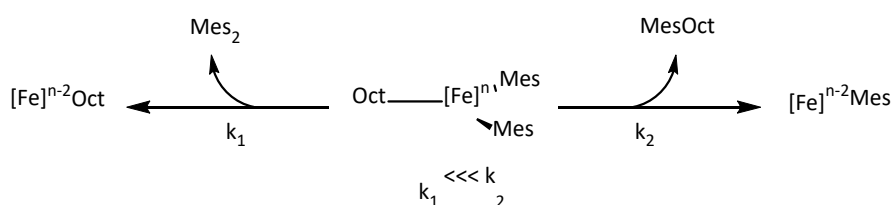
Scheme 3.12: The competing formation of Mes_2 and MesOct by reductive elimination from an iron intermediate.

The observed concentrations for each component were then converted to percentage yields with respect to iron (per iron centre).

Table 3.8: The percentage yields observed for OctBr, MesOct, and Mes_2 in the reaction of $[FeMes_3]^-$ with OctBr.

time /min	OctBr yield /%	MesOct yield /%	Mes_2 yield /%
10	96.8	0.0	3.7
20	95.4	0.0	3.7
30	95.2	0.0	4.0
40	96.2	0.1	4.1
50	94.0	0.2	3.8
60	92.5	0.6	4.0
120	84.9	2.7	4.9
180	81.8	5.3	5.4
240	71.6	7.2	5.7
300	70.5	9.8	6.5
360	67.9	11.9	7.1

Notably, the consumption of OctBr appears to greatly outpace the production of MesOct, with 32% of OctBr consumed with 360 minutes, but only 12% of MesOct produced. Analysing the reaction mixture by GC-MS showed no evidence of the homo-coupled product hexadecane being present, therefore the shortfall is likely made up by octene and octane. Unfortunately, these could not be quantified by GC-FID due to significant overlap with other low boiling point peaks.

To gain a further insight into the speciation of iron during processes occurring under these conditions, the reaction was monitored by taking aliquots for analysis by ^1H NMR at 30 minutes and 5 hours after the initiation of reaction, i.e. during the induction period and during turnover. (Figure 3.8)
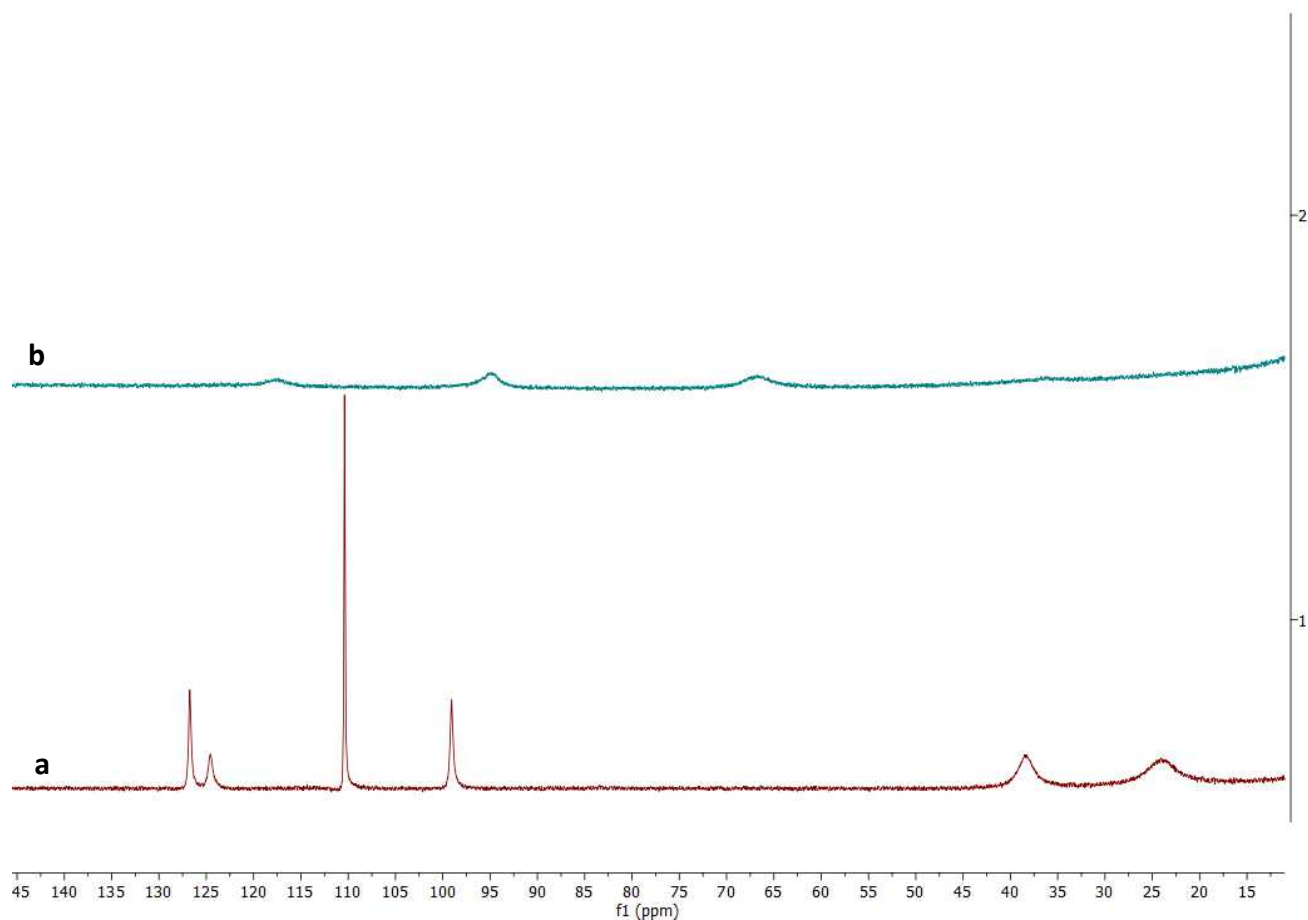
Figure 3.8: ^{1}H NMR spectra of the reaction between [FeMes$_3$]$^-$ and OctBr taken at a) 30 minutes and b) 5 hours after the addition of OctBr.

The sample taken at 30-minutes (Figure 3.8a) shows signals corresponding to two different forms of **7** (127, 124, 111, 98, 39, 24 ppm), previous work in the group has shown that simply changing the counterion of **7** can result in chemical shifts changing by several ppm,[121] therefore it is perhaps not so surprising that 2 different sets of chemical shifts are observed. The aliquot taken at 5 hours (Figure 3.8b) shows signals corresponding to the heteroleptic ferrate species **9**. While this data supports the supposition that **7** is not present in large quantities during the active phase of cross-coupling, the role of **8** remains ambiguous. Either the induction period corresponds to an OctBr-mediated conversion of **7** into **8**, which then reacts further with the electrophile to give the cross-coupled product, or **8** is the output of the reaction that releases the MesOct product. In order to determine the role of **8**, its reactivity with OctBr was also profiled.

Unfortunately, solid samples of crystallised **8** show rapid degradation at room temperature, meaning an isolated sample could not be weighed out for use in stoichiometric reactions. Luckily, it was confirmed by ^{1}H NMR that **8** is formed *in situ* by reaction of $FeBr_2$ with 2 equivalents of MesMgBr, absent of any other paramagnetic species.
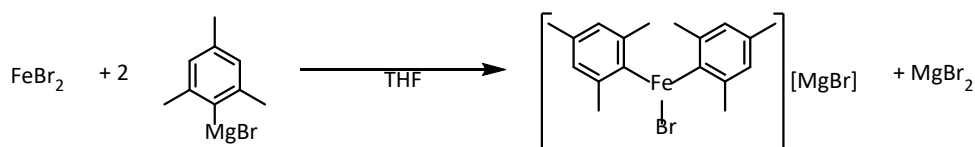
Scheme 3.13: The formation of [FeBrMes$_2$]$^-$ from FeBr$_2$ and MesMgBr.

With **9** in hand, the reaction with OctBr was investigated. In the case that it is the primary driver of cross-coupling, formation of MesOct would be expected to begin immediately, at an approximately similar rate to that observed subsequent to the induction period in the reaction with **7**. If, however, it is the species formed after the release of MesOct, formation of MesOct should be expected to occur at a lower rate than observed with **7**, if at all.
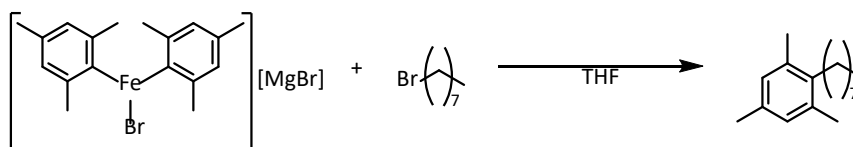
Scheme 3.14: The reaction of [FeBrMes$_2$]$^-$ with OctBr to form MesOct.
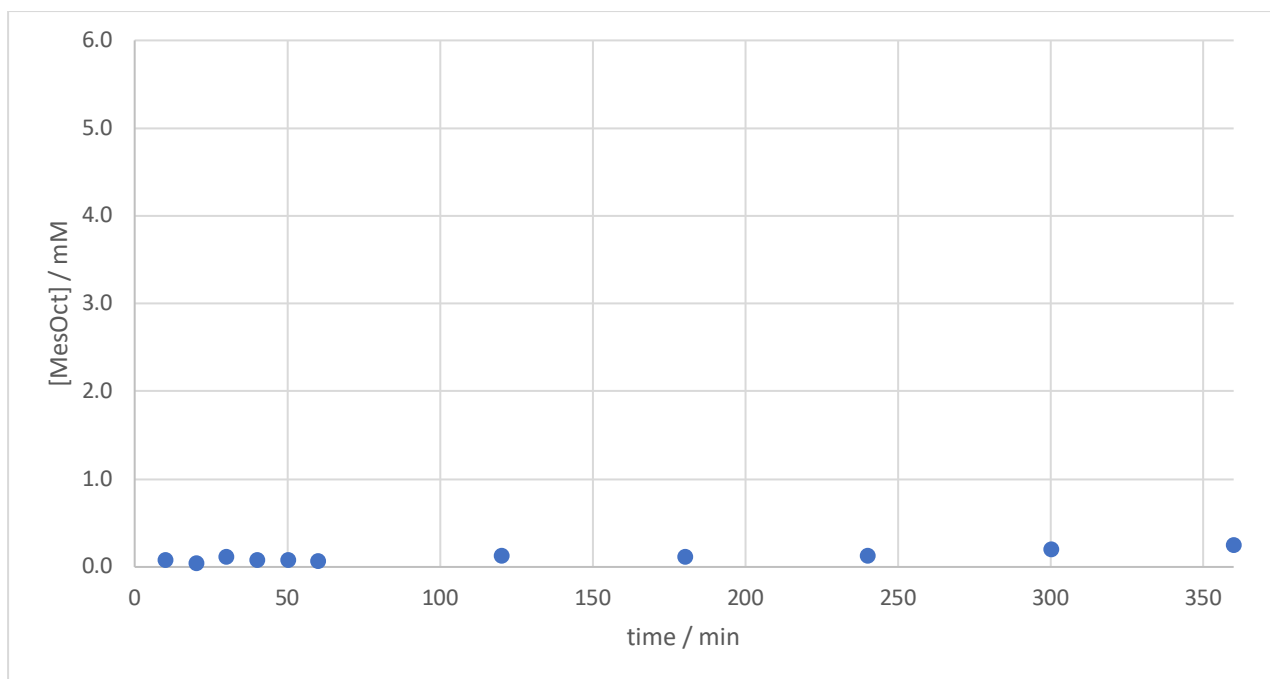
Figure 3.9: Profile showing the production of MesOct from the reaction of $[FeBrMes_2]^-$ with OctBr. Initial concentration of $[FeBrMes_2]^- = 33$ mM in THF.

Under these conditions, the reaction of **8** with OctBr showed only a trace level of cross-coupled product, giving a yield of less than 1% of MesOct with respect to Fe after 6 hours. Clearly, **8** cannot be the species predominately responsible for giving the cross-coupled product in catalysis.

It was therefore hypothesised that it may be an end state of iron after producing one equivalent of the cross-coupled product. If this is the case, then under catalytic conditions, the catalytic cycle may be closed by reaction of **8** with a further equivalent of MesMgBr to generate **7**.

In order to test this hypothesis, **8** was reacted overnight with 1 equivalent of OctBr, once again giving a yield of cross-coupled product below 1% after 24 hours. Subsequent to this, one further equivalent of MesMgBr was added to bring the total loading of MesMgBr in the solution to 3 equivalents with respect to iron, the same used to synthesise **8**.
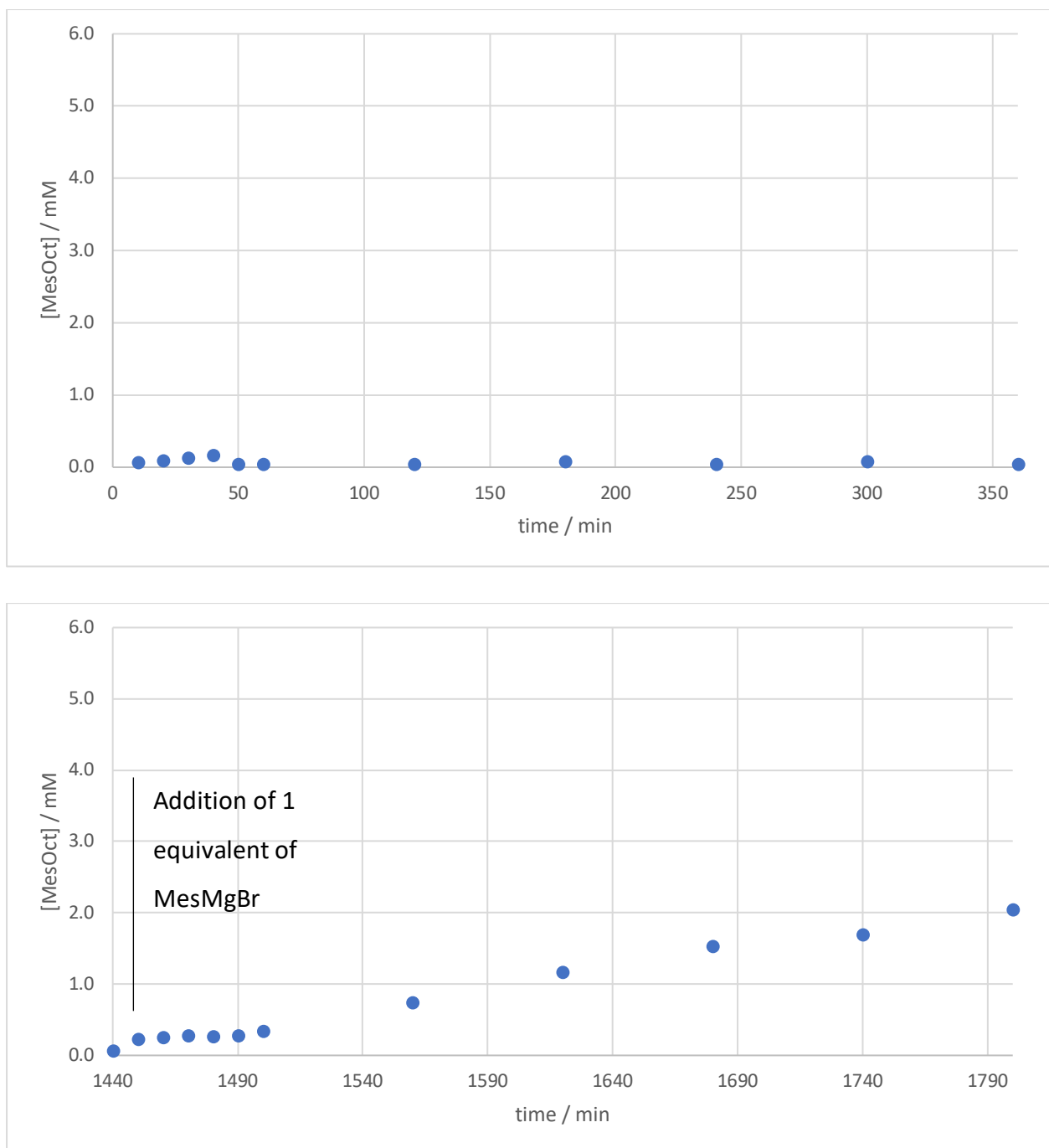
Figure 3.10: Profiles showing the production of MesOct from the reaction of $[FeBrMes_2]^-$ with OctBr before and after addition of 1 equivalent of MesMgBr. Initial concentration of $[FeBrMes_2]^-$ = 33 mM in THF.

From the addition of the third equivalent of MesMgBr, an induction period of 50 minutes precedes formation of MesOct at a linear rate, as observed with *in situ* formed **7**. The rate of MesOct formation is lower than the previous trial, although this may be explained by decomposition of **8** overnight to species that may not be brought into catalytic reaction.

While the catalytic failure of **8** to form cross-coupled product from reaction with electrophile has now been established, there exists the possibility that a complex of the type [FeBr$_2$Mes]$^-$ may have such competence. However, no such species has yet been reported. Therefore, the synthesis of such a complex was pursued in order to test its reactivity with an electrophile.

The initial synthetic route attempted was the simple reaction of FeBr$_2$ with 1 molar equivalent of MesMgBr. However, as determined by ^{1}H NMR, this reaction gave only **8** as the product. The bis-mesitylated product therefore appears to be a thermodynamic sink in solution, with its formation enabled by the equilibrium between the Grignard reagent and organoiron species that was investigated in Chapter 2. (Scheme 3.15)
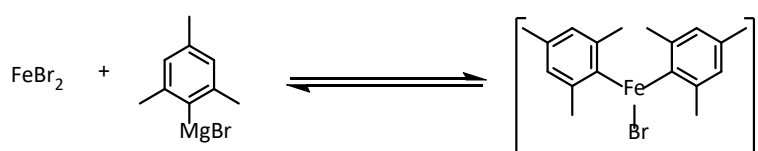
Scheme 3.15: The observed production of [FeBrMes$_2$]$^-$ from a 1 : 1 reaction of FeBr$_2$ with MesMgBr.

Therefore, to target a mono-mesitylated species this equilibrium must be 'switched off', requiring the exclusion of Mg salts. The product was therefore synthesised by reaction of FeBr$_2$ with MesLi.
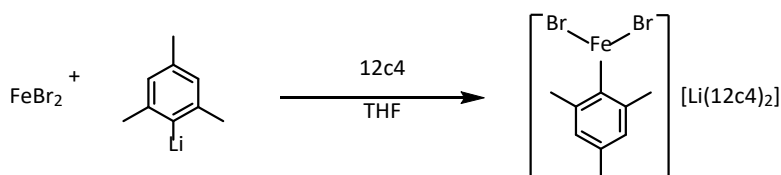
Scheme 3.16: Reaction of FeBr$_2$ with MesLi to form [FeBrMes$_2$]$^-$.

The species was first identified by its distinct ^{1}H NMR signals before crystals were grown by addition of 12-crown-4 to chelate the lithium counterion and cooling to 0 °C overnight. X-ray diffraction data was then collected to confirm its structure as [FeBr$_2$Mes][Li(12c4)$_2$] (**17**).
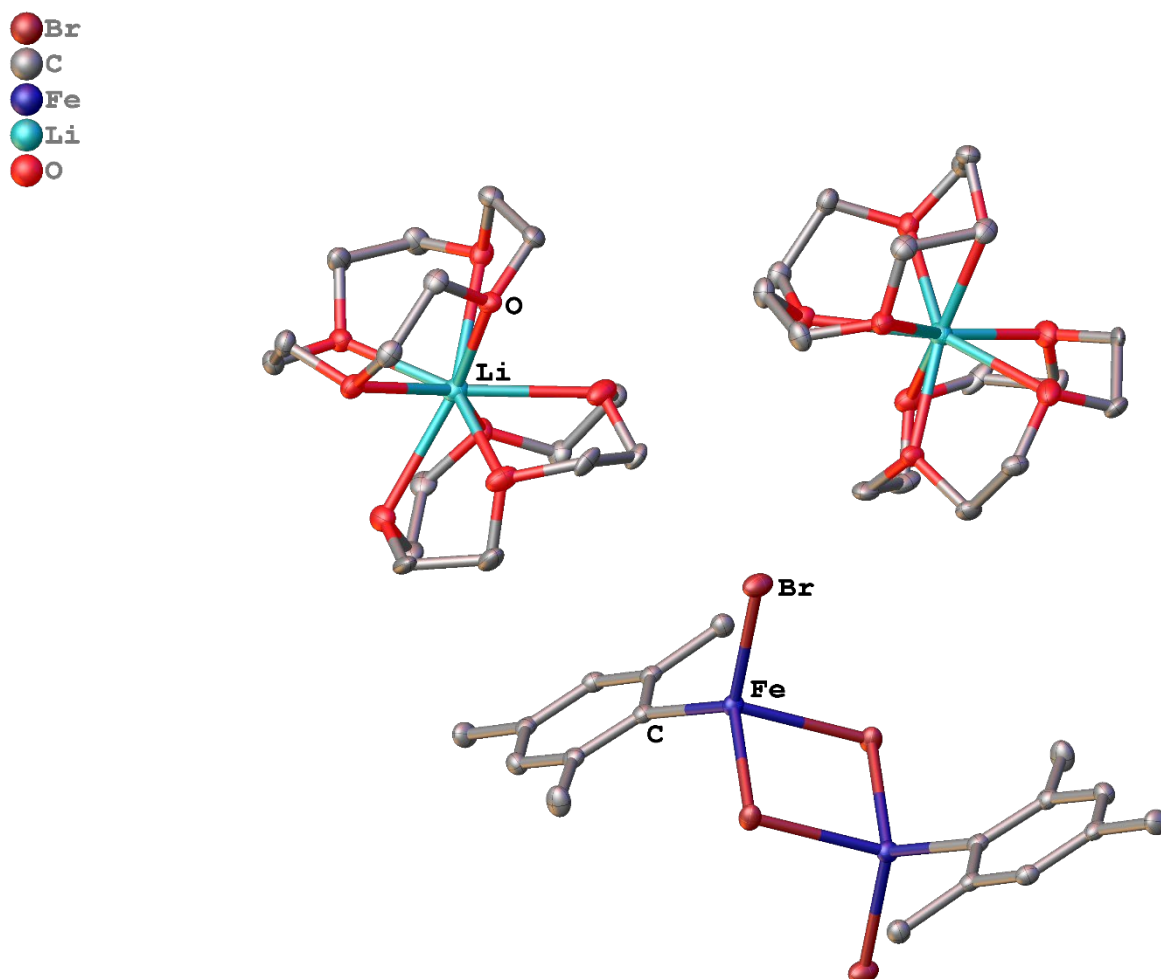
Figure 3.11: X-Ray crystal structure of [FeBr$_2$Mes]$_2$[Li(12c4)$_2$]$_2$, with hydrogen atoms omitted for clarity.

The crystal structure shows the complex as a bromide-bridged dimer, with the mesityl moieties on each iron trans to each other.

Comparing to the crystal structure of **8** discussed in the previous chapter, the Fe-C for **17** is 2.081(2) Å, slightly longer than the 2.0650(18) Å measured for **8**. The Fe-Br bond lengths are also of a comparable length in each structure, being 2.4239(4) Å and 2.4155(3) Å for **17** and **8** respectively.

As with the other iron-mesityl complexes, the reactivity of **17** with OctBr was monitored and production of MesOct examined. (Figure 3.12)
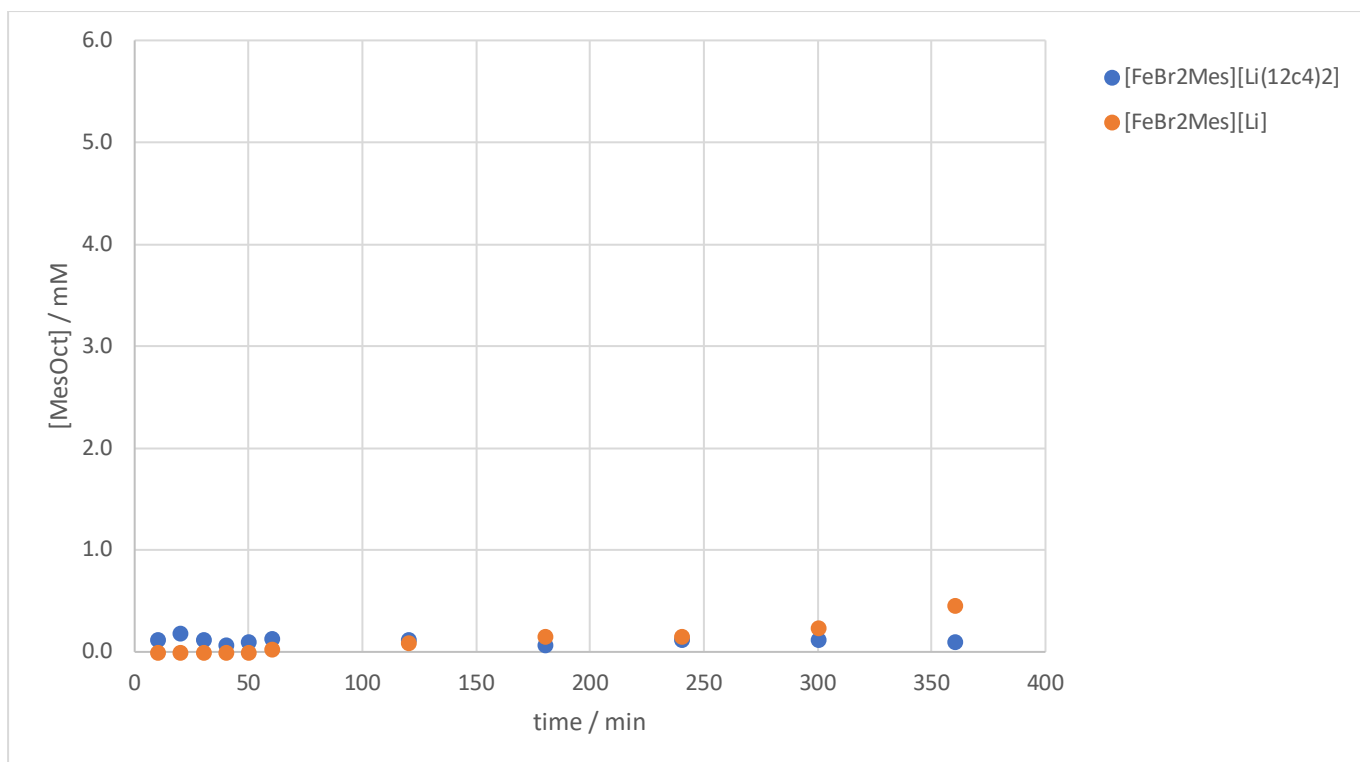
Figure 3.12: Reaction profiles showing the production of MesOct from the reaction of [FeBr$_2$Mes]$^-$ with OctBr with either a Li$^+$ or [Li(12c4)$_2$]$^+$ counterion. Initial concentration of [FeBr$_2$Mes]$^-$ = 33 mM in THF.

As was the case with the other heteroleptic complex, **8**, reacting **17** with OctBr (in the presence or absence of 12-crown-4) gave only trace amounts of MesOct over 24 hours, indicating that it is unlikely to be a driver of turnover under catalytic conditions. This is, of course, assuming that this species is accessible in catalytic solution at all, which is perhaps unlikely due to the excess of MesMgBr present, along with the apparent thermodynamic factors disfavouring its formation as compared to **8**.

Having tested the reactivity of OctBr with **7, 8,** and **17**, the only remaining reported complex to test is Fe$_2$Mes$_4$ (**6**). **6** is a well-characterised and well-studied complex, although it is perhaps unlikely to be present in catalytic solution at appreciable concentration. Notably, it appears to be synthesised only by reaction of an iron source with Mes$_2$Mg, not with MesMgBr. Reported syntheses for this complex uniformly involve the addition of 1,4-dioxane in addition to MesMgBr.[54,122] As found earlier (Scheme 2.9), the reaction of FeBr$_2$ with 2 equivalents of MesMgBr in the absence of dioxane gives only **8**, with no evidence of the formation of **6**. **6** has been shown to be reactive with both MesMgBr and MgBr$_2$, to form

7 and **8** respectively. Both of these compounds are present in large quantities with respect to iron in catalytic solution and, therefore, the lifetime of **6** in catalytic solution is likely to be very short. Despite this, due to the possibility that **6** transiently exists in solution, its reactivity with an electrophile was investigated.
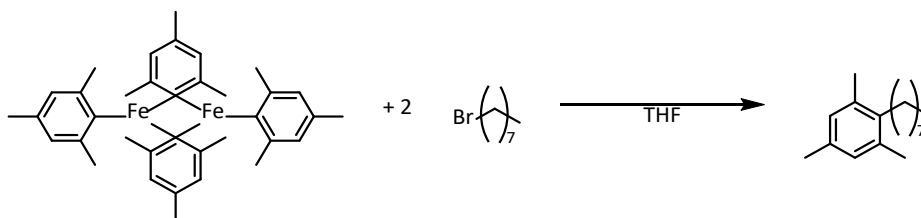
Scheme 3.17: The reaction of Fe$_2$Mes$_4$ with OctBr to give the cross-coupled product MesOct.
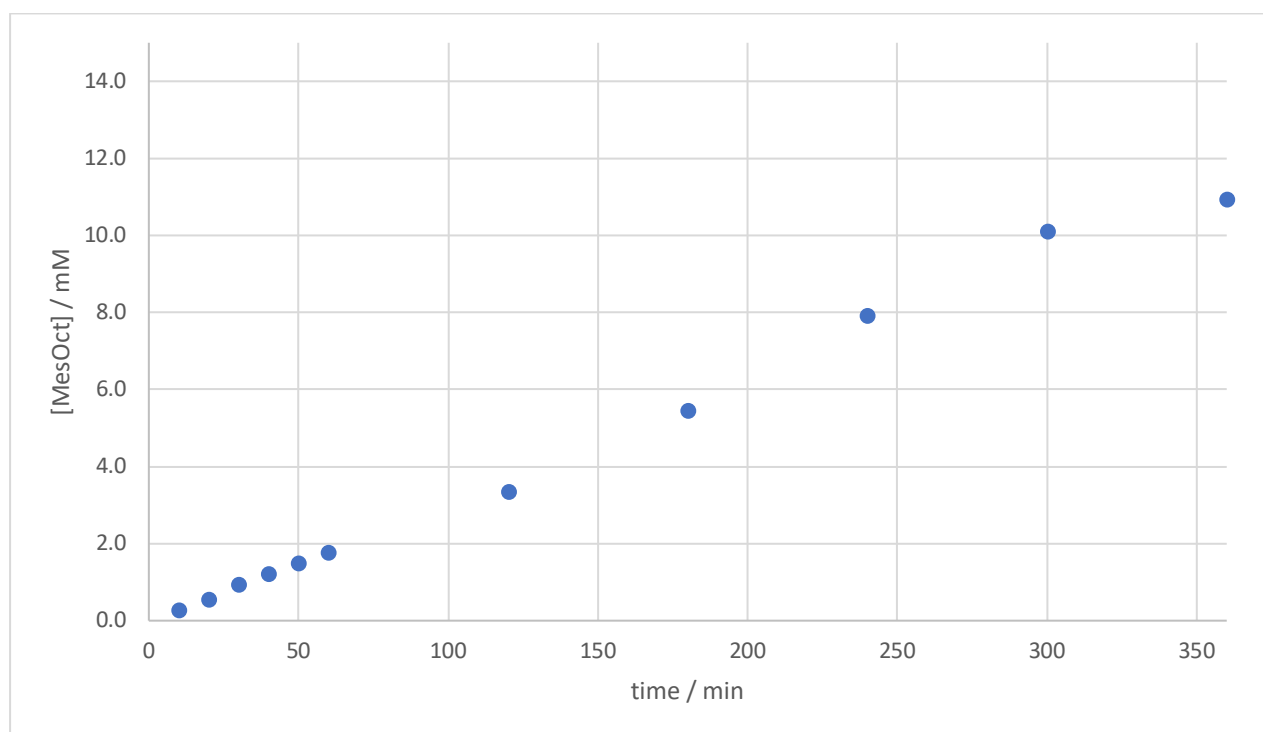
Figure 3.13: Profile showing the formation of MesOct from the reaction of Fe$_2$Mes$_4$ with OctBr. Initial concentration of Fe$_2$Mes$_4$ = 16.5 mM in THF.

Interestingly, **6** reacts with OctBr at a rate outpacing all other trialed species, including **7**, reaching a conversion of 33% within the first 6 hours with no perceptible induction period. Intrigued by this, a parallel reaction was analysed by ^{1}H NMR spectroscopy.
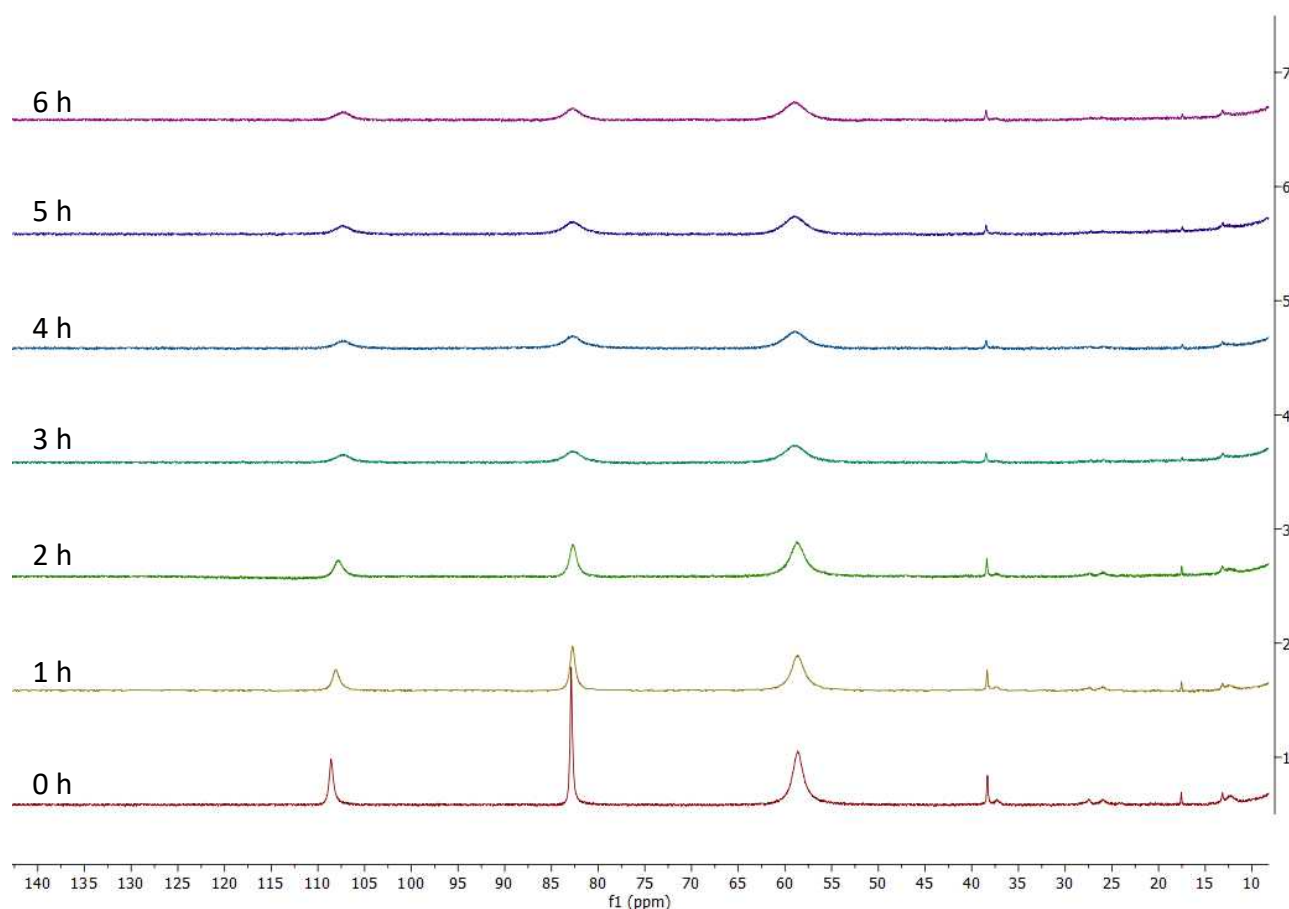
Figure 3.14: Stacked ^1H NMR of the reaction of Fe_2Mes_4 with OctBr, scans taken every hour.

Signals for Fe_2Mes_4 are persistent for at least the first 6 hours of reaction, with signals present alongside them at chemical shifts of 38, 26, and 13 ppm from the onset of reaction, that appear to reduce in intensity as reaction continues.

These signals match precisely with those observed in the reaction of Fe_2Mes_4 with ^nBuBPin (Figure 2.9). Previously they were assigned to either a $[Fe_2Mes_3]^+$ cation, or a mixed Fe^I/Fe^{II} $[Fe_4Mes_6]$ cluster analogous to the phenyl cluster reported by Neidig.[49] Observing the same signals reappearing in this case would seem to disprove the assignment of a cluster, given the oxidative conditions of the stoichiometric reaction. The structure is therefore proposed as $[Fe_2Mes_3]^+$ (**18**).

The synthesis of this complex was targeted by selective protonation of one mesityl group per dimer of **6** using Brookhart's acid ($[H(OEt_2)_2][BAr^F]$). (Scheme 3.18)
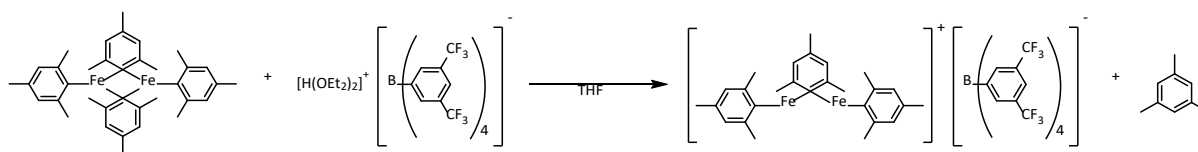
Scheme 3.18: The attempted synthesis of [Fe$_2$Mes$_3$][BAr^F] by selective protonation of Fe$_2$Mes$_4$ with Brookhart's Acid.

^{1}H NMR analysis of the reaction mixture showed signals at similar chemical shifts to those previously observed, indicating that these may be the same complex, but no further structural characterisation was performed to confirm the structure.

Having performed the similar set of reactions for each available iron-mesityl species, their capacity for giving the cross-coupled product can be compared directly.
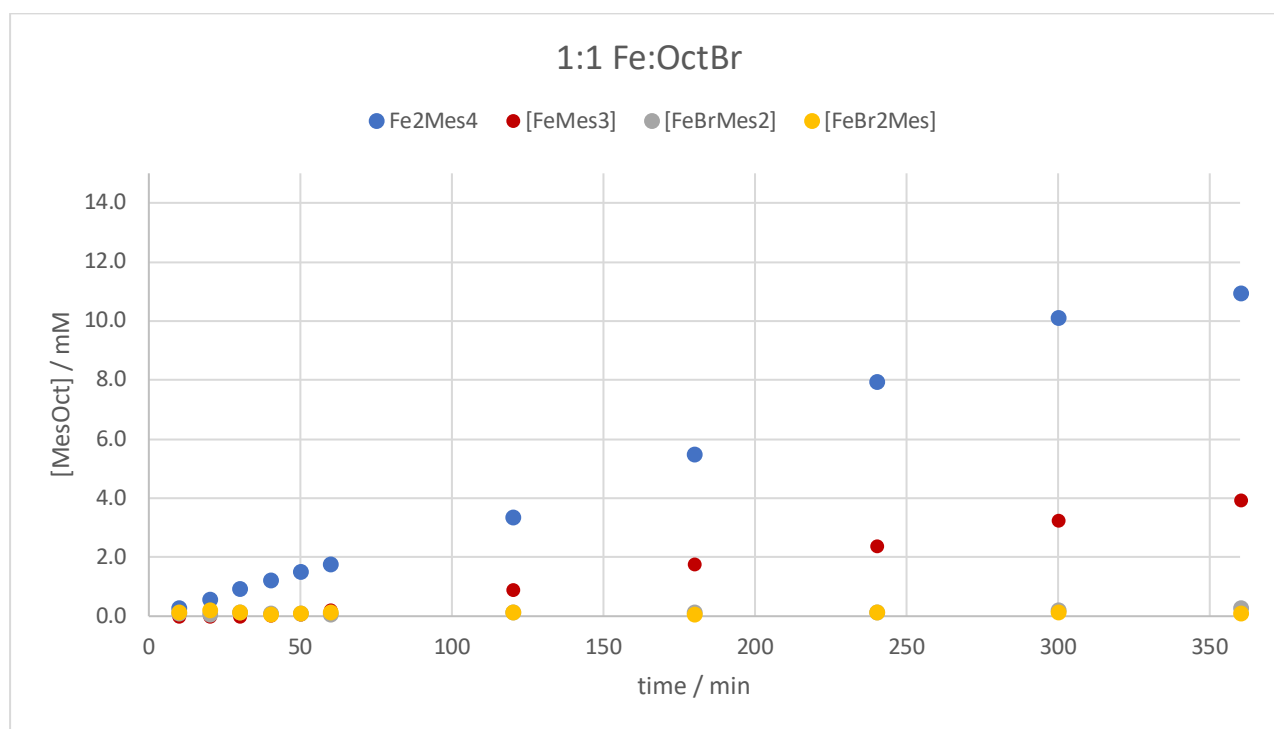
Figure 3.15: The rates of formation of MesOct from 1 : 1 reactions of OctBr with [FeMes$_3$]$^-$, [FeBrMes$_2$]$^-$, [FeBr$_2$Mes]$^-$, and Fe$_2$Mes$_4$. Initial [Fe] = 33 mM in THF.

The fastest reaction occurs with **6**, reaching a yield almost 3 times that of **7** over the first 6 hours of reaction, **7** giving the next fastest reaction rate, with the heteroleptic complexes **8** and **17** giving only trace conversion over the sampled time period.

3.2.1 – Mechanistic Implications

The observation of an induction period in the reaction of OctBr with **7** indicates that this species, despite being the dominant observable compound under catalytic conditions, cannot be directly on the catalytic cycle, but is a pre-catalyst that requires an activation step to form an active catalyst. The fact that the reaction with **6** does not have an observable induction period may provide clues as to what form this activation step may take.

The expulsion of a Mes⁻ moiety from **7** *via* recombination with the [MgBr]⁺ counterion would generate a neutral, low-coordinate FeMes₂ complex which may be more susceptible to reaction with electrophile than the anionic, sterically hindered **7**. Such a species would also be accessible by a splitting of the **6** dimer, which may explain the lack of an induction period in that reaction.
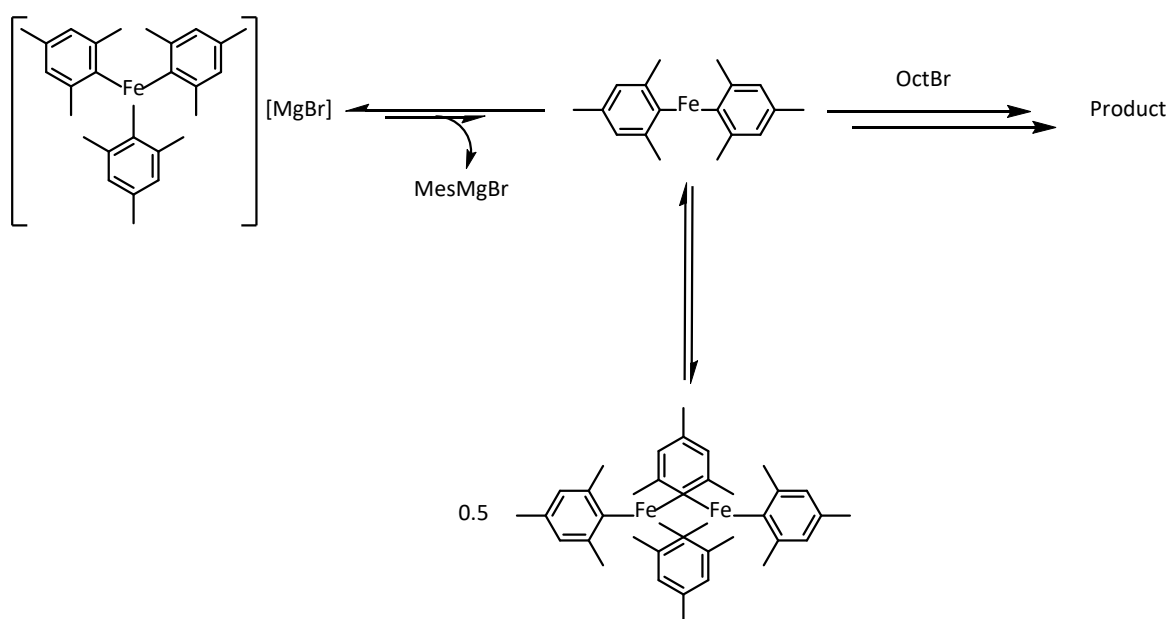
Scheme 3.19: A potential activation phase of [FeMes₃]⁻ occurring prior to catalysis.

If this assignment of the induction process is correct, the addition of an excess of OctBr would be expected to shorten the induction period through the lowered concentration of FeMes₂, shifting the equilibrium. The reaction of [FeMes₃]⁻ with 2 equivalents of OctBr was therefore profiled.
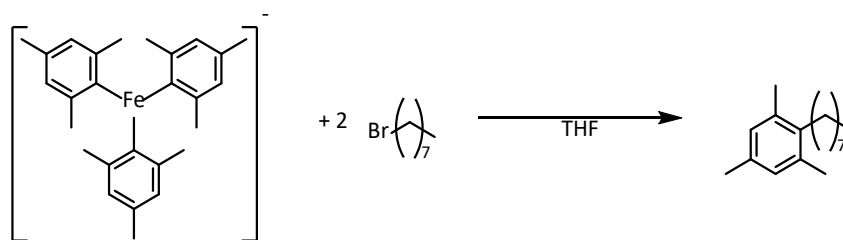
Scheme 3.20: The reaction of [FeMes₃]⁻ with 2 equivalents of OctBr.
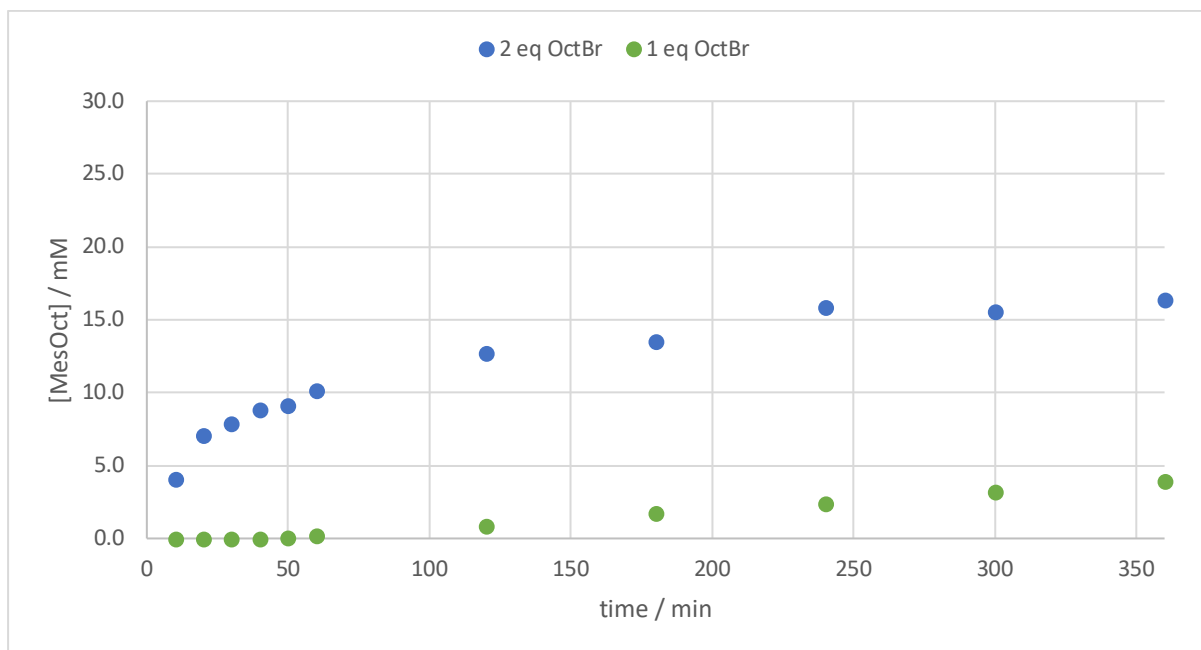
Figure 3.16: Profile comparing the formation of MesOct from the reaction of [FeMes₃]⁻ with 1 or 2 equivalents of OctBr. Initial concentration of [FeMes₃]⁻ = 33 mM in THF.

In this reaction, no induction period is observed. In fact, the reaction appears to initiate with a burst phase before beginning to plateau. This does fit in with prediction, although suggests a greater level of complexity than initially assumed. To investigate this phenomenon further, the characterised organoiron complexes were reacted with excesses of electrophile.

3.3 – Reactions of Organoiron Species with Excess Electrophile

While 1 : 1 reactions of electrophile with iron species are useful for discerning elementary reactivity, they are not entirely representative of catalytic conditions, in which iron species are present as a small proportion with respect to the electrophile. For example, in the case of the 5 mol% loading of $FeBr_2$ used in the catalytic reaction under investigation (Scheme 3.8), this would correspond to a loading of 20 equivalents of OctBr with respect to iron.   For this reason, it is beneficial to investigate the relative rates of reaction of these species with such a large excess of electrophile.

The first species trialled was **7**, made *in situ* by the same route as used previously (See Scheme 3.9).
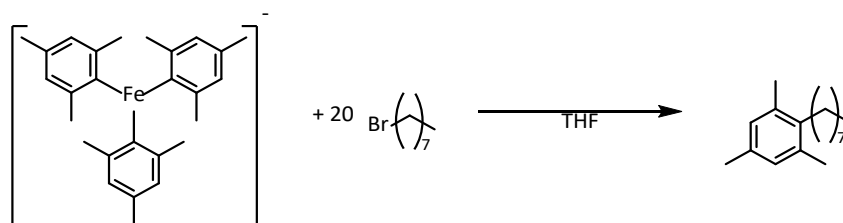
Scheme 3.21: The reaction of [FeMes$_3$]$^-$ with an excess of OctBr.
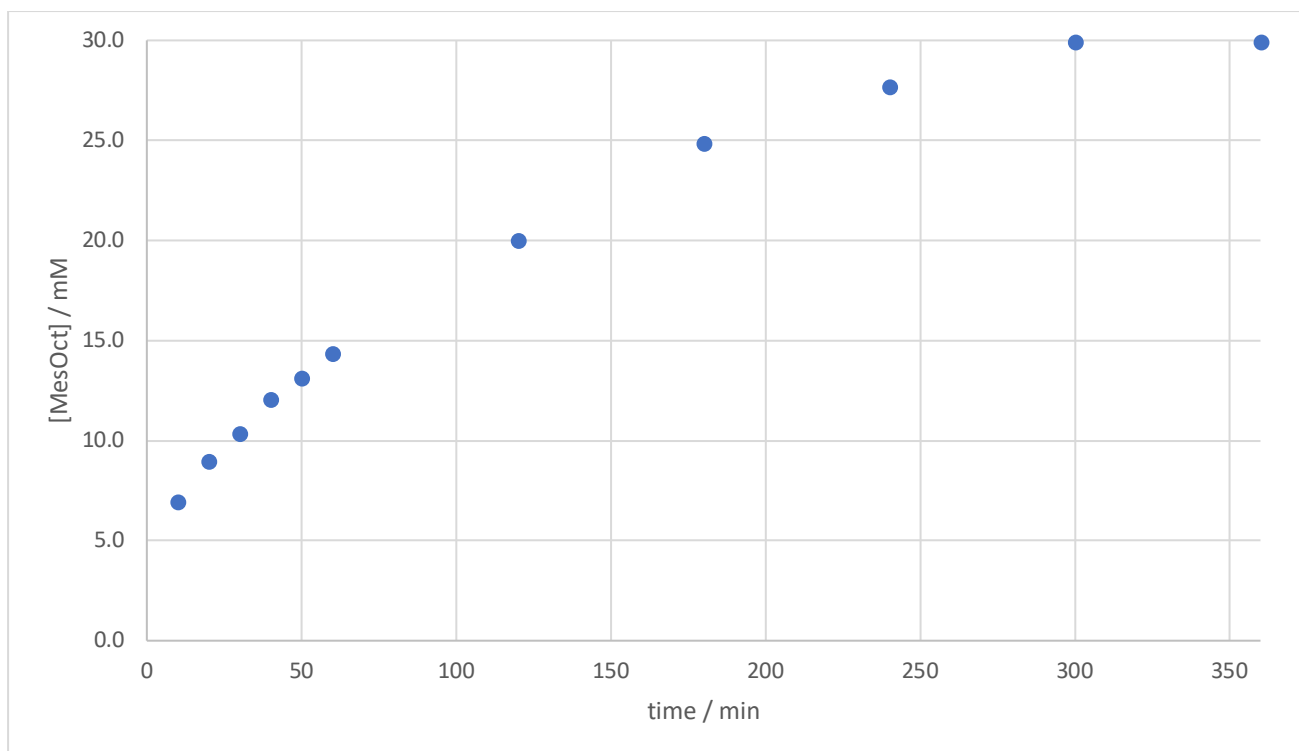
Figure 3.17: Profile showing the formation of MesOct from the reaction of [FeMes$_3$]$^-$ with an excess of OctBr. Initial concentration of [FeMes$_3$]$^-$ = 33 mM in THF.

Under these conditions, no induction period is observed. In fact, production of MesOct begins at very fast rate, reaching a yield of 21% within the first 10 minutes of addition of electrophile, eventually reaching a yield of 92% after 5 hours before plateauing. Notably, this corresponds to only 1 of the 3 iron-bound mesityl groups being transformed into cross-coupled product before turnover halts.

The reactivity of each of the heteroleptic ferrate complexes with excess electrophile was then trialed.
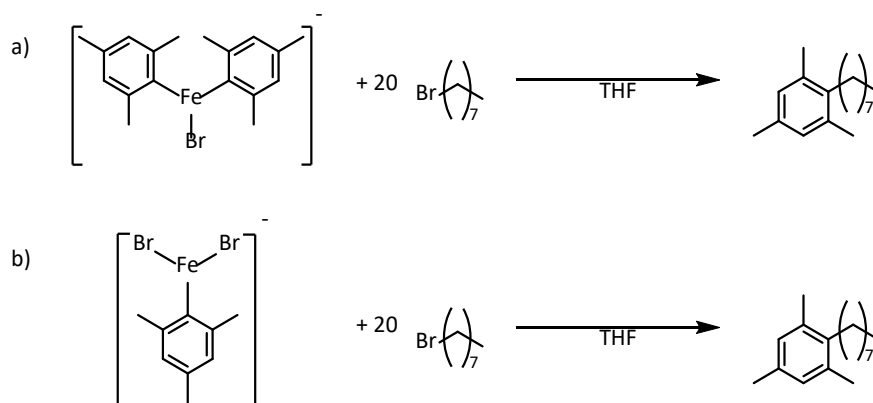
Scheme 3.22: The reactions of heteroleptic complexes [FeBrMes$_2$]$^-$ (a) and [FeBr$_2$Mes]$^-$ (b) with excess OctBr.
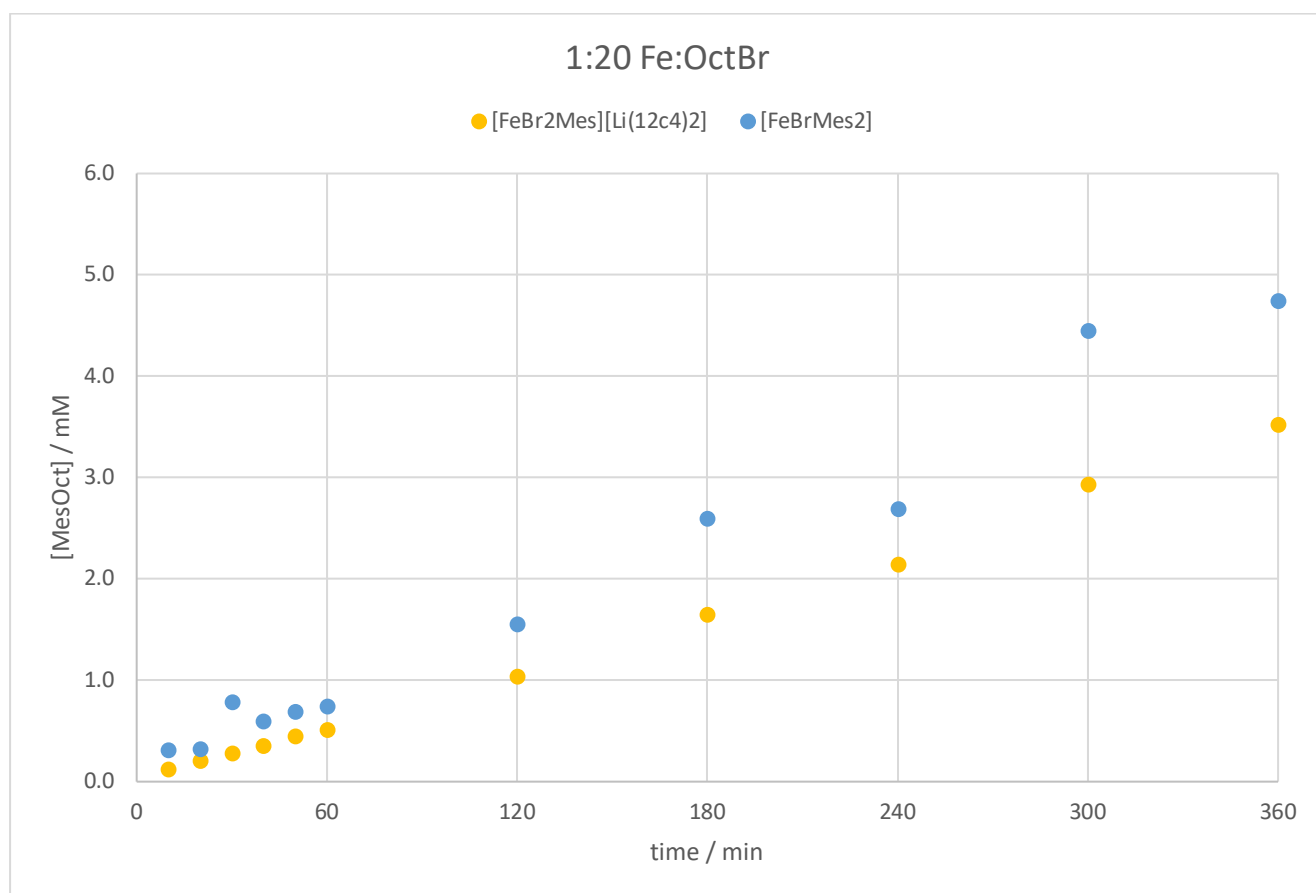
Figure 3.18: Profiles of the reactions of [FeBrMes$_2$]$^-$ and [FeBr$_2$Mes]$^-$ with 20 equivalents of OctBr. Initial [Fe] = 33 mM in THF.

While greatly accelerated as compared to the 1 : 1 reactions, they still both give a rate of

MesOct production far lower than **7**, and are therefore unlikely to be responsible for much

product in catalysis, particularly in the early stages in which MesMgBr is present in great excess as compared to iron. Finally, **6** was reacted with an excess of OctBr.
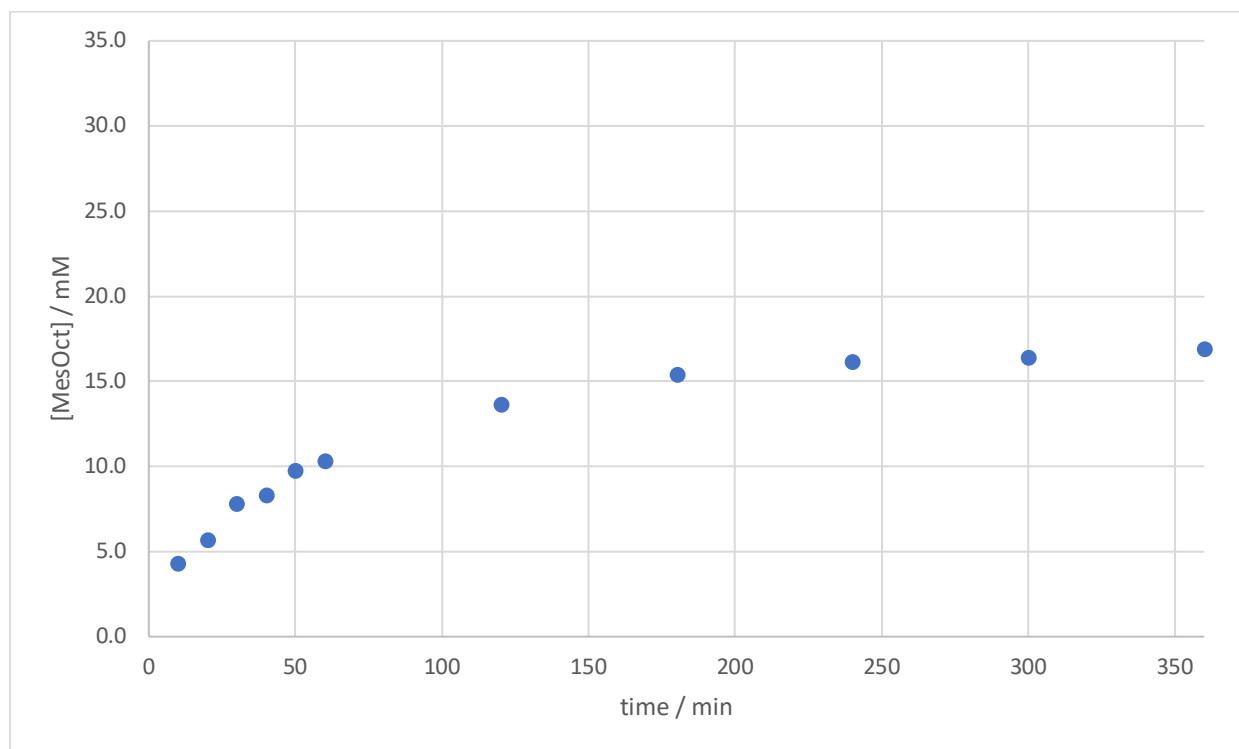
Figure 3.19: Profile of the reaction of Fe_2mes_4 with 10 equivalents of OctBr. Initial [Fe] = 33 mM in THF.

The product profile of this reaction follows a similar shape that observed for **7**, with turnover plateauing at a yield of approximately 50% percent with respect to iron. That is to say for each molecule of the dimer, 1 mesityl moiety is coupled before turnover appears to halt.

3.3.1 – Mechanistic Implications

The production of 92% of MesOct in the reaction of $[FeMes_3]^-$ with excess OctBr indicates that only 1 molecule of MesOct is produced per anion of **7**, despite 3 mesityl moieties being present. This fits in with the data showing that **8** is not competent at performing catalysis, and turnover only occurs with a sacrificial 2 equivalents of nucleophile that may only act as spectator ligands.

98

We can therefore infer a truncated, simplified cycle in which 1 reaction of one equivalent of OctBr with **7** produces 1 equivalent of MesOct and **8**, which has shown limited reactivity with electrophile. Reaction with MesMgBr may then (reversibly) regenerate **7**.
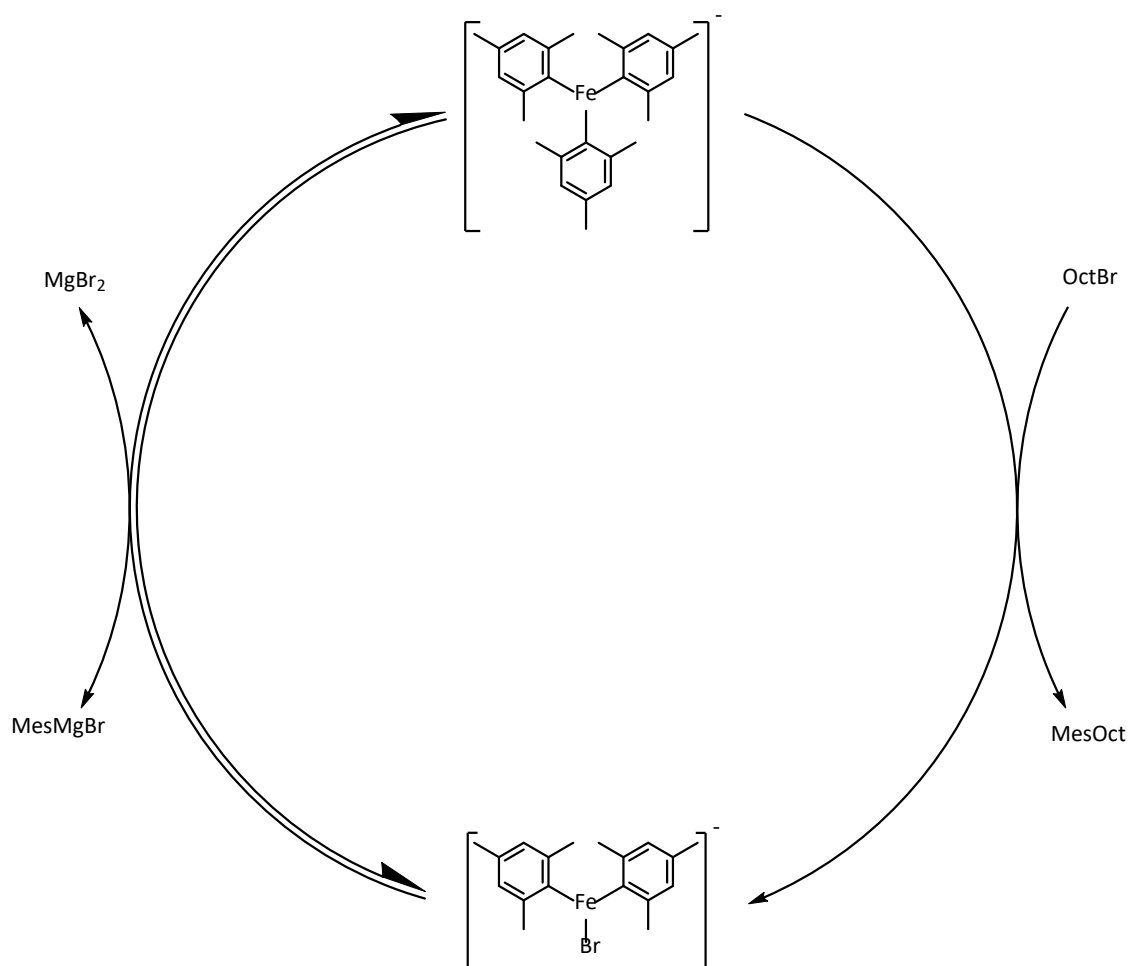
Scheme 3.23: A simplified catalytic cycle showing the production of MesOct and [FeBrMes$_2$]$^-$ from [FeMes$_3$]$^-$.

Interestingly, TON reaching close to 1 within 5 hours is much faster than the corresponding catalytic reaction, even in the absence of further Grignard reagent to drive reaction.

3.4 – The effect of Excess MesMgBr

From the observation that the reaction of **7** with OctBr appears to halt after turnover of only 1 equivalent of cross-coupled product, despite the presence of 3 iron-bound Mes groups, and that **8** is inactive to reaction with electrophile, it was hypothesised that 2 sacrificial equivalents of MesMgBr are required as a 'baseline', with any excess above this going on to give the cross-coupled product. Therefore, reaction of $FeBr_2$ with n equivalents of MesMgBr in the presence of excess OctBr, should facilitate formation of no more than $n\text{-}2$ equivalents of MesOct. To test this hypothesis, $FeBr_2$ was reacted with 4 and 5 equivalents of MesMgBr.
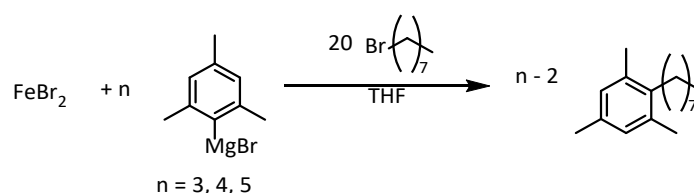
Scheme 3.24: The reaction of $FeBr_2$ with varying quantities of MesMgBr in the presence of excess OctBr.
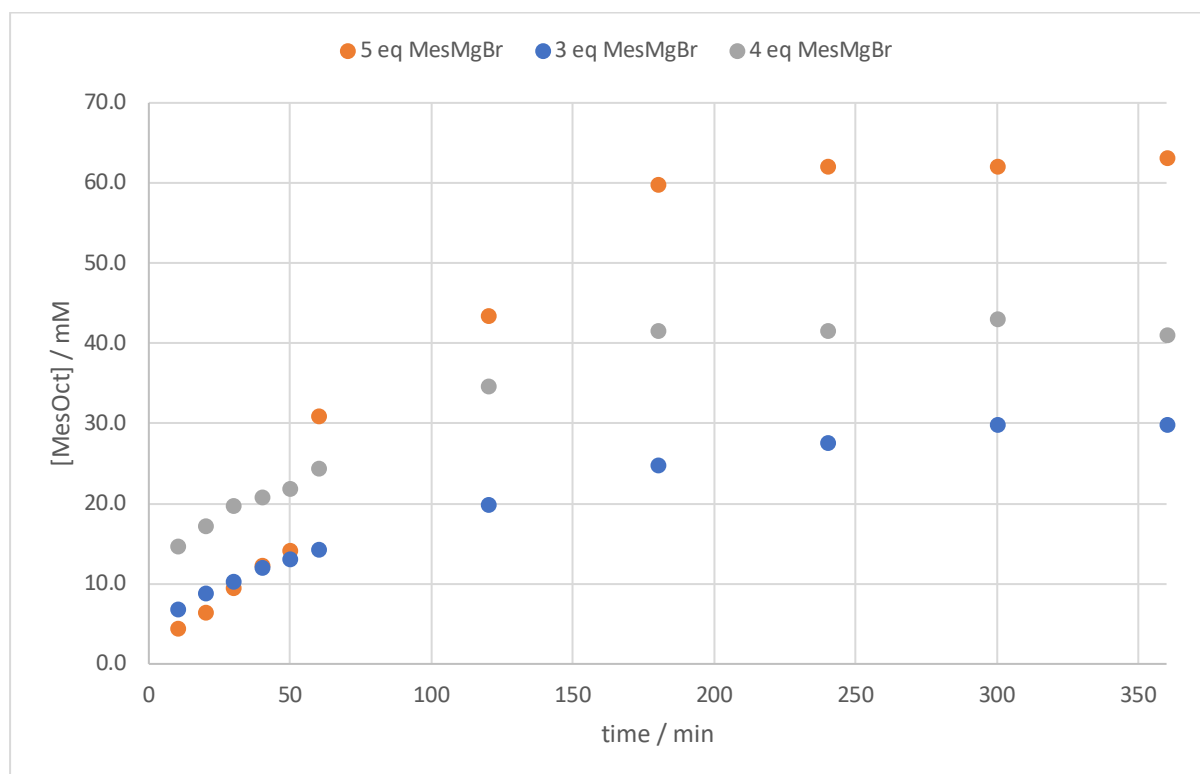
Figure 3.20: The production of MesOct with the reaction of excess OctBr with a pre-stirred mixture of $FeBr_2$ with 3, 4, and 5 equivalents of MesMgBr. [Fe] = 33 mM.

The profiles of the above reactions support this hypothesis, albeit with a lower-than-expected conversion. With 4 equivalents of MesMgBr, 150% conversion to MesOct is observed (i.e. 1.5 equivalents with respect to iron), rather than the theoretical 200% expected. Similarly, with 5 equivalents of MesMgBr, only 190% of product is observed before plateauing.

These results may be indicative of an effect of a higher quantity of $MgBr_2$ in solution, pushing the equilibrium away from **7** and towards **8**, in effect giving diminishing returns with higher loadings of MesMgBr. In each case, the consumption of OctBr greatly outpaces the production of MesOct, although the high uncertainty associated with quantification of organic bromides by GC-FID, along with its high concentration as compared to the other reactants rendered any attempt to determine the precise ratio between the two unreliable.

Looking at the profile for 4 equivalents, an interesting feature is that the conversion appears to be 'shifted' to a higher conversion than would be expected if you were to extrapolate back to the origin, seeming to be almost parallel with the profile for 3. The 5-equivalent profile, conversely, has a clear burst phase occurring between the aliquots taken at 50 and 60 minutes.

Additionally, colour changes could be observed in the reaction vessel occurring 9 minutes from the start of reaction in the 4-equivalent reaction and 59 minutes in the 5-equivalent reaction, from a milky-white suspension to dark brown.
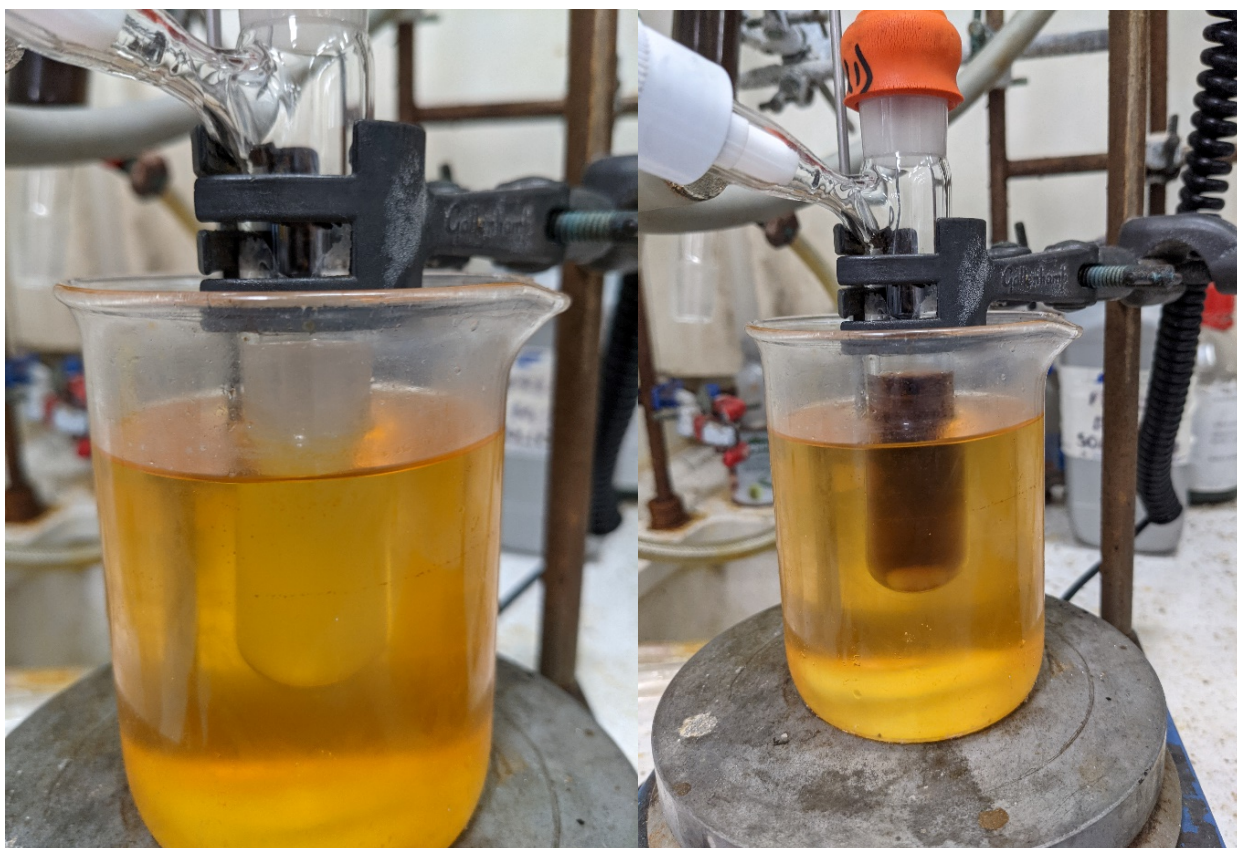
Figure 3.21: Photos showing a colour change in the reaction of [FeMes$_3$]$^-$ with OctBr with 1 excess equivalent of MesMgBr added. Photos taken at 1 minute (left) and 11 minutes (right) from the addition of OctBr initiating reaction.

To gain a clearer insight into the process causing this colour change and burst in MesOct production. Each of the reactions with 3, 4, and 5 equivalents of MesMgBr was repeated with more frequent taking of aliquots over the first 20 minutes of reaction.
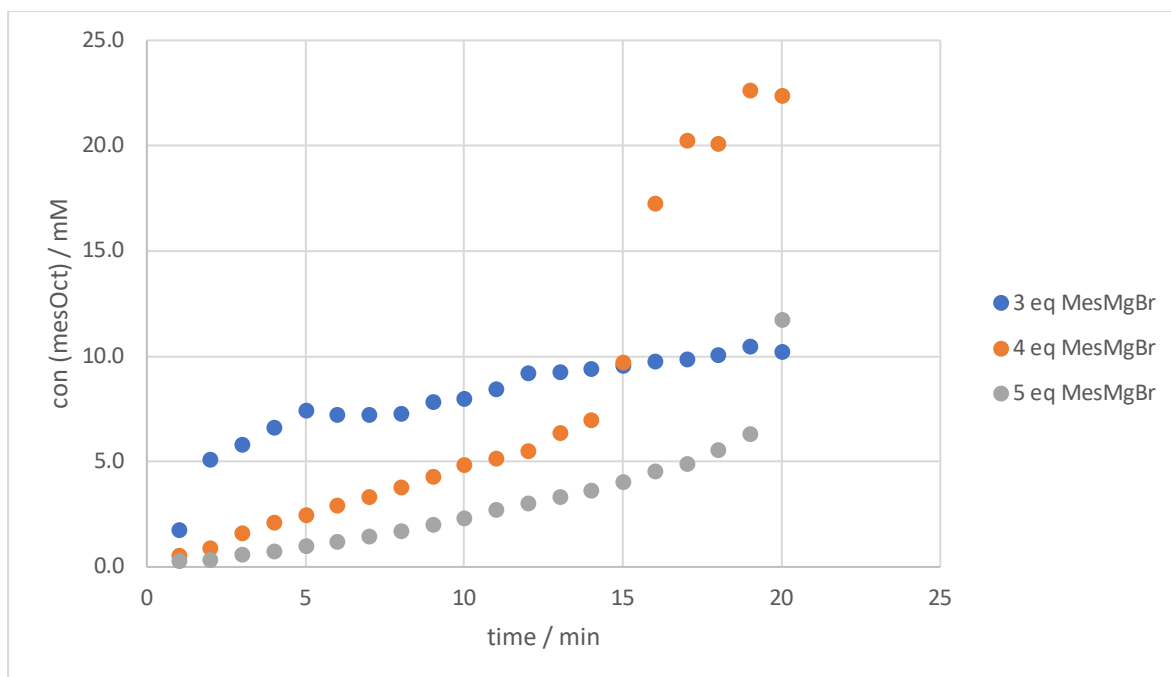
Figure 3.22: Reaction profile comparing the rate of MesOct formation from OctBr reacting with **7** formed by $FeBr_2$ reacting with 3, 4, and 5 equivalents of MesMgBr. Initial [Fe] = 33 mM.

For the above reactions, the colour changes were observed at 30 seconds, 15 minutes, and 19 minutes after reaction initiation with 3, 4, and 5 equivalents respectively, in conjunction with the burst phases observed in the profile. The more frequent taking of aliquots appears to have changed the position of the burst phase while maintaining the same relative order.

Interestingly, prior to the burst phases, the rate of MesOct production is faster with 4 MesMgBr equivalents than with 5, supporting the proposed slowing of reactivity induced by the presence of a higher concentration of $MgBr_2$.

From the shape of the curve being relatively unaffected by the burst phase, it is potentially the case that the process causing the burst phase is entirely independent from that which is responsible for the majority of turnover.

3.4.1 – The Effect of Excess MgBr$_2$

From the observation that an excess of MgBr$_2$ seems to slow down the rate of reaction, routes to synthesise **7** that minimise that the inclusion of MgBr$_2$ were considered. The route that includes the lowest production of MgBr$_2$ was the reaction of isolated **6** with 1 equivalent per iron of MesMgBr, forming **7** *in situ* with only one equivalent of [MgBr]$^+$ present, and no MgBr$_2$.
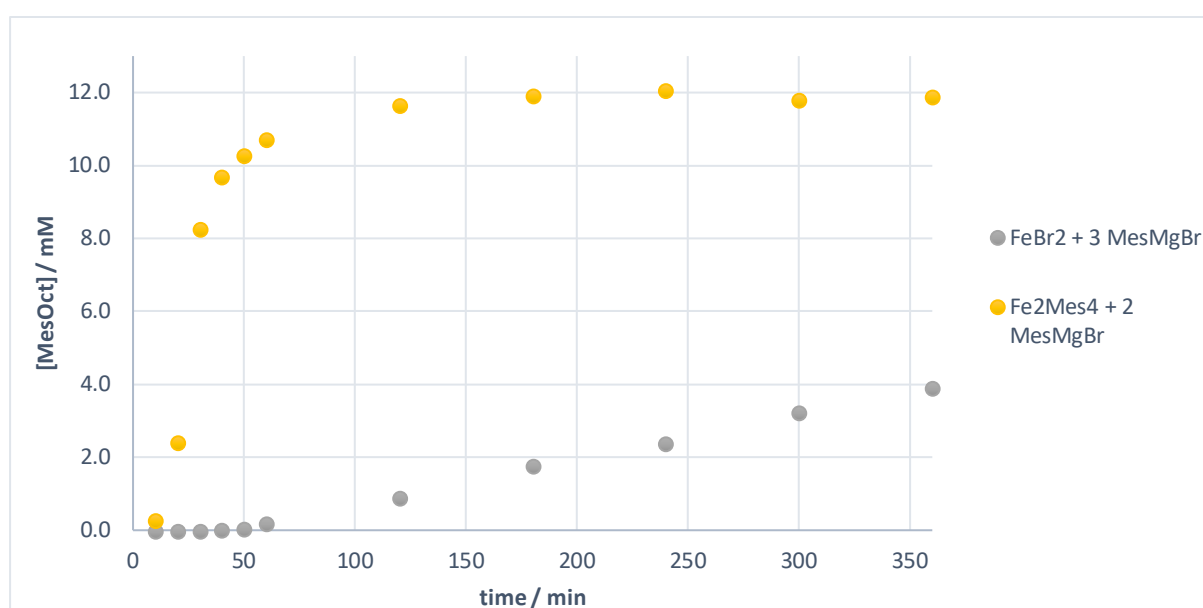
Figure 3.23: Profile of the production of MesOct from the Reaction of OctBr with [FeMes$_3$]$^-$ produced by two separate routes. Initial [Fe] = 33 mM.

Addition of 1 equivalent of OctBr gave a vastly improved rate of reaction as compared with the equivalent with excess MgBr$_2$ present, as well as outpacing any other Fe-Mes species tested, including **6**. However, turnover only reached 36% before plateauing due to complete depletion of the OctBr electrophile, implying a ratio of consumed OctBr to produced MesOct of approximately 3:1.
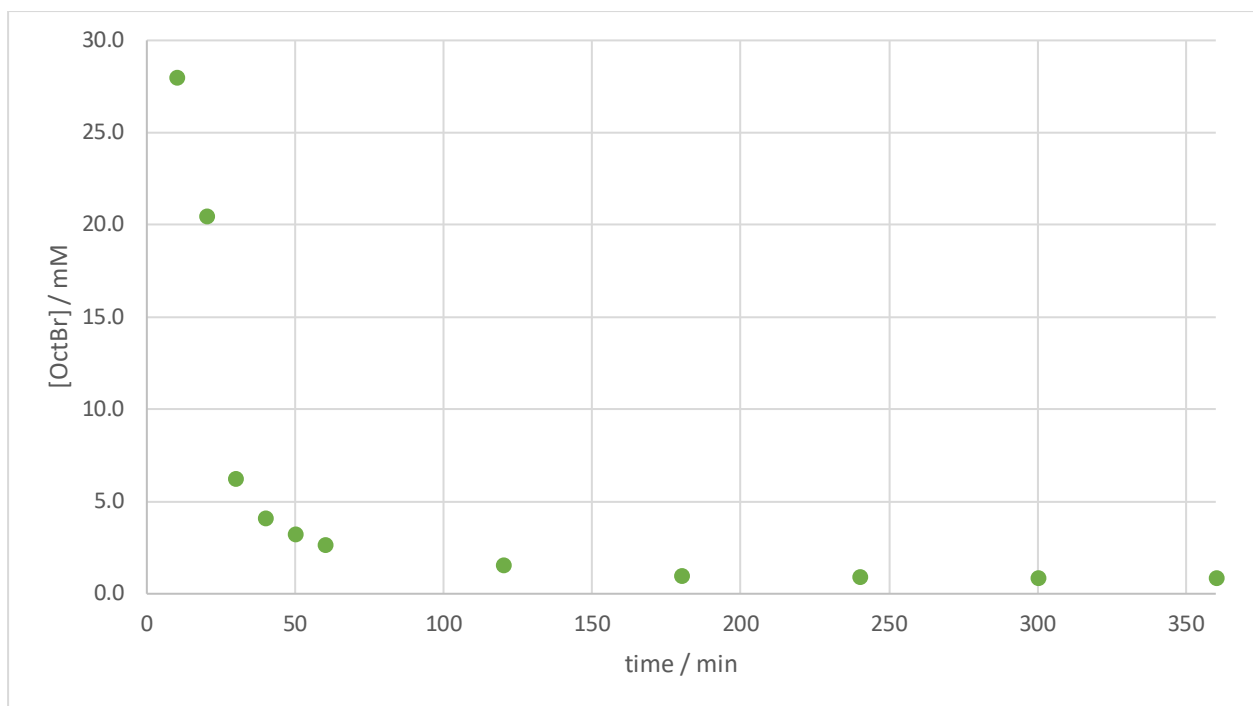
Figure 3.24: The concentration of OctBr in the reaction of [FeMes$_3$][MgBr] with OctBr. Initial [OctBr] = 33 mM.

By increasing the loading of OctBr to 20 equivalents, a conversion of approximately 60% was achieved, lower than the 90% observed for the [FeMes$_3$]$^-$ produced from FeBr$_2$ and 3 equivalents of MesMgBr.
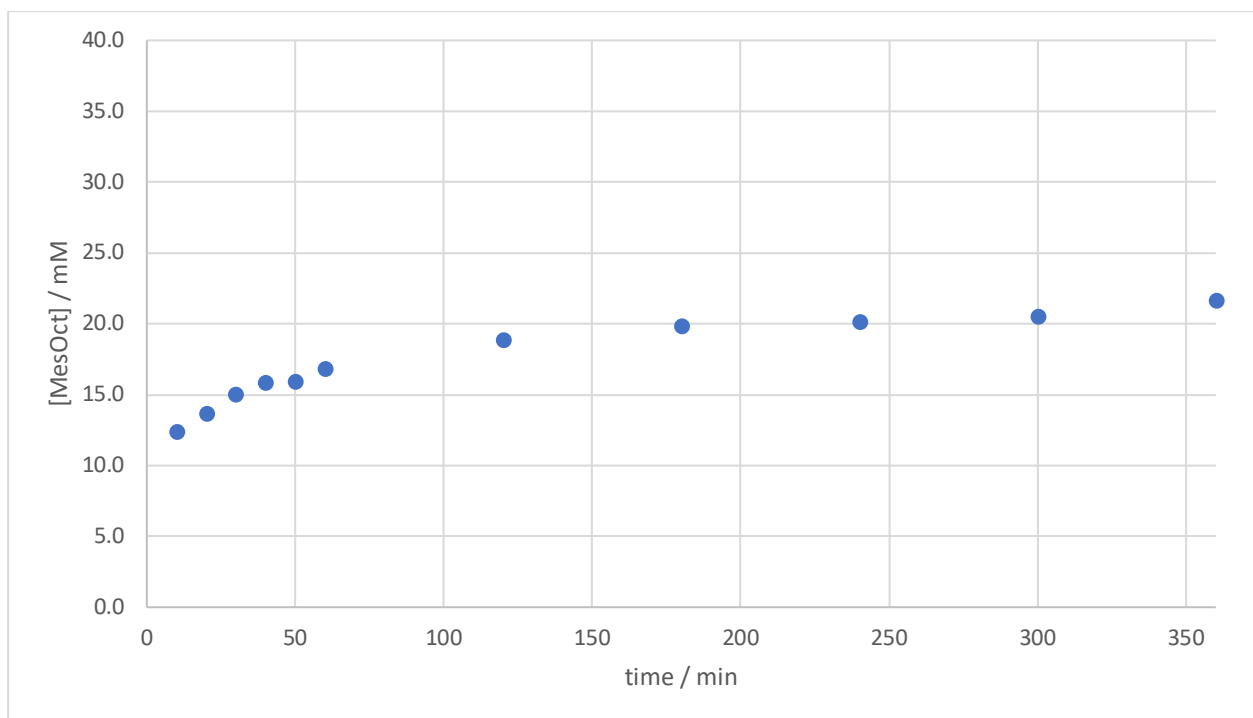
Figure 3.25: The production of MesOct from [FeMes$_3$][MgBr] and excess OctBr. [Fe] = 33 mM.

These data seem to suggest that while the presence of MgBr$_2$ slows the production of cross-coupled product, its presence also greatly increases the yield of reaction between the organoiron species and electrophile.

A potential cause for this observed MgBr$_2$ effect could be the capacity for MgBr$_2$ to provide bromide in solution. In a mechanistic investigation of an iron-catalysed Negishi cross-coupling, Bedford reported that the presence of MgBr$_2$ was vital to prevent the reduction of FeBr$_2$ to Fe^0 upon reaction with Zn(p-tol)$_2$.[107]
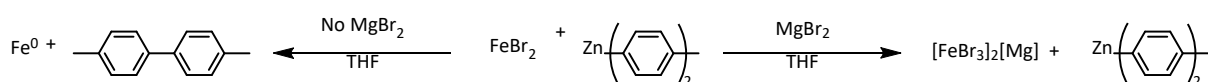
Scheme 3.25: The observed role of MgBr$_2$ in the reaction of FeBr$_2$ with Zn(p-tol)$_2$.

The reaction of MgBr$_2$ with FeBr$_2$ produced the [FeBr$_3$]$^-$ ferrate species, which was not susceptible to transmetallation from the organozinc species in the absence of phosphine

106

ligand. Without MgBr$_2$ present, FeBr$_2$ remains, and is quickly reduced to Fe^0 by reductive elimination of the p-tol groups.

It is possible, therefore, that in the absence of soluble bromide, one intermediate on the catalytic cycle is susceptible to reduction to Fe^0, which may not be brought back into productive reaction. This could also have the effect of depleting the OctBr electrophile by a process Bedford showed in which Fe^0 nanoparticles may be oxidized and resolubilised by excess electrophile.[105] It is possible that the species produced by this reaction may not be able to give the MesOct product.

Another effect of MgBr$_2$ that is worth consideration is its capacity to react with **7** directly. In the previous chapter, the presence of an equilibrium between **7** and **8** was demonstrated, facilitated by transmetallation to MgBr$_2$ to give the corresponding Grignard reagent.

The increasing the concentration of MgBr$_2$ as the reaction progresses will therefore have a concomitant effect of gradually decreasing the concentration of **7** and increasing the concentration of the catalytically inactive **8**.

This also appears to be the case in the stoichiometric reaction of **6** which also reacts with MgBr$_2$ to give **8**, albeit *via* bromide transfer rather than transmetallation. It is perhaps unsurprising then that addition of 1 equivalent of MgBr$_2$ to the stoichiometric reaction of Fe$_2$Mes$_4$ with OctBr has a significantly deleterious effect on the rate of production of MesOct.
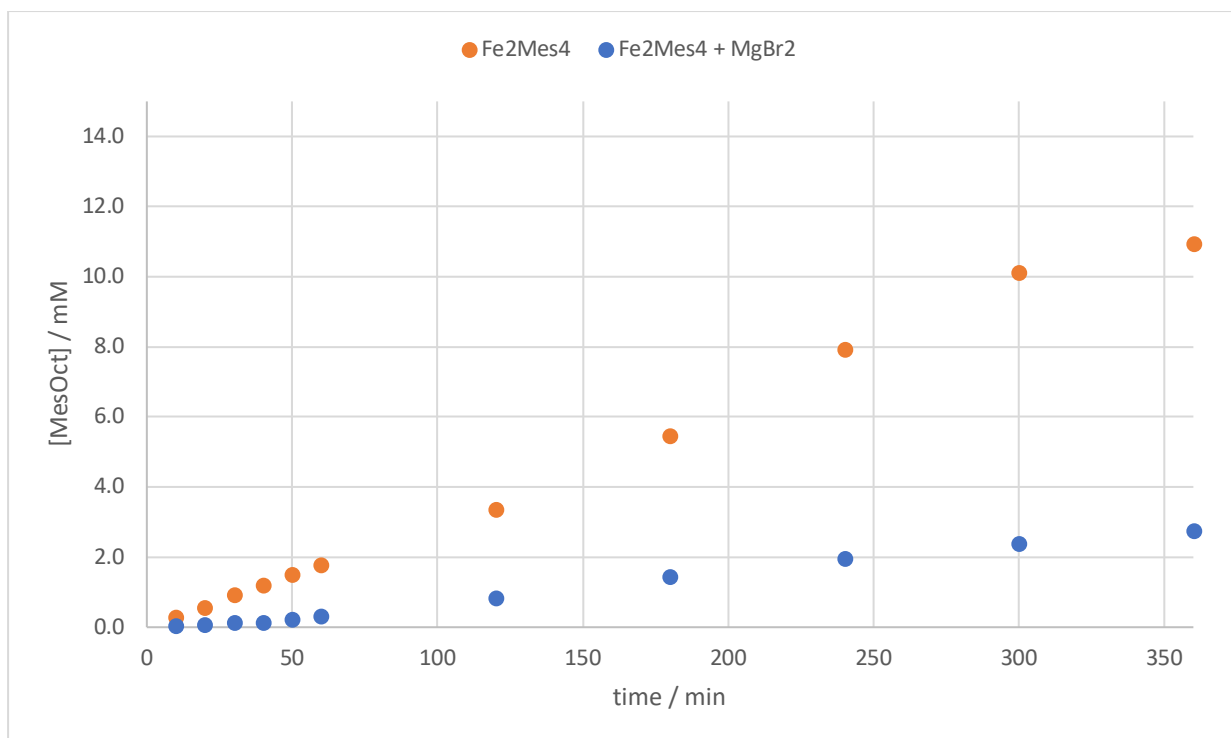
Figure 3.26: The rate of MesOct production in the reaction of OctBr with Fe_2Mes_4 in the presence and absence of $MgBr_2$.

Having observed the deleterious effect of $MgBr_2$ on the stoichiometric reactions of iron nucleophiles with OctBr, an investigation was performed on the effect of addition of $MgBr_2$ to the catalytic reaction. Accordingly, the $FeBr_2$ catalysed reaction was repeated with $MgBr_2$ added at loadings of between 0 and 25 mol%.
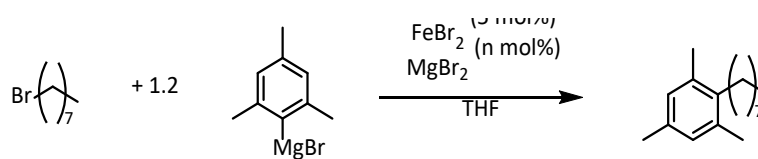
Scheme 3.26: The Kumada cross-coupling of MesMgBr with OctBr catalysed by $FeBr_2$ with $MgBr_2$ added.
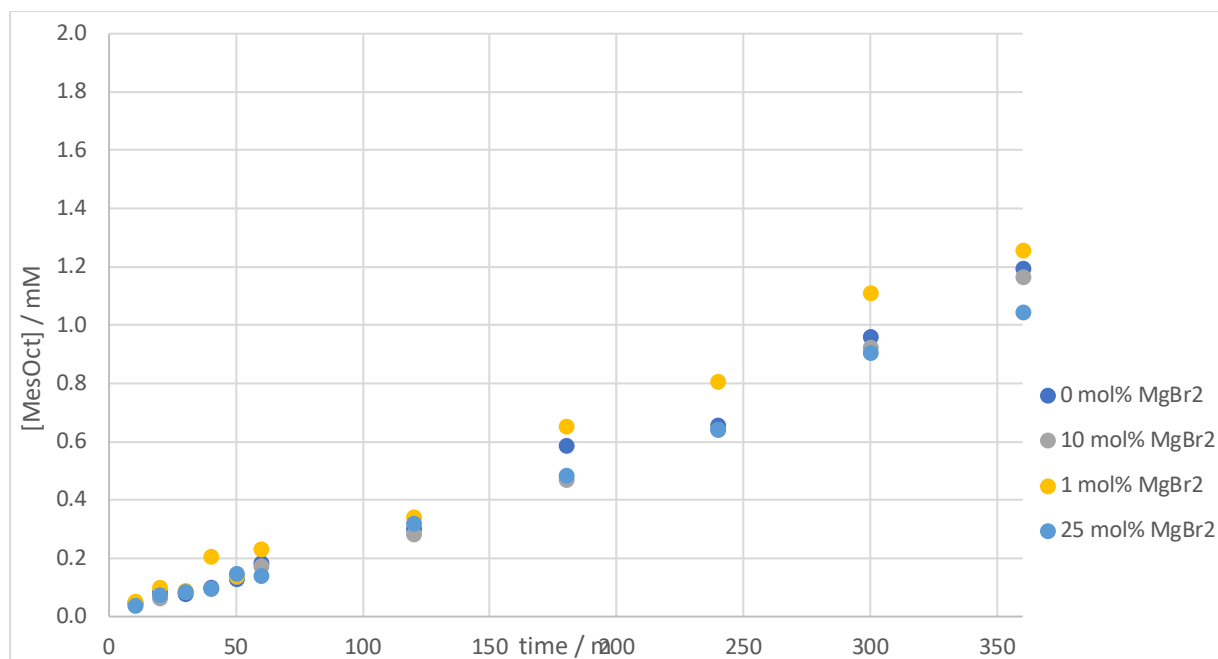
Figure 3.27: The rate of MesOct formation in a Kumada cross-coupling reaction with varied loadings of $MgBr_2$ added. Initial [OctBr] = 67 mM in THF.

Counter to expectation, no significant difference in the rate of product formation was observed over this range of $MgBr_2$ concentrations. It is possible that the loading of Grignard being in such excess relative to the iron means that any $MgBr_2$ effect is already occurring, and the additional 25 mol% of Mg is not having enough of a significant further effect to be detected. If excess Grignard has the same deleterious effect on reactivity as $MgBr_2$ does, this may explain why many reports of iron-catalysed Kumada cross-couplings observe greater turnover with slow addition of Grignard, as this would decrease the concentration of Mg species earlier in the reaction.[37,105,118]

Therefore, in order to increase the rate of the catalytic reaction, it may be desirable to actively remove $MgBr_2$ from solution as it is produced. This may be accomplished by addition of 1,4-dioxane to the reaction. 1,4-dioxane is able to bind to magnesium halides in solution, forming an insoluble chelate and drawing the halide out of solution.

The catalytic reaction was therefore run with 1,4-dioxane added as a co-solvent with THF and profiled for the formation of MesOct.
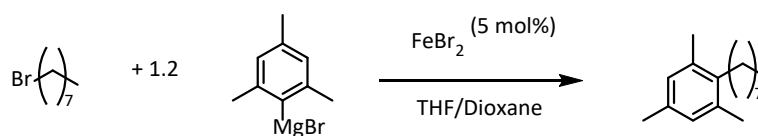
Scheme 3.27: FeBr$_2$-catalysed Kumada cross-coupling of MesMgBr with OctBr with added 1,4-dioxane as co-solvent.
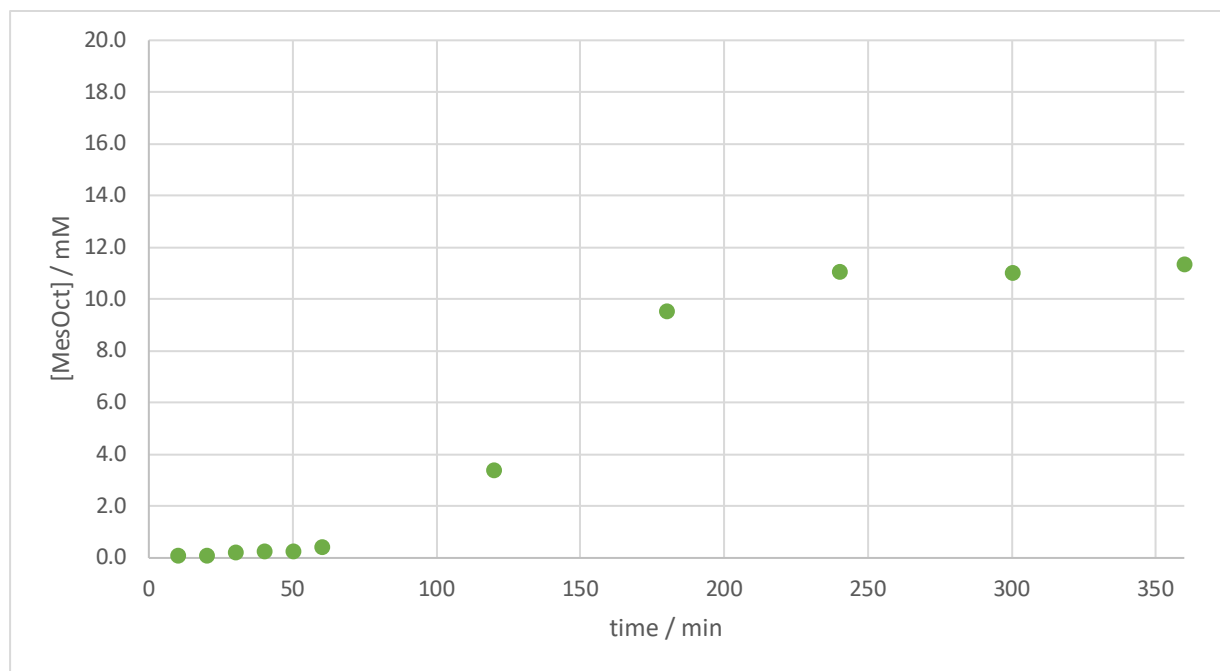
Figure 3.28: The production of MesOct from the FeBr$_2$-catalysed reaction of MesMgBr with OctBr in dioxane solution.

The production of MesOct proceeds after an induction period lasting approximately 50 minutes, the same as that observed in the stoichiometric reaction of **7** with OctBr. The presence of this induction period in a catalytic reaction, in which iron exists as a small proportion compared to other components is striking. A potential explanation could be a dioxane-induced shift in the Schlenk equilibrium. As MgBr$_2$ is drawn out of solution, Mes$_2$Mg dominates over MesMgBr as the predominate nucleophile. It is likely that due to steric effects, this reacts more slowly with FeBr$_2$ than MesMgBr, leading to the observation of an induction period before cross-coupling occurs.

Subsequently, formation of product occurs at a rate greatly outpacing the reaction omitting dioxane. However, the reaction plateaus after reaching a yield of 16.6%. This plateauing was

observed over a range of loadings of dioxane and reaction temperatures, all at values approximating 15% conversion.

Table 3.2: The production of MesOct from the Kumada coupling of MesMgBr with OctBr.

Entry	Reaction Temperature /°C	THF : Dioxane	MesOct Yield /%
a	30	2:1	14.9
b	50	2:1	17.5
c	70	2:1	15.1
d	30	4:1	10.8
e	30	1:1	12.6

This figure of 15% does therefore seem to be intrinsic to this reaction manifold. In the case of a catalyst loading of 5 mol%, the 15% yield figure corresponds to a TON of 3. It is therefore possible that the complete absence of $MgBr_2$ in solution somehow enables transfer of all 3 mesityl moieties from each **7** complex but disables any route to reform any catalytically active iron-mesityl species.

3.5 – Further mechanistic findings

Alongside the mechanistic revelations uncovered by the profiling study, which include bulk oxidation state being Fe^{II}, **7** being a pre-catalyst, and heteroleptic species being inactive to reaction with electrophile, profiling experiments were used to gain further insights into the mechanism.

3.5.1 – Test for Radical Intermediacy

An important initial step for discerning potential mechanistic pathways is to determine if the metal-electrophile interaction is of a radical or ionic character. This could be determined by the use of (bromomethyl)cyclopropane as the electrophile. This substrate has been used extensively in mechanistic investigations as a 'radical clock' reagent, to determine whether coupling reactions go through a step in which the electrophile bears a radical. If such a

radical is generated in the course of catalysis, the cyclopropane moiety rapidly ring-opens to release ring-strain, giving the corresponding terminal alkene.
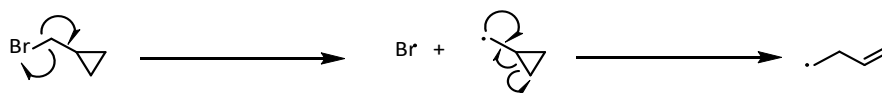
Scheme 3.28: The radical ring-opening of (bromomethyl)cyclopropane.

The presence of the coupled product of the alkene is therefore evidence of a radical pathway in catalysis. While other radical clock reagents tend to show a distribution of products, with the relative ratio of products used as an indication of the rate of coupling, the ring opening step for this substrate is very fast, so tends to go exclusively to the alkene product in radical reactions.

This radical clock test has previously been used as a probe in cross-coupling reactions catalysed by iron-diphosphine and diamine[37,118,124] catalyst systems, in which results suggested a radical, SET interaction was operative. No such test has been reported for a ligand-free system, however.
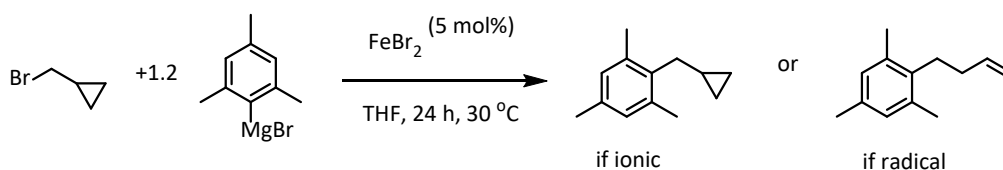
Scheme 3.29: The possible products of the FeBr$_2$-catalysed cross-coupling of (bromomethyl)cyclopropane and MesMgBr.

Analysis of the reaction mixture by ^{1}H NMR and GC-MS, showed exclusive formation of the ring-opened alkene product, with none of the cyclopropane-coupled product detected.
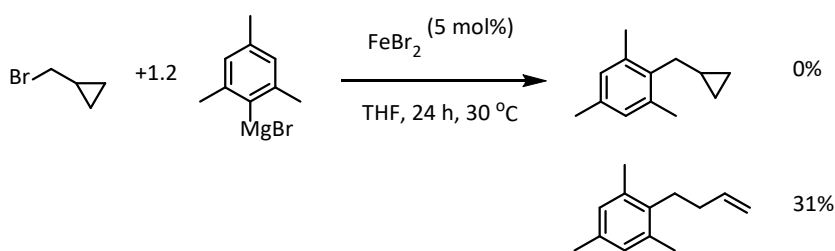
Scheme 3.30: The observed product distribution of the cross-coupling of (bromomethyl)cyclopropane and MesMgBr.

This indicates that during turnover a radical is formed on the electrophile. We can therefore assume that any iron-electrophile interaction is of an SET type, likely a halide abstraction.

3.5.2 – Assignment of highest oxidation state.

While a halide abstraction as described above leads to an oxidized iron centre, the oxidation state that is reached prior to the release of product, either Fe^{III} or Fe^{IV}, is not known, though both have been previously proposed as highest oxidation states in iron-catalysed cross-coupling reactions.[36]

Notably, Nakamura assigned an Fe^{II}/Fe^{IV} catalytic cycle in the reported coupling of aryl chlorides with alkyl Grignard reagents in which the NHC ligands SIPr.HCl was used. (Scheme 3.31)
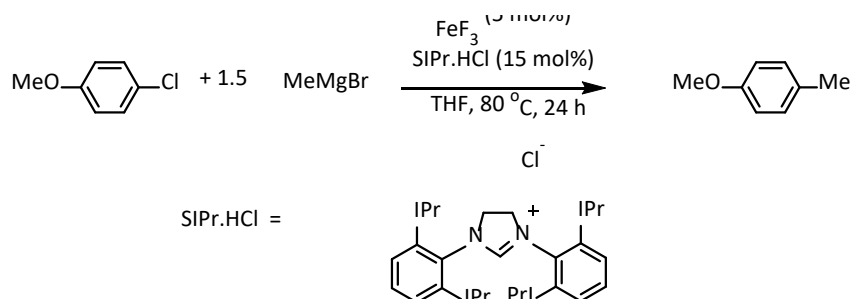
Scheme 3.31: Nakamura's report of an sp^2-sp^3 Kumada cross-coupling.[36]

A radical probe experiment showed that a 2-electron mechanism was occurring, with no evidence for a radical intermediate formed from the aryl halide.
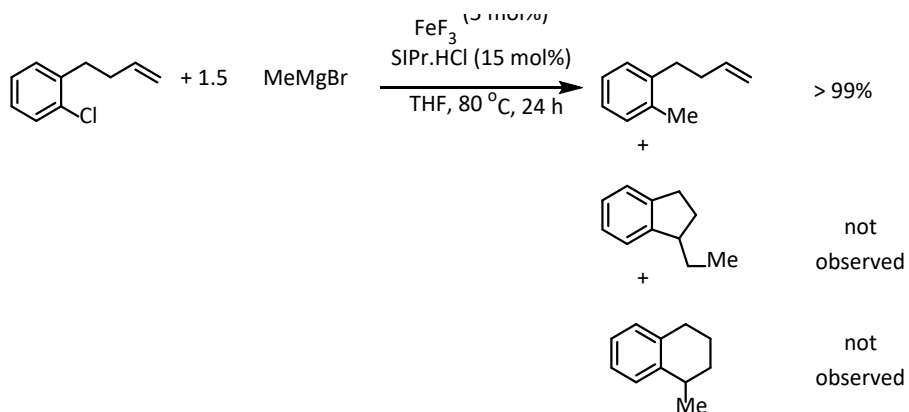
Scheme 3.32: The radical probe experiment used for the coupling of aryl halides with alkyl Grignard reagents.[36]

Along with DFT studies, X-ray absorption spectroscopy (XAS) measurements and further reactivity studies, a catalytic cycle was proposed.
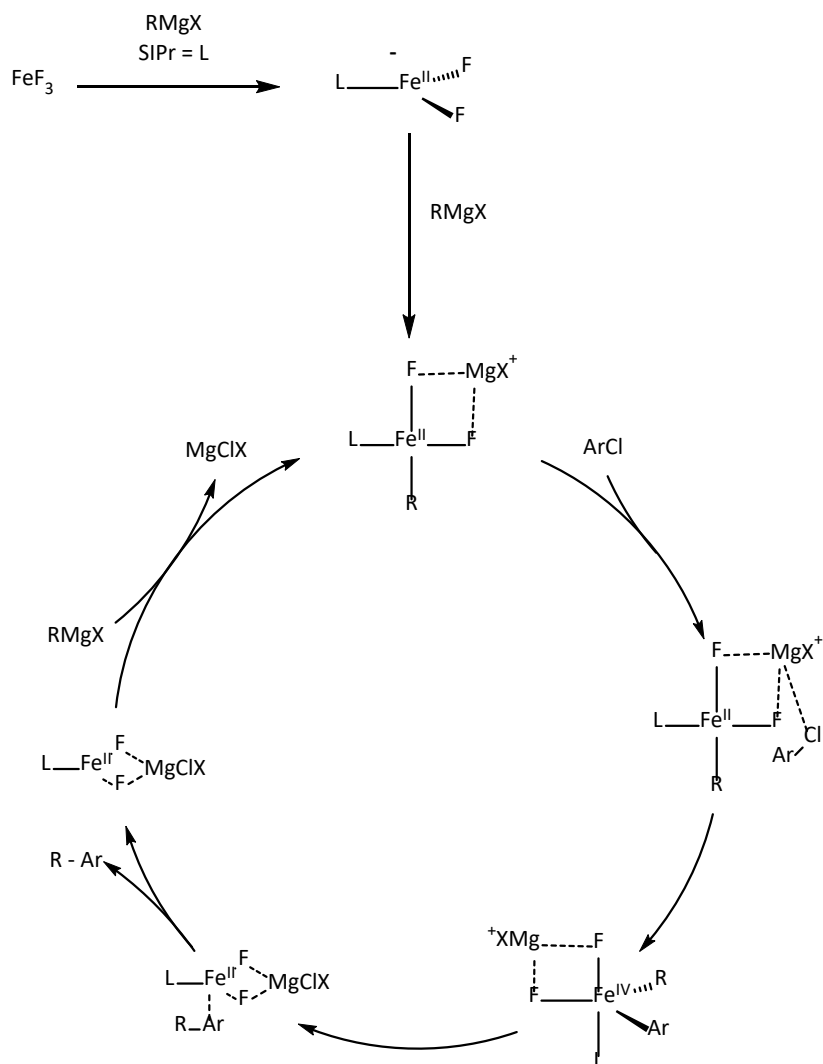
Scheme 3.33: Nakamura's proposed Fe^{II}/Fe^{IV} catalytic cycle for the cross-coupling of alkyl Grignard reagents with aryl halides.[36]

A common observation recurring in the stoichiometric reactions performed throughout this work was that the quantity of electrophile consumed is far larger than the quantity of cross-coupled product, almost always by a factor of 2 or more. This consumption may be evidence that a 2-stage oxidation is taking place, potentially to an Fe^{IV} before product may be released.

To determine which oxidation state is reached, **7** was reacted with varying quantities of the 2-electron oxidant 1,2-dibromoethane (DBE), oxidizing the iron centre, and inducing a reductive elimination of the homocoupling product Mes_2. If we assume a Fe^{IV} oxidation state must be reached to induce reductive elimination, then the quantity of Mes_2 released

will match the loading of DBE (i.e. 25% loading of DBE will give 25% Mes_2 product), whereas if we assume only Fe^{III} must be reached, then the quantity of Mes_2 released will be double the quantity of DBE provided.
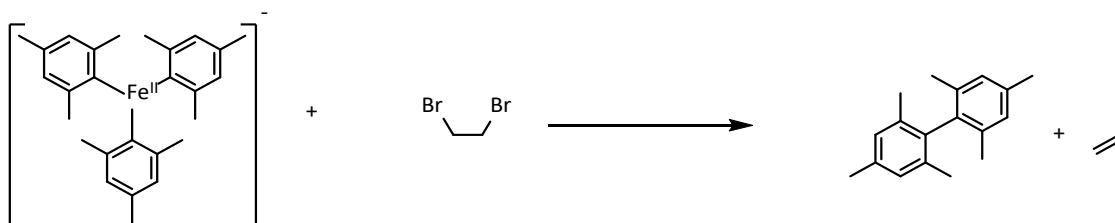
Scheme 3.34: The oxidation of $[FeMes_3]^-$ with 1,2-dibromoethane to reductively eliminate Mes_2.

Table 3.3: The yield of Mes_2 released with varied loadings of 1,2-dibromoethane.

Entry	DBE Loading /equiv.	Yield of Mes_2 /%
a	0.25	26.9
b	0.50	53.8
c	1.0	90.9

As shown in Table 3.3, the observed production of Mes_2 matches closely with the quantity of DBE added, implying a Fe^{IV} oxidation state is being reached before elimination.

While DBE does tend to act as a 2-electron oxidant, it is theoretically possible for it to solely act as a 1-electron oxidant, donating only one bromine and forming EtBr. In order to determine if that is the case here, **7** was also reacted with EtBr, giving the coupling product MesEt before being analysed by GC-MS.
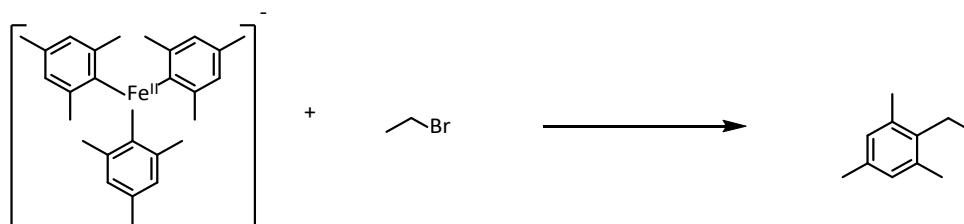
Scheme 3.35: The reaction of $[FeMes_3]^-$ with EtBr.

By comparing GC-MS signals for both reactions, the absence of MesEt in the DBE reaction was confirmed. This indicates clearly that EtBr was not present in reaction solution, implying that DBE is acting as a 2-electron oxidant in this case. Therefore, we can assign an oxidation state of Fe^{IV} as being reached before reductive elimination occurs.

3.6 – Proposed Catalytic cycle

From data collected in this investigation, a catalytic cycle for Kumada cross-coupling with sterically hindered aryl halides can be proposed.
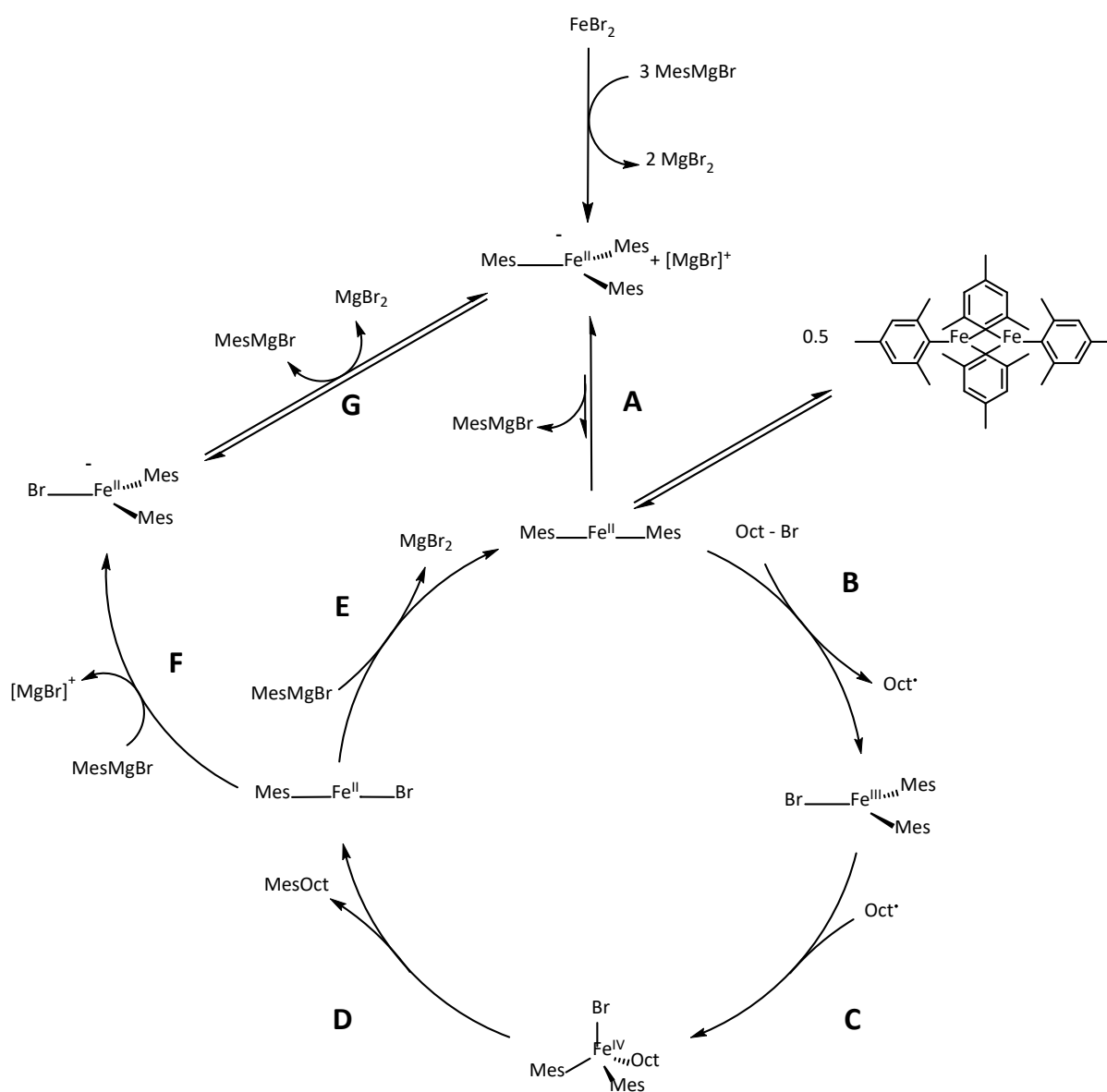
After initial formation of [FeMes$_3$]$^-$ from the iron source and MesMgBr, the reaction proceeds as follows:

A – Combination of one Mes$^-$ moiety from **7** with the [MgBr]$^+$ counterion to reform and expel one equivalent of MesMgBr and a neutral Fe^{II}Mes$_2$ species. This is supported by the observation of an induction period for the stoichiometric reaction of **7** with OctBr, indicating that it is not an active catalyst. There was no such induction period observed in the stoichiometric reaction with **6** indicating that the activation step is likely to produce a species similar in structure to **6**.

B – Halide abstraction from OctBr by FeMes$_2$, releasing an Octyl radical and forming a neutral Fe^{III} intermediate. This is supported by the radical clock experiment, indicating an electrophile-bound radical is formed on the catalytic cycle. This is also consistent with other studies of coupling reactions with alkyl halides going by Atom Transfer Radical Polymerisation (ATRP)-type mechanisms.[61,102,118]

C – Reaction of an octyl radical with the Fe^{III} intermediate, producing an Fe^{IV} intermediate. This may be the same radical produced in the Step B, but not necessarily. The significant loss of electrophile observed in all cases indicates an 'outer sphere' mechanism, in which the radical is not kept close to the iron species during turnover. This is also supported by the observation of large quantities of Cy$_2$ being formed when CyBr is used as the electrophile.

D – Reductive elimination of MesOct, leaving a heteroleptic Fe^{II}BrMes complex. From the fact that production of the homocoupling product Mes$_2$ is observed to occur concomitantly with the production of MesOct, indicating the elimination step likely occurs from a species bearing at least one octyl residue, and 2 mesityl residues.

E – Reaction of the heteroleptic Fe^{II}BrMes with a further equivalent of MesMgBr to reform Fe^{II}Mes$_2$.

F – Alternatively, this reaction may instead form the anionic **8**.

G – 8 may react reversibly with MesMgBr to reform **7**. This step has been observed directly by ^{1}H NMR spectroscopy and is supported by a kinetic study (Figure 3.10).

3.7 – Conclusions

An investigation into the iron-catalysed Kumada-Corriu cross-coupling of an alkyl halide, OctBr, with an aryl Grignard reagent, MesMgBr, has been performed, uncovering a complex series of relationships between the *in situ* generated iron species and many of the other components of the reaction.

Firstly, it was shown that the accessible mechanisms of coupling are changed by the identity of the nucleophilic substituent. Groups that are resistant to reductive elimination, such as the mesityl group, are unable to reach the Fe^I active species which forms the bulk in catalytic solution for less hindered groups, therefore an alternative mechanism is active.

The iron species implicated in previous reports as present during catalytic turnover, $[FeMes_3]^-$ (**7**), was determined by stoichiometric reactions with electrophile to be a pre-catalyst, while the main catalytic cycle is carried out by neutral species. The heteroleptic species $[FeBrMes_2]^-$ (**8**) and $[FeBr_2Mes]^-$ (**17**) were both found to be inactive in reaction with electrophile.

The inorganic product of Kumada-Corriu cross-coupling, $MgBr_2$, was found to have numerous roles in catalysis, both beneficial and deleterious to facilitating turnover. It has been shown to react with **7** at concentrations relevant to catalysis, pushing an equilibrium toward the catalytically inactive **8**, slowing the rate of reaction. However, if the reaction is performed with 1,4-dioxane added to precipitate out any formed $MgBr_2$, turnover halts at 15% yield. This highlights a vital role of $MgBr_2$ for maintaining turnover.

From these results, a $Fe^{II}/Fe^{III}/Fe^{IV}$ catalytic cycle has been proposed, although this should come with the caveat that such a cycle may be drastically altered by the identities of each coupling partner, and even may only be one of several operating in this specific system.

4. Chapter 4 – Syntheses of Complexes Relevant to Iron-Catalysed N_2 Reduction

4.1 – Introduction

While it has been shown in Chapter 3 that iron in cross-coupling catalysis requires little-to-no interaction with ligands in order to achieve turnover, investigations of iron-catalysed N_2 reductions have generally shown a great degree of cooperative interactions take place either with ligands or other metal atoms in order to accommodate the wide gulf of electronic states between an N_2 ligand and an NH_3, or alternative N^{3-} species.

This is shown most plainly in nature's solution for N_2 reduction, the FeMoco nitrogenase cofactor [Fe_7CS_9Mo],[69,70] in which the N_2-bound Fe atom is supported by a both a carbide and 3 sulphur atoms.
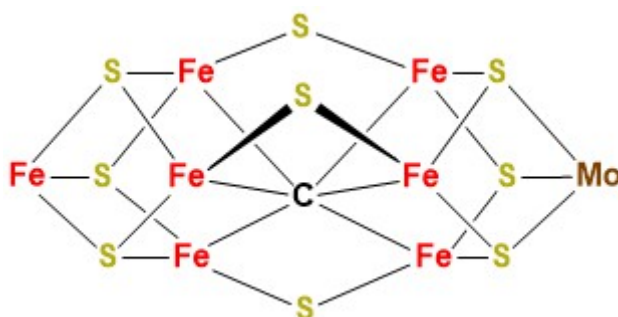
Figure 4.1: The iron-molybdenum cofactor FeMoco in molybdenum-nitrogenase.

Synthetic homogenous N_2 reduction catalysts display this behaviour as well. Peters' reported iron complexes for N_2 reduction showed a strong dependence on the hemi-lability of a Fe-B/C bond.[93,125] In these systems, the initial, N_2-bound intermediate shows a relatively short Fe-B/C bond, but as the nitrogenous moiety is reduced further and further, this bond lengthens, concomitant with a greater activation of the N_2 moiety. (Scheme 4.1)
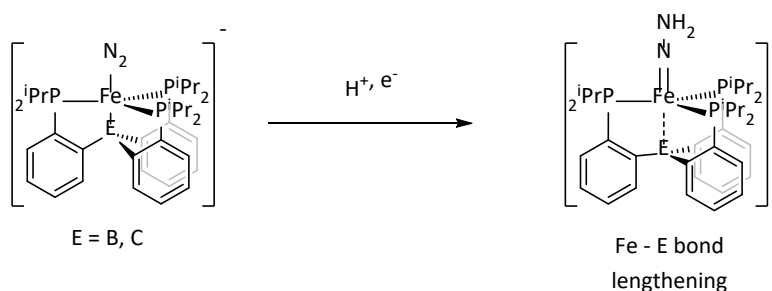
Scheme 4.1: The observed lability of the Fe-E bond upon reduction of an N_2 ligand in Peters' reported tripodal phosphine complex for N_2 reduction.

Similar effects were shown in a report of a N_2 silylation to form $N(SiMe_3)_3$ with an iron-diphosphine complex. Reaction of the Fe-N_2 complex with excess Me_3SiCl and KC_8 enabled isolation of an Fe-$NN(SiMe_3)_2$ complex in which one of the diphosphines is partially decoordinated.[97]
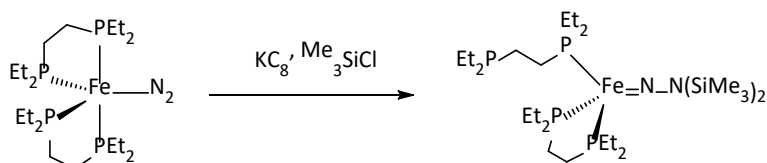
Scheme 4.2: The silylation of N_2 resulting in partial ligand decoordination from $FeN_2(depe)_2$.

Molybdenum complexes too have shown catalytic benefits from the incorporation of cooperative metal groups in their structure.

Nishibayashi later reported the highest achieved turnover of a catalytic N_2 silylation with a molybdenum complex bearing depf (1,1'-bis(diethylphosphino)ferrocene) ligands, $Mo(N_2)_2(depf)_2$, achieving far greater turnover that analogous species bearing other phosphines such as PMe_2Ph or dppe.[89] In their reports they assign this increased turnover to not only the steric bulk of the depf moiety, shielding the iron centre from attack by the *in situ* generated $SiMe_3\cdot$ radicals, but also to the lability of the Mo-P bond afforded by the ligand's electronic properties.

Turning to the acidification of N_2, Nishibayashi found that incorporation of a ferrocenyl-type moiety into one of their reported PNP-Mo catalysts improved turnover from 22 equivalents of NH_3 to 37 equivalents.[126]
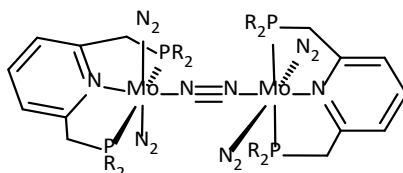
Figure 4.2: Nishibayashi's ferrocenyl-PNP ligand system for N_2 acidification.[126]

Aside from examples of incorporating ferrocenyl groups in the catalyst, the effectiveness of metallocene-based reductant is also striking. The choice of reductant seems to play a big part in the effectiveness of N_2 reduction in many systems, with a commonly recurring reductant choice being cobaltocene ($CoCp_2$) or its permethylated derivative ($CoCp^*_2$). This reductant sensitivity has 2 potential explanations. Firstly, reduction potentials in ammonia production must strike a balance; being reducing enough to drive the reduction of the metal-N_2 complex to drive reaction, but without being so reducing as to directly reduce the Bronsted acid, in turn producing H_2. $CoCp^*_2$ seems to balance this for many reported systems, sometimes aided by choice of solvent or other reaction parameters.[83]

Cobaltocene reductants have also been identified as having a more specialised role in acidification catalysis, in which they serve as a shuttle for the proton-coupled electron transfer, being first protonated, before transferring that proton concomitantly with the electron to the metal catalyst.[127] Aside from cobaltocene specifically, they also show the capacity for decamethylnickelocene to perform the same reaction, therefore it is not unreasonable to propose that ferrocenyl moieties may also have some capacity to perform this function.

Despite these results, no iron-based catalysts for N_2 reduction have yet incorporated metallocenyl moieties. The synthesis of such complexes was therefore pursued.

4.2 - Ferrocenyl-phosphine complex Synthesis

Aiming to exploit the cooperative metal-metal action observed as being operative in previous reports of homogeneous catalytic systems for N_2 reduction, the synthesis of iron complexes bearing metallocenyl-phosphine ligands was pursued. A recurring motif in the synthesis of pre-catalysts for TM-catalysed N_2 reduction is the reduction of high oxidation state metal-halide complexes under an N_2 atmosphere to give the N_2-bound complex (usually as the M^0).

The first synthesis of a complex of this type attempted was $FeCl_2(dppf)_2$, due to the low cost and commercial availability of the starting materials.
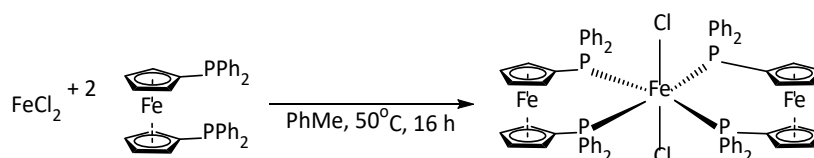
Scheme 4.3: The proposed synthesis of $FeCl_2(dppf)_2$ from $FeCl_2$ and dppf.

This synthesis was performed *via* heating of $FeCl_2$ with 2 equivalents of the dppf ligand in toluene overnight, layering of this solution with hexane and cooling to -25 °C gave the product as blocky orange crystals that were characterised by XRD.
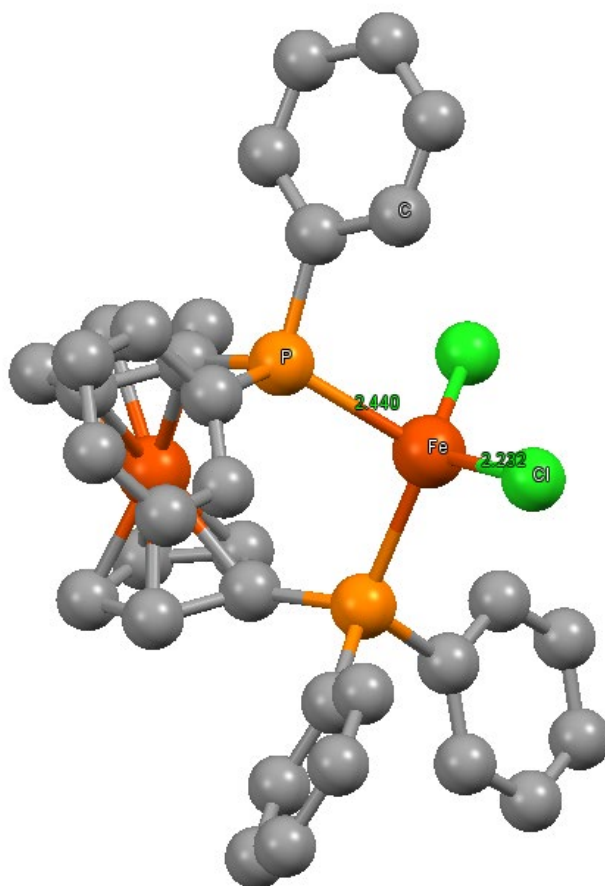
Figure 4.3: X-ray structure of FeCl$_2$(dppf) with H-atoms omitted for clarity.

Interestingly, despite the presence of excess dppf in reaction, XRD displayed that only the mono-chelated FeCl$_2$(dppf) (**19**) species was formed. Extending reaction time to several days did not give any indication of bis-ligation occurring by XRD or ^{1}H or ^{31}P NMR spectroscopies. It was hypothesised that this may be due to the steric bulk of the phosphine-bound phenyl groups; therefore the analogous complexes with depf (1,2-bis(diethylphosphino) ferrocene) and dippf (1,2-dis(diisopropylphosphino) ferrocene) were synthesised.

The dippf analogue complex was synthesised and characterised by the same method used for the dppf complex using commercially available dippf whereas the depf ligand was synthesised by a previously reported method.[128]
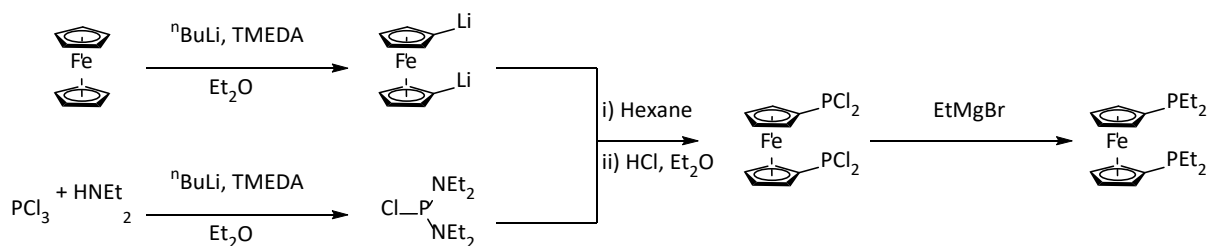
Scheme 4.4: Synthetic route to make 1,2-bis(diethylphosphino)ethane (depf).

The complexes $FeCl_2(dippf)_2$ and $FeCl_2(depf)_2$ were targeted via the same route, with the same results in each case; the formation of the mono-ligated analogues $FeCl_2(dippf)$ (**20**) and $FeCl_2(depf)$ (**21**).
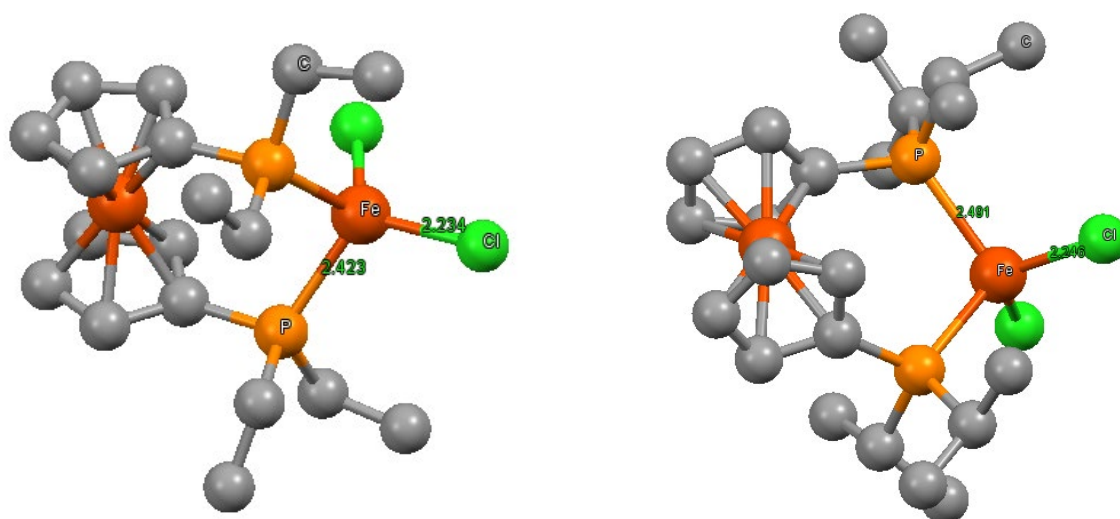
Figure 4.4: Crystal structures of $FeCl_2(depf)$ **21** and $FeCl_2(dippf)$ **20**. H atoms omitted for clarity**.**

The differing steric bulk of the ethyl and iso-propyl groups in these complexes as compared to the phenyl groups does not appear to have a significant effect on the Fe-P or Fe-Cl bond lengths, with each remaining at approximately 2.4 Å and 2.2 Å respectively for each of the 3 complexes. Interestingly, the P-Fe-P bond angle does appear to change depending on the substituent on the phosphine. While both **19** and **20** both have P-Fe-P bond angles of 108°, the corresponding angle for **21** is noticeably more acute at 95°.

Regardless of steric bulk on the phosphines, it appears that the 4-coordinate complex is preferred. This may present issues for forming the corresponding N_2 complexes as no examples of 3-coordinate iron-phosphine-N_2 complexes have been reported.

6-coordinate complexes were therefore targeted by reaction with further phosphine, the species were reacted with two equivalents of PMe_3.
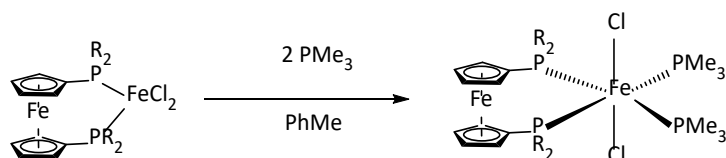
Scheme 4.5: The addition of PMe_3 to **19** to give a six-coordinate product.

Addition of PMe_3 to a solution of **19** induced an instantaneous colour change from orange to a deep red. Analysis of the reaction mixture by ^{1}H NMR showed signals for a new paramagnetic species, with no species visible by ^{31}P NMR. However, all crystals grown from were found to be of the dppf ligand, indicating a ligand substitution occurring instead of ligand addition. A 4-coordinate complex does therefore seem to be the limit when using ferrocenyl ligands on an Fe^{II}-chloride centre.

4.2.1 - Complex Reduction

Despite the failure to synthesise 6-coordinate analogues, the corresponding Fe^0-N_2 analogues to the ferrocenyl-phosphine complexes were targeted by their reduction under an atmosphere of N_2. Alkali metals are most commonly used for this step in other reported TM-N_2 syntheses, although the use of Group II metals for this transformation have also been reported, such as in the use of Mg in the synthesis of $Mo(depf)_2(N_2)_2$.[129]

Therefore, in the pursuit of a 5-coordinate Fe^0 product, **19** was reacted with KC_8 in the presence of an additional equivalent of dppf ligand added under an atmosphere of N_2. The mixture was then sealed in a Young's flask in order to maintain the N_2 atmosphere.
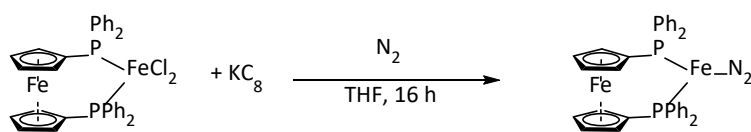
Scheme 4.6: The proposed reduction of $FeCl_2(dppf)$ with KC_8 and added dppf ligand.

Analysis of the reaction mixture by ^{31}P NMR spectroscopy did not show signals corresponding to a 5-coordinate Fe^0 complex, which would theoretically be diamagnetic and therefore visible by ^{31}P NMR, but instead showed that signals corresponding to the potassium salt of the $[C_5H_4PPh_2]^-$ anion, indicating that the KC_8 had reduced the dppf ligand, producing the salt pair along with Fe^0.

Even if the excess ligand is omitted, production of the reduced, unbound ligand is still observed, a strong indication that KC_8 is too harsh a reagent for this reduction.
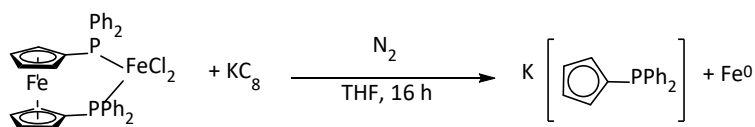
Scheme 4.7: The reduction of $FeCl_2(dppf)$ with KC_8 to give $K[C_5H_4PPh_2]$ and Fe^0.

In the synthesis of their ferrocenyl-phosphine-bearing molybdenum complex $Mo(depf)_2(N_2)_2$, the Nishibayashi group reported the use of activated Mg metal as the reductant, and did not observe reduction of the depf ligand.[129] Unfortunately, when applying this knowledge the reduction of **19** by using Mg in place of KC_8, no product of reduction is observed. It appears then that if this reaction is to be performed, a reductant must be found with a reduction potential intermediate between Mg and KC_8.
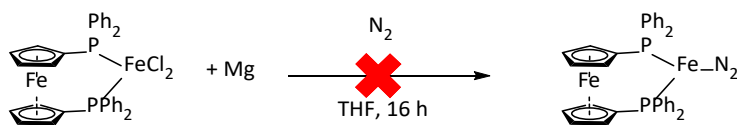
Scheme 4.8: The attempted reduction of $FeCl_2(dppf)$ with Mg under N_2.

As such a reductant was not readily available, efforts were diverted in a different direction.

4.3 - Synthesis of cobaltocenyl-phosphines

As ferrocenyl-phosphine ligand complexes were found to be unsuitable owing to their electropotential rendering them too susceptible to reduction, the synthesis of a cobaltocenyl phosphine ligand was pursued.

Cobaltocene and its derivative are commonly used as reductants, owing to a relatively high reduction potential.[130] The permethylated derivative in particular is a very strong reductant, commonly used for N_2-reduction catalysis.[131]

The use of both of these species as reductants has become well established for the homogenous catalytic N_2 reduction reaction, but no catalysts for this reaction have been reported bearing cobaltocenyl phosphine ligands.

The synthesis of a cobaltocenyl-1,1'-bis(phosphine)-type ligand was first reported in 1978 by Rudie and co-workers,[132] with the synthesis improved in 2000 by Salzer and co-workers.[133] Salzer then used the ligand in its oxidised form in a rhodium-catalysed hydroformylation.

In fact, all reported uses and syntheses of a 1,1-bis(phosphino)cobaltocene ligand have been in its oxidised form.[134,135] Albeit, they are usually synthesised *via* the neutral species which is not isolated. Along with the cobaltocenium's relative stability under aerobic conditions, its use may potentially be due to the fact that such species are isoelectronic to the ferrocenyl analogues, which have significant precedent for use as ligands.

For this reason, synthesis of the cobaltocenium analogue of dppf was pursued. Synthesis was first attempted by treatment of cobaltocenium hexafluorophosphate [CoCp$_2$][PF$_6$], with ^{n}BuLi and TMEDA, in analogy to the procedure for lithiation of ferrocene,[136] before reaction with ClPPh$_2$.
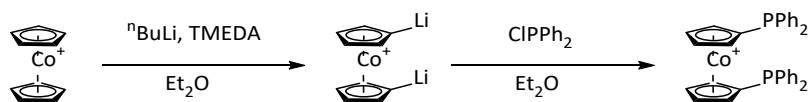
Scheme 4.9: The attempted synthesis of 1,1'-bis(diphenylphosphino)cobaltocenium.

^{1}H NMR analysis of the reaction mixture showed signals corresponding to a paramagnetic species, despite cobaltocenium species being diamagnetic. This indicates that rather than acting solely as a base as was desired, ^{n}BuLi is reducing cobalt to the Co^{II} oxidation state, reforming the paramagnetic cobaltocene. This appears to indicate that direct lithiation-phosphination of the cobaltocenium species may not be accomplished, therefore the neutral species was targeted instead.

This synthetic route involved forming the cyclopentadienyl phosphine first before coordination to cobalt.
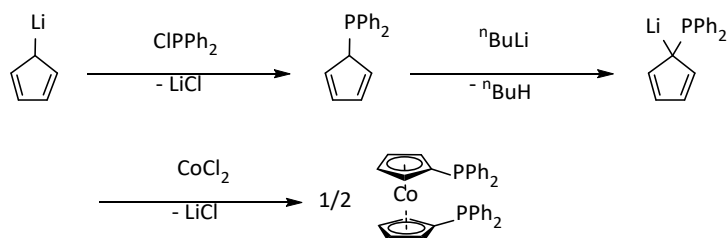
Scheme 4.10: The synthesis of 1,1'-bis(diphenylphosphino)cobaltocene.

Unfortunately, upon ^{1}H NMR analysis of the reaction mixture for the final step, no signals corresponding to a paramagnetic species were observed. However, ^{31}P NMR also showed no signals, which is indicative of paramagnetic species in solution. Unfortunately, attempts to grow crystals from this solution were unsuccessful.

4.4 – Synthesis and Functionalisation of simple Fe-S halide complexes

Moving on from iron- metallocenyl phosphine complexes, research interest was turned to emulating nature's solution to N_2 fixation, through the use of iron-sulphur complexes.

Beginning from the identification of iron-sulphur clusters in biological processes, the pursuit of synthetic mimics has occurred. The first such examples was reported by Weiher in the 1970s, reporting both $[Fe_4S_4]$ and $[Fe_2S_2]$ complexes supported by thiolate ligands.[137,138] Following from this, synthetic iron-sulphur clusters were reported with a wide range of supporting ligands including halides,[139,140] cyanides,[141] cyclopentadienes,[142] and carbonyls.[143]

Aside from their uses as models for biological systems, iron-sulphur clusters have shown catalytic activity for the hydrogenation of C1 substrates to C1-C5 hydrocarbons.[144–146] Such a reactivity, along with other factors such as the identification a carbide centre in the iron-molybdenum cofactor and an organometallic intermediate being identified in an Fe-S cluster-catalysed biological transformation[147,148] have led efforts to synthesise iron-sulphur complexes bearing Fe-C bonds. This was first accomplished in 2020 with Suess' reports of iron-sulphur clusters in the $[Fe_4S_4]^{2+}$ and $[Fe_4S_4]^{3+}$ oxidation states bearing an alkyl moiety, supported by an expansive scorpionate ligand.[149,150] Other than this report, examples of organometallic iron-sulphur clusters are exceedingly rare, despite the wide biological relevance and catalytic significance, not least in the reduction of dinitrogen. For this reason, the synthesis of such species was pursued.

Initial investigations into the feasibility of synthesising organometallic iron-sulphur clusters began with the synthesis of the simple, previously reported, iron-sulphur-halide clusters, $[Fe_2S_2Cl_4][NEt_4]$ (**22**) and $[Fe_4S_4Br_4][NBu_4]$ (**23**).

$$2\ [FeCl_4][NEt_4]\ +\ 2\ S(SiMe_3)_2 \xrightarrow{\text{THF, 2 h}} \left[\begin{array}{c} Cl_{\prime\prime\prime\prime\prime}Fe \overset{S}{\underset{S}{\diagup\diagdown}} Fe^{\backslash\backslash\backslash\backslash}Cl \\ Cl \end{array} \right][NEt_4]_2\ +\ 4\ ClSiMe_3$$

$$4\ FeBr_3 + 4\ Na_2S + 2\ [NBu_4][Br] \xrightarrow{\text{DMF, 24 h}} \left[\text{Fe}_4\text{S}_4\text{Br}_4 \right] [NBu_4]_2 + 8\ NaBr$$
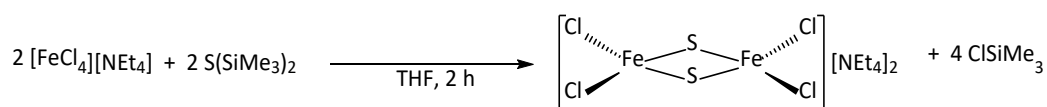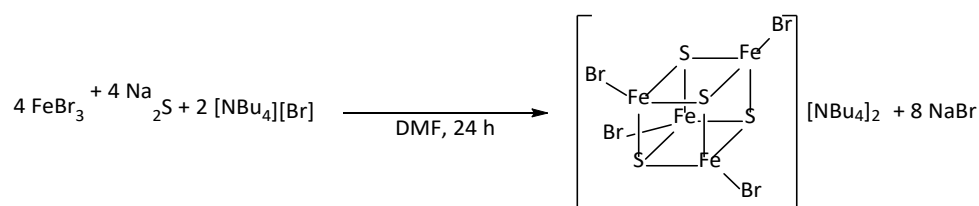
Scheme 4.11: The syntheses of $[Fe_2S_2Cl_4][NEt_4]_2$ and $[Fe_4S_4Br_4][NBu_4]_2$.

The iron-bound halides on these clusters may serve as reactive sites to organic nucleophiles, enabling substitution reactions to form organometallic products. Additionally, as these complexes lack any protons in paramagnetic environments, any formation of such products will be relatively simple to identify by ^{1}H NMR by looking for signals indicative of paramagnetic complexes.

Initial attempts to functionalise **22** were undertaken with aryl Grignard reagent MesMgBr. The ortho-methyl groups on this substituent have, as discussed previously, been shown to stabilise organometallic derivatives with transition metals, due to a kinetic effect that discourages reductive elimination relative to less sterically hindered aryl groups.
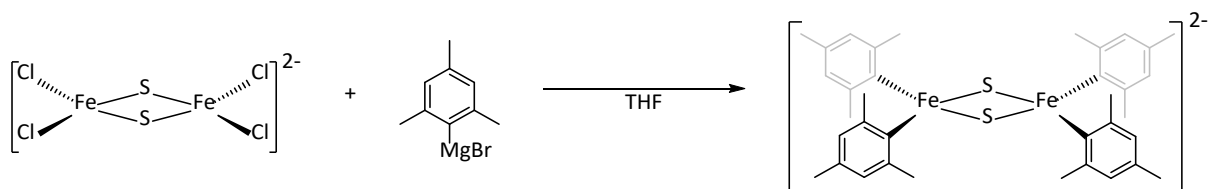
Scheme 4.12: The proposed mesitylation of $[Fe_2S_2Cl_4]^{2-}$ with MesMgBr.

Unfortunately, ^{1}H NMR analysis of the reaction mixture revealed that even upon slow addition at low temperature, or with lower loading of Grignard reagent, the $[Fe_2S_2]$ core was not conserved, the reaction instead proceeding directly to form the heteroleptic ferrate species $[FeMes_3]^-$. (Scheme 4.13)
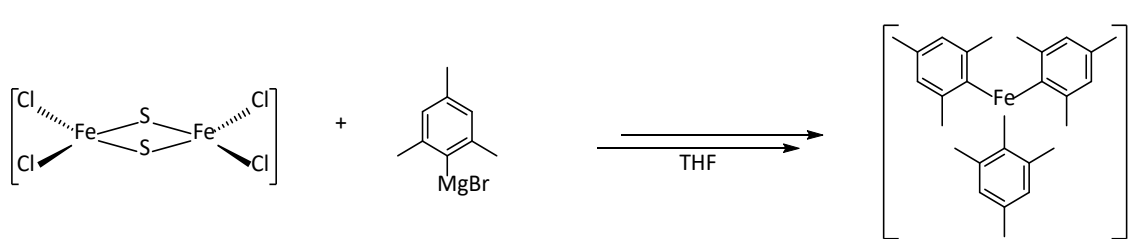
Scheme 4.13: The reaction of $[Fe_2S_2Cl_4]^{2-}$ with MesMgBr to form $[FeMes_3]^-$.

This preferential splitting of the $[Fe_2S_2]$ core suggests that the planar nature and exposed Fe-S bonds are susceptible to attack from the nucleophilic carbon and, therefore, the reactivity of the cubane cluster **23** was explored with the same reagent, hypothesising that this will have a greater stability. Analysis of the reaction mixture by ^1H spectroscopy showed no evidence of the formation of a paramagnetic product, indicating reaction with the Grignard reagent unlikely to have occurred. (Scheme 4.14)
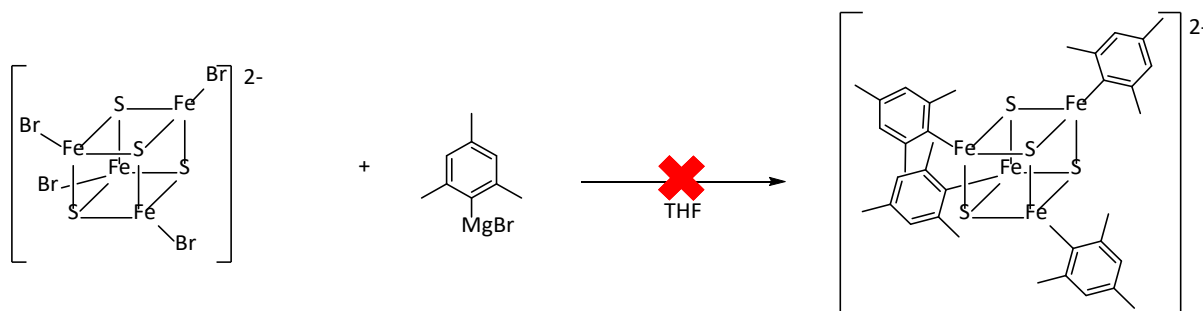
Scheme 4.14: The proposed mesitylation of $[Fe_4S_4Br_4]^{2-}$ with MesMgBr.

When switching to the corresponding, harsher, organolithium, formation was observed once again to the homoleptic ferrate **7**, It therefore seems that a nucleophile of a 'hardness' between a Grignard reagent and an organolithium may lead to the desired product in which the cubane is functionalised without compromising the structure of the core. In this interest, the reactivity of **22** was tested with the diaryl magnesium compound Mes_2Mg, produced by addition of dioxane to the reaction solution, giving Mes_2Mg through exploitation of the Schlenk equilibrium.

^{1}H NMR analysis of this reaction mixture showed signals indicating formation of a paramagnetic product, albeit at very low concentration. Attempts were made to isolate this product; however, its formation was observed only in low quantities, hindering its separation from the **24** starting material and rendering its isolation unsuccessful.

As well as the simpler iron-sulphur-halide complexes, mixed sulphide/amide iron clusters of similar structure have been reported and their chemistry investigated.[151,152] Integration of nitrogenous moieties with iron-sulphur complexes has obvious relevance to the chemistry of nitrogenases.

The complex [Fe$_2$(μ-N^{t}Bu)(μ-S)Cl$_4$][NEt$_4$]$_2$ (**24**) was synthesised by the multi-step procedure reported by Lee and co-workers.[151]
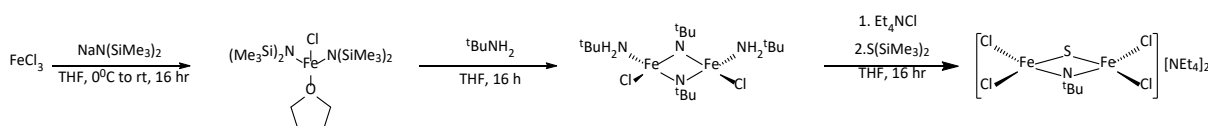
Scheme 4.15: The synthesis of [Fe$_2$(μ-N^{t}Bu)(μ-S)Cl$_4$][NEt$_4$]$_2$.

As with compounds **22** and **23** the reactivity of this complex was investigated with organic nucleophiles. Again, reaction with MesLi and MesMgBr gave only **7**; however, reaction with Mes$_2$Mg gave new signals observed by ^{1}H NMR for a paramagnetic species.
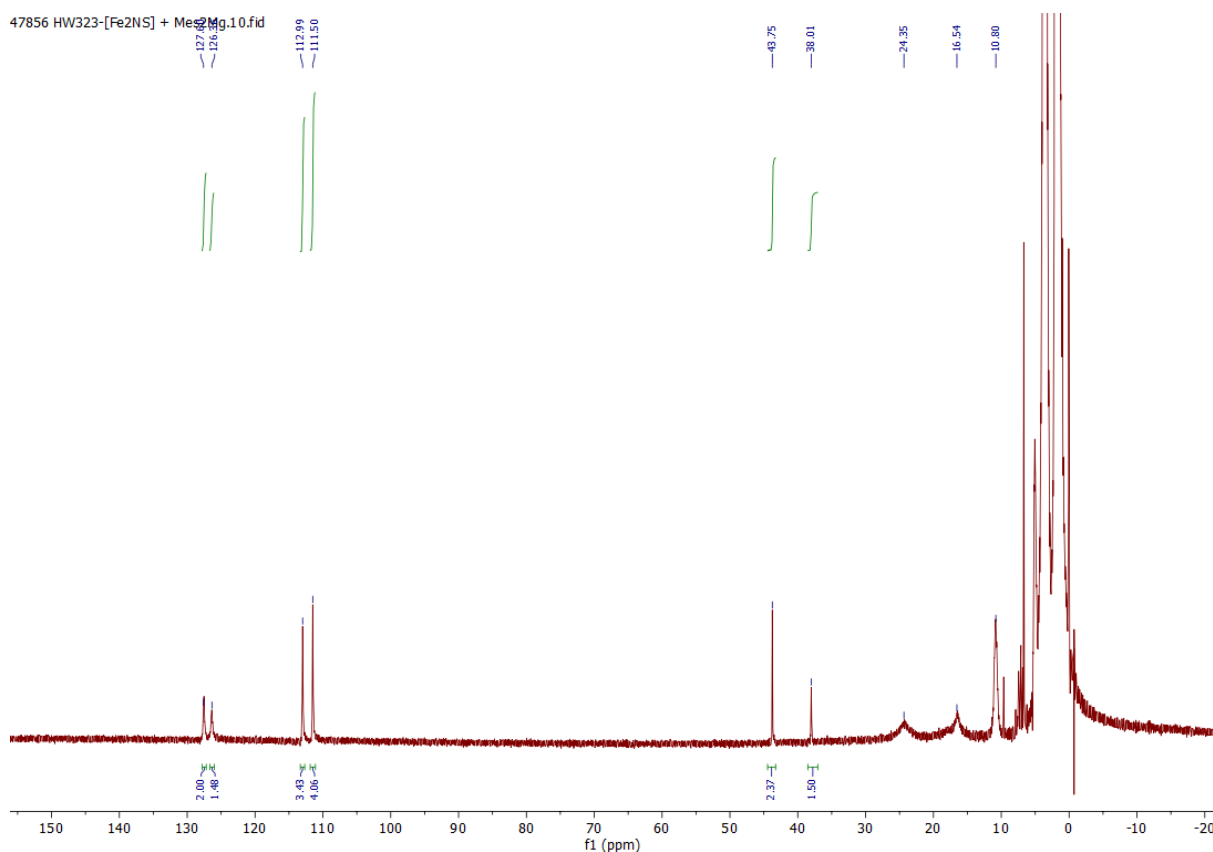
Figure 4.5: ^1H NMR spectrum of the reaction of $[Fe_2(\mu-N^tBu)(\mu-S)Cl_4]^-$ with Mes_2Mg.

While the majority of product seems to be forms of **7**, signals can be observed at 25 and 17 ppm that are likely to be resultant from a paramagnetic product, tentatively suggesting functionalisation of the $[Fe_2NS]$ core has occurred. Unfortunately, despite repeated efforts, this complex was not isolated.

4.5 - Synthesis of a class of $[Fe_8S_4]$ Clusters

As the organometallic functionalisation of simpler $[Fe_xS_yN_z]$ could not be accomplished, interest was diverted to more complex clusters with iron-bound halides with a ligand environment that may better stabilise organometallic derivatives. In this interest, a previously published, all Fe^{III} cluster $Fe_8O_4pz_{12}Cl_4$ **(25)** was synthesised.[153]
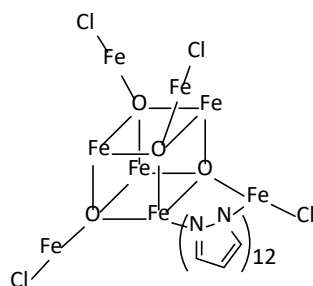
Scheme 4.16: The structure of $Fe_8O_4(pz)_{12}Cl_4$ as reported by Raptis and co-workers.[153]

The structure comprises a central $[Fe_4O_4]$ cubane core with each oxygen having a pendant iron attached, with a terminal chloride on each of these iron atoms. Pyrazole ligands bridge between each of the core and pendant iron atoms. The complex is enantiomeric, with P- and M- isomers resulting from a propeller-like tilt of pyrazole ligands.[154]
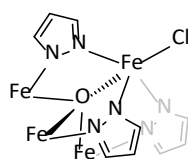
Scheme 4.17: The structure of pyrazolate ligands around the terminal iron atoms of $Fe_8O_4(pz)_{12}Cl_4$.

The complex is synthesised by a self-assembly reaction under aerobic conditions by combination of $FeCl_3$ and sodium pyrazolate. Isotopic labelling experiments with $H_2^{18}O$ confirmed that the incorporated oxygen is introduced by water rather than O_2, this can also be rationalised in redox terms.

$$8\ FeCl_3 + 12\ Napz \xrightarrow[\text{DCM, 24 hr}]{H_2O} Fe_8O_4pz_{12}Cl_4 + 12\ NaCl + 8\ HCl$$
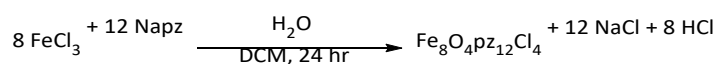
Scheme 4.18: The synthesis of $Fe_8O_4(pz)_{12}Cl_4$.

Adapting this synthesis, the sulphur analogue of **25** was targeted, performing the reaction under anaerobic conditions and substituting H_2O with $S(SiMe_3)_2$ as a S^{2-} source.

$$8\ FeCl_3 \xrightarrow[\text{DCM, 24 hr}]{\substack{+\ 12\ Napz \\ S(SiMe_3)_2}} Fe_8S_4pz_{12}Cl_4 \quad +\ 12\ NaCl + 8\ ClSiMe_3$$
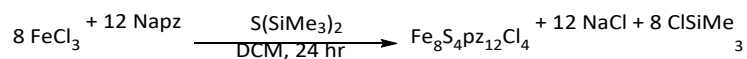
Scheme 4.19: The synthesis of $Fe_8S_4(pz)_{12}Cl_4$.

The addition of $S(SiMe_3)_2$ to a stirred suspension of $FeCl_3$ and Napz in dichloromethane instantly induced a colour change from a rust-red colour to black. Upon work-up, a tan-brown product was recovered and analysed by ^1H NMR.
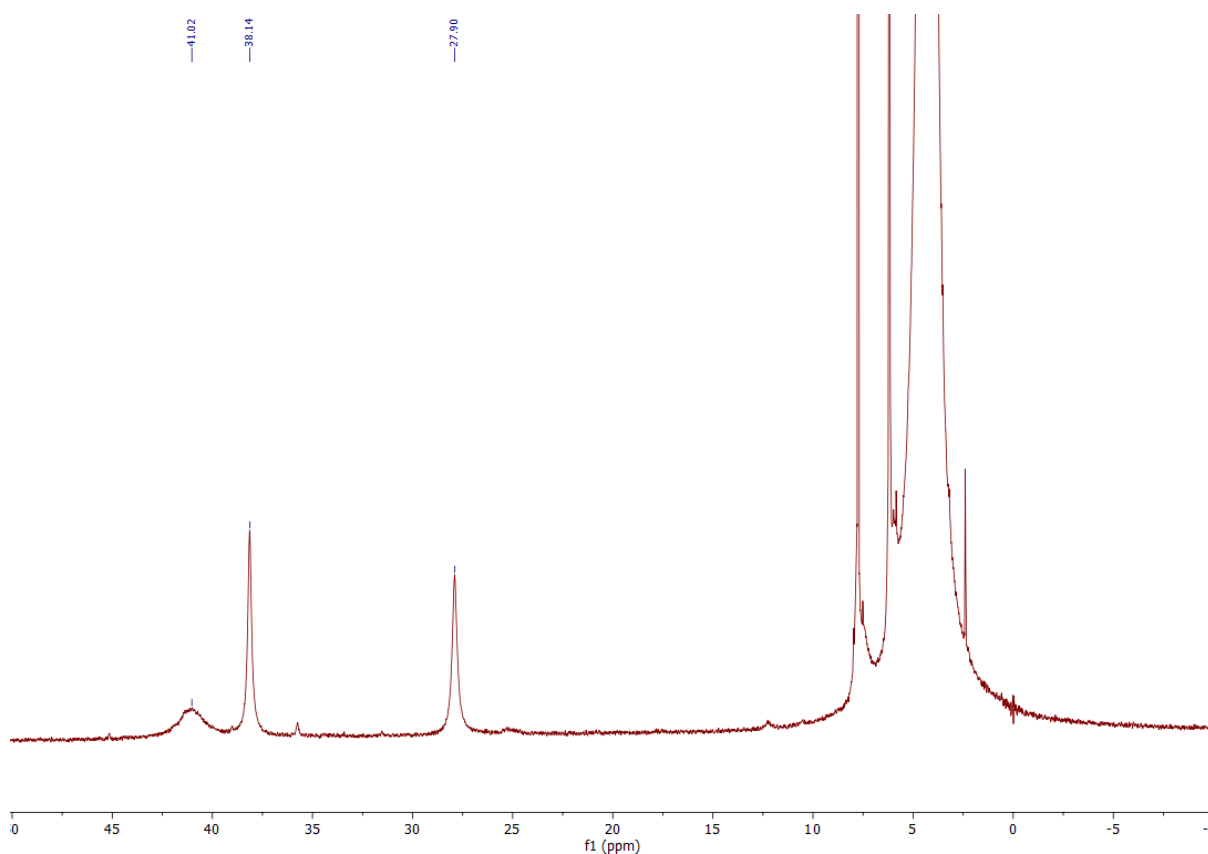
Figure 4.6: ^1H NMR spectrum of $Fe_8S_4(pz)_{12}Cl_4$.

^{1}H NMR showed 3 signals at chemical shifts characteristic for paramagnetic species, of equal integration. This data points to the proposed sulphur analogue of **25**, $Fe_8S_4pz_{12}Cl_4$ (**26**) being synthesised.
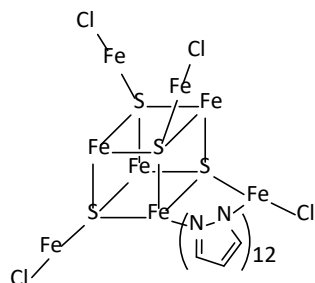
Figure 4.7: The proposed structure of an iron-sulphur cluster $Fe_8S_4pz_{12}Cl_4$.

Encouraged by this result, several substituted pyrazolate salts were used, forming a library of derived clusters.

R = 3,5-Me, 3,5-iPr, 4-Br
X = Br, Cl
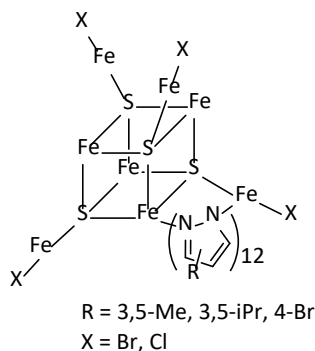
Figure 4.8: The variety of $Fe_8S_4(pz)_{12}X_4$-type clusters identified by ^{1}H NMR.

Several attempts were made to grow crystals of these complexes that were suitable for X-ray diffraction in order to confirm their structure, but none of the methods attempted were successful. On a few occasions, crystals grown from solutions of **26** were found to be crystals of **25**, implying that the transformation of these sulphur complexes to the oxygen analogue is possible through reaction with O_2.
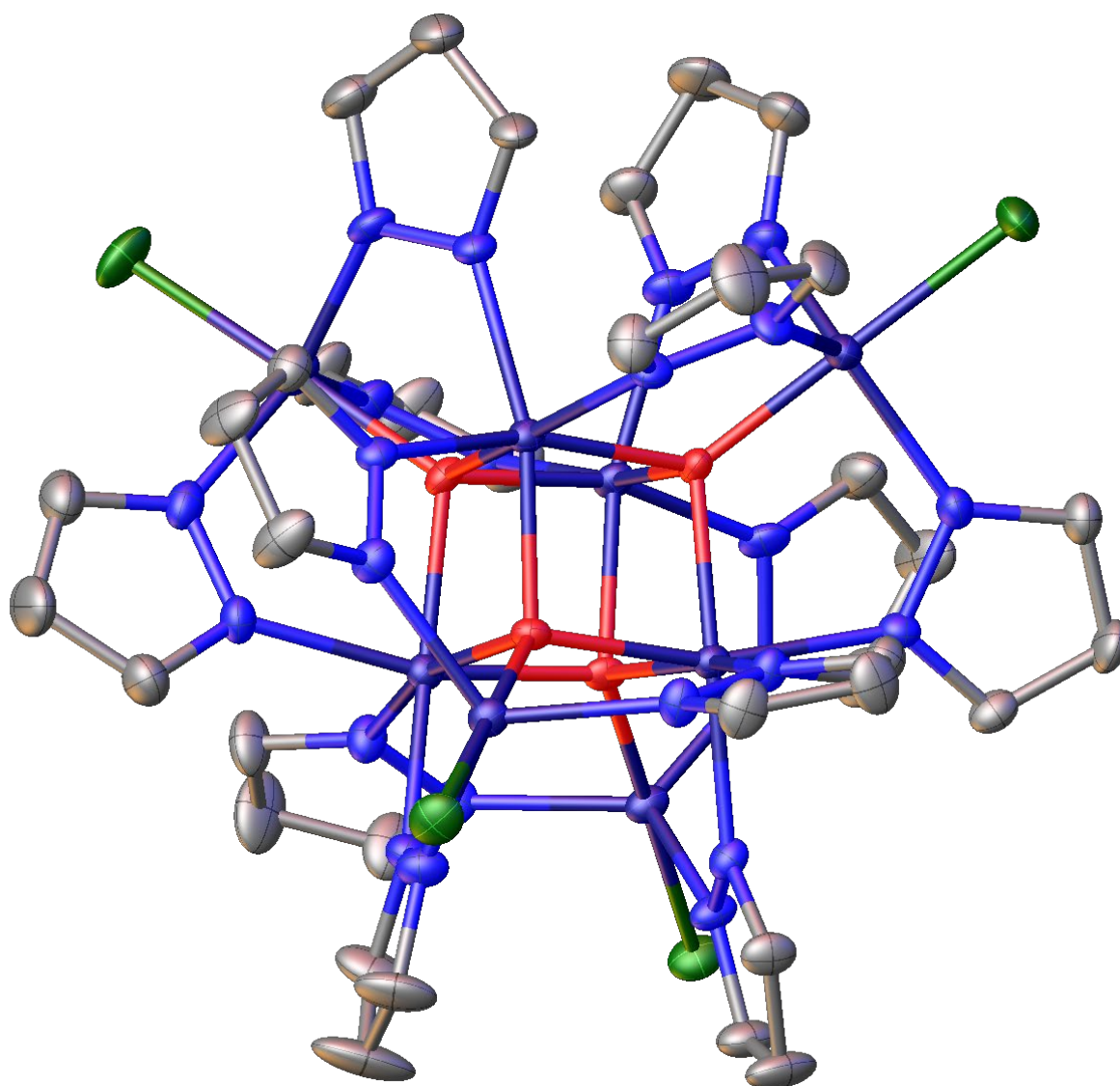
Figure 15: A crystal structure of **25** collected from a solution of **26** exposed to oxygen. Co-crystallised solvent molecules and H-atoms have been omitted for clarity. Fe: purple, O: red, N: blue, Cl: green, C: grey.

In order to investigate this transformation, a solution of **26** was analysed by ^{1}H NMR before being opened to air and a colour change tracked over the course of one hour.
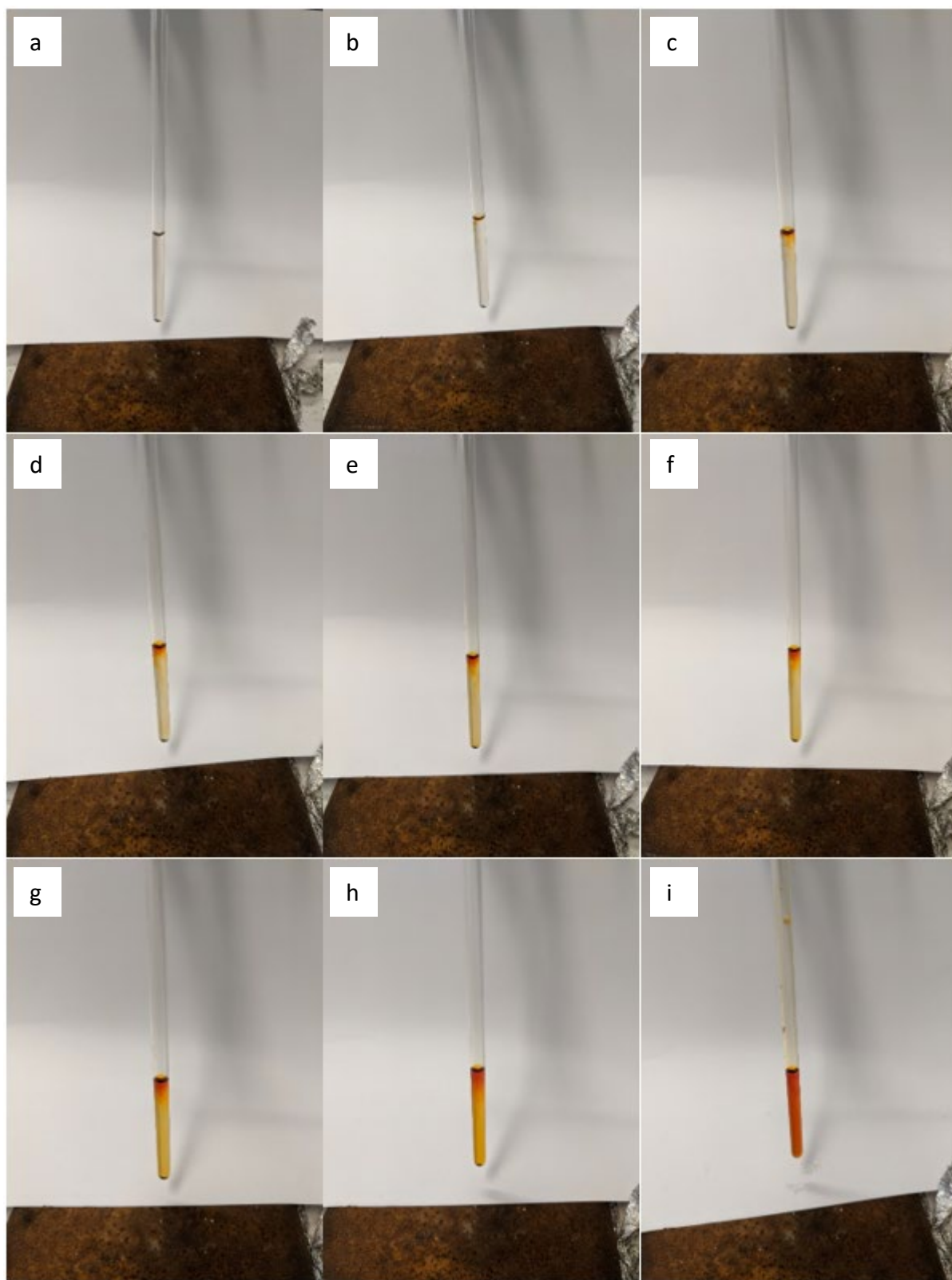
Figure 4.9: A solution of $Fe_8S_4(pz)_{12}Cl_4$ opened to air. Pictures taken 0 (a), 5 (b), 10 (c), 15 (d), 20 (e), 25 (f), 30 (g), or 60 (h) minutes after opening, and then after one inversion under air (i).

As can be seen in Figure 4.9, as the solution is exposed to air for longer, the red colour indicative of the formation of **25** becomes more prominent. ^{1}H NMR analysis before and after the exposure supports this, showing the characteristic signals for the oxide cluster.
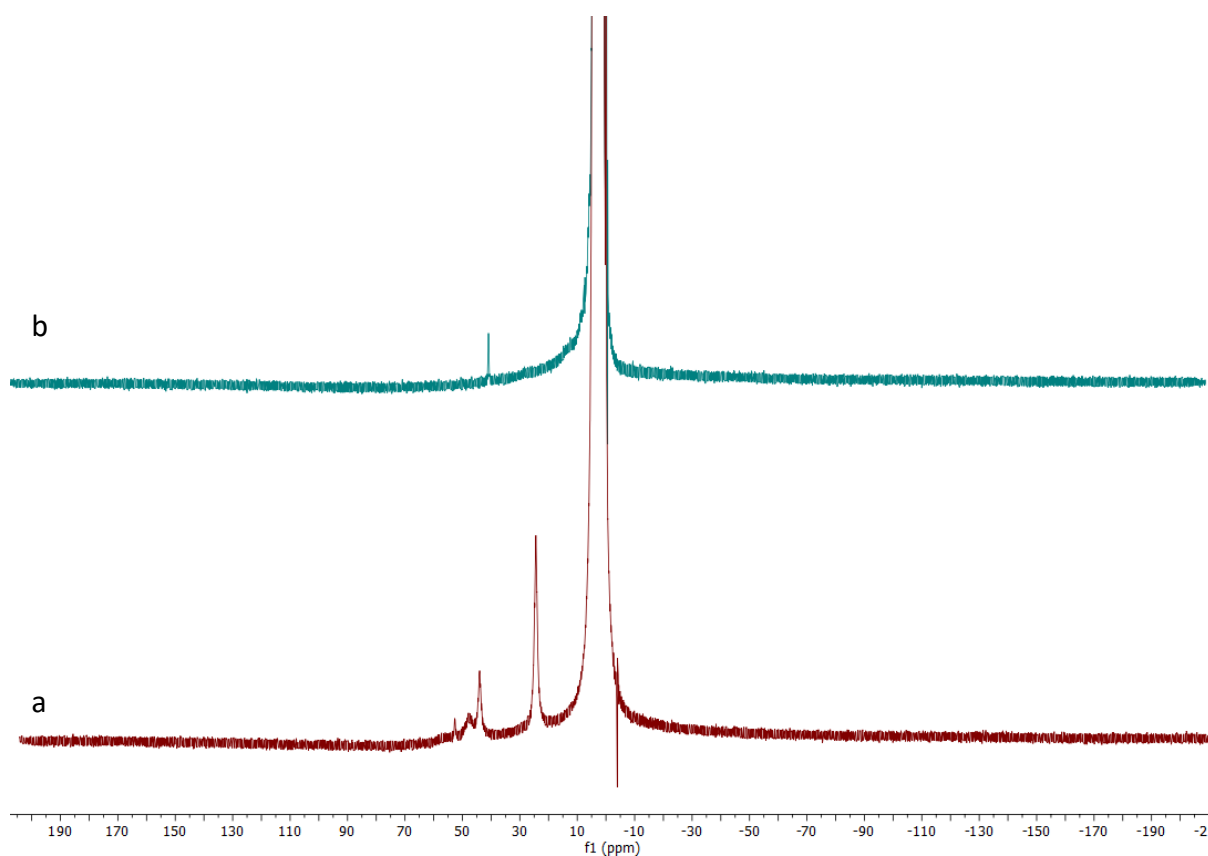
Figure 4.10: ^{1}H NMR spectra of $Fe_8S_4pz_{12}Cl_4$ before (a) and after (b) exposure to atmospheric oxygen, showing the production of $Fe_8O_4pz_{12}Cl_4$.

4.5.1 - Fe-Se Clusters

Although they have lesser biological relevance than their sulphurous counterparts, there are several reported examples in literature of Fe-Se analogues of Fe-S clusters being synthesised, and their chemistry investigated.[139,155] In this interest, the selenium analogues of **26** were synthesised.

As the Se analogue of the sulphur source used previously, $S(SiMe_3)_2$, was not commercially available, Na_2Se was used instead as a source of Se^{2-}.

$$8 \text{ FeCl}_3 \xrightarrow[\text{DCM, 24 hr}]{\text{Na}_2\text{Se}} \text{Fe}_8\text{Se}_4\text{pz}_{12}\text{Cl}_4 + 16 \text{ NaCl}$$

with + 12 Napz shown above the left side.
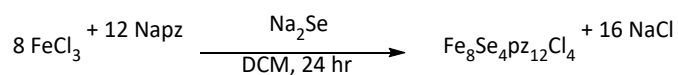
Scheme 4.20: The synthesis of $\text{Fe}_8\text{Se}_4(\text{pz})_{12}\text{Cl}_4$.

^{1}H NMR analysis of the product of this reaction showed the characteristic 3 paramagnetically shifted signals for the pyrazolate backbone, with some other signals observed.
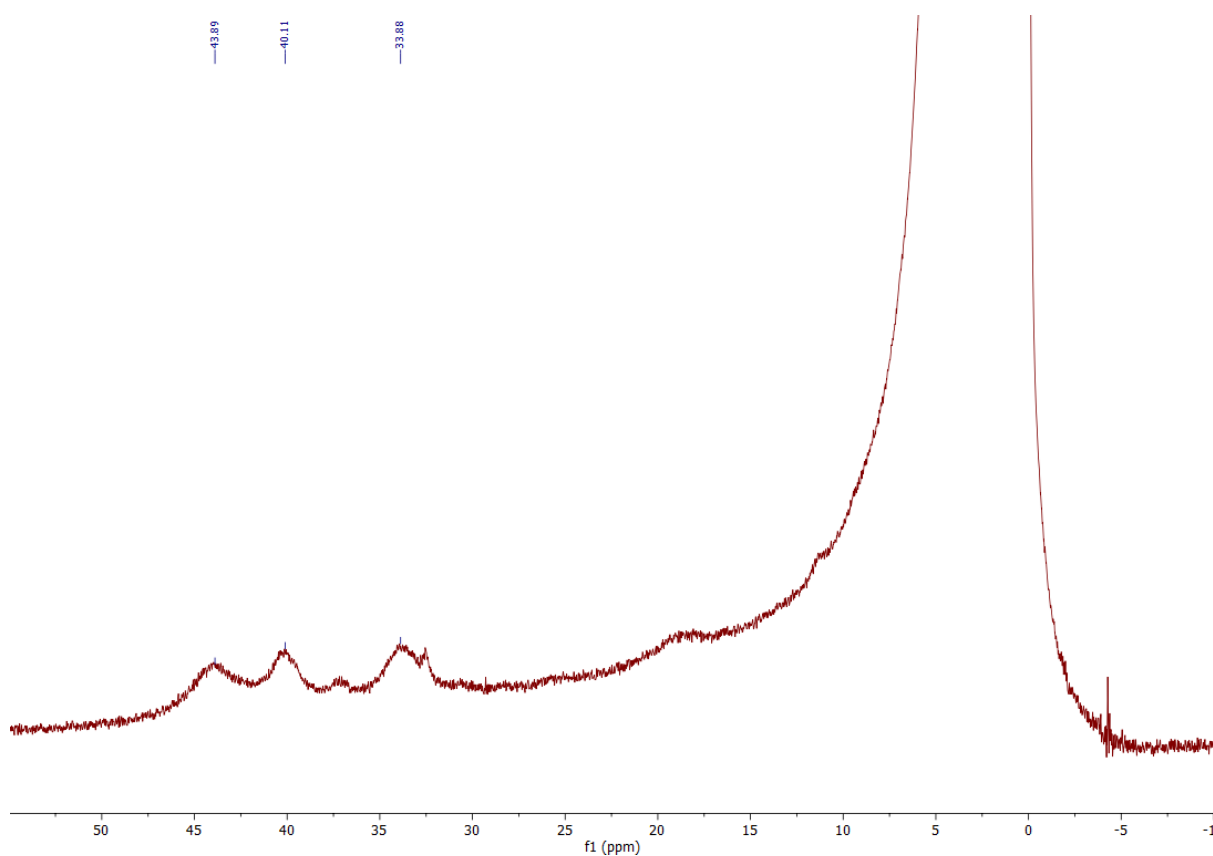
Figure 4.11: *In situ* ^{1}H NMR spectrum of $\text{Fe}_8\text{Se}_4(\text{pz})_{12}\text{Cl}_4$.

Exposure of a sample of this product to air showed the same decomposition to **25** as observed for the sulphur analogue, along with deposition of red elemental selenium of the walls of the vessel. Attempts to crystallise this product were unsuccessful.

After having synthesised a library of [Fe$_8$S$_4$] clusters, their reactivity to organic nucleophiles was trialled with the aim to substitute the terminal chlorides on each pendant iron atom with an organic moiety. The trio of pyrazolate ligands binding to each of these iron atoms in addition to the sulphur bond were predicted to stabilise the structure upon attack by the nucleophile, in contrast to the observed reactivity of the simpler iron-sulphur halide clusters. The coverage of the pyrazolate is also likely to shield the [Fe$_4$S$_4$] core.

Firstly, the oxo cluster was reacted with PhMgBr, but ^{1}H NMR analysis of the reaction mixture showed no functionalisation, even when the harsher reagent PhLi was used.
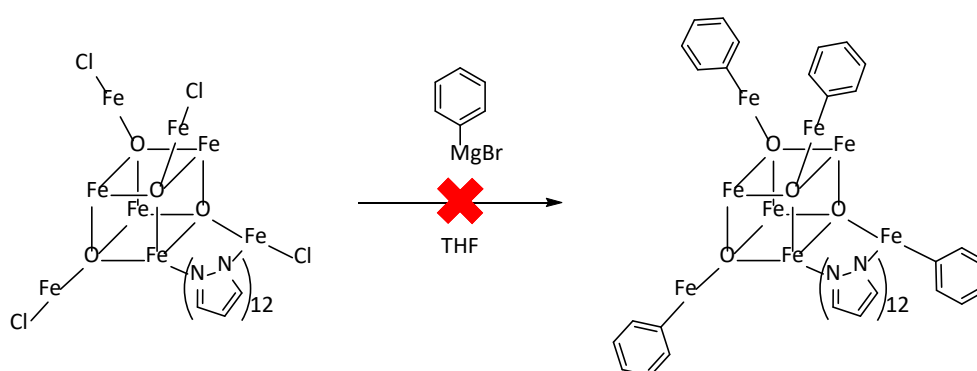
Scheme 4.21: The attempted functionalisation of Fe$_8$O$_4$(pz)$_{12}$Cl$_4$ with PhMgBr.

Conversely, ^{1}H analysis of the reaction of **26** with PhLi showed depletion of signals for **26**, indicating that activation of the cubane core is occurring. The product of this activation appears, however, to be decomposing immediately upon formation. Having observed similar reactivity for other iron-phenyl complexes such as the homoleptic ferrates, this was perhaps not surprising. When PhLi was substituted with XylLi, a new set of signals were observed.
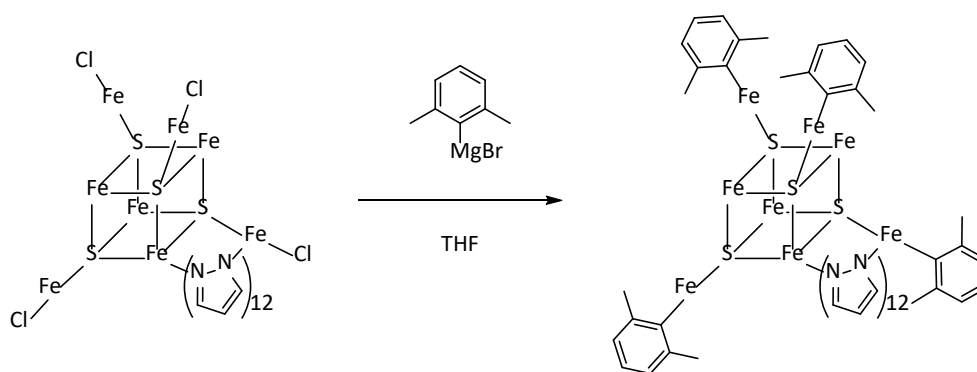
Scheme 4.22: The functionalisation of $Fe_8S_4(pz)_{12}Cl_4$ with XylLi.
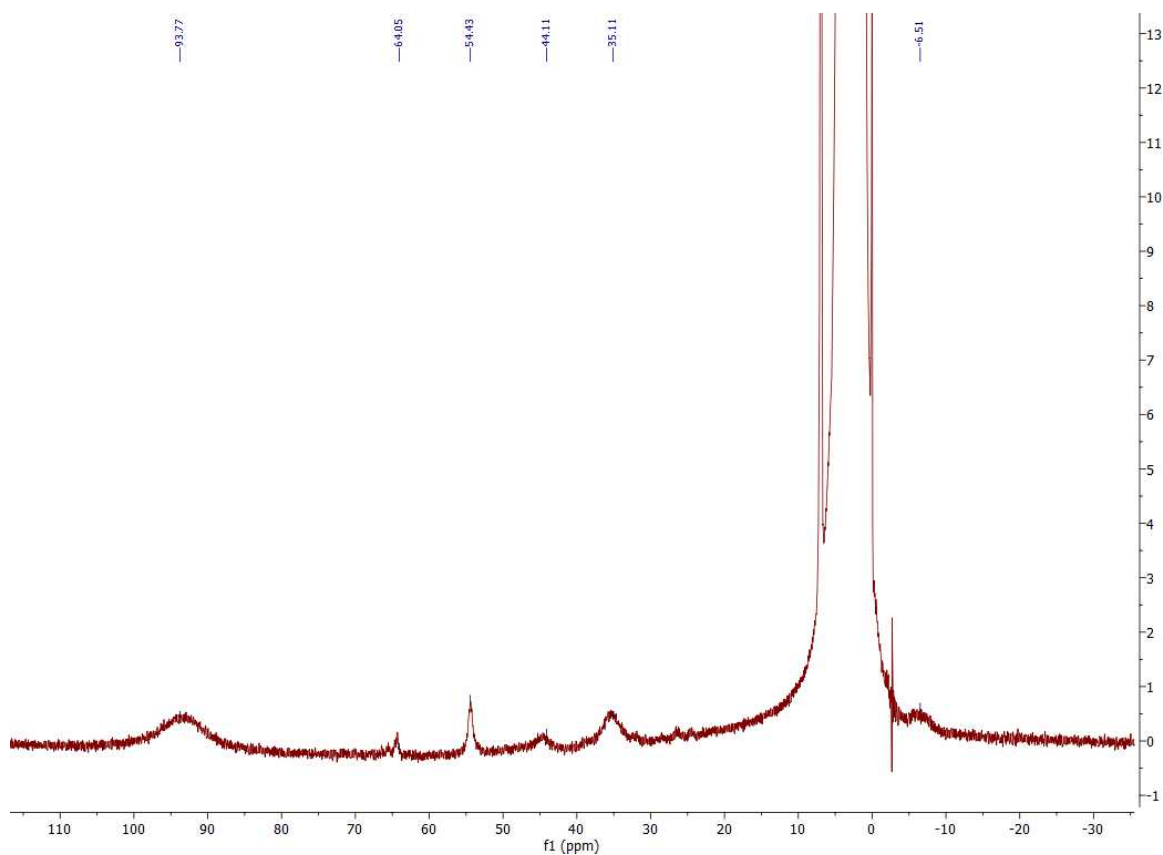
Figure 4.12: *In situ* ^1H NMR of the reaction of XylLi with $Fe_8S_4(pz)_{12}Cl_4$.

The shifting of known signals for the pyrazolate, along with new signals appearing, appears to indicate that functionalisation of the terminal iron atoms has occurred, to form a stable product. Encouraged by this result, further reactions were performed with a range of organolithium reagents and with substituted pyrazole ligands.

Interestingly, of the pyrazolate ligands used, the only species not amenable to functionalisation were those bearing 4-Br-pz. In this case, the starting material was decomposed by reaction with XylLi. Potentially, the more electron withdrawing character of the bromide substituent has a destabilising effect on the ligand environment of the terminal iron atoms, preventing the formation of a stable organometallic product. As well as aryl nucleophiles, reaction was also accomplished using the alkynic nucleophile lithium (p-tolyl)acetylide, forming a stable product only if the nucleophile loading was strictly controlled to not be excess with respect to distal iron atoms. Unfortunately, the extreme sensitivity of these complexes, along with their high solubility in all tested solvents prevented their characterisation by X-ray Diffraction.

4.6 - Cobalt and Manganese Pyrazolate Clusters

While iron-sulphur clusters have extensive presence in biological systems, there is also academic interest in sulphur clusters incorporating other first-row transition metals such as manganese and cobalt. Notably, a manganese-oxide cluster is used in Photosystem II, a key cofactor in the biological oxidation of water.[156,157]

In 2018, Raptis and co-workers published the structure of an octanuclear manganese oxo-pyrazolate cluster, $Mn^{III}_8(\mu_3-O)_4(\mu-pz)_8(\mu-OMe)_4(OMe)_4$ (**27**).[158] Despite the similarity in component moieties, the structure differs considerably from that of **25**; alongside O-atoms incorporated from atmospheric O_2, deprotonated MeOH moieties are also incorporated from the reaction solvent. Additionally, while **25** is formed without oxidation of the iron, formation of **27** proceeds *via* an oxidation from Mn^{II} to Mn^{III} by O_2.

To adapt this synthesis to a sulphur analogue, S_8 was therefore used as the sulphur source.

$$8 \text{ Mn(OAc)}_2 \xrightarrow[\text{MeOH, 24 hr}]{+ 8 \text{ Napz} \quad S_8} \text{[Cluster]}$$
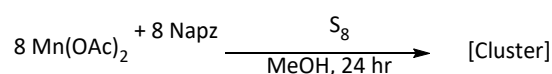
Scheme 4.23: The attempted synthesis of a manganese-sulphur cluster.

Addition of solid S_8 to a stirred suspension of Mn(OAc)$_2$ and Napz induced an instantaneous darkening of the solution from a pale beige to dark brown. Analysis of the reaction mixture by ^{1}H NMR showed only 2 signals for paramagnetic species, indicating a symmetrical structure with respect to the pyrazolate moiety.
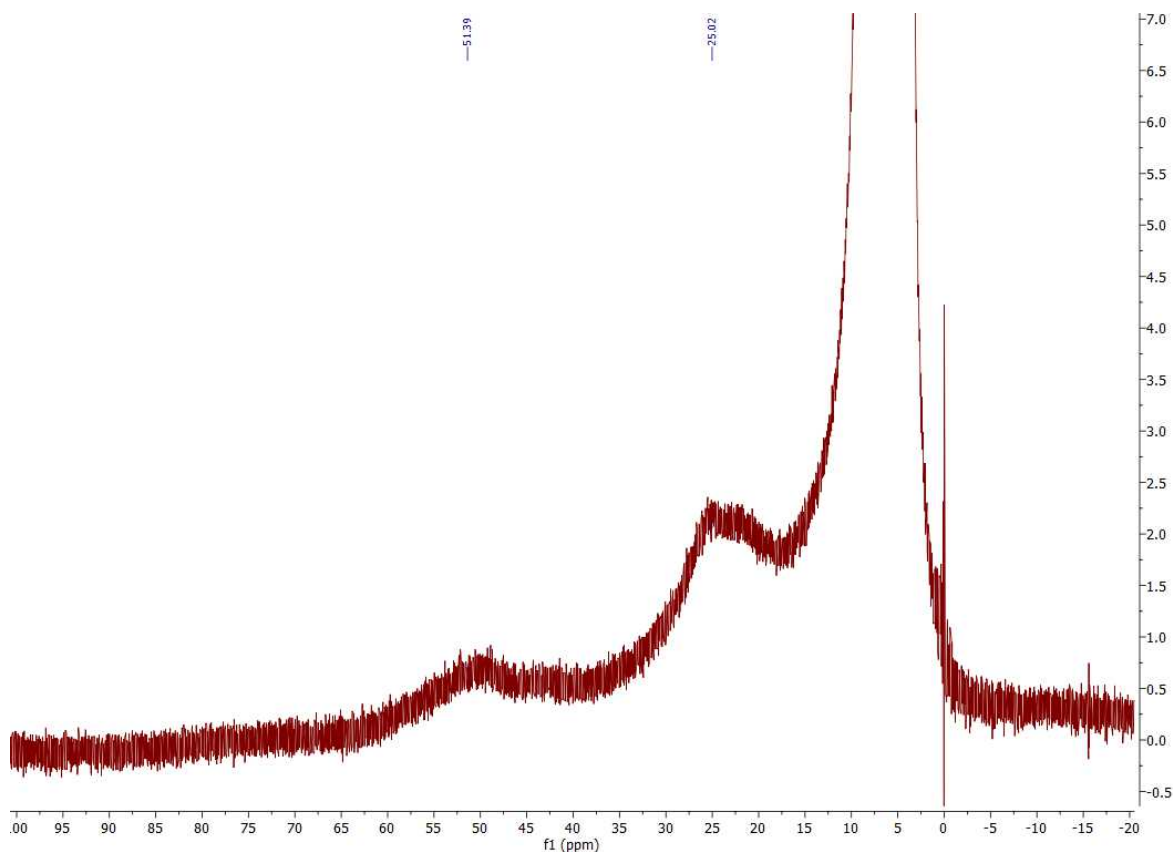
Scheme 4.24: ^{1}H NMR spectrum of a proposed manganese-sulphur cluster.

The same signals were observed for a range of Mn sources (MnCl$_2$ and Mn(OAc)$_2$) , solvents (DCM, THF, MeOH), and sulphur sources (S$_8$ and S(SiMe$_3$)$_2$) . It is likely, therefore, that this species is a linear chain of Mn^{II} atoms bridged by pz groups, and sulphur is not coordinated at all.
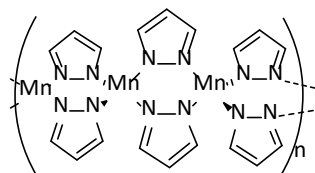
Figure 4.13: A proposed structure for the product of the reaction of $MnCl_2$ with S_8.

However, if instead of unsubstituted pyrazolate, the 3,5-methyl analogue was used, a new complex was observed. In this case, ^{1}H NMR analysis showed 3 new signals in regions indicative of a paramagnetic product, characteristic of an asymmetrically substituted pyrazolate complex being formed.
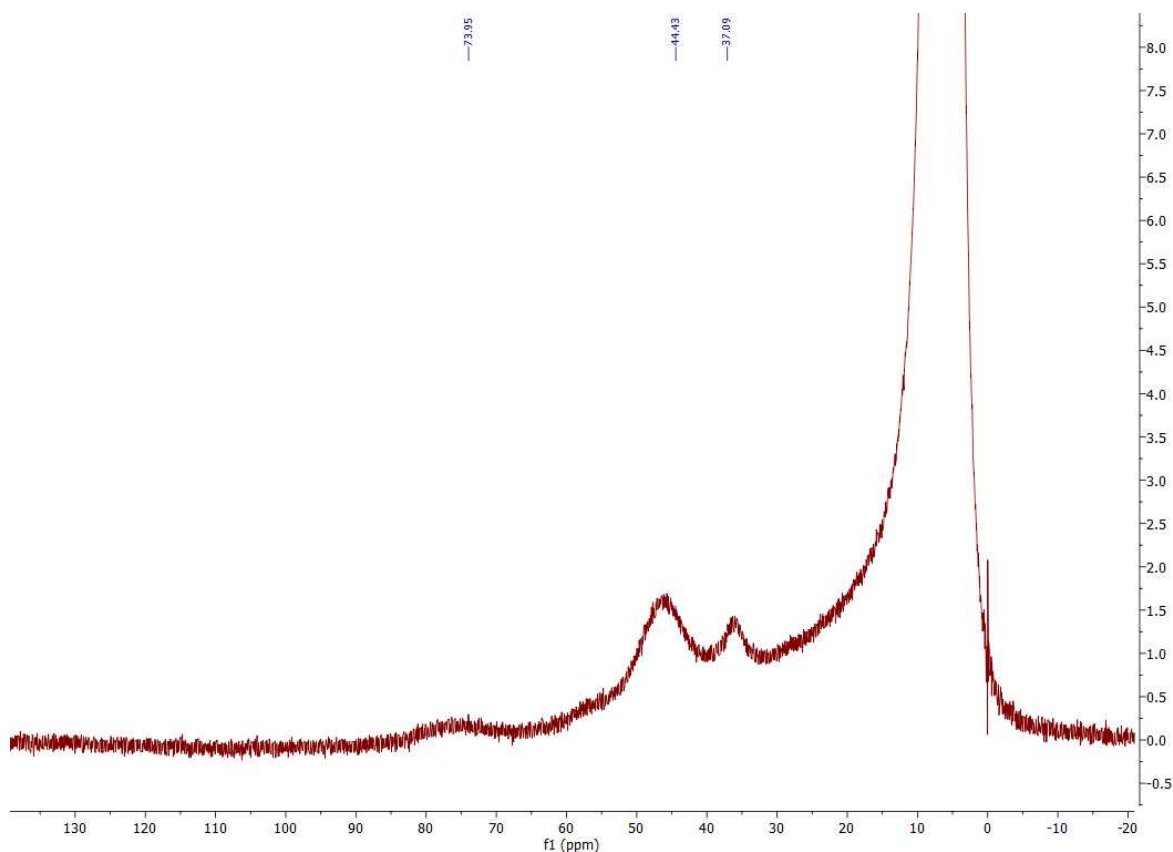
Scheme 4.25: ^{1}H NMR spectrum of a proposed manganese-3,5-dimethylpyrazole species.

Unfortunately, these complexes could not be isolated cleanly in order to perform further characterisation and determine their structures.

As with manganese, there are several reports of multinuclear complexes of cobalt with pyrazolate ligands. In 1993, Trotter and co-workers reported a range of Co-(3,5-Me-pz) complexes synthesised by reaction of $CoCO_3$ under air with the protonated pyrazole.[159]
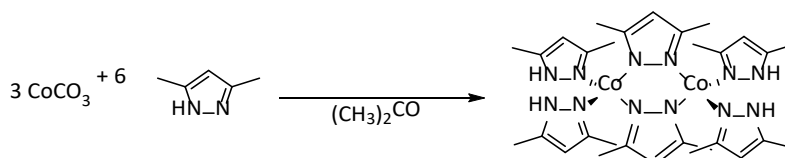
Scheme 4.26: A di-nuclear Co-pz complex reported by Trotter *et al*.[159]

Alongside the di-nuclear complex pictured above, they also reported tri- and mono-nuclear complexes of a similar form.

Another series of cobalt-pyrazole complexes was reported by Yuge and co-workers, showing sequential substituting of pyrazolate ligands from a cobalt-acetate complex, giving a series a of complexes of the general form $[Co_3O(\mu\text{-}OAc)_{6-n}(\mu\text{-}pz)_n(pzH)_3]^+$ in which n = 1 – 4.[160] Interestingly, the group did not report any complex that does not include acetate ligands alongside pyrazolate.
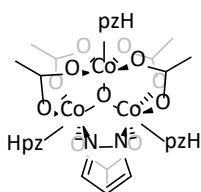
Figure 4.14: One of the series of Co-pz complexes reported by Yuge and co-workers.[160]

As with previous examples, the production of a cobalt-sulphur complex was targeted by addition of S_8 to a stirred suspension $CoCl_2$ with the pyrazolate salt.
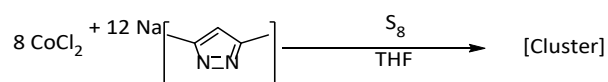
Scheme 4.27: The attempted synthesis of a cobalt-sulphur cluster.

Analysis of the reaction mixture by ^{1}H NMR showed a high number of signals at low intensity between approximately -10 and 70 ppm, indicating a range of products being formed. Potentially this could be a range of oligomers analogous to those observed in Trotter's work.[159]
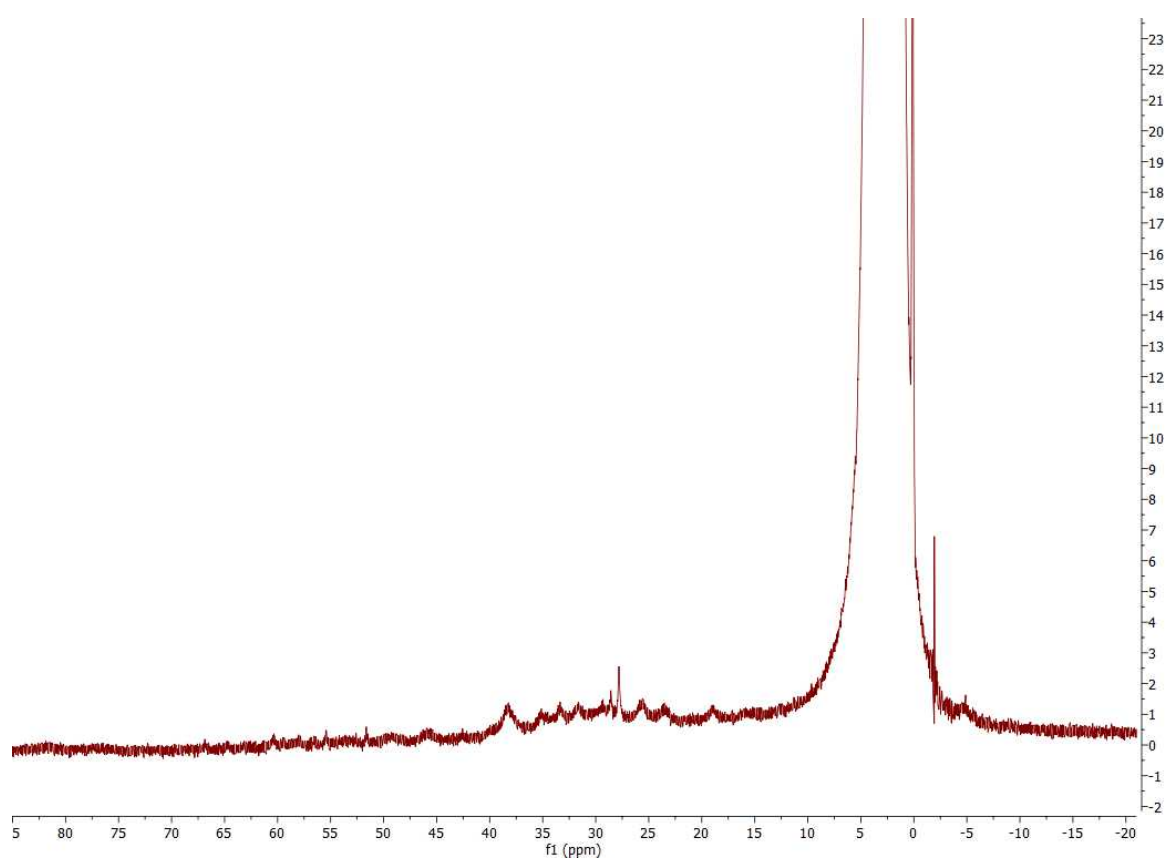
Figure 4.15: ^{1}H NMR spectrum of the reaction of CoCl$_2$ with Napz and S$_8$.

4.7 – Conclusions and Future Work

A range of complexes with potential relevance to the necessity of cooperative metal effects in catalytic reduction of N_2 have been synthesised.

A range of ferrocenyl-phosphine ligated iron complexes have been synthesised and characterised crystallographically. The Fe^{II} complexes synthesised preferentially formed 4-coordinate complexes, even with an excess of ligand present. Reduction of these complexes with KC_8 under an atmosphere of N_2 did not facilitate formation of an Fe^0-N_2 complex, but instead led to reduction of the ferrocenyl ligands to give the potassium salt of the Cp ligand. Attempts to synthesise cobaltocenyl phosphine analogues of commercially available ferrocenyl phosphine ligands were unsuccessful.

A series of iron-sulphur complexes were synthesised and functionalised with sp^2 and sp^3 nucleophiles, as evidenced by ^1H NMR, although none were characterised crystallographically.

^1H NMR evidence was also collected for the formation of multinuclear manganese and cobalt pyrazolate complexes, with two different manganese structures observed depending on the identity of the pyrazolate ligand used. ^1H NMR analysis of the reaction of cobalt sources with pyrazolate salts gave evidence of the formation of a range of oligomers.

A great deal of useful data could be gained from an electrochemical investigation of the complexes synthesised in this work. In the case of the metallocenyl-phosphine complexes, determination of their reduction potentials could aid with identification of an appropriate reductant to synthesise the N_2 analogues by a reductive route. Cyclic voltammetry would also aid with the structural determination of the species observed by ^1H NMR that were assigned as clusters. By determining the number of redox events accessible, this could aid in finding a minimum for the number of metal centres in each of their structures.

5. Chapter 5 - Experimental

5.1 – General Experimental Procedures

All reactions were carried out under N_2 atmosphere using standard Schlenk-line techniques or in an argon-filled glovebox, unless otherwise stated. THF, DCM, hexane, toluene and Et2O were obtained from an Anhydrous Engineering double alumina column drying system, stored over 3 Å molecular sieves and degassed prior to use. Other dry solvents were dried over 3 Å molecular sieves for at least 48 hours prior to use. Commercial grade solvents were used for chromatography and work-up procedures. Reagents purchased from commercial suppliers were used without further purification unless specifically stated. Column chromatography was conducted using technical grade silica gel (pore size 60 Å, 230-400 mesh particle size), or where stated, alumina (~ 150 mesh particle size).

NMR spectra were recorded on Bruker Nano 400 or Varian 500 spectrometers. Chemical shifts ($δ$) are quoted in parts per million (ppm), referenced to the residual solvent peak and coupling constants (J) are given in Hz. Multiplicities are abbreviated as: br (broad), s (singlet), d (doublet), t (triplet), q (quartet), m (multiplet) or combinations thereof.

X-ray crystal structure determination was carried out on either a Bruker Microstar or APEX II diffractometer, by Dr. Roberto Nolla Saltiel, Dr Sanita Tailor, Dr Natalie Pridmore, or Dr. Hazel Sparkes. Data collections were performed using a CCD area detector from a single crystal mounted on a glass fibre. Intensities were integrated from several series of exposures measuring 0.5° in ω or ϕ. Absorption corrections were based on equivalent reflections using SADABS. The structures were solved using SHELXS and refined against all Fo2 data with hydrogen atoms riding in calculated positions using SHELXL

5.2 – Experimental Details for Chapter 2

5.2.1 – Synthetic Procedures for Organometallic Iron Complexes

Fe$_2$Mes$_4$ (6)
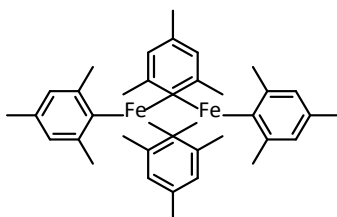
FeCl$_2$ (630 mg, 5 mmol) was suspended in THF (25 mL) and 1,4-dioxane (4 mL) and cooled to -40 °C. MesMgBr (10 mL, 10 mmol, 1.0 M solution in THF) was added gradually over the course of 5 minutes with stirring. The solution was then allowed to warm to room temperature and stirred for 4 h, forming a deep red solution with a tan precipitate. The precipitate was then removed *via* cannula filtration and the volatiles removed *in vacuo*. The red residue was then extracted with Et$_2$O (3 x 5 mL) and the filtrate cooled to -30 °C overnight to give the product as red blocks (215 mg, 3.72 mmol, 74.4%)

^{1}H NMR (400 MHz, THF) δ 106.9 (2H), 82.5 (3H), 58.5 (6H).

[FeMes$_3$][MgBr(THF)$_6$] (7[MgBr(THF)$_6$])
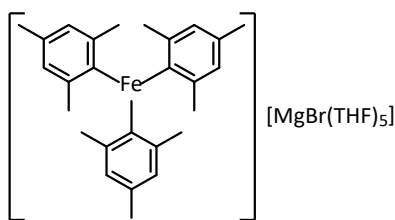
FeCl$_2$ (250 mg, 2 mmol) was suspended in THF (5 mL), and cooled to 0 °C, MesMgBr (8 mL, 8 mmol, 1.0 M solution in THF) was added gradually over the course of 5 minutes before the solution was allowed to warm to room temperature and stirred for 1 h. The solution was then filtered *via* cannula, layered with Et$_2$O (15 mL) and cooled to -30 °C overnight to give the product as colourless needles. (1.05 g, 1.21 mmol, 60.7%)

^{1}H NMR (400 MHz, THF) δ 116.1 (2H), 94.1 (3H), 70.0 (6H)

[FeBrMes₂]₂[Mg(THF)₆] (8[Mg(THF)₆])
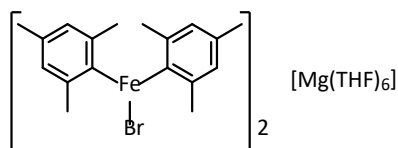
Fe$_2$Mes$_4$ (147 mg, 0.25 mmol) was suspended in THF (5 mL) and MgBr$_2$ (12.5 mL, 1.25 mmol, 0.1 M solution in THF) was added. The solution was stirred for 1 h, forming a beige solution which was reduced by half *in vacuo*, the solution layered with HMDSO (10 mL) and cooled to -30 °C for 48 hours to give the product as pale yellow blocks suitable for X-ray.

^{1}H NMR (400 MHz, THF) δ 117 (1H), 93 (2H), 61 (3H)

5.2.2 – Speciation Study Procedures

Speciation studies with Fe₂Mes₄

Under an atmosphere of Argon, screw-top vials were loaded with Fe$_2$Mes$_4$ (100 µl, 85 mM stock solution in THF) and the required volume of stock solution of MgBr$_2$, ZnBr$_2$, ^{n}BuBpin, ^{t}BuBPin, or FeBr$_2$ according to the tables below and then topped up with THF in order to bring the reaction volume to 1 ml. An aliquot was then transferred to a J. Youngs NMR tube and analysed by NMR spectroscopy.

MgBr$_2$ (100 mM stock solution in THF)
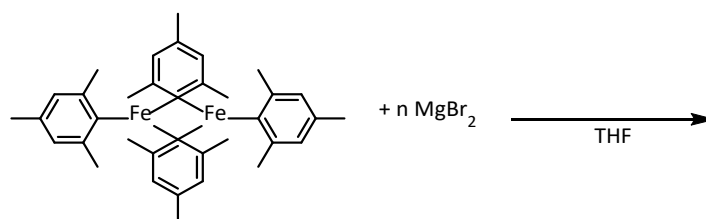
Entry	Mg:Fe	µmol	µl
a	0.125	2.1	21
b	0.250	4.2	42
c	0.375	6.3	63
d	0.500	8.4	84
e	0.625	10.6	106
f	1.25	21.2	212
g	2.50	42.5	425
h	5.00	84.9	849

ZnBr$_2$ (500 mM stock solution in THF)
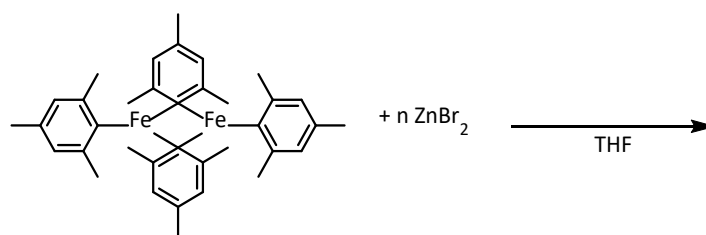
Entry	Zn:Fe	μmol	μl
a	0.125	2.1	4.2
b	0.250	4.2	8.5
c	0.375	6.3	12.7
d	0.500	8.4	17.0
e	0.625	10.6	21.2
f	1.25	21.2	42.5
g	2.50	42.5	85.0
h	5.00	84.9	170
i	10.0	212	425
j	25.0	424	850

FeBr₂ (40 mM stock solution in THF)
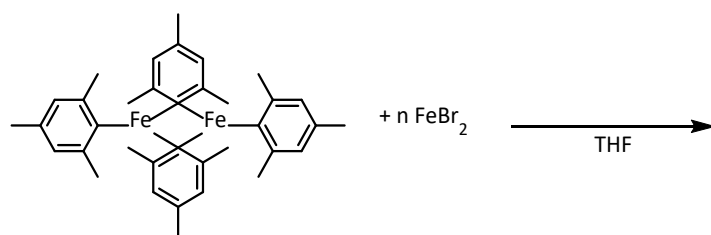
Entry	Br:Mes	μmol	μl
a	0.125	2.1	52.5
b	0.250	4.2	105.0
c	0.375	6.3	157.5
d	0.500	8.4	210.0
e	0.625	10.6	265.0
f	0.750	12.8	319.0
g	0.875	14.9	351.0
h	1.000	17.0	425
i	1.125	19.1	478
j	1.250	21.2	530

^{n}BuBPin (500 mM stock solution in THF)
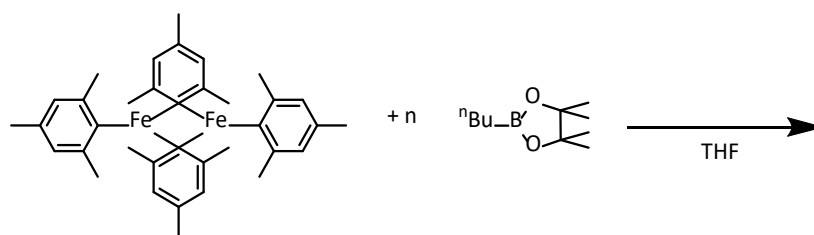
Entry	B:Fe	μmol	μl
a	0.125	2.1	4.2
b	0.250	4.2	8.5
c	0.375	6.3	12.7
d	0.500	8.4	17.0
e	0.625	10.6	21.2
f	1.25	21.2	42.5
g	2.50	42.5	85.0
h	5.00	84.9	170
i	10.0	212	425
j	25.0	424	850

Speciation studies with [FeMes₃]⁻

Under an atmosphere of Argon, screw-top vials were loaded with [FeMes₃]⁻ (200 µl, 21.25 mM stock solution in THF) and the required volume of stock solution of $MgBr_2$ or $FeBr_2$ according to the tables below and then topped up with THF in order to bring the reaction volume to 1.2 ml. An aliquot was then transferred to a J. Youngs NMR tube and analysed by NMR spectroscopy.

MgBr₂ (100 mM stock solution in THF)
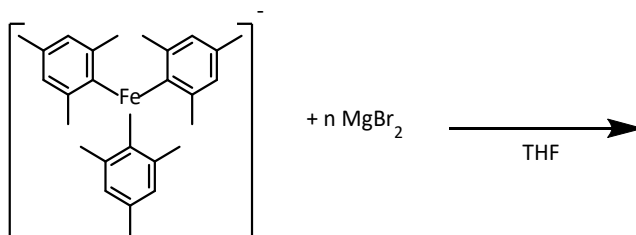
Entry	Mg:Fe	µmol	µl
a	0.125	2.1	21
b	0.250	4.2	42
c	0.500	6.3	63
d	0.750	12.8	128
e	1.000	17.0	170
f	1.250	21.2	212
g	2.500	42.5	425
h	5.000	85.0	850

FeBr₂ (40 mM stock solution in THF)

+ n FeBr₂ → (THF)
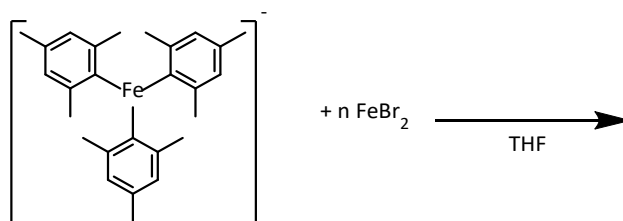
Entry	FeBr₂:[FeMes₃]⁻	μmol	μl
a	0.125	2.1	52.5
b	0.250	4.2	105
c	0.375	6.3	158
d	0.500	8.4	210
e	0.625	10.6	265
f	0.750	14.9	350
g	1.000	17.0	425
h	1.125	19.1	478
i	1.250	21.2	530
j	1.500	25.4	636

5.3 – Experimental Details for Chapter 3

5.3.1 – Catalytic Reactions

FeBr₂-catalysed cross-coupling of NaphMgBr and CyBr
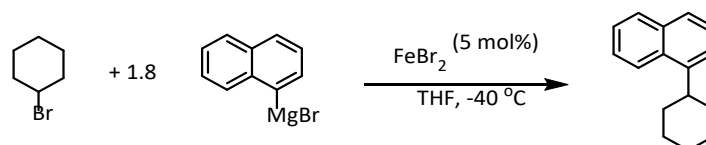
A jacketed Schlenk flask with internal cooling coil was loaded with NaphMgBr (10 ml, 1.8 mmol, 0.18 M in THF), n-dodecane (0.5 ml, 0.5 mmol, 1 M in THF), and CyBr (1 ml, 1 mmol, 1 M in THF). The solution was then cooled to -20 °C with a Julabo F81-ME cryostat. Reaction was initiated by addition of FeBr₂ (1.25 ml, 0.05 mmol, 0.040 M in THF). Progress of the reaction was monitored by GC-FID.

FeBr₂-catalysed cross-coupling of NaphMgBr and CyBr
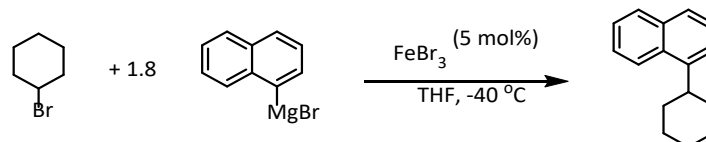
A jacketed Schlenk flask with internal cooling coil was loaded with NaphMgBr (10 ml, 1.8 mmol, 0.18 M in THF), n-dodecane (0.5 ml, 0.5 mmol, 1 M in THF), and CyBr (1 ml, 1 mmol, 1 M in THF). The solution was then cooled to -20 °C with a Julabo F81-ME cryostat. Reaction was initiated by addition of FeBr₃ (0.5 ml, 0.05 mmol, 0.1 M in THF). Progress of the reaction was monitored by GC-FID.

Radical clock test
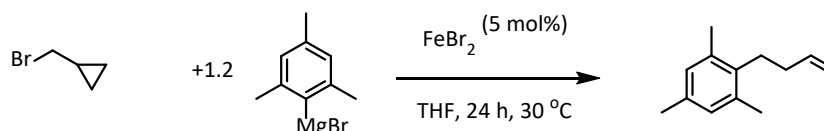
A Schlenk flask was loaded with THF (2 mL), MesMgBr (1.2 mL, 1.2 mmol, 1 M in THF), and (bromomethyl)cyclopropane (0.1 mL, 1 mmol) and warmed to 30 °C. FeBr₂ (1.25 mL, 0.05

mmol, 40 mM in THF) was then added and the solution was stirred overnight. The solution was then quenched with 1 M aqueous HCl, extracted with DCM (3 x 20 mL) and volatiles removed *in vacuo*. The crude was then analysed by ^{1}H NMR spectroscopy relative to a 1,3,5-trimethoxybenzene standard. (1.2

^{1}H NMR (400 MHz, CDCl$_3$) δ 6.76 (s, 2H), 5.92-5.79 (m, 1H), 5.06-4.88 (m, 2H), 2.65-2.54 (m, 2H), 2.15-2.06 (m, 2H)

Signals in agreement with literature values.[124]

5.3.2 – Stoichiometric Reactions

General Procedure for reaction monitoring of iron-mediated Kumada cross-coupling of MesMgBr and OctBr

All reaction components were added before being made up with THF such that total volume was 15 mL. Samples were taken at appropriate intervals by drawing aliquots (0.1 mL) from the reaction solution and quenching in a vial pre-loaded with 1 M aqueous HCl (approximately 1 mL) and diluting with DCM (1 mL). Quantities of MesOct, Mes$_2$, OctBr, and MesH were quantified by a pre-calibrated GC-FID relative to a dodecane standard.

FeBr$_2$-catalysed cross-coupling of MesMgBr and OctBr
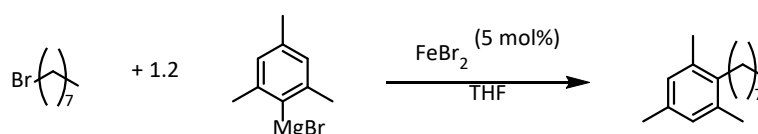
A Schlenk flask was loaded with THF (11.2 mL), MesMgBr (1.1 mL, 1.2 mmol, 1.1 M solution in THF), OctBr (1 mL, 1 mmol, 1 M solution in THF), and dodecane (0.5 mL, 0.5 mmol, 1 M solution in THF) and warmed to 30 °C in an oil bath. The reaction was initiated by addition of FeBr$_2$ (1.25 mL, 0.05 mmol, 0.04 M solution in THF).

Equimolar reaction of [FeMes₃]⁻ with OctBr
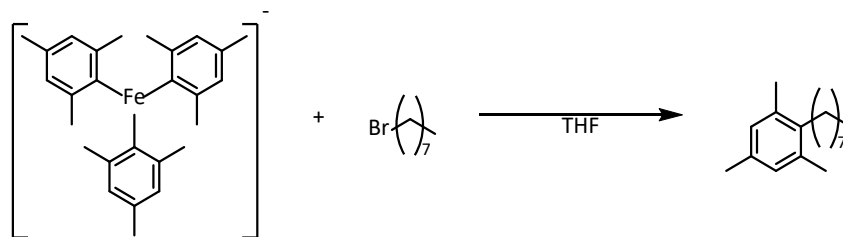
A Schlenk flask was loaded with FeBr$_2$ (107 mg, 0.5 mmol), THF (12.5 mL) Dodecane (0.5 mL, 0.5 mmol, 1 M in THF), and MesMgBr (1.5 mL, 1.5 mmol, 1 M in THF) and stirred for 30 minutes at 30 °C. OctBr (0.5 mL, 0.5 mmol, 1 M in THF) was then added in one portion. Progress of the reaction was monitored by GC-FID.

Reaction of [FeMes₃]⁻ with excess OctBr

A Schlenk flask was loaded with FeBr$_2$ (107 mg, 0.5 mmol), THF (11.3 mL) Dodecane (0.5 mL, 0.5 mmol, 1 M in THF), and MesMgBr (1.5 mL, 1.5 mmol, 1 M in THF) and stirred for 30 minutes at 30 °C. OctBr (1.73 mL, 10 mmol) was then added in one portion. Progress of the reaction was monitored by GC-FID.

Reaction of [FeBrMes₂]⁻ with OctBr
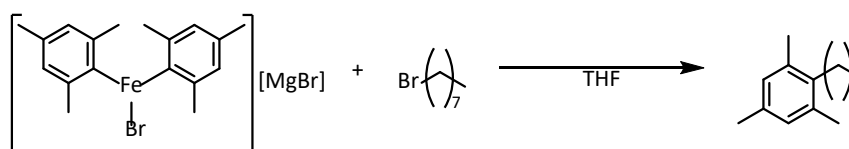
A Schlenk flask was loaded with FeBr$_2$ (107 mg, 0.5 mmol), THF (11.3 mL) Dodecane (0.5 mL, 0.5 mmol, 1 M in THF), and MesMgBr (1.0 mL, 1.0 mmol, 1 M in THF) and stirred for 30 minutes at 30 °C. OctBr (0.5 mL, 0.5 mmol, 1 M in THF) was then added in one portion. Progress of the reaction was monitored by GC-FID.

Reaction of [FeBrMes₂]⁻ with excess OctBr
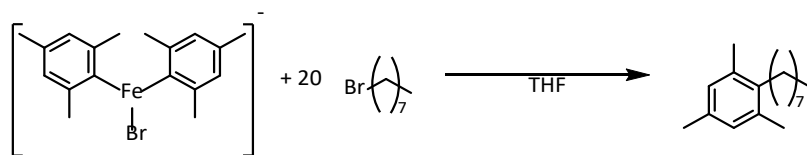
A Schlenk flask was loaded with $FeBr_2$ (107 mg, 0.5 mmol), THF (11.3 mL), dodecane (0.5 mL, 0.5 mmol, 1 M in THF), and MesMgBr (1.0 mL, 1.0 mmol, 1 M in THF) and stirred for 30 minutes at 30 °C. OctBr (1.73 mL, 10 mmol) was then added in one portion. Progress of the reaction was monitored by GC-FID.

Equimolar reaction of [FeBr₂Mes][Li] with OctBr
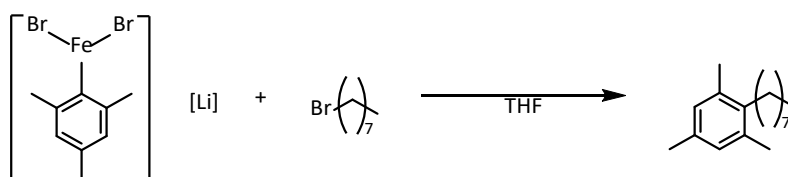
A Schlenk flask was loaded with $FeBr_2$ (107 mg, 0.5 mmol), MesLi (63.5 mg, 0.5 mmol) THF (14.0 mL), and dodecane (0.5 mL, 0.5 mmol, 1 M in THF) and stirred for 30 minutes at 30 °C. OctBr (0.5 mL, 0.5 mmol, 1 M in THF) was then added in one portion. Progress of the reaction was monitored by GC-FID.

Reaction of [FeBr₂Mes][Li] with excess OctBr
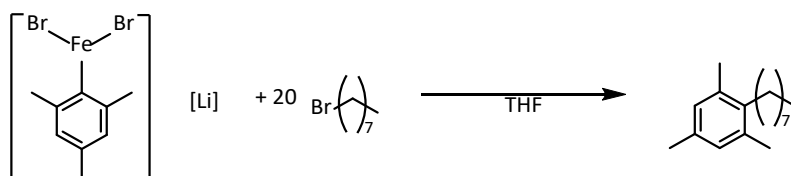
A Schlenk flask was loaded with $FeBr_2$ (107 mg, 0.5 mmol), MesLi (63.5 mg, 0.5 mmol) THF (12.8 mL), and dodecane (0.5 mL, 0.5 mmol, 1 M in THF) and stirred for 30 minutes at 30 °C. OctBr (1.73 mL, 10 mmol) was then added in one portion. Progress of the reaction was monitored by GC-FID.

Equimolar reaction of [FeBr$_2$Mes][Li(12c4)$_2$] with OctBr
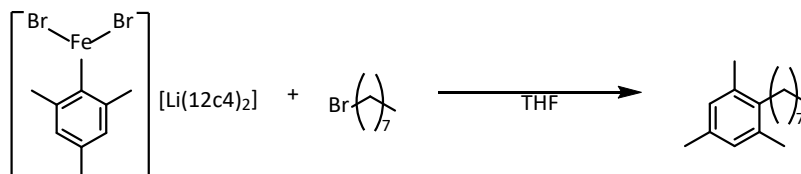
A Schlenk flask was loaded with FeBr$_2$ (107 mg, 0.5 mmol), MesLi (63.5 mg, 0.5 mmol) THF (13.8 mL), 12-crown-4 (0.2 mL, 1 mmol) and dodecane (0.5 mL, 0.5 mmol, 1 M in THF) and stirred for 30 minutes at 30 °C. OctBr (0.5 mL, 0.5 mmol, 1 M in THF) was then added in one portion. Progress of the reaction was monitored by GC-FID.

Equimolar reaction of Fe$_2$Mes$_4$ with OctBr
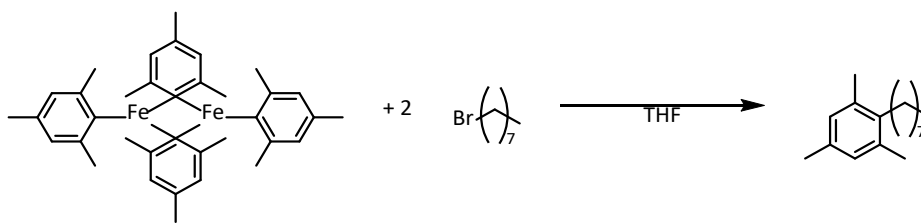
A Schlenk flask was loaded with Fe$_2$Mes$_4$ (147 mg, 0.25 mmol), THF (14 mL), and dodecane (0.5 mL, 0.5 mmol, 1 M in THF) and stirred for 30 minutes at 30 °C. OctBr (0.5 mL, 0.5 mmol, 1 M in THF) was then added in one portion. Progress of the reaction was monitored by GC-FID.

Reaction of Fe$_2$Mes$_4$ with excess OctBr
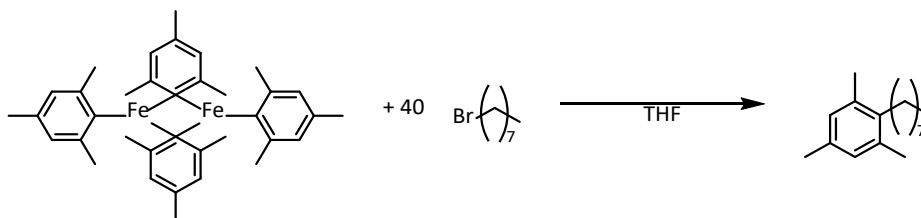
A Schlenk flask was loaded with Fe$_2$Mes$_4$ (147 mg, 0.25 mmol), THF (12.8 mL), and dodecane (0.5 mL, 0.5 mmol, 1 M in THF) and stirred for 30 minutes at 30 °C. OctBr (1.73 mL, 10 mmol) was then added in one portion. Progress of the reaction was monitored by GC-FID.

Equimolar reaction of Fe$_2$Mes$_4$ with OctBr with MgBr$_2$ added.
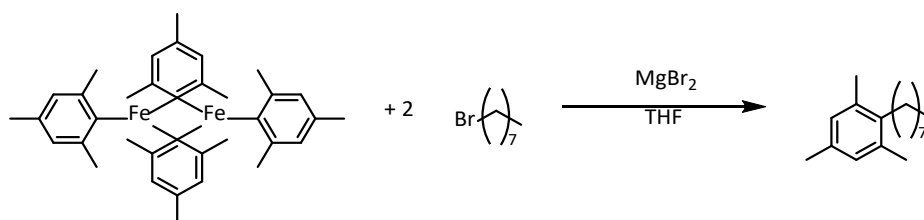
A Schlenk flask was loaded with Fe$_2$Mes$_4$ (147 mg, 0.25 mmol), THF (11.5 mL), MgBr$_2$ (2.5 mL, 0.25 mmol, 0.1 M in THF) and dodecane (0.5 mL, 0.5 mmol, 1 M in THF) and stirred for 30 minutes at 30 °C. OctBr (0.5 mL, 0.5 mmol, 1 M in THF) was then added in one portion. Progress of the reaction was monitored by GC-FID.

Oxidation of [FeMes$_3$]$^-$ with DBE
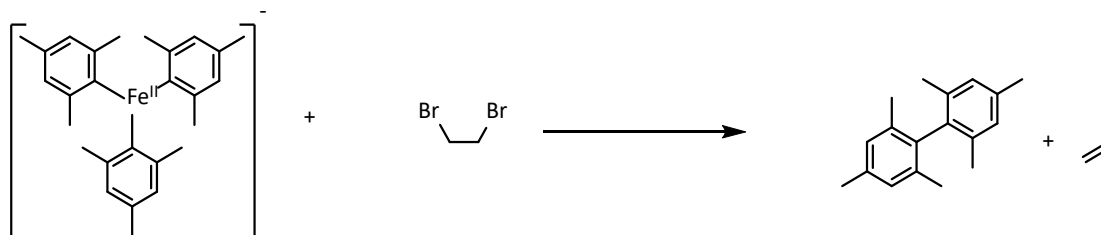
FeBr$_2$ (107 mg, 0.5 mmol) was suspended in THF (13 mL) and dodecane added (0.5 mL, 0.5 mmol, 1 M solution in THF). MesMgBr (1.25 mL, 1.5 mmol, 1.2 M solution in THF) was then added slowly and the solution stirred for 30 minutes. The required quantity of DBE (1 M solution in THF) was then added and stirring continued for 1 hour. A 0.1 mL aliquot was then removed before quenching in a vial pre-loaded 1 M aqueous HCl (approximately 1 mL) and diluting with DCM (1 mL). Quantity of Mes$_2$ was then determined by GC-FID relative to the dodecane standard.

Entry	DBE Loading	Yield of Mes$_2$ /%
a	0.25	26.9
b	0.50	53.8
c	1.0	90.9

[Fe₂Mes₃][BArᶠ]
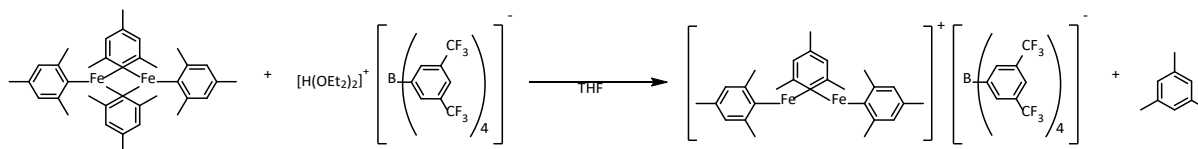
In separate Schlenk flasks, Fe_2Mes_4 (294 mg, 0.5 mmol) and $[H(OEt_2)_2][BAr^F]$ (507 mg, 0.5 mmol) were each suspended in THF (5 mL) and cooled to -40 °C in an acetonitrile/LN2 bath. $[H(OEt_2)_2][BAr^F]$ was added to Fe_2Mes_4 solution slowly *via* cannula. Once addition was completed, the solution was allowed to warm to room temperature. An aliquot was then analysed by ^1H NMR spectroscopy.

^1H NMR (400 MHz, THF) δ 36, 26, 13 ppm

Synthesis of [FeBr₂Mes][Li(12c4)₂] (17[Li(12c4)₂])
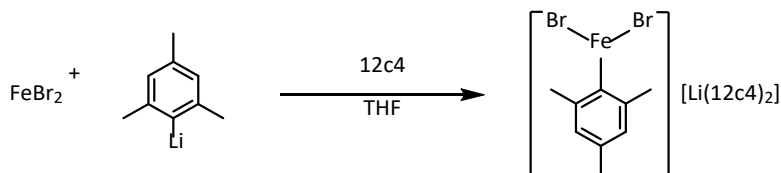
A Schlenk flask was loaded with $FeBr_2$ (215 mg, 1 mmol) and cooled to 0 °C in an ice bath. A solution of MesLi (126 mg, 1 mmol) in THF (5 mL) was added slowly *via* cannula with stirring before the solution was allowed to warm to room temperature, giving a dark brown solution. 12-crown-4 (0.3 mL, 2 mmol) was then added in one portion and stirring continued for a further 10 minutes. The solution was then filtered *via* cannula and the filtrate kept at 5 °C overnight to give the product as pale-yellow blocks suitable for X-ray diffraction.

^1H NMR (400 MHz, THF) δ 114.6 (1H), 90.6 (2H), 54.0 (3H)

5.4 – Experimental Details for Chapter 5

5.4.1 - Syntheses of iron-ferrocenyl-phosphine complexes.

FeCl$_2$(dppf) (19)
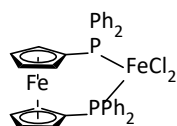
FeCl$_2$ (32 mg, 0.25 mmol, 1 equiv.) and dppf (278 mg, 0.5 mmol, 2 equiv.) were suspended in toluene 20 mL and warmed at 50 ^{O}C for 16 hours with stirring. The solution was then filtered and the filtrate layered with hexane (20 mL) to give the product as orange blocky crystals that were analysed by X-ray diffraction. (150 mg, 0.21 mmol, 87.7%)

No signals were observed corresponding to the product by ^{1}H or ^{31}P NMR spectroscopies.

FeCl$_2$(dippf) (20)
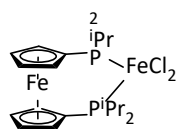
FeCl$_2$ (32 mg, 0.25 mmol, 1 equiv.) and dippf (210 mg, 0.5 mmol, 2 equiv.) were suspended in toluene 20 mL and warmed at 50 ^{O}C for 16 hours with stirring. The solution was then filtered, and the filtrate layered with hexane (20 mL) to give the product as orange blocky crystals that were analysed by X-ray diffraction. (126 mg, 0.23 mmol, 91.9%)

^{1}H NMR (400 MHz, toluene) δ 75.1

ClP(NEt₂)₂

$$Et_2N \atop Et_2N \diagdown P-Cl$$

PCl₃ (1.3 mL, 15 mmol, 1 equiv.) was suspended in Et₂O (50 mL) and cooled to 0 °C in an ice bath. HNEt₂ (6,2 mL, 60 mmol, 4 equiv.) was added dropwise with rigorous stirring, forming copious white precipitate. After addition, the vessel was allowed to warm to room temperature and stirred overnight. The precipitate was removed by cannula filtration, and extracted with Et₂O (3 x 20 mL). Solvent was then removed *in vacuo*. Product formation was confirmed by ³¹P NMR then used without further purification.

³¹P NMR (122 MHz, chloroform) δ 147.9

1,1'-bis(dichlorophosphino)ferrocene
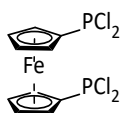
FcLi₂ (1.4 g, 7 mmol, 1 equiv.) was suspended in hexane (30 mL) and cooled to -40 °C in an LN2/acetonitrile bath. ClP(NEt₂)₂ was then added dropwise *via* cannula before being warmed to room temperature and stirred for 4 days. An aliquot was then analysed by ³¹P NMR to confirm formation of 1,1'-bis(di(diethylamino)phosphino)ferrocene *in situ*. HCl (40 mL, 80 mmol, 2 N solution in Et₂O) was then added gradually and stirring continued for a further 16 hours. Salts were then removed *via* cannula filtration and the solids washed with hexane (3 x 10 mL) before solvent was removed *in vacuo*, giving the product as a bright orange solid. (1.34 g, 3.45 mmol, 49.2% yield)

1,1'-bis(di(diethylamino)phosphino)ferrocene

³¹P NMR (122 MHz, hexane) δ 91.9

1,1'-bis(dichlorophosphino)ferrocene

³¹P NMR (122 MHz, hexane) δ 162.8

1,1'-bis(diethylphosphino)ferrocene (depf)
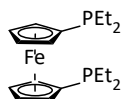
1,1'-bis(dichlorophosphino)ferrocene (500 mg, 1.3 mol, 1 equiv.) was suspended In Et_2O (15 mL) and cooled to 0 °C in an ice bath. EtMgBr (2.1 mL, 5.2 mmo, 4.1 equiv., 2.0 M solution in THF) was added dropwise and the reaction allowed to warm to room temperature and stirred for 3 hours. This was then quenched with nitrogen-sparged water (1 mL). Solvent was then removed *in vacuo* and the residue redissolved in toluene (25 mL) and filtered *via* cannula. Solvent was then once again removed *in vacuo*, leaving the product as an orange solid. (206 mg, 0.57 mmol, 43.7%)

^{31}P NMR (122 MHz, chloroform) δ -26.1

FeCl$_2$(depf) (21)
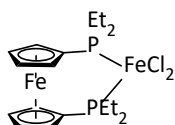
FeCl$_2$ (44 mg, 0.35 mmol, 1 equiv.) and depf (260 mg, 0.7 mmol, 2 equiv.) were suspended in toluene (10 mL) and warmed at 50 °C for 16 hours with stirring. The solution was then filtered, and the filtrate layered with hexane (20 mL) to give the product as large red blocks that were analysed by X-ray diffraction. (166 mg, 0.33 mmol, 95.4%)

FeBr$_2$(depf)
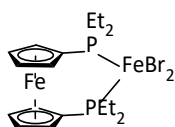
FeBr$_2$ (160 mg, 0.75 mmol, 1 equiv.) and depf (543 mg, 1.5 mmol, 2 equiv.) were suspended in toluene (20 mL) and warmed at 50 °C for 16 hours with stirring. The solution was then filtered, and the filtrate layered with hexane (20 mL) to give the product as large red blocks that were analysed by X-ray diffraction. (356 mg, 0.62 mmol, 82.6%)

[FeCl₄][NEt₄]

A flame-dried Schlenk was charged with $FeCl_3$ (1.62 g, 10 mmol) and Et_4NCl (1.22 g, 12.5 mmol) before being cooled to 0 °C. Anhydrous MeOH (25 ml) was added *via* cannula in one portion. The mixture was stirred for 2 h at 0 °C forming a pale-yellow precipitate which was collected by filtration, washed with anhydrous MeOH (2 x 10ml) and dried *in vacuo* (2.62 g, 80.1%).

5.4.2 – Synthesis of Metal-Chalcogenide Complexes

[Fe₂S₂Cl₄][NEt₄]₂ (22)
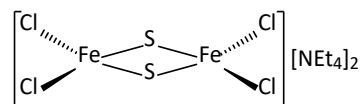
Adapted from a literature procedure.[161]

[FeCl₄][NEt₄] (2.60 g, 8.0 mmol) was suspended in THF (25 ml). $S(SiMe_3)_2$ (1.69 ml, 8.0 mmol) was added dropwise with stirring. The mixture was then stirred at room temperature for 2 h to give a dark-red solution with a black precipitate which was retrieved by filtration and washed with THF (3 x 10 ml) and Et_2O (1 x 10 ml) to give a purple-black solid (2.13 g, 92.2%).

^{1}H NMR (400 MHz, MeCN-d₃) δ 3.12 (q, $^3J_{HH}$ = 6 Hz, 2H, NCH_2), 1.21 (t, $^3J_{HH}$ = 6 Hz, 3H, NCH₂CH_3)

[Fe₄S₄Br₄][NBu₄]₂ (23)
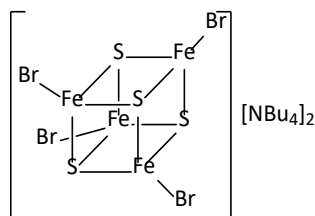
Made according to a literature procedure.[139]

A flame-dried Schlenk was charged with [Bu₄N][Br] (1.36 g, 4.23 mmol), Na_2S (0.82 g, 10.56 mmol), and $FeBr_3$ (2.50 g, 8.45 mmol) and DMF (30 ml) added. The solution was stirred for

20 h producing a dark-brown solution which was then filtered, and volatiles removed *in vacuo*. The residue was then redissolved in MeCN (20 ml) and layered with Et$_2$O (20 ml), separating the product as black crystals (3.17 g, 65.0%).

FeCl(N(SiMe$_3$)$_2$)$_2$(THF)
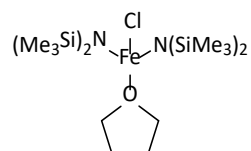
Adapted from a literature procedure.[162]

FeCl$_3$ (1.62 g, 10 mmol, 1 equiv.) was suspended in THF (20 ml) and cooled to 0^{0}C. NaN(SiMe$_3$)$_2$ (10 ml, 2M in THF, 2 equiv.) was added slowly dropwise forming a red solution which was stirred for 16 hours. The solution was then filtered, and the residue washed with THF (3 x 5 ml), the extracts were then combined and solvent removed *in vacuo* leaving a residue that was extracted thoroughly with hexane (5 x 10 ml). The volume of these extracts was then reduced to ~20 ml and stored at -20^{0}C to collect the product as red crystals (2.08 g, 4.33 mmol, 43.2%)

Fe$_2$(μ-N^{t}Bu)$_2$Cl$_2$(NH$_2$^{t}Bu)$_2$
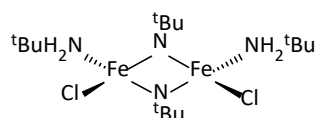
Adapted from a literature procedure.[163]

FeCl(N(SiMe$_3$)$_2$)$_2$)(THF) (966 mg, 2.0 mmol, 1 equiv.), was suspended in THF (15 ml). ^{t}BuNH$_2$ (0.84 ml, 8.0 mmol, 4 equiv.) was added in one portion. The solution was then stirred for 16 hours. Solvent was then removed *in vacuo* to leave a rust-coloured solid which was washed with pentane (2 x 10 ml) (257 mg, 0.54 mmol, 54.0%).

[Fe$_2$(μ-N^{t}Bu)(μ-S)Cl$_4$][NEt$_4$]$_2$ (24)
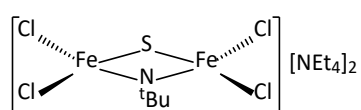
Adapted from a literature procedure.[151]

Et$_4$NCl (297 mg, 1.8 mmol, 2 equiv.) was suspended in MeCN (6 ml) and added in one portion to a solution of Fe$_2$(μ-N^{t}Bu)$_2$Cl$_2$(NH$_2$^{t}Bu)$_2$ (425 mg, 0.9 mmol, 1 equiv.) in MeCN (30 ml) and stirred for 4 hours. S(SiMe$_3$)$_2$ (0.21 ml, 1 mmol, 1.1 equiv.) was added dropwise and stirring continued for 16 hours. Solvent was then removed *in vacuo* leaving the product as a black flaky solid (430 mg, 0.63 mmol, 69. 7%).

General procedure for synthesis of pyrazolate salts

A flame-dried Schlenk was charged with NaH (60% dispersion in mineral oil, 1.95 g, 48.6 mmol, 1 equiv.) and washed with hexane (4 x 10 ml). The remaining white solid was then suspended in THF (20 ml) and cooled to 0°C in an ice bath. A separate flame-dried flask was charged with the relevant pyrazole derivative (48.6 mmol, 1 equiv.) and dissolved in THF (20 ml). This solution was then added to the NaH suspension slowly via cannula, causing rapid bubbling. When addition was finished, a gas bubbler was attached to the flask to allow H$_2$ gas to escape and stirring was continued for one hour, forming a beige solution. The solvent was removed *in vacuo* and the remaining solid was washed with hexane (3 x 10 ml) to give the product.

Napz
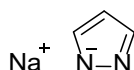
pzH (3.31 g) was reacted with NaH (1.95 g, 48.6 mmol) to give Napz as a powdery white solid. (4.46 g, 41.2 mmol, 84.7 % yield).

Na (3,5-Me-pz)
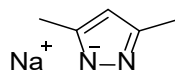
3, 5-Me-pzH (4.80 g, 48.6 mmol) was reacted with NaH (1.95 g, 48.6 mmol) to give Na (3, 5-Me-pz) as a powdery white solid. (5.9 g, 42.3 mmol, 87.0%)

Na (3,5-iPr-pz)
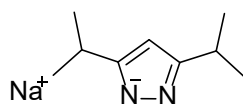
3, 5-iPr-pzH (7.60 g, 48.6 mmol) was reacted with NaH (1.95 g, 48.6 mmol) to give Na (3, 5-Me-pz) as a powdery white solid. (7.91 g, 39.9 mmol, 82.3%)

Na (4-Br-pz)
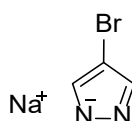
4-Br-pzH (3.67 g, 25.0 mmol) was reacted with NaH (1.0 g, 25.0 mmol) to give Na (3, 5-Me-pz) as a powdery white solid. (2.65 g, 15.7 mmol, 62.9%)

$Fe_8O_4pz_{12}Cl_4$ (25)
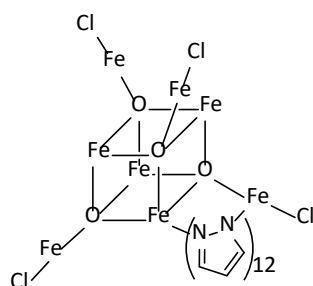
Adapted from a literature procedure.[153]

A flame-dried Schlenk flask was charged with $FeCl_3$ (1.20 g, 7.39 mmol), Napz (1.0 g, 11.10 mmol) under an Argon atmosphere. Dry DCM (50 ml) was added and the mixture stirred for 2 h forming a dark solution. Air was then admitted to the flask forming a rust-coloured suspension that was stirred for 16 hours. The solution was then filtered and the solvent removed *in vacuo*, leaving the crude product as a brown-red solid. This was purified was layering a saturated DCM solution with hexane, inducing crystallisation of the product as red-brown needles. (119 mg, 0.094 mmol, 8.8%)

^{1}H NMR (400 MHz, $CDCl_3$): δ (ppm) 42.1 (1H), 10.5 (1H), 3.5 (1H)

Fe$_8$S$_4$pz$_{12}$Cl$_4$ (26)
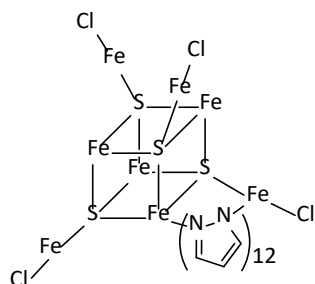
A flame-dried Schlenk flask was charged with FeCl$_3$ (648 mg, 4 mmol, 8 equiv.) and Napz (540 mg, 6 mmol, 12 equiv.) and cooled to 0°C in an ice bath. DCM (10 ml) was added and the mixture stirred for 1 hr to give a dark red solution. S(SiMe$_3$)$_2$ (0.45 ml, 2 mmol, 4 equiv.) was added dropwise forming a black suspension which was stirred for 16 hours. After this, solvent was removed *in vacuo* and the resultant black solid extracted with THF (3 x 10 ml) which was then removed *in vacuo* to give a powdery tan solid. (504 mg, 0.31 mmol, 62.5%).

^{1}H NMR (400 MHz, THF): δ (ppm) 44.5 (1H), 39.3 (1H), 22.7 (1H)

Fe$_8$S$_4$pz$_{12}$Br$_4$
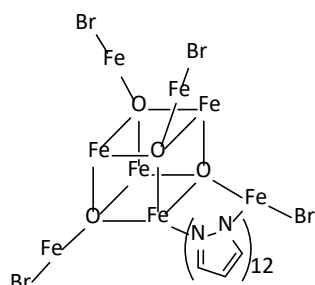
A flame-dried Schlenk flask was charged with FeBr$_3$ (860 mg, 4 mmol, 8 equiv.) and Napz (540 mg, 6 mmol, 12 equiv.) and cooled to 0°C in an ice bath. DCM (10 ml) was added and the mixture stirred for 1 hr to give a dark solution. S(SiMe$_3$)$_2$ (0.45 ml, 2 mmol, 4 equiv.) was added dropwise forming a black suspension which was stirred for 16 hours. After this, solvent was removed *in vacuo* and the resultant black solid extracted with THF (3 x 10 ml) which was then removed *in vacuo* to give a powdery tan solid. (436 mg, 0.24 mmol, 48.8%)

^{1}H NMR (400 MHz, THF): δ (ppm) 61.8 (1H), 43.8 (1H), 30.1 (1H)

Fe$_8$S$_4$(3,5-Me-pz)$_{12}$Cl$_4$
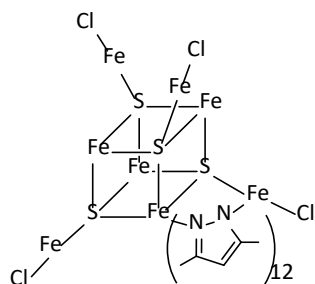
A flame-dried Schlenk was charged with FeCl$_3$ (648 mg, 4 mmol, 8 equiv.) and Na(3,5-Me-pz) (1.04 g mg, 6 mmol, 12 equiv.) and cooled to 0°C in an ice bath. DCM (10 ml) was added and the mixture stirred for 1 hr to give a dark solution. S(SiMe$_3$)$_2$ (0.45 ml, 2 mmol, 4 equiv.) was added dropwise forming a black suspension which was stirred for 16 hours. After this, solvent was removed *in vacuo* and the resultant black solid extracted with THF (3 x 10 ml) which was then removed *in vacuo* to give a powdery tan solid. (360 mg, 0.19 mmol, 38.7 %)

^{1}H NMR (400 MHz, THF): δ (ppm) 53.1, 44.8, 23.4.

Fe$_8$S$_4$(3,5-iPr-pz)$_{12}$Cl$_4$
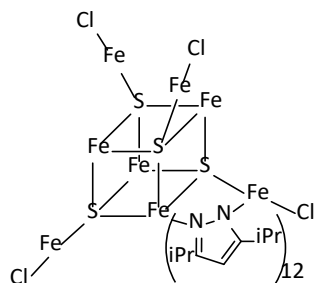
A flame-dried Schlenk flask was charged with FeCl$_3$ (648 mg, 4 mmol, 8 equiv.) and Na(3,5-iPr-pz) (1.04 g mg, 6 mmol, 12 equiv.) and cooled to 0°C in an ice bath. DCM (10 ml) was added and the mixture stirred for 1 hr to give a dark solution. S(SiMe$_3$)$_2$ (0.45 ml, 2 mmol, 4 equiv.) was added dropwise forming a black suspension which was stirred for 16 hours. After this, solvent was removed *in vacuo* and the resultant black solid extracted with THF (3 x 10 ml) which was then removed *in vacuo* to give the product as a powdery tan solid. (500 mg, 0.20 mmol, 39.5 %)

^{1}H NMR (400 MHz, THF): δ (ppm) 55.1, 44.3, 16.83, -2.78, -17.8

Fe₈Se₄pz₁₂Cl₄
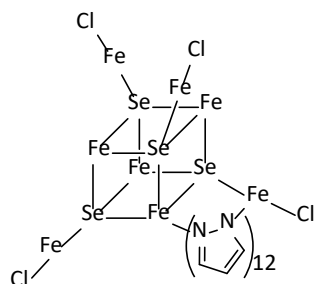
A flame dried-Schlenk flask was charged with FeCl$_3$ (648 mg, 4 mmol, 8 equiv.), Napz (540 mg, 6 mmol, 12 equiv.) and Na$_2$Se (250 mg, 2 mmol, 4 equiv.) and cooled to 0^{0}C. DCM (10 ml) was added and the mixture stirred overnight giving a black solution. Solvent was removed *in vacuo* and the resultant black solid extracted thoroughly with THF (3 x 10 ml). THF was then removed *in vacuo* to give the product as a brown oil which was triturated with hexane (10 ml) to give the product as a dark red solid. (195 mg, 0.113 mmol, 22.8%).

^{1}H NMR (400 MHz, THF): δ (ppm) 48.9 (1H), 44.1 (1H), 37.8 (1H)

MnCl₂ + Na(3,5-Me-pz) + S₈

A flame-dried Schlenk was charged with MnCl$_2$ (250 mg, 2 mmol, 2 equiv.), and Na(3,5-Me-pz) (472 mg, 4 mmol, 4 equiv.) and THF (10 ml) added. The solution was stirred for 30 minutes before S$_8$ (32 mg, 0.125 mmol, 0.125 equiv.) was added as a solid in one portion against a flow of N$_2$ causing a darkening of the brown-yellow solution and formation of copious tan precipitate. The suspension was stirred for 16 hours before being filtered through a Celite frit leaving a brown solution was which analysed by NMR.

CoCl₂ + Na(3,5-Me-pz) + S₈

A flame-dried Schlenk was charged with CoCl$_2$ (260 mg, 2 mmol, 2 equiv.), and Na(3,5-Me-pz) (354 mg, 3 mmol, 3 equiv.) and THF (10 ml) added. The solution was stirred for 30 minutes before S$_8$ (32 mg, 0.125 mmol, 0.125 equiv.) was added as a solid in one portion against a flow of N$_2$ causing a gradual change of colour from blue to purple. The suspension was stirred for 16 hours before being filtered through a Celite frit leaving a blue solution was which analysed by NMR.

Lithium (p-tolyl)acetylide
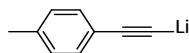
p-tolylethyne (0.6 ml, 5.0 mmol, 1 equiv.) was suspended in hexane (10 ml) and cooled to -40^0C. ^{n}BuLi (3.5 ml, 5.5 mmol, 1.1 equiv.) was added dropwise to the stirred solution over a period of 10 minutes. The solution was held at -40^0C for 30 minutes before being allowed to warm to room temperature and stirred for a further 1 hr, forming a white precipitate which was collected by filtration. The precipitate was then washed with hexane (3 x 5 ml) to retrieve a white solid (530 mg, 4.3 mmol, 86.9%).

General Procedure for reaction of Organolithium Reagents with Iron-Sulphur Clusters

A J. Young valve NMR tube was loaded with the relevant metal cluster (0.01 mmol 1 equiv.) and organolithium reagent (0.04 mmol, 4 equiv.). THF (0.6 ml) was then added before being analysed by ^{1}H NMR.

Fe$_8$S$_4$pz$_{12}$Mes$_4$
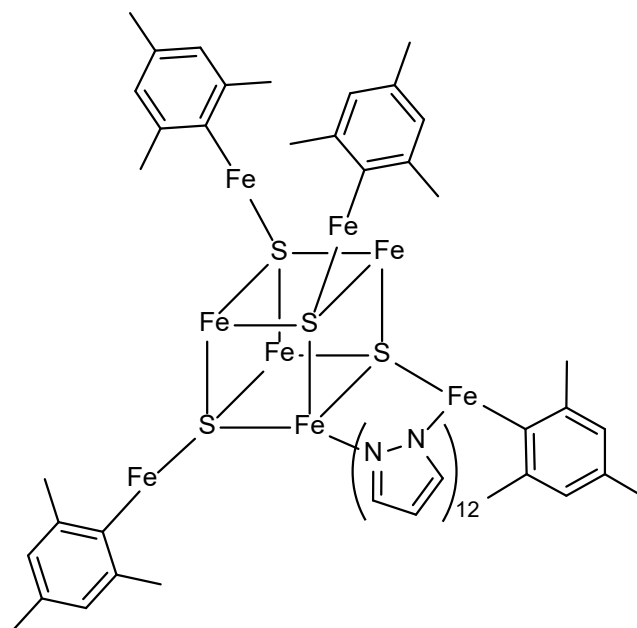
^{1}H NMR (400 MHz, THF): δ (ppm): 127.8, 66.7, 53.9, 41.4, 27.7, -4.48

Fe$_8$S$_4$pz$_{12}$XyI$_4$
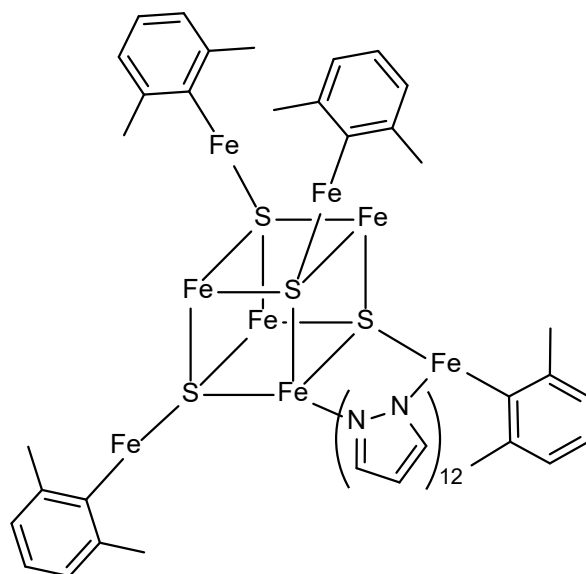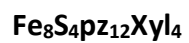
^{1}H NMR (400 MHz, THF): δ (ppm): 93.0, 64.4, 54.3 44.8, 35.6, -6.70

Fe$_8$S$_4$pz$_{12}$(C$_2$-p-tol)$_4$
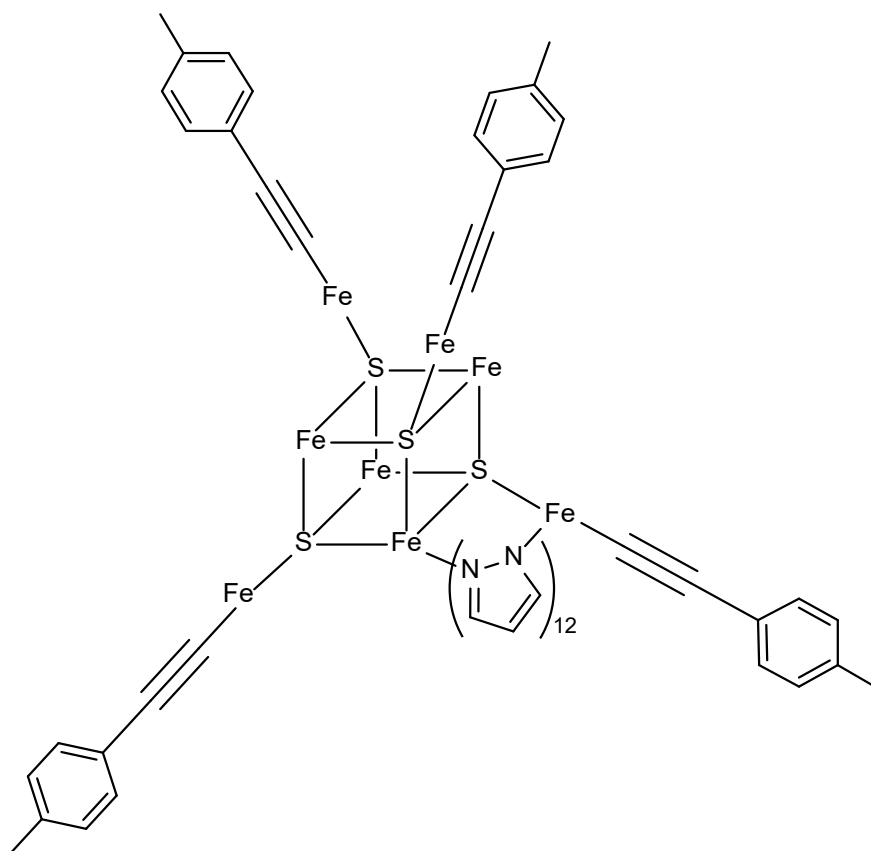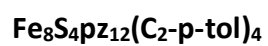
^{1}H NMR (400 MHz, THF): δ (ppm): 90.1, 66.7, 53.2, 41.4, 36.0

Fe₈S₄(3,5-Me-pz)₁₂Mes₄
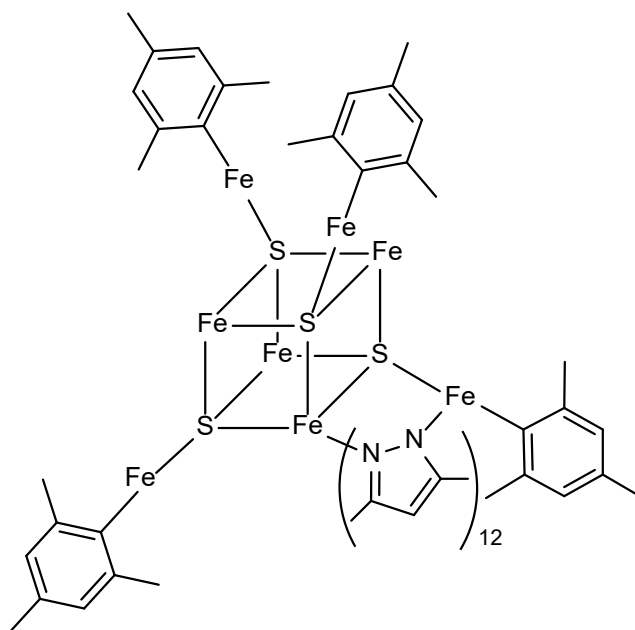
^{1}H NMR (400 MHz, THF): δ (ppm) 108.9, 103.8, 96.6, 44.6, 37.0, 31.1

Fe₈S₄(3,5-Me-pz)₁₂Xyl₄

^{1}H NMR (400 MHz, THF): δ (ppm): 95.6, 64.3, 54.7, 44.2, 36.0

Fe₈S₄(3,5-Me-pz)₁₂(C₂-p-tol)₄

^{1}H NMR (400 MHz, THF): δ (ppm) 90.1, 64.1, 53.5, 36.0, 28.9

Fe₈S₄(3,5-iPr-pz)₁₂Mes₄

^{1}H NMR (400 MHz, THF): δ (ppm) 84.8, 83.7, 49.9, 41.7, 21.1, 16.7, -2.42, -6.61

Fe₈S₄(3,5-iPr-pz)₁₂XyI₄
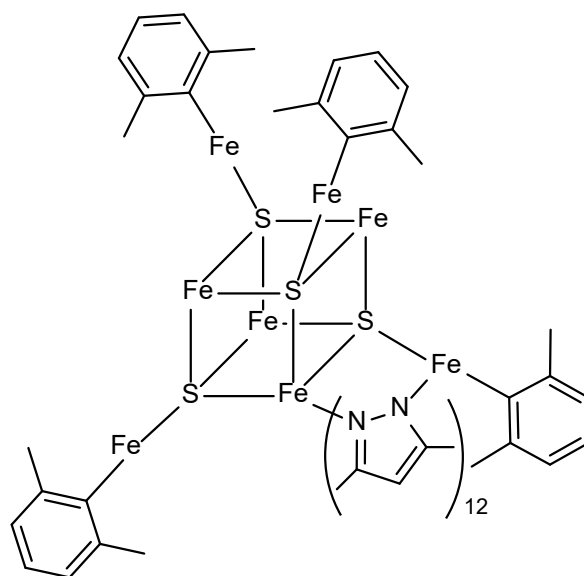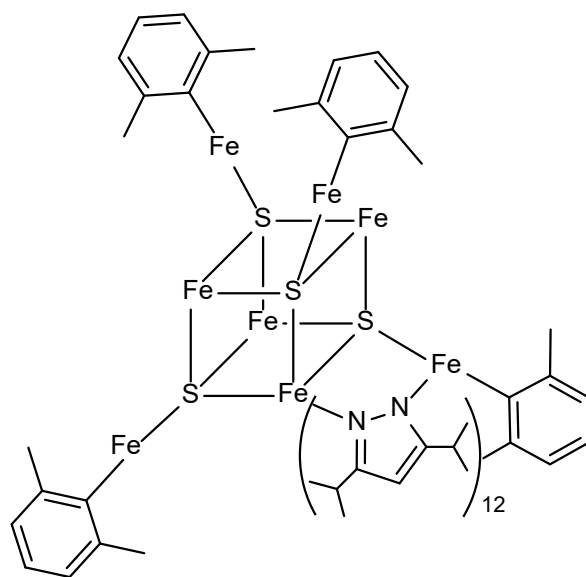
^{1}H NMR (400 MHz, THF): δ (ppm) 84.7, 83.7, 49.8, 42.0, 20.5, 16.9, -2.47

Fe₈S₄(3,5-iPr-pz)₁₂(C₂-p-tol)₄
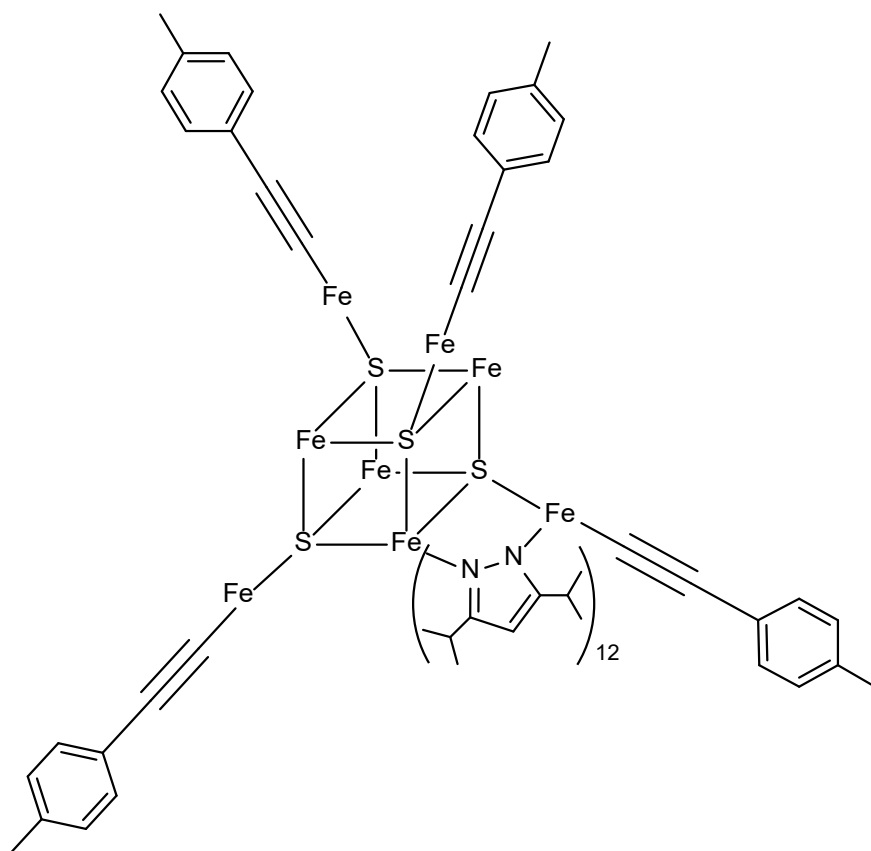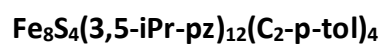
^{1}H NMR (400 MHz, THF): δ (ppm): 50.1, 15.1, -4.49, -6.68

6. References

1. The Nobel Prize in Chemistry 2010. https://www.nobelprize.org/prizes/chemistry/2010/summary/.

2. Harrington, P. J. & Lodewijk, E. Summary of Lecture Transcripts Twenty Years of Naproxen Technology. *Org. Process Res. Dev.* **1**, 72–76 (1997).

3. Miyaura, N., Yamada, K. & Suzuki, A. A new stereospecific cross-coupling by the palladium-catalyzed reaction of 1-alkenylboranes with 1-alkenyl or 1-alkynyl halides. *Tetrahedron Lett.* **20**, 3437–3440 (1979).

4. Yamamoto, K. *et al.* Selective carbon-carbon bond formation by cross-coupling of Grignard reagents with organic halides. Catalysis by nickel-phosphine complexes. *J. Am. Chem. Soc.* **94**, 4374–4376 (2002).

5. Baba, S. & Negishi, E. ichi. A novel stereospecific alkenyl-alkenyl cross-coupling by a palladium- or nickel-catalyzed reaction of alkenylalanes with alkenyl halides. *J. Am. Chem. Soc.* **98**, 6729–6731 (2002).

6. Xue, L. & Lin, Z. Theoretical aspects of palladium-catalysed carbon–carbon cross-coupling reactions. *Chem. Soc. Rev.* **39**, 1692-1705 (2010).

7. Canty, A. J., H In, M. J. & J Chem, A. H. Development of organopalladium(IV) chemistry: fundamental aspects and systems for studies of mechanism in organometallic chemistry and catalysis. *Acc. Chem. Res.* **25**, 83–90 (2002).

8. Amatore, C., Catellani, M., Deledda, S., Jutand, A. & Motti, E. Rates of the oxidative addition of benzyl halides to a metallacyclic palladium(II) complex and of the reductive elimination from a benzyl-palladium(IV) complex. *Organometallics* **27**, 4549–4554 (2008).

9. Kirchhoff, J. H., Netherton, M. R., Hills, I. D. & Fu, G. C. Boronic acids: New coupling partners in room-temperature Suzuki reactions of alkyl bromides. Crystallographic characterization of an oxidative-addition adduct generated under remarkably mild conditions. *J. Am. Chem. Soc.* **124**, 13662–13663 (2002).

10.   Stille, J. K. *et al.* Oxidative Addition of Aryl Bromide after Dissociation of Phosphine from a Two-Coordinate Palladium(0) Complex, Bis(tri-o-tolylphosphine)Palladium(0). *J. Am. Chem. Soc.* **117**, 5373–5374 (2002).

11.   Senn, H. M. & Ziegler, T. Oxidative addition of aryl halides to palladium(0) complexes: A density-functional study including solvation. *Organometallics* **23**, 2980–2988 (2004).

12.   Bedford, R. B., Hazelwood, S. L. & Limmert, M. E. Extremely high activity catalysts for the Suzuki coupling of aryl chlorides: the importance of catalyst longevity. *Chem. Commun.* **2**, 2610–2611 (2002).

13.   Bedford, R. B., Cazin, C. S. J. & Hazelwood (néeWelch), S. L. Simple Mixed Tricyclohexylphosphane–Triarylphosphite Complexes as Extremely High-Activity Catalysts for the Suzuki Coupling of Aryl Chlorides. *Angew. Chem. Int. Ed.* **41**, 4120–4122 (2002).

14.   Bedford, R. B. *et al.* High-activity catalysts for Suzuki coupling and amination reactions with deactivated aryl chloride substrates: Importance of the palladium source. *Organometallics* **22**, 987–999 (2003).

15.   Martin, R. & Buchwald, S. Palladium-Catalyzed Suzuki–Miyaura Cross-Coupling Reactions Employing Dialkylbiaryl Phosphine Ligands. *Acc. Chem. Res.* **41**, 1461-1473 (2008).

16.   Arvela, R. K. *et al.* A reassessment of the transition-metal free Suzuki-type coupling methodology. *J. Org. Chem.* **70**, 161–168 (2005).

17.   Avanthay, M., Bedford, R., Begg, C., Böse, D., Clayden, J., Davis, S., Eloi, J., Goryunov, G., Hartung, I., Heeley, J. *et al.* Identifying palladium culprits in amine catalysis. *Nat. Catal.* **4**, 994-998 (2021).

18.   Vinod, J., Wanner, A., James, E. & Koide, K. Fluorometric study on the amine-catalysed Suzuki–Miyaura coupling. *Nat. Catal.* **4**, 999-1001 (2021).

19.   Novák, Z., Adamik, R., Csenki, J., Béke, F., Gavaldik, R., Varga, B., Nagy, B., May, Z., Daru, J., Gonda, Z. *et al*. Revisiting the amine-catalysed cross-coupling. Nature

Catalysis **4**, 991-993 (2021).

20. Nuss, P. & Eckelman, M. Life Cycle Assessment of Metals: A Scientific Synthesis. PLoS ONE 9, e101298 (2014).

21. Purdie & Florine P. Elemental Impurities in Drug Products Guidance for Industry. (2018).

22. Phillips, S., Holdsworth, D., Kauppinen, P. & Mac Namara, C. Palladium Impurity Removal from Active Pharmaceutical Ingredient Process Streams. *Johnson Matthey Technol. Rev.* **60**, 277–286 (2016).

23. Hayler, J. D., Leahy, D. K. & Simmons, E. M. A Pharmaceutical Industry Perspective on Sustainable Metal Catalysis. *Organometallics* **38**, 36–46 (2018).

24. O'Brien, H. M. *et al.* Iron-catalysed substrate-directed Suzuki biaryl cross-coupling. *Nat. Catal. 2018 16* **1**, 429–437 (2018).

25. Bedford, R. B., Gallagher, T., Pye, D. R. & Savage, W. Towards Iron-Catalysed Suzuki Biaryl Cross-Coupling: Unusual Reactivity of 2-Halobenzyl Halides. *Synthesis (Stuttg).* **47**, 1761–1765 (2015).

26. Crockett, M. P., Tyrol, C. C., Wong, A. S., Li, B. & Byers, J. A. Iron-Catalyzed Suzuki-Miyaura Cross-Coupling Reactions between Alkyl Halides and Unactivated Arylboronic Esters. *Org. Lett.* **20**, 5233–5237 (2018).

27. Adams, C. J. *et al.* Iron(I) in Negishi cross-coupling reactions. *J. Am. Chem. Soc.* **134**, 10333–10336 (2012).

28. SWP & QWP. Committee for Human Medicinal Products (CHMP) Draft Guideline on the Specification for Residues of Metal Catalysts Draft Agreed by the Safety Working Party Adoption by CHMP (1998).

29. Kharasch, M. S. & Tawney, P. O. Factors Determining the Course and Mechanisms of Grignard Reactions. II. The Effect of Metallic Compounds on the Reaction between Isophorone and Methylmagnesium Bromide. *J. Am. Chem. Soc.* **63**, 2308–2316 (1941).

30. Tamura, M. & Kochi, J. K. Vinylation of Grignard reagents. Catalysis by iron. *J. Am. Chem. Soc.* **93**, 1487–1489 (1971).

31. Cahiez, G. & Avedissian, H. Highly stereo and chemoselective iron-catalyzed alkenylation of organomagnesium compounds. *Synthesis (Stuttg).* **1998**, 1199–1205 (1998).

32. Nakamura, M., Matsuo, K., Ito, S. & Nakamura, E. Iron-Catalyzed Cross-Coupling of Primary and Secondary Alkyl Halides with Aryl Grignard Reagents. *J. Am. Chem. Soc.* **126**, 3686–3687 (2004).

33. Bedford, R., Huwe, M. & Wilkinson, M. Iron-catalysed Negishi coupling of benzylhalides and phosphates. *Chem. Commun.* 600-602 (2009).

34. Hatakeyama, T., Hashimoto, T., Kondo, Y., Fujiwara, Y., Seike, H., Takaya, H., Tamada, Y., Ono, T. & Nakamura, M. Iron-Catalyzed Suzuki–Miyaura Coupling of Alkyl Halides. *J. Am. Chem. Soc.* **132**, 10674-10676 (2010).

35. Fürstner, A., Leitner, A., Méndez, M. & Krause, H. Iron-Catalyzed Cross-Coupling Reactions. *J. Am. Chem. Soc.* **124**, 13856–13863 (2002).

36. Agata, R., Takaya, H., Matsuda, H., Nakatani, N., Takeuchi, K., Iwamoto, T., Hatakeyama, T. & Nakamura, M. Iron-Catalyzed Cross Coupling of Aryl Chlorides with Alkyl Grignard Reagents: Synthetic Scope and Fe^{II}/Fe^{IV} Mechanism Supported by X-ray Absorption Spectroscopy and Density Functional Theory Calculations. *Bulletin of the Chemical Society of Japan* **92**, 381-390 (2019).

37. Hatakeyama, T., Fujiwara, Y., Okada, Y., Itoh, T., Hashimoto, T., Kawamura, S., Ogata, K., Takaya, H. & Nakamura, M. Kumada–Tamao–Corriu Coupling of Alkyl Halides Catalyzed by an Iron–Bisphosphine Complex. *Chem. Let.* **40**, 1030-1032 (2011).

38. Scott Smith, R. & Kochi, J. K. Mechanistic Studies of Iron Catalysis in the Cross Coupling of Alkenyl Halides and Grignard Reagents. *J. Org. Chem* **41**, (1976).

39. Kwan, C. & Kochi, J. Electron spin resonance studies of the reduction of transition metal complexes with Grignard reagents. 1. Dianion radicals of .beta.-diketonates. *J. Am. Chem. Soc.* **98**, 4903-4912 (1976).

40. Kleimark, J., Hedström, A., Larsson, P. F., Johansson, C. & Norrby, P. O. Mechanistic investigation of iron-catalyzed coupling reactions. *ChemCatChem* **1**, 152–161 (2009).

41. Muñoz, S. B., Daifuku, S. L., Brennessel, W. W. & Neidig, M. L. Isolation, Characterization, and Reactivity of $Fe_8Me_{12}^-$: Kochi's S = 1/2 Species in Iron-Catalyzed Cross-Couplings with MeMgBr and Ferric Salts. *J. Am. Chem. Soc.* **138**, 7492–7495 (2016).

42. Muñoz, S. B. *et al.* The N-Methylpyrrolidone (NMP) Effect in Iron-Catalyzed Cross-Coupling with Simple Ferric Salts and MeMgBr. *Angew. Chem. Int. Ed.* **57**, 6496–6500 (2018).

43. Bogdanovic, B. & Schwickardi, M. Transition Metal Catalyzed Preparation of Grignard Compounds**. *Angew. Chem. Int. Ed* **39**, (2000).

44. Fürstner, A. *et al.* Preparation, structure, and reactivity of nonstabilized organoiron compounds. Implications for iron-catalyzed cross coupling reactions. *J. Am. Chem. Soc.* **130**, 8773–8787 (2008).

45. Hedström, A., Izakian, Z., Vreto, I., Wallentin, C. J. & Norrby, P. O. On the Radical Nature of Iron-Catalyzed Cross-Coupling Reactions. *Chem. − A Eur. J.* **21**, 5946–5953 (2015).

46. Schoch, R., Desens, W., Werner, T. & Bauer, M. X-ray Spectroscopic Verification of the Active Species in Iron-Catalyzed Cross-Coupling Reactions. *Chem. − A Eur. J.* **19**, 15816–15821 (2013).

47. Aleandri, L. E. *et al.* Inorganic Grignard Reagents. Preparation and Their Application for the Synthesis of Highly Active Metals, Intermetallics, and Alloys. *Chem. Mater.* **7**, 1153–1170 (2002).

48. Fürstner, A. & Martin, R. Advances in Iron Catalyzed Cross Coupling Reactions. *Chem. Lett.* **34**, 624–629 (2005).

49. Carpenter, S. H., Baker, T. M., Muñoz, S. B., Brennessel, W. W. & Neidig, M. L. Multinuclear iron–phenyl species in reactions of simple iron salts with PhMgBr: identification of $Fe_4(\mu-Ph)_6(THF)_4$ as a key reactive species for cross-coupling catalysis. *Chem. Sci.* **9**, 7931–7939 (2018).

50. Hedström, A., Izakian, Z., Vreto, I., Wallentin, C. J. & Norrby, P. O. On the Radical

Nature of Iron-Catalyzed Cross-Coupling Reactions. *Chem. – A Eur. J.* **21**, 5946–5953 (2015).

51.   Bedford, R., Brenner, P., Elorriaga, D., Harvey, J. & Nunn, J. The influence of the ligand chelate effect on iron-amine-catalysed Kumada cross-coupling. *Dalt. Trans.* **45**, 15811-15817 (2016).

52.   Bedford, R., Brenner, P., Carter, E., Cogswell, P., Haddow, M., Harvey, J., Murphy, D., Nunn, J. & Woodall, C. TMEDA in Iron-Catalyzed Kumada Coupling: Amine Adduct versus Homoleptic "ate" Complex Formation. *Angew. Chem. Int. Ed.* **53**, 1804-1808 (2014).

53.   Sears, J. D., Muñoz, S. B., Cuenca, M. C. A., Brennessel, W. W. & Neidig, M. L. Synthesis and characterization of a sterically encumbered homoleptic tetraalkyliron(III) ferrate complex. *Polyhedron* **158**, 91–96 (2019).

54.   Wowk, V., Rousseau, L. & Lefèvre, G. Importance of Two-Electron Processes in Fe-Catalyzed Aryl-(hetero)aryl Cross-Couplings: Evidence of Fe^0/Fe^{II} Couple Implication. *Organometallics* **40**, 3253–3266 (2021).

55.   Daifuku, S., Kneebone, J., Snyder, B. & Neidig, M. Iron(II) Active Species in Iron–Bisphosphine Catalyzed Kumada and Suzuki–Miyaura Cross-Couplings of Phenyl Nucleophiles and Secondary Alkyl Halides. *J. Am. Chem. Soc.* **137**, 11432-11444 (2015).

56.   Noda, D., Sunada, Y., Hatakeyama, T., Nakamura, M. & Nagashima, H. Effect of TMEDA on Iron-Catalyzed Coupling Reactions of ArMgX with Alkyl Halides. *J. Am. Chem. Soc.* **131**, 6078–6079 (2009).

57.   Sharma, A. & Nakamura, M. A DFT Study on $Fe^I/Fe^{II}/Fe^{III}$ Mechanism of the Cross-Coupling between Haloalkane and Aryl Grignard Reagent Catalyzed by Iron-SciOPP Complexes. *Mol.* 25, 3612 (2020).

58.   Sharma, A. K. *et al.* DFT and AFIR Study on the Mechanism and the Origin of Enantioselectivity in Iron-Catalyzed Cross-Coupling Reactions. *J. Am. Chem. Soc.* **139**, 16117–16125 (2017).

59. Jin, M., Adak, L. & Nakamura, M. Iron-Catalyzed Enantioselective Cross-Coupling Reactions of α-Chloroesters with Aryl Grignard Reagents. *J. Am. Chem. Soc.* **137**, 7128–7134 (2015).

60. Jin, M., Adak, L. & Nakamura, M. Iron-Catalyzed Enantioselective Cross-Coupling Reactions of α-Chloroesters with Aryl Grignard Reagents. *J. Am. Chem. Soc.* **137**, 7128–7134 (2015).

61. Sharma, A. K. *et al.* DFT and AFIR Study on the Mechanism and the Origin of Enantioselectivity in Iron-Catalyzed Cross-Coupling Reactions. *J. Am. Chem. Soc.* **139**, 16117–16125 (2017).

62. Humphreys, J., Lan, R. & Tao, S. Development and Recent Progress on Ammonia Synthesis Catalysts for Haber–Bosch Process. *Adv. Energy Sustain. Res.* **2**, 2000043 (2021).

63. The Nobel Prize in Chemistry 1918 - NobelPrize.org. https://www.nobelprize.org/prizes/chemistry/1918/summary/.

64. Howarth, R. W. Coastal nitrogen pollution: A review of sources and trends globally and regionally. *Harmful Algae* **8**, 14–20 (2008).

65. Smil. Enriching the earth and the transformation of world food production. 338 (2001).

66. Rees, D. C. *et al.* Structural basis of biological nitrogen fixation. *Philos. Trans. R. Soc. A Math. Phys. Eng. Sci.* **363**, 971–984 (2005).

67. Burgess, B. K. & Lowe, D. J. Mechanism of Molybdenum Nitrogenase. *Chem. Rev.* **96**, 2983–3011 (1996).

68. Einsle, O., Tezcan, F., Andrade, S., Schmid, B., Yoshida, M., Howard, J. & Rees, D. Nitrogenase MoFe-Protein at 1.16 Å Resolution: A Central Ligand in the FeMo-Cofactor. *Science* **297**, 1696-1700 (2002).

69. Lancaster, K., Roemelt, M., Ettenhuber, P., Hu, Y., Ribbe, M., Neese, F., Bergmann, U. & DeBeer, S. X-ray Emission Spectroscopy Evidences a Central Carbon in the Nitrogenase Iron-Molybdenum Cofactor. *Science* **334**, 974-977 (2011).

70. Spatzal, T. *et al.* Evidence for Interstitial Carbon in Nitrogenase FeMo Cofactor. *Science (80-.).* **334**, 940–940 (2011).

71. Hoffman, B. M., Lukoyanov, D., Yang, Z. Y., Dean, D. R. & Seefeldt, L. C. Mechanism of nitrogen fixation by nitrogenase: The next stage. *Chem. Rev.* **114**, 4041–4062 (2014).

72. Čorić, I., Mercado, B. Q., Bill, E., Vinyard, D. J. & Holland, P. L. Binding of dinitrogen to an iron–sulfur–carbon site. *Nature* **526**, 96–99 (2015).

73. Rittle, J. & Peters, J. C. Fe–N$_2$/CO complexes that model a possible role for the interstitial C atom of Femo-cofactor (FeMoco). *Proceedings of the National Academy of Sciences* **110**, 15898–15903 (2013).

74. Siegbahn, P. E. M. The mechanism for nitrogenase including all steps. *Phys. Chem. Chem. Phys.* **21**, 15747–15759 (2019).

75. Buscagan, T. & Rees, D. Rethinking the Nitrogenase Mechanism: Activating the Active Site. *Joule* **3**, 2662-2678 (2019).

76. Zhang, Y. et al. A thiolate-bridged Fe^{IV}Fe^{IV} μ-nitrido complex and its hydrogenation reactivity toward Ammonia Formation. *Nat. Chem.* **14**, 46–52 (2021).

77. McSkimming, A. & Suess, D. L. M. Dinitrogen binding and activation at a molybdenum–iron–sulfur cluster. *Nat. Chem. 2021 137* **13**, 666–670 (2021).

78. Kuriyama, S. *et al.* Direct Transformation of Molecular Dinitrogen into Ammonia Catalyzed by Cobalt Dinitrogen Complexes Bearing Anionic PNP Pincer Ligands. *Angew. Chem.* **128**, 14503–14507 (2016).

79. Sekiguchi, Y. *et al.* Catalytic Reduction of Molecular Dinitrogen to Ammonia and Hydrazine Using Vanadium Complexes. *Angew. Chem. Int. Ed.* **57**, 9064–9068 (2018).

80. Fajardo, J. & Peters, J. C. Catalytic Nitrogen-to-Ammonia Conversion by Osmium and Ruthenium Complexes. *J. Am. Chem. Soc.* **139**, 16105–16108 (2017).

81. Yandulov, D. V., Schrock, R. R., Rheingold, A. L., Ceccarelli, C. & Davis, W. M. Synthesis and reactions of molybdenum triamidoamine complexes containing hexaisopropylterphenyl substituents. *Inorg. Chem.* **42**, 796–813 (2003).

82. Yandulov, D. V. & Schrock, R. R. Studies relevant to catalytic reduction of dinitrogen to ammonia by molybdenum triamidoamine complexes. *Inorg. Chem.* **44**, 1103–1117 (2005).

83. Pappas, I. & Chirik, P. J. Catalytic Proton Coupled Electron Transfer from Metal Hydrides to Titanocene Amides, Hydrazides and Imides: Determination of Thermodynamic Parameters Relevant to Nitrogen Fixation. *J. Am. Chem. Soc.* **138**, 13379–13389 (2016).

84. Chalkley, M. J., Del Castillo, T. J., Matson, B. D., Roddy, J. P. & Peters, J. C. Catalytic N2-to-NH3 Conversion by Fe at Lower Driving Force: A Proposed Role for Metallocene-Mediated PCET. *ACS Cent. Sci.* **3**, 217–223 (2017).

85. Yandulov, D. V. & Schrock, R. R. Catalytic reduction of dinitrogen to ammonia at a single molybdenum center. *Science (80-.).* **301**, 76–78 (2003).

86. Hetterscheid, D. G. H., Hanna, B. S. & Schrock, R. R. Molybdenum Triamidoamine Systems. Reactions Involving Dihydrogen Relevant to Catalytic Reduction of Dinitrogen. *Inorg. Chem.* **48**, 8569–8577 (2009).

87. Wickramasinghe, L. A., Ogawa, T., Schrock, R. R. & Müller, P. Reduction of Dinitrogen to Ammonia Catalyzed by Molybdenum Diamido Complexes. *J. Am. Chem. Soc.* **139**, 9132–9135 (2017).

88. Arashiba, K., Miyake, Y. & Nishibayashi, Y. A molybdenum complex bearing PNP-type pincer ligands leads to the catalytic reduction of dinitrogen into ammonia. *Nat. Chem. 2010 32* **3**, 120–125 (2010).

89. Tanaka, H. *et al.* Molybdenum-Catalyzed Transformation of Molecular Dinitrogen into Silylamine: Experimental and DFT Study on the Remarkable Role of Ferrocenyldiphosphine Ligands. *J. Am. Chem. Soc.* **133**, 3498–3506 (2011).

90. Yuki, M., Midorikawa, T., Miyake, Y. & Nishibayashi, Y. Synthesis and protonolysis of tungsten- and molybdenum - Dinitrogen complexes bearing ruthenocenyldiphosphines. *Organometallics* **28**, 4741–4746 (2009).

91. Yuki, M., Miyake, Y. & Nishibayashi, Y. Preparation and protonation of tungsten- and

molybdenum-dinitrogen complexes bearing bis(dialkylphosphinobenzene)chromiums as auxiliary ligands. *Organometallics* **28**, 5821–5827 (2009).

92. Yuki, M., Miyake, Y., Nishibayashi, Y., Wakiji, I. & Hidai, M. Synthesis and Reactivity of Tungsten– and Molybdenum–Dinitrogen Complexes Bearing Ferrocenyldiphosphines toward Protonolysis. *Organometallics* **27**, 3947-3953 (2008).

93. Anderson, J. S., Rittle, J. & Peters, J. C. Catalytic conversion of nitrogen to ammonia by an iron model complex. *Nat.* **501**, 84–87 (2013).

94. Creutz, S. E. & Peters, J. C. Catalytic reduction of N_2 to NH_3 by an Fe-N 2 complex featuring a C-atom anchor. *J. Am. Chem. Soc.* **136**, 1105–1115 (2014).

95. Hill, P. J., Doyle, L. R., Crawford, A. D., Myers, W. K. & Ashley, A. E. Selective Catalytic Reduction of N_2 to N_2H by a Simple Fe Complex. *J. Am. Chem. Soc.* **138**, 13521–13524 (2016).

96. Ung, G. & Peters, J. C. Low-Temperature N_2 Binding to Two-Coordinate L_2Fe^0 Enables Reductive Trapping of L2FeN2– and NH3 Generation. *Angew. Chem. Int. Ed.* **54**, 532–535 (2015).

97. Piascik, A., Li, R., Wilkinson, H., Green, J. & Ashley, A. Fe-Catalyzed Conversion of N_2 to $N(SiMe_3)_3$ via an Fe-Hydrazido Resting State. *J. Am. Chem. Soc.* **140**, 10691-10694 (2018).

98. Sandl, S., Jacobi von Wangelin, A., Sc Sandl, M. S. & Jacobi von Wangelin, A. The Role of Organoferrates in Iron-Catalyzed Cross-Couplings. *Angew. Chem. Int. Ed.* **59**, 5434–5437 (2020).

99. Bedford, R. et al. Iron—Phosphine, —Phosphite, —Arsine, and —Carbene Catalysts for the Coupling of Primary and Secondary Alkyl Halides with Aryl Grignard Reagents. *ChemInform* **37**, (2006).

100. Agrawal, T. & Cook, S. P. Iron-catalyzed cross-coupling reactions of alkyl grignards with aryl sulfamates and tosylates. *Org. Lett.* **15**, 96–99 (2013).

101. Teng, Q., Wu, W., Duong, H. A. & Huynh, H. V. Ring-expanded N-heterocyclic carbenes as ligands in iron-catalysed cross-coupling reactions of arylmagnesium reagents and

aryl chlorides. *Chem. Commun.* **54**, 6044–6047 (2018).

102. Guisán-Ceinos, M., Tato, F., Buñuel, E., Calle, P. & Cárdenas, D. J. Fe-catalysed Kumada-type alkyl–alkyl cross-coupling. Evidence for the intermediacy of Fe(I) complexes. *Chem. Sci.* **4**, 1098–1104 (2013).

103. Bedford, R. B., Bruce, D. W., Frost, R. M. & Hird, M. Simple iron-amine catalysts for the cross-coupling of aryl Grignards with alkyl halides bearing β-hydrogens. *Chem. Commun.* 4161–4163 (2005)

104. Cahiez, G., Habiak, V., Duplais, C. & Moyeux, A. Iron-Catalyzed Alkylations of Aromatic Grignard Reagents. *Angew. Chemie Int. Ed.* **46**, 4364–4366 (2007).

105. Bedford, R. B. *et al.* TMEDA in iron-catalyzed Kumada coupling: Amine adduct versus homoleptic 'ate' complex formation. *Angew. Chem. Int. Ed.* **53**, 1804–1808 (2014).

106. Bedford, R. B., Brenner, P. B., Elorriaga, D., Harvey, J. N. & Nunn, J. The influence of the ligand chelate effect on iron-amine-catalysed Kumada cross-coupling. *Dalt. Trans.* **45**, 15811–15817 (2016).

107. Messinis, A. M. et al. The highly surprising behaviour of diphosphine ligands in iron-catalysed Negishi cross-coupling. *Nat. Cat.* **2**, 123–133 (2018).

108. Seeman, J. I. The Curtin-Hammett Principle and the Winstein-Holness Equation New Definition and Recent Extensions to Classical Concepts. 227 (1983).

109. Guo, Y., Young, D. J. & Andy Hor, T. S. Palladium-free Suzuki–Miyaura cross-coupling at elevated pressures. *Tetrahedron Lett.* **49**, 5620–5621 (2008).

110. Bedford, R. B., Hall, M. A., Hodges, G. R., Huwe, M. & Wilkinson, M. C. Simple mixed Fe–Zn catalysts for the Suzuki couplings of tetraarylborates with benzyl halides and 2-halopyridines. *Chem. Commun.* 6430–6432 (2009)

111. Bedford, R. B. *et al.* Simplifying Iron–Phosphine Catalysts for Cross-Coupling Reactions. *Angew. Chem. Int. Ed.* **52**, 1285–1288 (2013).

112. Hatakeyama, T. *et al.* Iron-Catalyzed Alkyl–Alkyl Suzuki–Miyaura Coupling. *Angew. Chem Int. Ed.* **51**, 8834–8837 (2012).

113. Tailor, S. B., Manzotti, M., Smith, G. J., Davis, S. A. & Bedford, R. B. Cobalt-Catalyzed Coupling of Aryl Chlorides with Aryl Boron Esters Activated by Alkoxides. *ACS Catal.* **11**, 3856–3866 (2021).

114. Asghar, S., Tailor, S. B., Elorriaga, D. & Bedford, R. B. Cobalt-Catalyzed Suzuki Biaryl Coupling of Aryl Halides. *Angew. Chem. Int. Ed.* **56**, 16367–16370 (2017).

115. Vasil'ev, L. S., Azarevich, O. G., Bogdanov, V. S., Bochkareva, M. N, Dorokhov, V. A. Boron chelates with 5,5,5-trifluoro- and 5,5,5-trichloro-4-aminopent-3-en-2-ones. *Bulletin of the Russian Academy of Sciences Division of Chemical Science* **41**, 2104–2107 (1992).

116. Procter, R. J. *et al.* A Zinc Catalyzed C(sp^3)–C(sp^2) Suzuki–Miyaura Cross-Coupling Reaction Mediated by Aryl-Zincates. *Chem. – A Eur. J.* **23**, 15889–15893 (2017).

117. Firth, J. D. *et al.* Light- and Manganese-Initiated Borylation of Aryl Diazonium Salts: Mechanistic Insight on the Ultrafast Time-Scale Revealed by Time-Resolved Spectroscopic Analysis. *Chem. – A Eur. J.* **27**, 3979–3985 (2021).

118. Daifuku, S. L., Al-Afyouni, M. H., Snyder, B. E. R., Kneebone, J. L. & Neidig, M. L. A Combined Mössbauer, Magnetic Circular Dichroism, and Density Functional Theory Approach for Iron Cross-Coupling Catalysis: Electronic Structure, In Situ Formation, and Reactivity of Iron-Mesityl-Bisphosphines. *J. Am. Chem. Soc.* **136**, 9132–9143 (2014).

119. Hatakeyama, T. *et al.* Kumada–Tamao–Corriu Coupling of Alkyl Halides Catalyzed by an Iron–Bisphosphine Complex. **40**, 1030–1032 (2011).

120. Lingg, R. D., Melton, R. G., Kopfler, F. C., Coleman, W. E. & Mitchell, D. E. Quantitative Analysis of Volatile Organic Compounds by GC-MS. *J. Am. Water Works Assoc.* **69**, 605–612 (1977).

121. Sharma, N. R. A Mechanistic Investigation into Iron Catalysed Kumada Cross-Coupling Reactions. (University of Bristol, 2017).

122. Klose, A. *et al.* Magnetic Properties Diagnostic for the Existence of Iron(II)-Iron(II) Bonds in Dinuclear Complexes Which Derive from Stepwise Insertion Reactions on

Unsupported Iron-Aryl Bonds. *J. Am. Chem. Soc.* **116**, 9123–9135 (1994).

123. Sun, C.-L., Krause, H. & Fürstner, A. A Practical Procedure for Iron-Catalyzed Cross-Coupling Reactions of Sterically Hindered Aryl-Grignard Reagents with Primary Alkyl Halides. *Adv. Synth. Catal.* **356**, 1281–1291 (2014).

124. Buscagan, T. M., Oyala, P. H. & Peters, J. C. N2-to-NH3 Conversion by a triphos–Iron Catalyst and Enhanced Turnover under Photolysis. *Angew. Chem. Int. Ed.* **56**, 6921–6926 (2017).

126. Kuriyama, S. *et al.* Azaferrocene-Based PNP-Type Pincer Ligand: Synthesis of Molybdenum, Chromium, and Iron Complexes and Reactivity toward Nitrogen Fixation. *Eur. J. Inorg. Chem.* **2016**, 4856–4861 (2016).

127. Chalkley, M. J., Oyala, P. H, Peters, J. C. Cp* noninnocence leads to a remarkably weak C–H bond via metallocene protonation. *J. Am. Chem. Soc.* **141**, 4721–4729 (2019).

128. Gusev, O. V. *et al.* Palladium complexes with metallocene-bridged bidentate diphosphine ligands: Synthesis, structure, and catalytic activity in amination and cross-coupling reactions. *Organometallics* **25**, 2750–2760 (2006).

129. Yuki, M., Miyake, Y., Nishibayashi, Y., Wakiji, I. & Hidai, M. Synthesis and reactivity of tungsten- and molybdenum-dinitrogen complexes bearing ferrocenyldiphosphines toward protonolysis. *Organometallics* **27**, 3947–3953 (2008).

130. Connelly, N. G. & Geiger, W. E. Chemical redox agents for Organometallic Chemistry. *Chemical Reviews* **96**, 877–910 (1996).

131. Am, H. J., Tilborg, van, Electron Spectrosc Relat, J. J. & results, unpublished. Syntheses and Structures of Decamethylmetallocenes Most of the decamethylmetallocenes and their monocationic deriva-tives exhibit Dsd molecular symmetry in the solid state: *Org. Chem* **104**, 3–83 (1982).

132. Rudie, A. W., Lichtenberg, D. W., Katcher, M. L. & Davison, A. Comparative Study of Bidentate Ligands Contribution from the Comparative Study of 1,1-Bis(diphenylphosphino)cobaltocenium Hexafluorophosphate and 1,1-Bis

(diphenylphosphino) ferrocene as Bidentate Ligands. *Inorg. Chem.* **17**, 2859 (1978).

133. Brasse, C. C., Englert, U., Salzer, A., Waffenschmidt, H. & Wasserscheid, P. Ionic phosphine ligands with cobaltocenium backbone: novel ligands for the highly selective, biphasic, rhodium-catalyzed hydroformylation of 1-octene in Ionic liquids. *Organometallics* **19**, 3818–3823 (2000).

134. Reichl, K. D. *et al.* Synthesis and electrochemistry of 1,1'-bis(phosphino)cobaltocenium compounds. *J. Organomet. Chem.* **696**, 3882–3894 (2011).

135. Guan, J. *et al.* Dppc+PF6–—PdCl2–[bmim][PF6]–a copper-free recyclable catalytic system for Sonogashira coupling reaction. *Appl. Organomet. Chem.* **21**, 355–359 (2007).

136. Sanders, R. & Mueller-Westerhoff, U. T. The lithiation of ferrocene and ruthenocene: a retraction and an improvement 1. *J. Organomet. Chem.* **512**, 219–224 (1996).

137. Herskovitz, T. et al. Structure and properties of a synthetic analogue of bacterial iron-sulfur proteins. *Proceedings of the National Academy of Sciences* **69**, 2437–2441 (1972).

138. Mayerle, J. J. et al. Synthetic analogs of the active sites of iron-sulfur proteins. structure and properties of bis[o-xylyldithiolato-μ-2-sulfidoferrate(iii)], an analog of the 2Fe-2S proteins. *Proceedings of the National Academy of Sciences* **70**, 2429–2433 (1973).

139. Rutchick, S., Kim, S. & Walters, M. A. Facile one-step synthesis of tetrachalcogenotetrairon(2+) (chalcogen = sulfur, selenium) cubane-like centers. *Inorg. Chem.* **27**, 1513–1515 (1988).

140. Do, Y., Simhon, E. D., Holm, R. H. Improved syntheses of tetrachlorodi-.Mu.-sulfidodiferrate(2-) ([Fe$_2$S$_2$Cl$_4$]$^{2-}$) and Hexachloro-.Mu.-oxodiferrate(2-) ([Fe$_2$OCl$_6$]$^{2-}$) and oxo/sulfido ligand substitution by use of silylsulfide reagents. *Inorg. Chem.* **22**, 3809–3812 (1983).

141. Scott, T. A. & Zhou, H.-C. The first all-cyanide Fe$_4$S$_4$ cluster: [Fe$_4$S$_4$(CN)$_4$]$_3$? *Angew.*

Chem. Int. Ed. **43**, 5628–5631 (2004).

142. Schunn, R. A., Fritchie, C. J. Prewitt, C. T. Syntheses of some cyclopentadienyl transition metal sulfides and the crystal structure of (C_5H_5FeS)$_4$. *Inorg. Chem.* **5**, 892–899 (1966).

143. Kunkely, H.; Vogler, A. Photoreactivity of $Fe_2S_2(CO)_6$ originating from dσ* metal-to-ligand charge transfer excitation. Journal of Organometallic Chemistry **568**, 291–293 (1998).

144. Sickerman, N. S. *et al.* Reduction of C 1 Substrates to Hydrocarbons by the Homometallic Precursor and Synthetic Mimic of the Nitrogenase Cofactor. *J. Am. Chem. Soc* **139**, 35 (2017).

145. Lee, C. C., Stiebritz, M. T; Hu, Y. Reactivity of [Fe_4S_4] clusters toward C1 substrates: Mechanism, implications, and potential applications. *Acc. Chem. Res*. **52**, 1168–1176 (2019).

146. Rettberg, L. A. *et al.* Structural and Mechanistic Insights into CO2 Activation by Nitrogenase Iron Protein. *Chem. - A Eur. J.* **25**, 13078–13082 (2019).

147. Dong, M. et al. Organometallic complex formed by an unconventional radical s-adenosylmethionine enzyme. *J. Am. Chem. Soc*. **138**, 9755–9758 (2016).

148. Dong, M. *et al.* Organometallic and radical intermediates reveal mechanism of diphthamide biosynthesis. *Science (80-.).* **359**, 1247–1250 (2018).

149. Ye, M., Thompson, N. B., Brown, A. C., Suess, D. L. A synthetic model of enzymatic [Fe_4S_4]–alkyl intermediates. *J. Am. Chem. Soc.* **141**, 13330–13335 (2019).

150. McSkimming, A., Sridharan, A., Thompson, N. B., Müller, P., Suess, D. L. An [Fe_4S_4]$^{3+}$–alkyl cluster stabilized by an expanded scorpionate ligand. *J. Am. Chem. Soc.* **142**, 14314–14323 (2020).

151. Chen, X.-D., Zhang, W., Duncan, J. S., Lee, S. C. Iron–amide–sulfide and iron–imide–sulfide clusters: Heteroligated core environments relevant to the nitrogenase FeMo cofactor. *Inorg. Chem. 51*, 12891–12904 (2012).

152. Pollock, C. J. et al. Light-atom influences on the electronic structures of iron–sulfur

clusters. *Inorg. Chem.* **53**, 2591–2597 (2014).

153. Baran, P. *et al.* Synthesis, Characterization, and Study of Octanuclear Iron-Oxo Clusters Containing a Redox-Active Fe$_4$O$_4$ -Cubane Core. *Inorg. Chem.* **47**, 645–655 (2008).

154. Lazarou, K. A., González-Nieves, K., Chakraborty, I. & Raptis, R. G. Spontaneous Resolution by Crystallization of an Octanuclear Iron(III) Complex Using Only Racemic Reagents. *Angew. Chem. Int. Ed.* **58**, 7324–7328 (2019).

155. Henthorn, J. T. et al. Localized electronic structure of nitrogenase FeMoco revealed by selenium K-edge high resolution X-ray absorption spectroscopy. *J. Am. Chem. Soc.* **141**, 13676–13688 (2019).

156. Umena, Y., Kawakami, K., Shen, J. R. & Kamiya, N. Crystal structure of oxygen-evolving photosystem II at a resolution of 1.9Å. *Nature* **473**, 55–60 (2011).

157. Mullins, C. S. & Pecoraro, V. L. Reflections on small molecule manganese models that seek to mimic photosynthetic water oxidation chemistry. *Coord. Chem. Rev.* **252**, 416–443 (2008).

158. Babic-Samardzija, K. *et al.* Structural and magnetic susceptibility study of an octanuclear Mn III -oxo-pyrazolido complex. *Polyhedron* **149**, 142–147 (2018).

159. Ehlert, M. K., Rettig, S. J., Storr, A., Thompson, R. C. & Trotter, J. Oligometallic cobalt 3,5-dimethylpyrazolate complexes: Synthesis, structural and magnetic studies. *Can. J. Chem.* **71**, 1425–1436 (1993).

160. Yoshida, J., Kondo, S.Yuge, H. A synthetic strategy for a new series of oxo-centered tricobalt complexes with mixed bridging ligands of acetate and pyrazolate anions. *Dalt. Trans.* **42**, 2406–2413 (2013).

161. Mayerle, J. J. et al. Synthetic analogs of the active sites of iron-sulfur proteins. structure and properties of bis[o-xylyldithiolato-μ 2-sulfidoferrate(iii)], an analog of the 2Fe-2S proteins. *Proceedings of the National Academy of Sciences* **70**, 2429–2433 (1973).

162. Duncan, J. S., Zdilla, M. J., Lee, S. C. Synthesis and elaboration of the dinuclear iron-

imide cluster core $[Fe_2(\mu\text{-}NR)_2]^{2+}$. *Inorg. Chem.* **46**, 1071–1080 (2007).

163.   Duncan, J. S., Nazif, T. M., Verma, A. K., Lee, S. C. Iron–arylimide clusters $[Fe_m(NAr)_nCl_4]^{2-}$ (m, n = 2, 2; 3, 4; 4, 4) from a ferric amide precursor: synthesis, characterization, and comparison to Fe–S chemistry. *Inorg. Chem.* **42**, 1211–1224 (2003).

Appendix

Crystallographic Data

Crystallographic Data for **17[Li(12c4)₂]**

Identification code	HW555
Empirical formula	$C_{50}H_{86}Br_4Fe_2Li_2O_{16}$
Formula weight	1388.40
Temperature/K	100(2)
Crystal system	monoclinic
Space group	$P2_1/c$
a/Å	11.9508(3)
b/Å	16.2993(4)
c/Å	15.6537(3)
α/°	90
β/°	107.4275(13)
γ/°	90
Volume/Å³	2909.21(12)
Z	2
ρ_{calc}g/cm³	1.585
μ/mm⁻¹	3.309
F(000)	1424.0
Crystal size/mm³	0.296 × 0.156 × 0.06
Radiation	MoKα (λ = 0.71073)
2Θ range for data collection/°	3.572 to 54.196
Index ranges	-15 ≤ h ≤ 15, -20 ≤ k ≤ 20, -20 ≤ l ≤ 20
Reflections collected	49230
Independent reflections	6406 [R_{int} = 0.0517, R_{sigma} = 0.0306]
Data/restraints/parameters	6406/316/404
Goodness-of-fit on F²	1.031
Final R indexes [I>=2σ(I)]	R_1 = 0.0294, wR_2 = 0.0618
Final R indexes [all data]	R_1 = 0.0424, wR_2 = 0.0658
Largest diff. peak/hole / e Å⁻³	0.78/-0.61

Crystallographic Data for **8[Mg(THF)₆]**

Identification code	HW556
Empirical formula	$C_{68}H_{108}Br_2Fe_2MgO_8$
Formula weight	1349.37
Temperature/K	99.99
Crystal system	monoclinic
Space group	$P2_1/n$
a/Å	10.7852(7)
b/Å	16.5842(10)
c/Å	19.4272(13)
α/°	90
β/°	92.1354(12)
γ/°	90
Volume/Å³	3472.4(4)
Z	2
ρ_{calc}g/cm³	1.291
μ/mm⁻¹	1.627
F(000)	1428.0
Crystal size/mm³	0.409 × 0.312 × 0.138
Radiation	MoKα (λ = 0.71073)
2Θ range for data collection/°	4.196 to 54.348
Index ranges	-13 ≤ h ≤ 13, -21 ≤ k ≤ 21, -24 ≤ l ≤ 24
Reflections collected	43332
Independent reflections	7700 [R_{int} = 0.0370, R_{sigma} = 0.0272]
Data/restraints/parameters	7700/114/410
Goodness-of-fit on F²	1.037
Final R indexes [I>=2σ (I)]	R_1 = 0.0283, wR_2 = 0.0642
Final R indexes [all data]	R_1 = 0.0407, wR_2 = 0.0682
Largest diff. peak/hole / e Å⁻³	1.03/-0.30

Crystallographic Data for **21**

Identification code	HW414_testO
Empirical formula	$C_{18}H_{28}Cl_2Fe_2P_2$
Formula weight	488.94
Temperature/K	100.0
Crystal system	orthorhombic
Space group	Pnma
a/Å	14.3326(3)
b/Å	16.4884(4)
c/Å	8.8649(2)
α/°	90
β/°	90
γ/°	90
Volume/Å^3	2094.97(8)
Z	4
ρ_{calc}g/cm^3	1.550
μ/mm^{-1}	1.791
F(000)	1008.0
Crystal size/mm^3	0.652 × 0.464 × 0.312
Radiation	MoKα (λ = 0.71073)
2Θ range for data collection/°	4.94 to 55.108
Index ranges	-18 ≤ h ≤ 18, -21 ≤ k ≤ 21, -11 ≤ l ≤ 11
Reflections collected	105303
Independent reflections	2511 [R_{int} = 0.0230, R_{sigma} = 0.0052]
Data/restraints/parameters	2511/0/117
Goodness-of-fit on F^2	1.099
Final R indexes [I>=2σ (I)]	R_1 = 0.0165, wR_2 = 0.0444
Final R indexes [all data]	R_1 = 0.0169, wR_2 = 0.0448
Largest diff. peak/hole / e Å^{-3}	0.35/-0.25

Crystallographic Data for **19**

Identification code	HW417
Empirical formula	$C_{34}H_{28}Cl_2Fe_2P_2$
Formula weight	681.10
Temperature/K	99.99
Crystal system	triclinic
Space group	P-1
a/Å	9.6323(15)
b/Å	9.7854(15)
c/Å	18.152(3)
α/°	96.389(8)
β/°	99.710(7)
γ/°	115.384(7)
Volume/Å^3	1490.9(4)
Z	2
ρ_{calc}g/cm^3	1.517
μ/mm^{-1}	1.283
F(000)	696.0
Crystal size/mm^3	0.528 × 0.477 × 0.395
Radiation	MoKα (λ = 0.71073)
2Θ range for data collection/°	4.654 to 41.624
Index ranges	-9 ≤ h ≤ 9, -9 ≤ k ≤ 9, -17 ≤ l ≤ 18
Reflections collected	12331
Independent reflections	2986 [R_{int} = 0.0337, R_{sigma} = 0.0295]
Data/restraints/parameters	2986/0/361
Goodness-of-fit on F^2	1.034
Final R indexes [I>=2σ (I)]	R_1 = 0.0219, wR_2 = 0.0554
Final R indexes [all data]	R_1 = 0.0262, wR_2 = 0.0566
Largest diff. peak/hole / e Å^{-3}	0.33/-0.29

Crystallographic Data for **20**

Identification code	HW463B
Empirical formula	$C_{22}H_{36}Cl_2Fe_2P_2$
Formula weight	545.05
Temperature/K	100.08
Crystal system	orthorhombic
Space group	Pbcn
a/Å	13.3574(3)
b/Å	13.6802(3)
c/Å	13.5542(3)
α/°	90
β/°	90
γ/°	90
Volume/Å^3	2476.78(10)
Z	4
ρ_{calc}g/cm^3	1.462
μ/mm^{-1}	1.523
F(000)	1136.0
Crystal size/mm^3	1.132 × 0.647 × 0.397
Radiation	MoKα (λ = 0.71073)
2Θ range for data collection/°	4.262 to 55.098
Index ranges	-17 ≤ h ≤ 17, -17 ≤ k ≤ 17, -13 ≤ l ≤ 17
Reflections collected	20447
Independent reflections	2860 [R_{int} = 0.0171, R_{sigma} = 0.0106]
Data/restraints/parameters	2860/0/132
Goodness-of-fit on F^2	1.066
Final R indexes [I>=2σ (I)]	R_1 = 0.0178, wR_2 = 0.0468
Final R indexes [all data]	R_1 = 0.0192, wR_2 = 0.0476
Largest diff. peak/hole / e Å^{-3}	0.37/-0.26